



HAL
open science

TOWARDS A COMPUTER VISION BASED QUALITY ASSESSMENT OF TAHITIAN PEARLS

Martin Loesdau

► **To cite this version:**

Martin Loesdau. TOWARDS A COMPUTER VISION BASED QUALITY ASSESSMENT OF TAHITIAN PEARLS: Automatic Nacre Thickness Measurement and Color Classification. Computer Science [cs]. Université de la Polynésie française, 2016. English. NNT: . tel-01484171

HAL Id: tel-01484171

<https://theses.hal.science/tel-01484171>

Submitted on 6 Mar 2017

HAL is a multi-disciplinary open access archive for the deposit and dissemination of scientific research documents, whether they are published or not. The documents may come from teaching and research institutions in France or abroad, or from public or private research centers.

L'archive ouverte pluridisciplinaire **HAL**, est destinée au dépôt et à la diffusion de documents scientifiques de niveau recherche, publiés ou non, émanant des établissements d'enseignement et de recherche français ou étrangers, des laboratoires publics ou privés.



UNIVERSITÉ DE LA POLYNÉSIE FRANÇAISE

ÉCOLE DOCTORALE DU PACIFIQUE ED 469

Laboratoire Géopôle du Pacifique Sud

THÈSE

présentée et soutenue publiquement par
Martin Loesdau

le 12 décembre 2016

en vue de l'obtention du titre de
Docteur de l'Université de Polynésie française en
Département : **Science**
Discipline : **Informatique CNU 27**
Spécialité : **Traitement d'images, apprentissage artificielle**

TOWARDS A COMPUTER VISION BASED QUALITY ASSESSMENT OF TAHITIAN PEARLS

Automatic Nacre Thickness Measurement and Color Classification

Sous la direction de : Alban Gabillon et Sébastien Chabrier

JURY

Luc BRUN, Professeur des Universités, ENSICAEN
Christophe ROSENBERGER, Professeur des Universités, ENSICAEN
Cédrik LO, Docteur, Direction des Ressources Marines et Minières
Jean-Martial MARI, Maître de conférences, Université de la Polynésie française
Sébastien CHABRIER, Maître de conférences, Université de la Polynésie française
Alban GABILLON, Professeur des Universités, Université de la Polynésie française

Rapporteur
Rapporteur
Examineur
Examineur
Directeur de thèse
Directeur de thèse

Abstract

The nacre thickness measurement of Tahitian pearls is part of an obligatory quality control for pearls deemed for exportation. It is currently done manually by government experts for over 7 million pearls annually with an export volume of over 61 million €. In Part I of this thesis our algorithm to automatize this procedure under consideration of the unique features of Tahitian pearls is presented. The developed algorithm was tested on X-ray images of 298 Tahitian pearls that were classified manually by government experts. The detection accuracy of our algorithm reaches 98% in its basic form and 100% with a proposed optimized version. A prototype was developed and is currently implemented at the governmental institution in charge of the obligatory control. In Part II of this thesis, our work on normalized *rgb* color space theory and the classification of Tahitian pearls based on their perceived color is presented. A quintessence of the presented work is the formalization of chromatic index calculation in the context of normalized *rgb* histogram binning. It is shown that every chromatic index based on a linear combination of normalized *rgb* channels can be expressed by a single variable; an angle that corresponds to the human perceptual parameter Hue. Experimental classifications based on Artificial Neural Networks and chromatic indices over the whole possible range of the normalized *rgb* color space were conducted by classifying 150 Tahitian pearls that were labeled by 7 experts. The results show that the choice of chromatic indices affects significantly the classification performance of an ANN with a given topology. The global performance varies within a range of up to 20% over the tested feature vectors. Furthermore does the classification accuracy of each class depend on the chosen index, with variations up to 100% between different feature vectors. These findings are of great importance for computer vision applied to color object classification, as currently only a handful of chromatic indices are used in the literature, which is a drastic limitation of possible classification results. Additionally, a new binning strategy is proposed that takes into account the topology of the normalized *rgb* color space. The application of the proposed topological binning has in tendency a positive effect on the global classification rate when compared to standard equidistant binning. For certain human classifications, the accuracy difference is significant with variations of up to 18%. Furthermore, it is shown that it is generally feasible to classify Tahitian pearls based on their perceived color. Classification rates of over 84% for training and over 79% for test data are reached for all 8 used human classifications.

Résumé

La mesure de l'épaisseur de la nacre des perles de Tahiti s'inscrit dans un processus de contrôle obligatoire de la qualité des perles destinées à l'exportation. Ce contrôle est actuellement opéré manuellement par des experts du Pays et porte sur plus de 7 millions de perles par an, pour un montant à l'exportation supérieur à 58 millions d'euros. Dans la première partie de cette thèse, nous présentons l'algorithme que nous avons développé afin d'automatiser ce contrôle. L'algorithme a été soumis à un banc d'essai de 298 perles classées par des experts du Pays et présentées sous forme d'images prises aux rayons X. La version standard de notre algorithme permet d'obtenir une précision de détection de 98%. Une version optimisée est proposée, qui atteint une précision de détection de 100%. Un prototype a été développé et est actuellement implémenté par les autorités chargées du contrôle. Dans la seconde partie, nous présentons notre travail sur la théorie de l'espace colorimétrique normalisée *rgb* ainsi que sur la classification des perles de Tahiti d'après leurs couleurs perçues. L'apport central de ce travail est la formalisation du calcul des indices chromatiques dans le contexte du calcul d'histogramme *rgb*. On montre notamment que tous les indices chromatiques basés sur une combinaison linéaire des canaux *rgb* peuvent être exprimés au moyen d'une variable unique : l'angle correspondant au paramètre perceptuel 'Teinte'. Des classifications expérimentales par réseau de neurones artificiels avec des indices chromatiques balayant tout l'espace *rgb* ont été conduites sur 150 perles étiquetées par 7 experts. Les résultats montrent que le choix de l'indice chromatique affecte grandement les performances d'un réseau de neurones pour une topologie de connections donnée, avec une variation de la performance globale dépassant 20%. De plus, la précision de classification de chaque classe dépend aussi de l'indice choisi, avec une variation allant jusqu'à 100% entre différents indices. Ces constatations sont d'une grande importance en matière de vision par ordinateur appliquée à la classification de la couleur des objets. En effet, seuls quelques indices chromatiques sont actuellement utilisés dans la littérature, ce qui constitue une limitation forte du potentiel de classification en termes de résultats. En outre, une nouvelle stratégie de répartition des classes des histogrammes *rgb* est proposée, qui prend en compte la topologie de l'espace *rgb* normalisé. Son application a un effet positif potentiel sur le taux global de classification comparativement à la classification avec une répartition équidistante standard. Pour certaines classifications humaines, la différence de précision est significative, avec des variations allant jusqu'à 18%. De plus, on montre qu'il est généralement possible de classer les perles de Tahiti selon leurs couleurs perçues. Pour chacune des 8 classifications humaines utilisées, le taux de classification est supérieur à 84% sur l'ensemble d'apprentissage et 79% sur l'ensemble de test.

Acknowledgements

First and foremost I would like to express my sincere gratitude to my PhD advisor Alban Gabillon. Not only has he been an excellent scientific mentor to me, but an example of professional and personal integrity. Besides his continuous commitment to my work and our project (throughout my work on this thesis he organized presentations for and meetings with those involved in the French Polynesian pearl business, hereby constantly increasing our network of support and cooperation, as well as he achieved substantial second- and third-party funding for our project from the Ministry of Overseas France and the French Polynesian Government) his support for his students exceeds by far the purely scientific level (he was for example the first one to visit me at the Ta'aone hospital after I underwent a rather nasty surgery). For all his support on so many levels I am sincerely grateful.

My sincere gratitude goes as well to my co-advisor Sébastien Chabrier for sharing his knowledge and experience in image processing and artificial intelligence. As Alban, Sébastien was an advisor to rely upon even if the matter was 'non-scientific'.

I am very grateful to the members of the reading committee Christophe Rosenberger and Luc Brun for their detailed and constructive reports on my manuscript. I am as well thankful to both for participating in the oral defense committee. I am thankful to Jean-Martial Mari for the fruitful discussions at the laboratory, as well as for his participation in the oral defense committee. Likewise I would like to thank Cédrik Lo for his participation in the oral defense committee, as well as for his support as member of the *Direction des Ressources Marines et Minières*, an essential partner of our project concerning the automatic nacre thickness measurement of Tahitian pearls. As well working at the DRMM, I would like to thank Hinano Teanotoga and Vaihere Moorria and all employees of the DRMM who supported this work with their knowledge and experience. Essential for my work on the color classification of Tahitian pearls was the collaboration with the IFEREMR institute. Here, I would like to thank especially Denis Saulnier and Gilles Le Moullac for their support.

I am very grateful to Jean-Pierre Barriot, the director of my laboratory, by far not only, but very specifically for the labs policy of providing financial support primarily to its PhD students to publish and participate in international conferences; a policy that is exemplary, especially seeing the high cost of travelling abroad from French Polynesia.

I am sincerely grateful to Firas al-Khalil, Aymeric Hermann, Jonathan Serafini, Elise Lacoste, Lucie Pheulpin, Gaëlle Legras, Nicolas Loiseau, Simon Van Wynsberge and all the others who, every once in a while, succeeded in dragging me away from my computer to enjoy the

pleasures that Tahiti and friendship can provide. I am equally thankful to all those who succeeded in dragging me back to my computer afterwards.

Finally, my utmost gratitude goes to my family. Seeing the son or the brother leave for a place 16000 km away on the other side of the globe might not have been easy. Still, you have been supporting me uncompromisingly (as you always did). I hope this work makes you proud, as you being proud is one of the main motivations for me doing what I do.

Martin Loesdau

Content

1	Introduction.....	12
1.1	Pearl Formation.....	14
1.2	The Tahitian Pearl.....	16
1.3	Cultivation of Tahitian Pearls	17
1.4	Pearl Quality Parameters	20
1.4.1	Color	20
1.4.2	Shape.....	20
1.4.3	Size	21
1.4.4	Luster	21
1.4.5	Surface Quality	21
1.4.6	Nacre Thickness.....	22
1.5	Pearl Business in French Polynesia.....	22
1.6	French Polynesian Research Landscape Concerning the Tahitian Pearl	25
1.6.1	Living conditions and threats to the pearl oyster	26
1.6.2	Pearl formation and pearl quality	26
1.6.3	Commercialization of the Tahitian pearl	26
1.7	The RAPA Project.....	27
1.7.1	Research projects concerning pearl formation and pearl quality.....	27
1.7.2	Commercialization of the Tahitian pearl	28
1.7.3	Pearl quality certificate	28
1.7.4	Alternative quality assessment	28
2	Computer Vision Applied to Pearl Classification: State of the Art	29
3	Structure and Contribution of this Thesis.....	33
3.1	Part I: Automatic Nacre Thickness Measurement.....	33
3.2	Part II: Automatic Color Classification.....	34
3.3	Oral Presentations	35
3.4	Publications	36
	List of Figures	37
	Bibliography.....	39

Part I

Automatic Nacre Thickness Measurement

Content	45	
1	Introduction.....	48
1.1	Manual Nacre Thickness Evaluation.....	49

1.2	Pearl Configuration	50
1.3	Automatizing the Nacre Thickness Evaluation	52
1.3.1	General Requirements	52
1.3.2	Automatic Image Acquisition	52
1.4	Acquired Images	53
1.4.1	Special Cases	54
1.4.2	Human Evaluation	55
1.5	Image Processing Methodology	56
1.5.1	Basic Concept	57
1.5.2	Pearl Segmentation	57
1.5.3	Nucleus Detection.....	58
1.5.4	Cavity Detection	59
1.5.5	Nacre Thickness Profile.....	60
1.5.6	Identification of Rejects and Certainty Value	60
1.5.7	Used Hard- and Software.....	62
1.6	Automatic Measurement Results	62
1.7	Structure of Part I	63
2	Related Work.....	65
3	Pearl Segmentation	67
3.1	Main Challenges.....	67
3.1.1	Region-Based Approach.....	69
3.1.2	Edge-Based Approach	70
3.1.3	Active Contours	71
3.1.4	Model Based Approach	73
3.2	Implemented Approach.....	74
3.2.1	Image Calibration	74
3.2.2	Synthetic Background Generation.....	77
3.2.3	Pearl Segmentation	79
3.2.4	Artefacts.....	80
3.2.5	Summary and Pseudocode	82
3.3	Precision of Results	82
3.3.1	Visual Analysis	83
3.3.2	Precision Measurement.....	86
3.4	Discussion	88
3.4.1	Discrepancy Types.....	89
3.4.2	Processing Time.....	90
3.4.3	Optimization Possibilities	90
3.4.4	Background Configuration	91
3.4.5	Alternative Support Configuration	92
3.5	Conclusion.....	93
4	Nucleus Detection.....	94
4.1	Main Challenges.....	94
4.1.1	Model-Based Approach	96

4.1.2	Region-Based Approach.....	96
4.1.3	Edge-Based Approach	97
4.1.4	Circular Hough Transform	99
4.1.5	Other Circle Detection Approaches	100
4.2	Our Approach.....	100
4.2.1	Intensity Based Probability Function.....	102
4.2.2	Gradient Based Probability Function.....	103
4.2.3	Moving Direction.....	106
4.2.4	Moving Speed and Radius Increment	107
4.2.5	Optimum Detection	108
4.2.6	Handling of Segmentation Artefacts	108
4.2.7	Summary and Pseudocode	109
4.3	Precision of Results	111
4.4	Discussion	112
4.4.1	Threshold Related Discrepancies	113
4.4.2	Cavity Related Discrepancies	114
4.4.3	Weak Boundary Related Discrepancies.....	114
4.4.4	Nucleus Visibility	118
4.4.5	Self-Evaluation	120
4.4.6	Processing Time.....	122
4.4.7	Optimization Possibilities	123
4.5	Conclusion.....	124
5	Cavity Detection	126
5.1	Main Challenges.....	126
5.1.1	Model Based Approach	128
5.1.2	Active Contour.....	129
5.1.3	Region Based Approach	129
5.1.4	Edge Based Approach.....	130
5.2	Implemented Approach.....	132
5.2.1	Neighborhood Range and Region Growing Rule	132
5.2.2	Previous Segmentation Artefacts.....	134
5.2.3	Pseudocode	135
5.3	Precision of Results	135
5.4	Discussion	137
5.4.1	Discrepancy to Intuitive Boundary Setting.....	138
5.4.2	Processing Time.....	140
5.4.3	Optimization Possibilities	140
5.5	Conclusion.....	141
6	Nacre Thickness Profile Calculation.....	142
7	Certainty Measurement.....	144
8	Results	146
9	Discussion.....	148

9.1	Intensity vs Gradient Based Cavity Detection	151
9.2	Manual vs Numerical Rejection	152
9.3	Summary	154
9.4	Processing Time	158
9.5	Optimization Possibilities	158
10	Prototype	160
11	Conclusion.....	162
12	Future Work	163
	List of Figures	164
	Bibliography.....	169

Part II

Color Classification

	Content	173
1	Introduction.....	175
1.1	Manual Classification.....	175
1.2	Data Acquisition.....	177
1.3	Theoretical Work on Normalized <i>rgb</i> Histograms.....	178
1.4	Experiments.....	178
1.5	Results	179
1.6	Structure of Part II.....	181
2	Related Work.....	182
3	On Normalized <i>rgb</i> Histogram Binning.....	184
3.1	The Normalized <i>rgb</i> Color Space.....	185
3.2	Histogram Calculation.....	186
3.2.1	One-Dimensional Data Distribution	186
3.2.2	Multidimensional Data Distributions	189
3.3	Standard Application.....	191
3.4	Formalizing Normalized <i>rgb</i> Histogram Calculation.....	194
3.5	Topology of the Normalized <i>rgb</i> Color Space.....	199
3.6	Summary	202
4	Data Acquisition.....	204
4.1	Image Acquisition and Preprocessing	204
4.2	Human Classification	206
5	Classification Method	210
5.1	Data Set Splitting	211

5.2	Feature Configuration	213
5.3	ANN Configuration.....	217
5.4	Training and Evaluation Values	218
5.4.1	Qualitative Analysis.....	220
5.4.2	Quantitative Analysis.....	220
5.5	Summary	220
6	Results and Discussion.....	222
6.1	Qualitative Analysis	222
6.1.1	Channel Redundancy	222
6.1.2	Influence of Histogram Orientation per Agent.....	223
6.1.3	Influence of Histogram Orientation per Color Class	225
6.1.4	Equidistant Binning vs Topological Binning	229
6.1.5	Summary	231
6.2	Quantitative Analysis	231
6.2.1	Accuracy Range	232
6.2.2	Generalization Capabilities.....	234
6.2.3	Preliminary Maximum Classification Results	235
7	Conclusion	236
8	Future Work.....	238
	List of Figures	239
	Bibliography.....	242

1 Introduction

The Tahitian pearl is a precious gem that is cultivated in the clear warm lagoons of French Polynesia. Due to its mystical dark colors and its brilliant luster the ‘Queen of Pearls’ achieves high prices on the international market. Accordingly, it is a vital source of income for the French Polynesian territory. In 2015, loose Tahitian pearls amounting to over 61 million Euros were exported, being with over 50% by far the most significant source of export income. Besides of contributing to the welfare of the whole French Polynesian community due to export taxes, pearl cultivation employs thousands within the territory. Especially in remote regions such as the Tuamotu islands, where employment possibilities are naturally limited, the cultivation of Tahitian pearls is a welcome source of revenue for the locals. Sustaining and improving the French Polynesian pearl economy is thus of vital interest and is pursued by the local government, local research bodies, pearl farmers and their unions, and various lobby groups.

The variety of scientific effort to support the local pearl economy is owed to its complexity: the balance of the whole lagoon ecosystem is substantial, as is skilled and sustainable oyster farming within the lagoons and an appropriate commercialization on the highly competitive international jewelry market. Accordingly, local research projects comprise the ecophysiology and physiology of pearl oysters, the physiology of pearl formation, the mineralogy of pearls, and the socioeconomics and economics of pearl commercialization. To contribute to the joint effort, the computer science group of the University of French Polynesia founded in 2013 the project RAPA¹ (**R**econnaissance **A**utomatique de la qualité des **P**erles de **T**Ahiti, *automatic quality assessment of Tahitian pearls*) adding the profession of computer science to the pearl related French Polynesian research landscape. The goal of this project is to assess the six pearl quality parameters color, size, form, luster, surface quality and nacre thickness automatically with computer vision techniques.

Currently, the quality of a pearl is assessed manually by experts. This process has two disadvantages. First, objective grades are difficult to assess for certain perceptual parameters such as the pearls color, luster or form. Hence, the assessed quality (and therefore the pearls price) is subjective and depends on the skills and expertise of the expert as well as it can

¹ 2 years project (2015-2016) funded by the Ministère des Outre-mer (Ministry of Overseas France)

depend on external parameters such as light source or viewing angle. Secondly, the manual assessment of pearls is time intense, which is an issue seeing the large amount of over 7 million exported pearls annually that have to be graded for valuation. A computer vision based quality assessment aims at objectifying and accelerating the currently manually conducted pearl grading.

This thesis is the first completed within the scope of the RAPA project. It reports on research conducted to automatically assess the two quality parameters nacre thickness and color. Those two parameters were prioritized for the following reasons: an automatized nacre thickness measurement has a direct impact on the current French Polynesian pearl export flux, as it is a crucial parameter of the obligatory quality control of pearls deemed for exportation. The color was chosen as partner institutes are currently working on projects aiming at identifying cultivation parameters that influence the color of the cultivated pearls. To obtain a suitable correlation function between both, a reliable mathematical description of the pearls color, that is as independent as possible from human subjectivity and other external parameters, is necessary. Additionally, the color is one of the most appealing and characteristic parameters of the Tahitian pearl, while being probably the most difficult to access numerically due to its perceptual character and the variety of colors and color combinations that can appear on Tahitian pearls. Tackling the difficult parameter from the beginning was deemed strategically advantageous, to allow a better prediction of the further ongoing of the project.

The two quality parameters color and nacre thickness are fundamentally different. The color is a perceptual parameter that is visually evaluated by observing the surface of the pearl. The computer vision equivalent is an analysis of color images of the pearls surface. The nacre thickness instead is a measurable physical parameter that depends on the internal structure of the pearl and has to be visualized with methods such as X-raying. Due to the different nature of both parameters and the according images, this thesis is divided in two parts. Part I covers the research conducted to automatize the nacre thickness out of X-ray images and Part II covers the color classification based on color images of the pearls surface. Both parts are independent and contain each a specific introduction, description of methods, results, discussion, conclusion, bibliography, etc. A general description of each part and its contribution is given in section 3 while a detailed summary of goals, used methods and results can be found in the introduction section of each part.

As this thesis is the first conducted within the scope of project RAPA this introduction comprises a compendium of topics that build the main motivation, and justification of the project as well as the basic procedures and processes of pearl cultivation in French Polynesia. The given information comprise how pearls are naturally formed within pearl oysters (section 1.1), what differs a Tahitian pearl from other commercialized pearls (section 1.2), the important grafting process during the cultivation to understand the internal structure of cultivated pearls (section 1.3) and the main six quality parameters used to grade pearls (section 1.4) whose automatic assessment is the goal of project RAPA. A summary of the historical and recent development of the pearl economy is given in section 1.5 to understand the reason for an obligatory quality control of Tahitian pearls deemed for exportation and the development of a pearl quality certificate, as well as the potential economic impact of this work. An overview of the French Polynesian research landscape concerning the pearl is given in section 1.6 to underline the complexity of pearl cultivation and its commercialization, as well as to understand current and identify possible future cooperation with project RAPA. The project is introduced more detailed in section 1.7. In section 2, the current state of the art concerning the application of computer vision for the purpose of pearl quality assessment is presented. In section 3, the two parts of this thesis are introduced and the contribution of each part is summarized. Oral presentations given at international conferences and within the scope of this thesis published papers are listed in section 3 as well.

1.1 Pearl Formation

The fundamental biological process of pearl formation is biomineralization of calcium carbonate. All shelled mollusks are capable of biomineralization, as their shell is the product of this very process. The shell is produced by the epithelial cells of the mantle of the soft body of these organisms. The cells secrete a matrix of organic material in which the also secreted calcium carbonate crystalizes, depending on the organic matrix, either to calcite or to aragonite (Figure 1). The composite of organic matrix and aragonite is called nacre or mother-of-pearl. Due to its iridescence, the appearance of different colors depending on view angle and light source, and its luster, nacre has been used for jewelry since centuries.

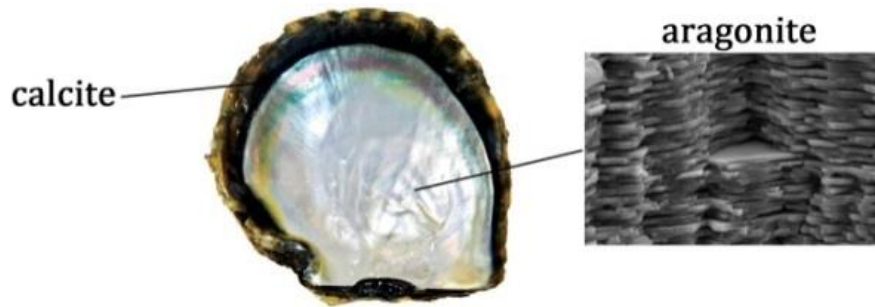


Figure 1: The shell of the pearl oyster *Pinctada margaritifera* contains both crystalline forms of calcium carbonate. The inner iridescent shell consists mainly of aragonite tablets, while the rest consists mainly of calcite prisms.

The same process that underlies the building of the shell forms as well part of the immunological reaction of the organism caused by intrusion of an organic or inorganic irritant. This reaction, which is the basis of pearl formation, is schematically shown in Figure 2. In this example an intruder (in blue) is drilling from the outside through the shell (white region). At a certain point the intruder has reached the outer layer of the mantle of the organism (mantle epithelium in red, third image on the top). As immunological reaction a cyst is formed by the epithelium that eventually surrounds the irritant completely (second image on the bottom, the cyst is commonly called pearl sac). In a similar way the epithelium cells build and maintain the shell of the organism, the pearl sac constantly secretes a composite of organic and inorganic material that is deposited around the irritant (third image on the bottom).

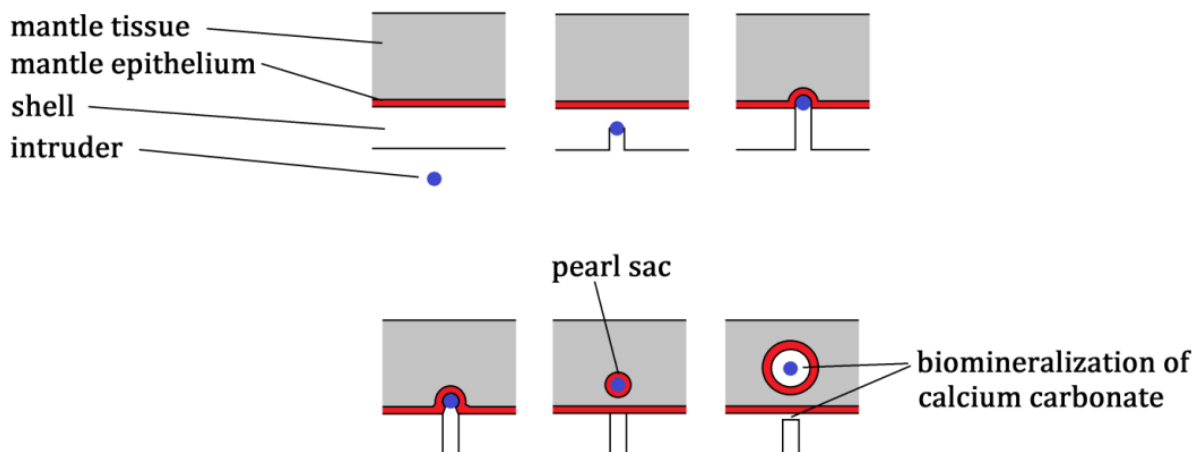


Figure 2: Schema of the immunological reaction of a shelled mollusk caused by intrusion of an irritant through its shell. When the irritant reaches the mantle epithelium it is encapsulated by a cyst formed by epithelium cells (pearl sac). Similar to the biomineralization process performed by the organism to build, maintain and repair the shell, calcium carbonate is deposited around the irritant.

Depending on the crystalline structure of the secreted calcium carbonate, two different geological terms are used for the resulting concretion produced within the pearl sac. The term ‘pearl’ or ‘true pearl’ is reserved for objects that consist mainly (especially the outer layers) of aragonite. Like the inner layers of the shell of the breeding species (Figure 1) pearls are iridescent and lustrous. The term calcareous concretion or non-nacreous pearl is used for objects that are mainly composed of calcite. Due to the different optical properties of calcite, these pearls are not iridescent. Still they can be of high value, mostly due to their rare appearance as they are currently not cultivated rather than found occasionally as byproduct of the fishing industry.

1.2 The Tahitian Pearl

The general characteristic appearance of pearls depends on the breeding pearl oyster species. Pearls produced by the pearl oyster *Pinctada margaritifera* are typically darker than other cultivated pearls, hence the brand ‘black pearl’ was established. As the inner nacreous shell of its breeding species, black pearls can contain a large variety of colors such as green, blue, pink, yellow, peacock and aubergine (Figure 3). The dark appearance and the variety of colors of black pearls is a unique feature compared to other popular cultivated pearls like Akoya, South Sea and Freshwater pearls (Figure 4). Black pearls are currently cultivated in several regions of the Pacific such as French Polynesia, Solomon Islands, Fiji or Kiribati. French Polynesia produces the majority of black pearls (>90%) and has established an own brand: the Tahitian pearl. The term Tahitian pearl is reserved for pearls produced by the pearl oyster species *Pinctada margaritifera* within the lagoons of the French Polynesian territory [CIB15]. The producing pearl oysters have to be collected from the natural stock of the lagoons of the territory. Registering the name ‘Tahitian pearl’ as trademark is currently discussed.

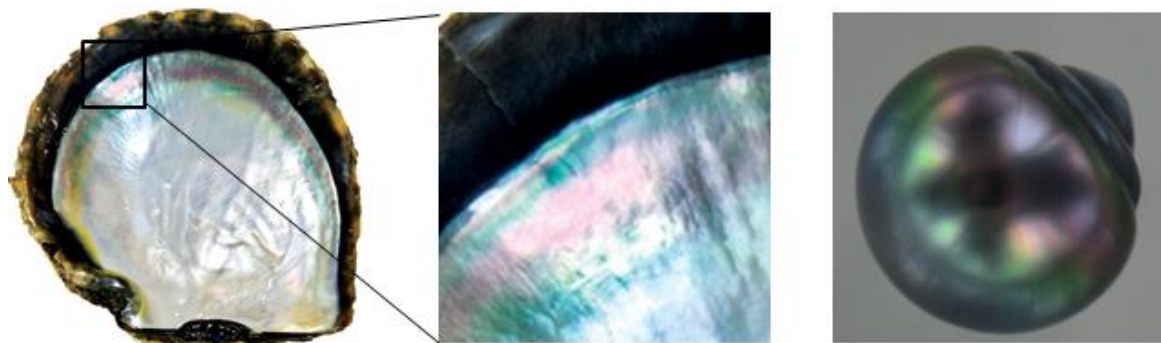


Figure 3: The shell of the pearl oyster *Pinctada margaritifera* (left, detail in the middle) and a Tahitian pearl produced by this species (right). Shell and pearl show similar characteristic color nuances like green, blue, aubergine and pink.






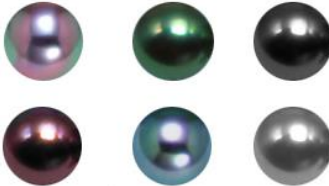




Breeding species		Product	Characteristic color nuances
<i>Pinctada fucata</i>		-Akoya pearl	
<i>Pinctada maxima</i>		-South Sea pearl	
<i>Pinctada margaritifera</i>		-Tahitian pearl -black pearl	
<i>Hyriopsis cumingii</i>		-freshwater pearl -Chinese pearl	
<i>Melo melo</i>		-melo pearl	

Figure 4: Different types of pearl producing species (first two columns), trade names of their pearls (third column) and characteristic color nuances of the pearls (last column). The pearls produced by the species of the first four rows are true pearls as they consist mainly of aragonite layers. The pearl produced by the *Melo melo* sea snail (last column) consist mainly of calcite prisms and is hence a non-nacreous pearl. Image properties: Gemological Institute of America.

1.3 Cultivation of Tahitian Pearls

Cultivating pearls is a complex endeavor beginning with the collection of spats (juvenile pearl oysters that underwent the transition of a free swimming larva to a settling oyster) in the French Polynesian lagoons, their rearing until the age of ~1.5-3 years, pre-grafting conditioning, the grafting to start the pearl formation within the oyster, post grafting care and monitoring (~1.5-2.5 years and more), and finally the harvest. In this section only the grafting process will be explained, as it is vital to understand the inner structure of cultivated pearls. Detailed information about all stages of pearl cultivation can be found in [GER92].

The grafting process is a surgical operation during which an ‘irritant’ is artificially inserted in the tissue of a pearl oyster (Figure 5). A successful grafting results in a process similar to the natural, previously explained immunological reaction of the oyster: the secretion of nacreous material around the inserted irritant that finally forms the pearl. The inserted irritant is composed of two parts: a nucleus and the graft. The graft is a small piece of outer mantle tissue cut from a therefor sacrificed donor oyster (Figure 5 top left). The nucleus is a polished sphere produced out of shell material, usually from North American freshwater mussels (Figure 5 top right). Both are inserted together into the gonad of the host oyster. In the optimal case, the epithelial cells of the inserted graft will form a pearl sac due to cell division that encapsulates the inserted nucleus. Nourished by the surrounding tissue of the host oyster, the epithelial cells are then starting to secrete nacreous material that is deposited around the nucleus.

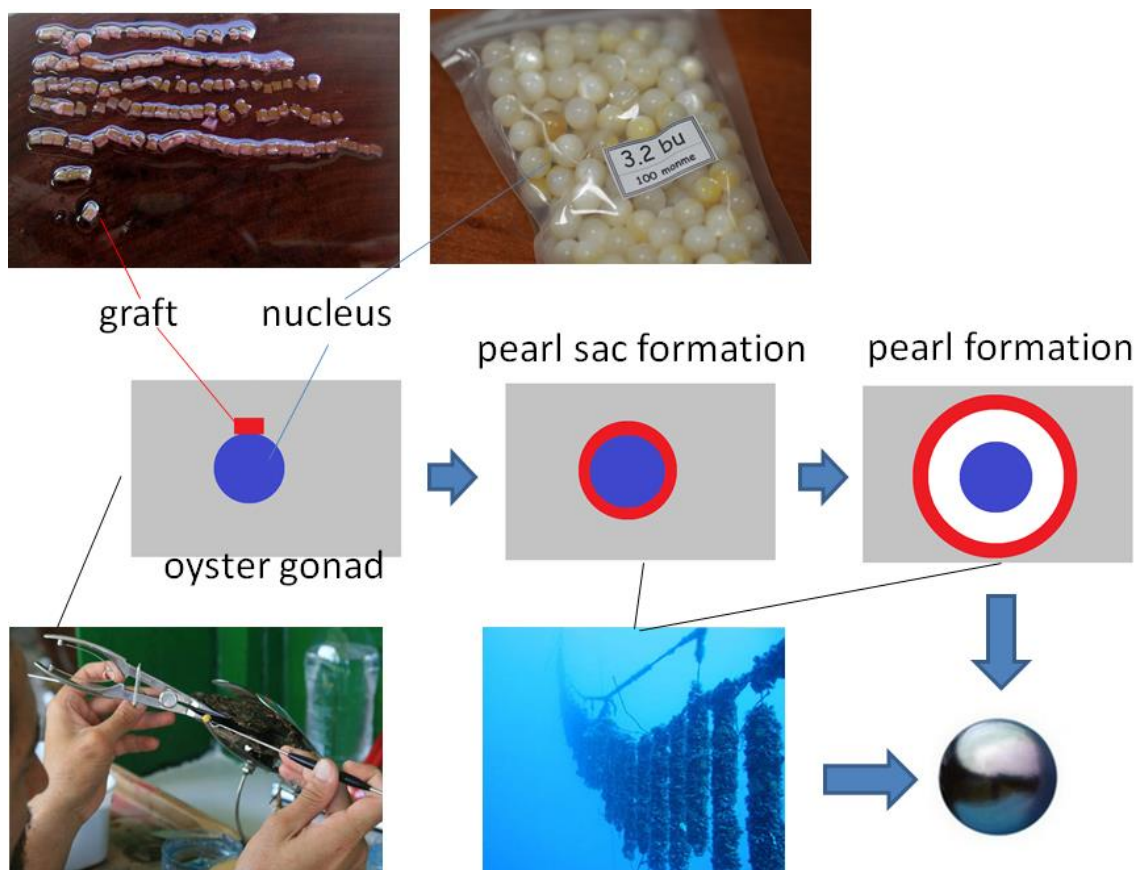


Figure 5: Schema of the grafting process (middle). A piece of mantle tissue (the graft) is placed together with a nucleus within the gonad of a pearl oyster. The grafted oyster is put back in the lagoons. In the optimal case the graft builds a pearl sac around the nucleus and a pearl is formed by biomineralization of calcium carbonate deposited by the cells of the pearl sac around the nucleus.

An important step during the grafting process is the choice of a suitable nucleus size for a given host oyster. On the one hand it should be as large as possible as a larger nucleus will result in a larger pearl and therefore a more valuable one. On the other hand the nucleus size has to correspond to the constitution of the oyster and its gonad. Therefore, nuclei are produced in almost any size ranging from ~2-18 *mm* of diameter. The choice of which nucleus might be optimal for a certain oyster is made by the grafting technician during the grafting process.

Frequently, the oyster rejects the nucleus (~30%). Still, the grafting might result in a nacreous concretion due to the formation of a pearl sac. The resulting product, that is of commercial value as well, is called 'Keshi'. Compared to nucleated pearls, Keshi-pearls are iridescent and lustrous as well but have typically a highly irregular shape. This phenomenon illustrates the role of the graft and the nucleus. While the graft is inserted to form the pearl sac within the gonad, the purpose of the nucleus is to increase the probability of the formation of a round or symmetric pearl. However, the presence of a nucleus within a nacreous concretion can only be evaluated with certainty by imaging techniques such as X-raying (Figure 6).

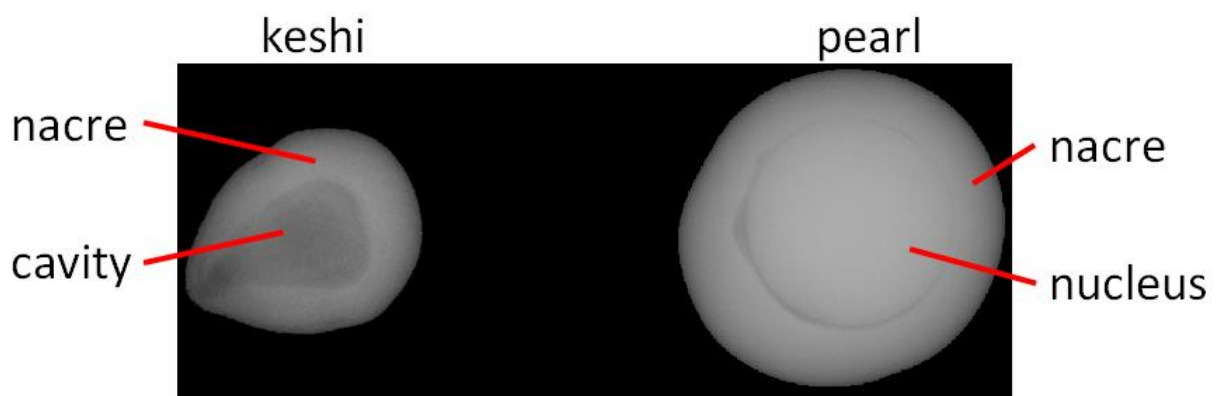


Figure 6: X-ray images of a keshi (left) and a regular cultivated Tahitian pearl (right). The regular pearl contains a nucleus, while the keshi is formed after the oyster rejected the nucleus.

1.4 Pearl Quality Parameters

The quality of cultivated pearls is commonly assessed based on the six parameters color, size, shape, luster, surface quality and nacre thickness. As many of those parameters are perceptual, the description in the following sections is to introduce the vocabulary rather than to give a precise definition (see as well [CIB15] for an extensive list of terms and definitions regarding the international pearl culture and trade).

1.4.1 Color

Evaluated based on the perceptual parameters hue, saturation and intensity. Especially for the Tahitian pearl two terms are used to take into account the appearance of multiple colors: The ‘primary color’ (as well ‘main color’ or ‘body color’) describes the predominant color of the pearl. ‘Secondary colors’ (or ‘overtones’) are those appearing additionally to the primary color and are mainly caused by iridescent effects. Typical colors are green, blue, grey, pink or aubergine.

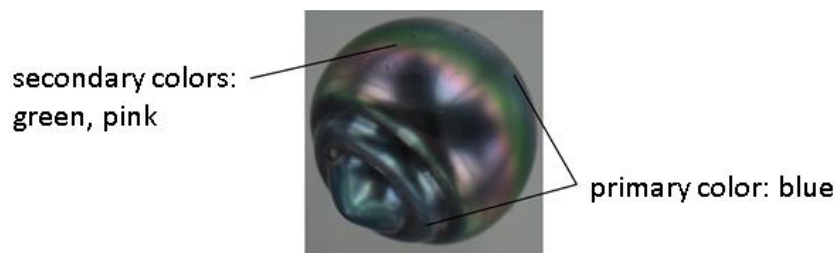


Figure 7: An example of a multi-color Tahitian pearl with blue as primary color and secondary colors green and pink.

1.4.2 Shape

The pearls shape is evaluated based on predefined geometric figures (Figure 8). The most common classes are round, semi-round, oval, drop, button, semi-baroque, baroque, and *cerclé* (circled). In the definition of the DRMM (‘Direction des Ressources Marines et Minières’, French Polynesian administration of marine and mineral resources), semi-baroque pearls have an irregular shape but at least one symmetry axis while baroque pearls have an irregular shape without any symmetry. Pearls that fall in the class *cerclé* contain one or multiple concentric circular indentations. In contrary to most other pearls on the international market, Tahitian pearls are as well traded when of irregular shape, providing that the remaining quality parameters were accordingly.



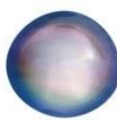





round	semi-round	button	drop	oval	semi-baroque	baroque	cerclé
							

Figure 8: Main pearl shape categories.

1.4.3 Size

The pearls size is typically described as a diameter in metric *mm*. For non-round shapes the minimal diameter and sometimes additionally the maximum diameter are used. A technique applied in French Polynesia is to use a support with through boreholes of different diameters. The size of a pearl is defined by the minimum diameter of all boreholes that the pearl cannot pass through. With this method, symmetric, as well as highly irregular forms can be measured based on a unique standard.

1.4.4 Luster

The parameter ‘luster’ (sometimes as well referred to as ‘gloss’ or ‘brilliance’) refers to the quality and quantity of light that is reflected from the surface of a pearl. Typical perceptual attributes are for example bright, clear, shiny, milky, chalky or dull. Grading classes are qualitative and depend on the grading institution. In French Polynesia the luster is graded as excellent, good, average or dull.



Figure 9: Pearls with different luster: left excellent, right dull.

1.4.5 Surface Quality

The surface quality is expressed quantitatively by the percentage of the surface covered with defects and qualitatively by describing the type and appearance of the defects. Common imperfections are for example pittings, devitalization, organic or non-organic deposits.

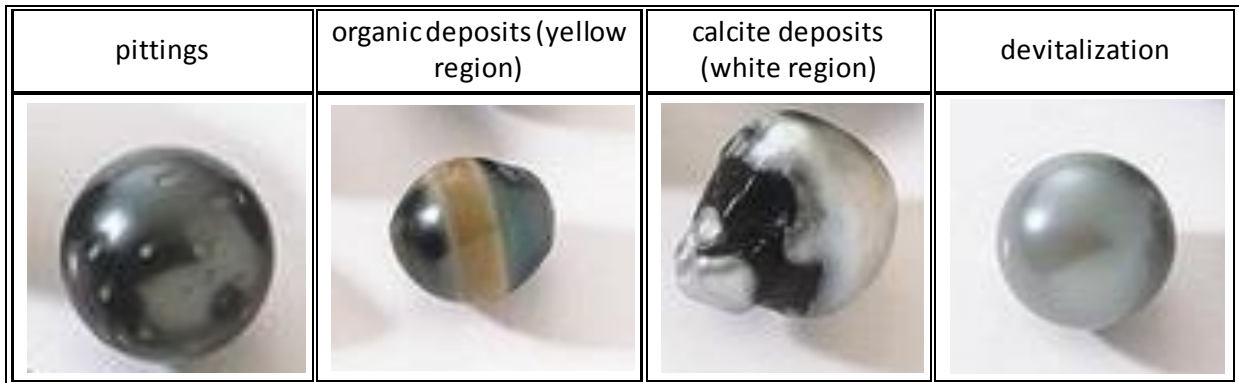


Figure 10: Different types of surface imperfection.

1.4.6 Nacre Thickness

While all previous parameters can be evaluated visually by examination of the surface of the pearl, the nacre thickness depends on the internal structure of a pearl. Accordingly, an analysis has to be done with non-destructive imaging methods such as X-ray, ultrasound or optical coherence tomography. Typical grades are minimal thickness or average thickness in *mm*, or the percentage of nacre thickness lower than a predefined threshold.

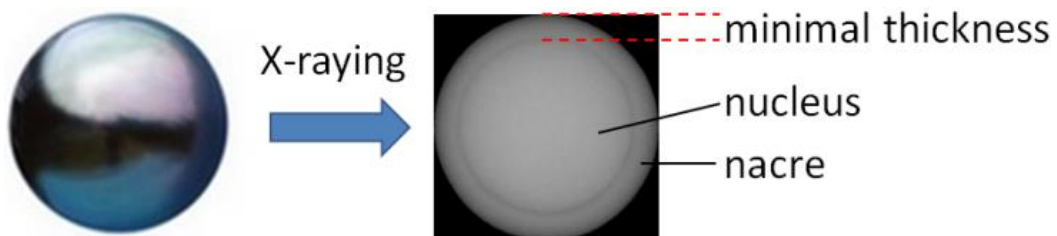


Figure 11: The internal structure of a Tahitian pearl visualized by X-raying for the purpose of nacre thickness evaluation.

1.5 Pearl Business in French Polynesia

The Tahitian pearl plays an essential role in the French Polynesian economy. It is the second largest source of domestically generated income after tourism, and the largest source of export income (Figure 12). Several thousand people are employed in the sector. Especially for the remote and small islands of the French Polynesian archipelagos pearl cultivation is a suitable way to maintain an authentic way of life while contributing to the value chain of French Polynesia.

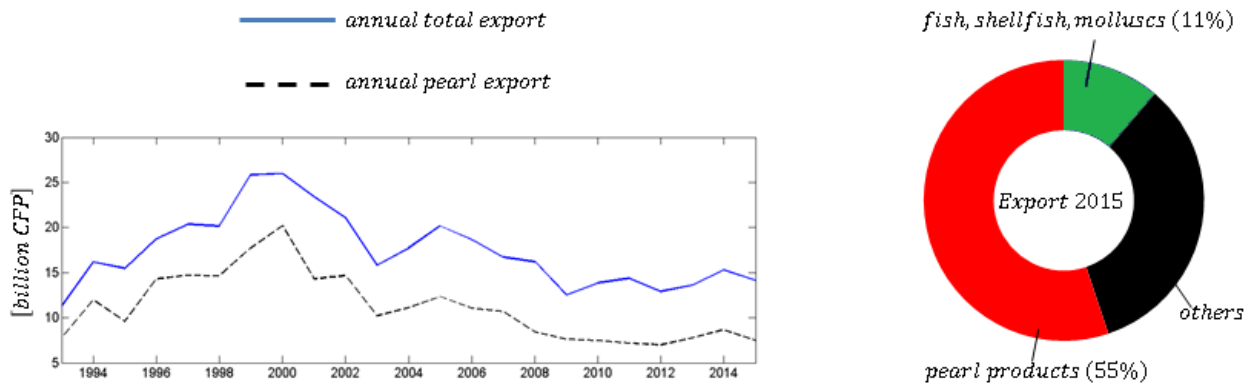


Figure 12: On the left side the total annual export volume of French Polynesia (straight Blue line) and the annual volume of exported pearls (dashed Black line). Currency: CFP, Change Franc Pacifique (Pacific Franc Exchange), 120 CFP ~ 1€. The pie diagram on the right shows pearl products as the main source of export income (55%), followed by fish, shellfish and mollusks (11%) in 2015. Source: Institut de la Statistique de la Polynésie Française (French Polynesian Institute of Statistics), Service des Douanes de Polynésie Française (French Polynesian Customs Service).

The first commercial export of cultivated Tahitian pearls dates back to the beginning of the 1970s. During the following decades, the Tahitian pearl evolved from a nearly unknown gem to a highly valued and well-known luxury good. Attracted by the promising gain, new pearl farms opened, especially in the Tuamotu atoll, where conditions for pearl cultivation are convenient. As a result, the initial export volume of less than 2 kg in 1973 was almost steadily increased up to more than 11 tons in the year 2000 (straight Blue line in Figure 13).

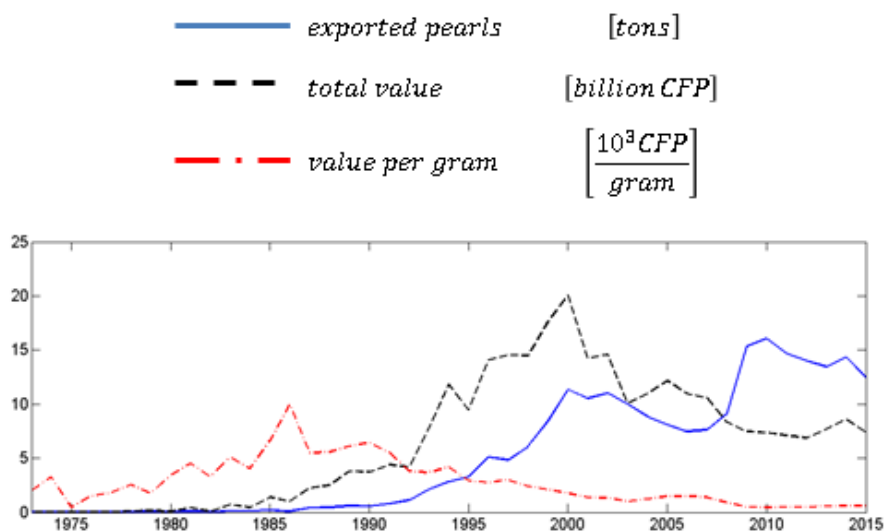


Figure 13: Graph on the left: Annual exportation indices of loose cultured Tahitian pearls 1973-2015. The straight Blue line shows the annually exported Tahitian pearls in tons. The dashed black line shows the total value of the exported pearls in billion CFP. The red dash-dotted line indicates the value per gram of exported pearls in thousand CFP per gram. Source: Institut de la Statistique de la Polynésie Française (French Polynesian Institute of Statistics), Service des Douanes de Polynésie Française (French Polynesian Customs Service).

As no market regulations were yet established, the fast increasing supply exceeded the demand, resulting in a steady devaluation of the pearl that basically lasts until today (red dash-dotted line in Figure 13 shows the evolution of prize per gram of pearls). The peak of 9980 CFP per gram (~83 € per gram) in 1986 has yet never been reached again. Due to overproduction and mismanagement, an increasing amount of pearls of low quality flooded the market, which led to an erosion of trust of the customers in the Tahitian pearl as a luxury item of exceptional quality. As result, the amount of exported pearls nearly stagnated in the years 2000-2003, while the total value for the exported pearls dropped from its overall peak of 20.1 billion CFP in 2000 to 10.1 billion CFP in 2003 (~167.5 million € to 84.2 million €, black dashed line in Figure 13). The halving of the total export value within only three years was a shock for the pearl producing industry.

To address the problem, the French Polynesian government issued several resolutions between the late 1900s and the early 2000s. Relevant administrative steps were handled more restrictively, such as the issuing of concessions for pearl farming and pearl selling, import and export regulations of pearl oysters and inter-and intra-island oyster transport regulations. A resolution outlining the necessary quality parameters for a Tahitian pearl to be exported was passed in 1999. The control of these parameters was not yet well organized, and lay mainly in the hand of the exporting parties themselves. In 2005, a resolution was passed that finally implemented an obligatory quality control for Tahitian pearls deemed for exportation. Since then, any pearl that is supposed to be exported has to be verified by an independent party as being of sufficient quality. Nowadays, the obligatory quality control is done manually at the 'Direction des Ressources Marines et Minières' (DRMM, administration of marine and mineral resources). Automatizing the currently manually conducted control of over 7 million pearls per year is one goal of project RAPA that will be introduced more detailed in section 1.7.

In parallel several lobby groups are until today promoting the Tahitian pearl on the international market and are organizing international pearl auctions, while three unions advocate the interests of the Polynesian pearl farmers (see table 1). Even though the valorization of the pearl could be stabilized during the last years, it is still at only 6% of the all-time high that was reached in 1986. Accordingly, the sector is still in motion. Lobby groups are merged and newly formed, research projects are created and the revoking, adaption or creation of regulations is discussed. Specifically the obligatory quality control was challenged repeatedly. Criticized as partially arbitrary and most of all slow-going, its global effect is still seen critically by some pearl farming parties.

Direction des Ressources Marines et Minières (DRMM)	governmental department, currently conducting the obligatory quality control of Tahitian pearls deemed for exportation
Syndicat des Petits et Moyens Perliculteurs de la Polynésie Française (SPMPPF)	pearl farmer unions
Syndicat Professionnel des Producteurs de Perles et d'Huîtres perlières des îles du Pacifique de la Polynésie française	
Syndicat Professionnel des Producteurs de Perles (SPPP)	
GIE Poe o te Ao Nui	GIE: groupement d'intérêt économique lobby groups mainly responsible for promotion and the organization of pearl auctions
GIE Poe o Rikitea	
GIE Pearls of Manihi	
GIE Poe no Raromatai	
GIE Tuamotu Pearls	
GIE Poe o Tahiti Nui	
GIE Tahiti Pearl Auction	
GIE TOARAVA	

Table 1: Main organizations of the French Polynesian pearl business.

A relatively new development in the sector is a joint effort to establish an independent pearl certificate. Two facts justify this development. First, due to the ongoing critics against the obligatory quality control implemented by the administration, a revocation of parts of the control (specifically the nacre thickness) or the control as such might be possible in the future. Still, it is consensus that an anarchic exportation of pearls might lead to further devaluation. An institution capable of issuing an independent quality label is seen as a suitable replacement on a voluntary basis. Second, independent certificates are common practice to assure customer security during the trade of high value gems and gemstones such as for example diamonds and gold. Certain institutions (such as the Gemological Institute of America) already issue certificates for Tahitian pearls. The expertise and experience of local experts can be used to establish an equivalently well reputed and internationally recognized quality certificate for the purpose of customer satisfaction.

1.6 French Polynesian Research Landscape Concerning the Tahitian Pearl

Understanding the mechanisms underlying the cultivation and commercialization of the Tahitian pearl is essential to manage and improve its exploitation and valorization. Research currently conducted within the French Polynesian territory concerning the pearl can be roughly divided in three interconnected areas: living conditions and threats to the pearl oyster, pearl formation and pearl quality, and commercialization of the Tahitian pearl.

1.6.1 Living conditions and threats to the pearl oyster

Research in this area focusses on the physiology and ecophysiology of *P. margaritifera* in the French Polynesian lagoons with and without the context of human interaction. Topics comprise for example nutrition and feeding [POU00], [FOU12], growth and reproduction [CHA11], [POU00b], biomineralization [LYD01], [FAR11], genetic diversity [ARN03], [ARN04], [ARN08], biofouling [LAC14], or the human impact on the lagoon ecosystem due to pollution or oyster farming itself [CHA12], [BOU12], [ARN03]. Main goals of research conducted in this area are to identify parameters that might disturb the natural occurrence and condition of pearl oysters in the French Polynesian lagoons as well as to identify parameters that guarantee their optimal and sustainable farming.

1.6.2 Pearl formation and pearl quality

Research in this area focusses on the physiology of pearl formation, the mineralogy of pearls and pearl farming and their influence on pearl quality. Topics comprise for example the characterization of molecular processes of pearl formation [GUE13], the description of pearl movements during its formation [GUE15], physical analysis of the crystalline structures of cultivated pearls [CUI11], mineralization disturbances [CUI96], possible causes for nucleus rejection [COC10] and the relation between pearl quality and nacre deposition rate [BLA14], grafting skill and grafting season [KY15] and selective breeding [KY13] [TAY12]. The main goal of research conducted in this area is to identify cultivation parameters that influence the pearl quality.

1.6.3 Commercialization of the Tahitian pearl

Research in this area focusses on socioeconomics and economics of pearl farming. Topics include quota regulation policies for oyster farming [POI03], social and economic impacts of overproduction and pearl price decrease [TIS00], pearl export in the context of French Polynesian and world economies [POI10], game theoretic analysis of commercialization and regulation policies [MON02] and market structures and marketing [CLE08]. The main goal of research conducted in this area is to identify economic parameters affecting the commercialization of Tahitian pearls.

1.7 The RAPA Project

With project RAPA, the profession of computer science was for the first time added to the pearl related French Polynesian research landscape. It was established by the computer science group of the University of French Polynesia and partners with DRMM, Centre IFREMER du Pacifique (French national research organism), GIE POE O TAHITI NUI and GIE POE O RIKITEA (French Polynesian pearl lobbies). The project received funding by the French Ministry of Overseas Territories. The general goal of this project is to evaluate the possibilities of an automatic quality assessment of Tahitian pearls with computer vision.

Currently the quality of a pearl is assessed manually by experts. The procedure has two disadvantages. First of all, the perceptual nature of certain parameters such as luster, color and form makes the grading of a pearl subject to the opinion of the beholder. The transition between round and semi-round or excellent and good luster for example is fluent and an exact description of grading classes is difficult. Hence, the manual evaluation is subjective as it depends on the skills, expertise and experience of the expert and furthermore on inspection conditions such as light sources and view angles. Second, a manual evaluation is time intense, which is particularly significant for the obligatory quality control of pearls deemed for exportation. The automation of the quality assessment aims accordingly at objectifying and accelerating the quality assessment of Tahitian pearls. Additionally, further improvement of pearl quality assessment via ultrasound imaging is tested within the RAPA project. The following list summarizes the main four goals and expected impacts of the project.

1.7.1 Research projects concerning pearl formation and pearl quality

As mentioned in the previous section, one part of research currently conducted in French Polynesia aims at identifying cultivation parameters that influence the pearl quality. A successful identification of those parameters can help to increase the production of high quality pearls. For this purpose, correlation measurements are done between parameters of pearl cultivation (like the mentioned nacre deposition rate, grafting skills, season, selective breeding, etc.) and pearl quality. But a correlation measurement between more or less precisely described cultivation parameters and a subjectively assessed quality that might change depending on the inspection circumstances or the experts is critical. One goal of project RAPA is to create a reliable mathematical description of pearl quality that is

independent of external parameters. With such a description, the correlation between pearl cultivation and pearl quality could be significantly improved.

1.7.2 Commercialization of the Tahitian pearl

As explained previously, all pearls deemed for exportation have to pass an obligatory quality control. This regulation was issued as reaction to the devaluation of the pearl due to overproduction and the uncontrolled exportation of pearls of low quality. Currently, this control focusses on surface quality and nacre thickness and is conducted manually at the governmental administration DRMM for over 7 million pearls annually. The procedure was repeatedly criticized as being slow and arbitrary. An automation of the obligatory control can remedy those deficiencies. A successful implementation of an automated quality control has a direct impact on the pearl exportation flux, as well as on the reputation of the obligatory control.

1.7.3 Pearl quality certificate

A relatively new motion in the French Polynesian pearl sector is to create a complete computer vision based 3D pearl quality grading system, with the goal of issuing an internationally recognized quality certificate that is independent of human subjectivity or external parameters such as light conditions or view angle. In contrary to the obligatory quality control, which mainly focusses on surface quality and nacre thickness, the certificate is meant to contain the grading of all six quality parameters. Project RAPA forms part of these efforts, evaluating the possibilities of an automated pearl quality assessment based on all parameters.

1.7.4 Alternative quality assessment

While a quality assessment with color and X-ray images can only be done after the pearl is harvested, ultrasound imaging might be applicable to the pearl still being within the oyster. A pearl not consisting of sufficient nacre thickness could be left for further growing. Additionally, ultrasound imaging is evaluated in regards of being a less expensive and more secure alternative to the current X-raying.

2 Computer Vision Applied to Pearl Classification: State of the Art

In [TAN14] a computer vision system is introduced, including remarks on mechanical components, image capturing and algorithmic processing to grade the pearls shape and size. The complete system contains three main parts: pearl feeding, image capturing and pearl sorting. The feeding system is sketched briefly as a pipe system in which the pearls are routed through their own weight to the image capturing device. The image capturing is done with a single camera and four mirrors, an interesting approach that allows the capturing of 5 view angles of a pearl with only one camera. The pearls shape is determined by a fuzzy membership function calculated of the Fourier transform of the radius variation of the outer boundary of the pearl subject to its centroid. The size of a pearl is assigned by using the minimum and maximum diameter. According to the automatic grading, a rotating sorting device, situated under the image capturing part, routes the pearl to one of several concentrically arranged containers. Additional topics, such as lightning sources for the image capturing and control procedures are discussed as well. Besides the image capturing system, of which an experimental device was built, the remaining parts for pearl routing seem to be theoretical. Specifically the routing in pipes might need experimental validation if used for an equivalent processing of Tahitian pearls. If the diameter of the pipe is big enough to let pass large pearls, several small pearls might pass in parallel. The blocking of the pipe by pearls of irregular shape has to be considered as well. An alternative might be the routing of pearls via a mechanical arm that picks pearls separately by suction as presented in [BAI14].

In contrary to the previously mentioned use of Fourier descriptors for shape analysis ([TAN14], as well used in [CAO10]), Zernike moments of the radial variation of the pearls shape subject to its centroid are used in [LI07]. The membership to five predefined classes is assigned as well with fuzzy logic. Even though the shape grades used in the mentioned articles differ from those used for Tahitian pearls, the approach of using rotational invariant descriptors such as Fourier or Zernike for shape description and a classification with fuzzy logic to take into account the smooth transition between shape classes is a general approach. Accordingly, such an approach will likely be suitable for classifying the shape of Tahitian pearls.

The automatic assessment of pearl luster is discussed in [CHE12]. Pearls are illuminated by a point light source and digital images of the illuminated surface are taken. A specular exponent is calculated based on the size of the area on the pearls surface that reflects the incoming light above a certain threshold. Ten pearls that are used for testing were sorted by experts from ‘worst’ to ‘best’. The calculated specular exponents showed the same hierarchy as the experts grading, thus indicating that the method is suitable to quantitatively describe a pearls luster. The problem of different shapes influencing the calculation is mentioned, and the uses of class dependent descriptors are suggested. This is relevant for a possible implementation for Tahitian pearls as different and irregular shapes are not an exception. In the same article a design of a complete inspection system is presented, here using mechanical and suction parts to route the pearls. Evaluation methods for shape, size, color and surface defects are briefly mentioned.

An interesting approach to analyze the correlation between physical pearl properties and perceptual appearance is presented in [NAG97]. A model of the optical properties of pearls is formulated that respects the mineral structure of a pearl in regards of reflectance and transmission of alternate aragonite and protein layers. The model is used to create synthetic pearl images whose appearance is generally validated as realistic by experts. The model is developed further in [DOB98]. The approach might be a way to quantize perceptual quality parameters such as color and luster that are currently evaluated qualitatively. In a second step, a validated model could help to investigate the correlation between pearl cultivation and the mineral structure of a pearl.

Pearl color and luster quantization is done in [MAM10] with UV-visible spectroscopy. The measured spectra of 8 South Sea Pearls are visually analyzed and a correlation between perceptual characteristics of the pearls and certain regions of the spectra identified. Further developments of this approach are presented in [AGA12] and [KUS15]. Here, the UV-visible spectra of 28 pearls including Akoya, South Sea, Freshwater and Tahitian pearls are measured. Artificial Neural Networks are used to automatically assess parameters such as donor oyster condition and type, breeding oyster type, pearl color, luster and surface quality and potential pearl treatment, all based on the measured spectra. Even though the results show a successful classification, the trained networks were validated with only four pearls, one pearl for each pearl type. The general suitability of this method has to be confirmed with a

larger set of pearls, as some correlations are not intuitive. Specifically the classification of surface quality for example is somewhat astonishing. Grades include the number of surface defects and their concentration over the complete pearl surface. But the spectra are measured at only two pearl surface areas of less than 1 *mm* diameter. The results suggest that the overall surface quality is encoded in any point of the pearl surface, which stands in contrast to the local character of surface defects caused by local mineralization disturbances [CUI96].

The use of a monochrome camera with different filters to obtain images sensitive to specific wavelength bands to classify the pearls color according to human perception is proposed in [NAG94]. 100 pearl samples are graded by experts in 10 classes from white to cream. An Artificial Neural Network (ANN) is used to identify wavelength bands that allow a maximum correlation between human and artificial classification. Therefore, an ANN is trained with all images, and bands with a small influence on the classification result are removed iteratively. The optimal classification is reached with 9 filters with a classification success of 91% for the training data and 71% for the testing data. This approach has the advantage of covering a larger area of the pearls surface when compared to the use of a spectrometer. Additionally, the instrumentation is generally cheaper.

A more classical approach for pearl color classification can be found in [TIA09]. Regular RGB color images are transposed to the HSV color space. The images undergo median filtering and areas containing reflections are segmented by thresholding the Value channel. For the remaining region, the averages of Hue and Saturation channels are calculated. An Artificial Neural Network is trained with the obtained Hue of 800 pearl images, based on the human classification of the pearls, in three color classes red, purple black and white. The trained network is tested with 10 images showing one misclassification. The average Saturation is clustered with fuzzy C-means in four classes A-D. The approach is straightforward but the averaging of Hue and Saturation is not applicable in the case of the Tahitian pearl, that is described by primary and secondary colors due to its multi-color appearance. Additionally, the illumination parameter is not used; a parameter vital for the classification of Tahitian pearls.

For the purpose of analyzing visually the internal structure of pearls, different X-ray based methods have been deemed suitable, such as X-ray microtomography ([STU09] and [KRZ10]) or X-ray phase contrast and scattering ([KRZ15]). As an alternative, optical

coherence tomography (OCT) is proposed in [JU10]. An integrated system that captures OCT images and spectral data based on fluorescence spectroscopy is described in [JU11], allowing an analysis of both, internal structure as well as for example color properties. The pearls are rotated and data is acquired repeatedly, assuring an evaluation of large surface areas. Rather than on the algorithmic classification, the articles focus on the suitability of a visual data inspection. The results show that according to the spectra, the pearl type and pearl quality enhancement treatment can be identified.

An automatic approach of nacre thickness measurement out of OCT images is presented in [LEI09]. The obtained OCT images are denoised and edge pixels of the outer boundary of the pearl and the nucleus are identified respectively with Canny edge detection and Support Vector Machine. Two circles are fitted with least squares that contain the identified edge pixels, describing the complete boundaries of the pearl and the nucleus within the pearl. The nacre thickness is calculated as distance between both circles. The approach is straight forward but assumes that the pearl is round, which in the case of the Tahitian pearl would suit only one shape grade out of several typical ones. Possible cavities between nacre and nucleus that occur often in Tahitian pearls are not considered. The approach is further developed in [SUN10] and [LIU13], but still under the condition that the contours of pearl and nucleus can be approximated by circles.

3 Structure and Contribution of this Thesis

In this thesis computer vision based approaches to automatically measure the nacre thickness of Tahitian pearls as well as to classify their color are proposed. These two parameters are fundamentally different. The color is a perceptual parameter that depends on the perception of the observer, while the nacre thickness is a measurable parameter. Furthermore, the color can be visually evaluated by analyzing the surface of the pearl, while the nacre thickness depends on the inner structure of the pearl and has hence to be visualized for example with X-ray imaging.

Due to the fundamental difference of the nature of these two quality parameters, as well as the difference in means of required computer vision approaches, it was decided to divide the thesis in two parts. Part I presents our work to automatically measure the nacre thickness of Tahitian pearls out of X-ray images. Part II presents our work to automatically classify the color of Tahitian pearls based on color images of their surface. To underline the different character of both applications, each part has its proper numeration, introduction, bibliography, etc. Every reference within the parts refers to sections, literature or images of the same part, meaning there is no cross reference between the two parts. Accordingly, both Part I and Part II stand for themselves and can be read independently of any other part of this thesis. Some redundancy to the related work presented in the previous section will hence occur. In the following two subsections a general description of each part and the corresponding contribution will be given.

3.1 Part I: Automatic Nacre Thickness Measurement

The work presented in Part I of this thesis concerns the automation of a quality control procedure currently applied manually. The parameter that is controlled is the nacre thickness of Tahitian pearls. This control is obligatory for all pearls deemed for exportation. As in many industrial applications, the goal of the automation is to accelerate the control and to avoid false classifications due to the subjective nature of the human control. The work presented in this part is hence mainly settled in applied science.

In the literature some approaches to automatically measure the nacre thickness of pearls can be found, but applied to pearls of different origin. All published approaches reviewed by the author are based on assumptions that do not hold for the Tahitian pearl and can hence not be

applied. Tahitian pearls have some unique features relevant for the nacre thickness measurement, namely the large variety of irregular shapes and the occurrence of cavities within the nacre that have to be addressed. This is done in this part of the thesis, making it hence a novelty in the domain of applied computer vision based quality control. Besides this novelty, a new heuristic circle detection algorithm was developed and successfully applied to detect the nucleus within the pearls.

Alongside with this scientific contribution comes the potential economic contribution. The pearl business is the main export income source of French Polynesia currently contributing with over 50% to the whole exportation income. The export volume of over 61 million Euros in 2015 is a considerable factor seeing the relatively small population of approximately 280000. An automation of the control procedure can support a steady export especially on a long term view, as a growth of pearl exportation in means of the number of exported pearls can be expected.

3.2 Part II: Automatic Color Classification

The work presented in Part II of this thesis concerns an automated color classification of Tahitian pearls. In contrary to the nacre thickness, a physical parameter that can be measured, pearl color is a perceptual parameter meaning its definition lies in the eye of the beholder. As the color of a pearl has influence on its economic value, the largely subjective manual classification results in inconsistent price generation. Additionally, a quantitative color measure is necessary for a correlation analysis between cultivation parameters of a pearl and its color. The goal of automatizing the color classification is to create a reliable color label that, on the one hand corresponds as much as possible to the human perception, but on the other hand reduces as much as possible the influence of subjectivity. In contrary to approaches found in the literature, the large variety of possible color occurrence as well as the possibilities of multiple colors appearing on one pearl has to be considered.

The main focus of the work presented in this part of the thesis lies on determining suitable color features for an artificial neural network based classification. In comparison to Part I, this part is mainly settled in theoretical science, namely normalized *rgb* color space theory.

A main contribution of this part is the formalization of chromatic index calculation in the context of normalized *rgb* histogram binning. It is shown that every chromatic index based on a linear combination of normalized *rgb* channels can be expressed by a single variable; an

angle that corresponds to the human perceptual parameter Hue. Experimental classifications with Artificial Neural Networks and feature vectors based on chromatic indices over the whole range of the normalized *rgb* color space were used. As data base serve color images of 150 Tahitian pearls that were manually classified by 7 experts. The results show that the choice of chromatic indices affects significantly the classification performance of an ANN with a given topology. The variance of classification *rate* stretches over the whole range of used indices. These findings are of great importance for computer vision applied to color object classification as currently only a handful of chromatic indices are used in the literature, which is a drastic limitation of possible classification results.

A new normalized *rgb* histogram binning strategy is proposed that takes into account the non-uniform distribution of normalized *rgb* vectors. The binning strategy is included in the experiments. The results show that the global classification rate can partially be increased by up to 18%.

The experimental results were as well analyzed under the aspect of the feasibility to automatically classify Tahitian pearls based on their perceived color. Classification rates of over 84% for training data and over 79% for test data are reached for all used human classifications. It can hence be generally concluded that, despite the occurrence of multiple colors and color combinations on Tahitian pearls, an artificial classification is possible.

3.3 Oral Presentations

Oral presentations of partial results were given at:

-12th Pacific Science Inter Congress 2013, Suva, FIJI.

-6th International Conference on Image and Signal Processing (ICISP) 2014, Cherbourg, France.

-6th International Conference on Image Processing & Communications (ICP) 2015, Bydgoszcz, Poland.

-12th International Conference on Image Analysis and Recognition (ICIAR) 2015, Niagara Falls, Canada.

3.4 Publications

Papers published within the scope of this thesis are:

Martin Loesdau, Sébastien Chabrier, Alban Gabillon: "*Hue and Saturation in the RGB Color Space*". In proceedings of the 6th International Conference ICISP 2014, France. Lecture Notes in Computer Science, Volume 8509, pp 203-212. Springer International Publishing, 2014.

Martin Loesdau, Sébastien Chabrier, Alban Gabillon: "*Automatic Classification of Tahitian Pearls*". In proceedings of the 6th international conference ICP 2015, Poland. Image Processing & Communications Challenges, Volume 6, pp 95-101. Springer International Publishing, 2015.

Martin Loesdau, Sébastien Chabrier, Alban Gabillon: "*Automatic Nacre Thickness Measurement of Tahitian Pearls*". In proceedings of the 12th international conference ICIAR 2015, Canada. Lecture Notes in Computer Science, Volume 9164, pp 446-455. Springer International Publishing, 2015.

Accepted papers to be published are:

Martin Loesdau, Sébastien Chabrier, Alban Gabillon: "*Computer Vision based Nacre Thickness Measurement of Tahitian Pearls*". Accepted for oral presentation at the 13th International Conference on Quality Control by Artificial Vision, 13-15 May, 2017, Japan. Proceedings will be published in the SPIE Digital Library.

List of Figures

- Figure 1: The shell of the pearl oyster *Pinctada margaritifera* contains both crystalline forms of calcium carbonate. The inner iridescent shell consists mainly of aragonite tablets, while the rest consists mainly of calcite prisms. 15
- Figure 2: Schema of the immunological reaction of a shelled mollusk caused by intrusion of an irritant through its shell. When the irritant reaches the mantle epithelium it is encapsulated by a cyst formed by epithelium cells (pearl sac). Similar to the biomineralization process performed by the organism to build, maintain and repair the shell, calcium carbonate is deposited around the irritant. 15
- Figure 3: The shell of the pearl oyster *Pinctada margaritifera* (left, detail in the middle) and a Tahitian pearl produced by this species (right). Shell and pearl show similar characteristic color nuances like green, blue, aubergine and pink. 16
- Figure 4: Different types of pearl producing species (first two columns), trade names of their pearls (third column) and characteristic color nuances of the pearls (last column). The pearls produced by the species of the first four rows are true pearls as they consist mainly of aragonite layers. The pearl produced by the *Melo melo* sea snail (last column) consist mainly of calcite prisms and is hence a non-nacreous pearl. . 17
- Figure 5: Schema of the grafting process (middle). A piece of mantle tissue (the graft) is placed together with a nucleus within the gonad of a pearl oyster. The grafted oyster is put back in the lagoons. In the optimal case the graft builds a pearl sac around the nucleus and a pearl is formed by biomineralization of calcium carbonate deposited by the cells of the pearl sac around the nucleus. 18
- Figure 6: X-ray images of a keshi (left) and a regular cultivated Tahitian pearl (right). The regular pearl contains a nucleus, while the keshi is formed after the rejection of the nucleus by the oyster. 19
- Figure 7: An example of a multi-color Tahitian pearl with blue as primary color and secondary colors green and pink. 20
- Figure 8: Main pearl shape categories 21
- Figure 9: Pearls with different luster, left excellent, right dull 21
- Figure 10: Different types of surface imperfection. 22
- Figure 11: Schema of the internal structure of a pearl visualized by X-raying for the purpose of nacre thickness evaluation..... 22
- Figure 12: On the left side the total annual export volume of French Polynesia (straight Blue line) and the annual volume of exported pearls (dashed Black line). Currency: CFP, Change Franc Pacifique (Pacific Franc Exchange), 120 CFP ~ 1€. The pie diagram on the right shows pearl products as the main source of export income (55%), followed by fish, shellfish and mollusks (11%) in 2015. Source: Institut de la Statistique de la Polynésie Française (French Polynesian Institute of Statistics),

Service des Douanes de Polynésie Française (French Polynesian Customs Service).
..... 23

Figure 13: Graph on the left: Annual exportation indices of loose cultured Tahitian pearls 1973-2015. The straight Blue line shows the annually exported Tahitian pearls in tons. The dashed black line shows the total value of the exported pearls in billion CFP. The red dash-dotted line indicates the value per gram of exported pearls in thousand CFP per gram. Source: Institut de la Statistique de la Polynésie Française (French Polynesian Institute of Statistics), Service des Douanes de Polynésie Française (French Polynesian Customs Service). 23

Bibliography

- AGA12 Agatonovic-Kustrin, S., & Morton, D. W. (2012). *The use of UV-visible reflectance spectroscopy as an objective tool to evaluate pearl quality*. *Marine drugs*, 10(7), 1459-1475
- ARN03 Arnaud-Haond, S., Vonau, V., Bonhomme, F., Boudry, P., Prou, J., Seaman, T., & Goyard, E. (2003). *Spat collection of the pearl oyster (Pinctada margaritifera cumingii) in French Polynesia: an evaluation of the potential impact on genetic variability of wild and farmed populations after 20 years of commercial exploitation*. *Aquaculture*, 219(1), 181-192.
- ARN04 Arnaud-Haond, S., Vonau, V., Bonhomme, F., Boudry, P., Blanc, F., Prou, J., & Goyard, E. (2004). *Spatio-temporal variation in the genetic composition of wild populations of pearl oyster (Pinctada margaritifera cumingii) in French Polynesia following 10 years of juvenile translocation*. *Molecular Ecology*, 13(7), 2001-2007.
- ARN08 Arnaud-Haond, Sophie, et al. "Genetic structure at different spatial scales in the pearl oyster (*Pinctada margaritifera cumingii*) in French Polynesian lagoons: beware of sampling strategy and genetic patchiness." *Marine Biology* 155.2 (2008): 147-157. 2008
- BAI14 Bai, Z. L., Wen, Q. R., & Yang, M. (2014, April). *A Pearl Automatic Sorting System Based on Image Identification*. In *Applied Mechanics and Materials* (Vol. 496, pp. 1574-1577).
- BLA14 Blay, C., Sham-Koua, M., Vonau, V., Tetumu, R., Cabral, P., & Ky, C. L. (2014). *Influence of nacre deposition rate on cultured pearl grade and colour in the black-lipped pearl oyster Pinctada margaritifera using farmed donor families*. *Aquaculture international*, 22(2), 937-953.
- BOU12 Bouvy, M., Dupuy, C., Pagano, M., Barani, A., & Charpy, L. (2012). *Do human activities affect the picoplankton structure of the Ahe atoll lagoon (Tuamotu Archipelago, French Polynesia)?* *Marine pollution bulletin*, 65(10), 516-524.
- CAO10 Cao, Y. L., Zheng, H. W., Yang, J. X., & He, Y. F. (2010, September). *Automatic Shape Grading of Pearl Using Machine Vision Based Measurement*. In *Key Engineering Materials* (Vol. 437, pp. 389-392).
- CHA11 Chávez-Villalba, J., Soyey, C., Huvet, A., Gueguen, Y., Lo, C., & Moullac, G. L. (2011). *Determination of gender in the pearl oyster Pinctada margaritifera*. *Journal of Shellfish Research*, 30(2), 231-240.
- CHA12 Charpy, L., Rodier, M., Fournier, J., Langlade, M. J., & Gaertner-Mazouni, N. (2012). *Physical and chemical control of the phytoplankton of Ahe lagoon, French Polynesia*. *Marine pollution bulletin*, 65(10), 471-477.

- CHE12 Chen, S. Y., Luo, G. J., Li, X., Ji, S. M., & Zhang, B. W. (2012). *The specular exponent as a criterion for appearance quality assessment of pearllike objects by artificial vision*. *Industrial Electronics, IEEE Transactions on*, 59(8), 3264-3272.
- CIB15 The Pearl Book, Confédération International de la Bijouterie, Joaillerie, Orfèvrerie des Diamantes, Perles et Pierres (CIBJO, World Jewelry Confederation), 2015
- CLE08 Clem Tisdell, Bernard Poirine. *Economics of Pearl Farming*. Paul Southgate, John Lucas. The pearl oyster, Elsevier Science, pp.473-496, 2008
- COC10 Cochenec-Laureau, N., Montagnani, C., Saulnier, D., Fougerouse, A., Levy, P., & Lo, C. (2010). *A histological examination of grafting success in pearl oyster Pinctada margaritifera in French Polynesia*. *Aquatic Living Resources*, 23(01), 131-140.
- CUI11 Cuif, J. P., Dauphin, Y., Howard, L., Nouet, J., Rouzière, S., & Salomé, M. (2011). *Is the pearl layer a reversed shell? A re-examination of the theory of pearl formation through physical characterizations of pearl and shell developmental stages in Pinctada margaritifera*. *Aquatic Living Resources*, 24(4), 411.
- CUI96 Cuif, J. P., & Dauphin, Y. (1996). *Occurrence of mineralization disturbances in nacreous layers of cultivated pearls produced by Pinctada margaritifera var. cumingi from French Polynesia. Comparison with reported shell alterations*. *Aquatic Living Resources*, 9(2), 187-193.
- DOB98 Dobashi, T., Nagata, N., Manabe, Y., & Inokuchi, S. (1998, April). *Implementation of a pearl visual simulator based on blurring and interference*. In *Knowledge-Based Intelligent Electronic Systems, 1998. Proceedings KES'98. 1998 Second International Conference on* (Vol. 3, pp. 274-281). IEEE.
- FAR11 Farre, B., Brunelle, A., Laprévotte, O., Cuif, J. P., Williams, C. T., & Dauphin, Y. (2011). *Shell layers of the black-lip pearl oyster Pinctada margaritifera: Matching microstructure and composition*. *Comparative Biochemistry and Physiology Part B: Biochemistry and Molecular Biology*, 159(3), 131-139.
- FOU12 Fournier, J., Dupuy, C., Bouvy, M., Couraudon-Réale, M., Charpy, L., Pouvreau, S., ... & Cochard, J. C. (2012). *Pearl oysters Pinctada margaritifera grazing on natural plankton in Ahe atoll lagoon (Tuamotu archipelago, French Polynesia)*. *Marine pollution bulletin*, 65(10), 490-499.
- GER92 Gervis, M. H., & Sims, N. A. (1992). *The biology and culture of pearl oysters (Bivalvia pteriidae)* (Vol. 21). WorldFish.
- GUE13 Gueguen, Y., Montagnani, C., Joubert, C., Marie, B., Belliard, C., Tayale, A., & Le Moullac, G. (2013). *Characterization of molecular processes involved in the pearl formation in Pinctada margaritifera for a sustainable development of pearl farming industry in French Polynesia*. *Recent Advances in Pearl Research—Proceedings of the International Symposium on Pearl Research 2011*

- GUE15 Gueguen, Y., Czorlich, Y., Mastail, M., Le Tohic, B., Defay, D., Lyonard, P., & Chabrier, S. (2015). *Yes, it turns: experimental evidence of pearl rotation during its formation*. *Royal Society open science*, 2(7), 150144.
- JU10 Ju, M. J., Lee, S. J., Min, E. J., Kim, Y., Kim, H. Y., & Lee, B. H. (2010). *Evaluating and identifying pearls and their nuclei by using optical coherence tomography*. *Optics express*, 18(13), 13468-13477.
- JU11 Ju, M. J., Lee, S. J., Kim, Y., Shin, J. G., Kim, H. Y., Lim, Y., & Lee, B. H. (2011). *Multimodal analysis of pearls and pearl treatments by using optical coherence tomography and fluorescence spectroscopy*. *Optics express*, 19(7), 6420-6432.
- KRZ10 Krzemnicki, M. S., Friess, S. D., Chalus, P., Hänni, H. A., & Karampelas, S. (2010). *X-ray computed microtomography: distinguishing natural pearls from beaded and non-beaded cultured pearls*. *Gems and Gemology*, 46(2), 128
- KRZ15 Krzemnicki, M. S., Revol, V., Hanser, C., Cartier, L., & Hänni, H. A. (2015) *X-ray phase contrast and X-ray scattering images of pearls*. 34th Gemological Conference Vilnius, Lithuania.
- KUS15 Kustrin, S. A., & Morton, D. W. (2015). *The use of probabilistic neural network and UV reflectance spectroscopy as an objective cultured pearl quality grading method*. *Modern Chemistry and Applications*, 3(152), 2.
- KY13 Ky, C. L., Blay, C., Sham-Koua, M., Vanaa, V., Lo, C., & Cabral, P. (2013). *Family effect on cultured pearl quality in black-lipped pearl oyster *Pinctada margaritifera* and insights for genetic improvement*. *Aquatic Living Resources*, 26(02), 133-145.
- KY15 Ky, C. L., Nakasai, S., Molinari, N., & Devaux, D. (2015). *Influence of grafter skill and season on cultured pearl shape, circles and rejects in *Pinctada margaritifera* aquaculture in Mangareva lagoon*. *Aquaculture*, 435, 361-370.
- LAC14 Lacoste, E., Le Moullac, G., Levy, P., Gueguen, Y., & Gaertner-Mazouni, N. (2014). *Biofouling development and its effect on growth and reproduction of the farmed pearl oyster *Pinctada margaritifera**. *Aquaculture*, 434, 18-26.
- LEI09 Lei, M., Sun, Y., Wang, D., & Li, P. (2009). *Automated thickness measurements of pearl from optical coherence tomography images*. In *Hybrid Intelligent Systems, 2009. HIS'09. Ninth International Conference on* (Vol. 1, pp. 247-251). IEEE.
- LI07 Li, B., Li, G., Wang, Y., Wang, X., & Wang, W. (2007, November). *A classification method of pearl shape based on Zernike moment*. In *Wavelet Analysis and Pattern Recognition, 2007. ICWAPR'07. International Conference on* (Vol. 3, pp. 1076-1079). IEEE.
- LIU13 Liu, J., Tian, X. L., & Sun, Y. K. (2013). *Pearl Thickness Measurements from Optical Coherence Tomography Images*. In *Applied Mechanics and Materials* (Vol. 421, pp. 415-420).

- LYD01 Lydie, M. A. O., Golubic, S., Le Campion-Alsumard, T., & Payri, C. (2001). *Developmental aspects of biomineralisation in the Polynesian pearl oyster Pinctada margaritifera var. cumingii*. *Oceanologica acta*, 24, 37-49.
- MAM10 Mamangkey, N. G. F., Agatonovic, S., & Southgate, P. C. (2010). *Assessing pearl quality using reflectance UV-Vis spectroscopy: does the same donor produce consistent pearl quality?*. *Marine drugs*, 8(9), 2517-2525.
- MON02 Montet, C. (2002). *Les enseignements du management stratégique pour la Polynésie française*. Yearbook of New Zealand.
- NAG94 Nagata, N., Kamei, M., & Usami, T. (1994). *Transferring Human Sensibilities to Machines-Sensitivity Analysis of Layered Neural Networks and Its Application to Pearl Color Evaluation*. In MVA (pp. 528-531).
- NAG97 Nagata, N., Dobashi, T., Manabe, Y., Usami, T., & Inokuchi, S. (1997). *Modeling and visualization for a pearl-quality evaluation simulator*. *Visualization and Computer Graphics, IEEE Transactions on*, 3(4), 307-315.
- POI03 Poirine, B. (2003). *Managing the commons: an economic approach to pearl industry regulation*. *Aquaculture Economics & Management*, 7(3-4), 179-193.
- POI10 Poirine, B. (2010). *The Economy of French Polynesia: past, present and future*. *Pacific Economic Bulletin*, 25(1), 24-34.
- POU00 Pouvreau, S., Bodoy, A., & Buestel, D. (2000). *In situ suspension feeding behaviour of the pearl oyster, Pinctada margaritifera: combined effects of body size and weather-related seston composition*. *Aquaculture*, 181(1), 91-113.
- POU00b Pouvreau, S., Bacher, C., & Héral, M. (2000). *Ecophysiological model of growth and reproduction of the black pearl oyster, Pinctada margaritifera: potential applications for pearl farming in French Polynesia*. *Aquaculture*, 186(1), 117-144.
- STU09 Sturman, N. (2009). *The Microradiographic Structures of Non-Bead Cultured Pearls*. GIA Lab Notes 20th August 2009.
- SUN10 Sun, Y., & Lei, M. (2010). *Automated thickness measurements of nacre from optical coherence tomography using polar transform and probability density projection*. In *Intelligent Signal Processing and Communication Systems (ISPACS), 2010 International Symposium on* (pp. 1-4). IEEE.
- TAN14 Tang, Y. P., Shao-jie, X., & Zhi-liang, Z. (2014). *Research on Pearl Detecting and Grading Based on Monocular Multi-view Machine Vision*. *British Journal of Applied Science & Technology*, 4(15), 2136
- TAY12 Tayale, A., Gueguen, Y., Treguier, C., Le Grand, J., Cochenec-Laureau, N., Montagnani, C., & Ky, C. L. (2012). *Evidence of donor effect on cultured pearl quality from a duplicated grafting experiment on Pinctada margaritifera using wild donors*. *Aquatic Living Resources*, 25(03), 269-280.

- TIA09 Tian, C. (2009). *A computer vision-based classification method for pearl quality assessment*. In *Computer Technology and Development, 2009. ICCTD'09. International Conference on* (Vol. 2, pp. 73-76). IEEE.
- TIS00 Tisdell, C. A., & Poirine, B.: *Socio-economics of pearl culture: industry changes and comparisons focussing on Australia and French Polynesia*. SPC Pearl Oyster Inf. Bull, 14, 2000

Part I

Automatic Nacre Thickness Measurement

Content

1	Introduction.....	48
1.1	Manual Nacre Thickness Evaluation.....	49
1.2	Pearl Configuration	50
1.3	Automatizing the Nacre Thickness Evaluation.....	52
1.3.1	General Requirements	52
1.3.2	Automatic Image Acquisition.....	52
1.4	Acquired Images	53
1.4.1	Special Cases	54
1.4.2	Human Evaluation	55
1.5	Image Processing Methodology.....	56
1.5.1	Basic Concept	57
1.5.2	Pearl Segmentation	57
1.5.3	Nucleus Detection.....	58
1.5.4	Cavity Detection	59
1.5.5	Nacre Thickness Profile.....	60
1.5.6	Identification of Rejects and Certainty Value	60
1.5.7	Used Hard- and Software.....	62
1.6	Automatic Measurement Results	62
1.7	Structure of Part I	63
2	Related Work.....	65
3	Pearl Segmentation	67
3.1	Main Challenges.....	67
3.1.1	Region-Based Approach.....	69
3.1.2	Edge-Based Approach	70
3.1.3	Active Contours	71
3.1.4	Model Based Approach	73
3.2	Implemented Approach.....	74
3.2.1	Image Calibration	74
3.2.2	Synthetic Background Generation.....	77
3.2.3	Pearl Segmentation	79
3.2.4	Artefacts.....	80
3.2.5	Summary and Pseudocode	82
3.3	Precision of Results	82
3.3.1	Visual Analysis	83
3.3.2	Precision Measurement.....	86
3.4	Discussion	88
3.4.1	Discrepancy Types.....	89
3.4.2	Processing Time.....	90
3.4.3	Optimization Possibilities	90
3.4.4	Background Configuration	91
3.4.5	Alternative Support Configuration.....	92

3.5	Conclusion.....	93
4	Nucleus Detection.....	94
4.1	Main Challenges.....	94
4.1.1	Model-Based Approach.....	96
4.1.2	Region-Based Approach.....	96
4.1.3	Edge-Based Approach.....	97
4.1.4	Circular Hough Transform.....	99
4.1.5	Other Circle Detection Approaches.....	100
4.2	Our Approach.....	100
4.2.1	Intensity Based Probability Function.....	102
4.2.2	Gradient Based Probability Function.....	103
4.2.3	Moving Direction.....	106
4.2.4	Moving Speed and Radius Increment.....	107
4.2.5	Optimum Detection.....	108
4.2.6	Handling of Segmentation Artefacts.....	108
4.2.7	Summery and Pseudocode.....	109
4.3	Precision of Results.....	111
4.4	Discussion.....	112
4.4.1	Threshold Related Discrepancies.....	113
4.4.2	Cavity Related Discrepancies.....	114
4.4.3	Weak Boundary Related Discrepancies.....	114
4.4.4	Nucleus Visibility.....	118
4.4.5	Self-Evaluation.....	120
4.4.6	Processing Time.....	122
4.4.7	Optimization Possibilities.....	123
4.5	Conclusion.....	124
5	Cavity Detection.....	126
5.1	Main Challenges.....	126
5.1.1	Model Based Approach.....	128
5.1.2	Active Contour.....	129
5.1.3	Region Based Approach.....	129
5.1.4	Edge Based Approach.....	130
5.2	Implemented Approach.....	132
5.2.1	Neighborhood Range and Region Growing Rule.....	132
5.2.2	Previous Segmentation Artefacts.....	134
5.2.3	Pseudocode.....	135
5.3	Precision of Results.....	135
5.4	Discussion.....	137
5.4.1	Discrepancy to Intuitive Boundary Setting.....	138
5.4.2	Processing Time.....	140
5.4.3	Optimization Possibilities.....	140
5.5	Conclusion.....	141
6	Nacre Thickness Profile Calculation.....	142

7	Certainty Measurement	144
8	Results	146
9	Discussion	148
9.1	Intensity vs Gradient Based Cavity Detection	151
9.2	Manual vs Numerical Rejection.....	152
9.3	Summary	154
9.4	Processing Time	158
9.5	Optimization Possibilities	158
10	Prototype	160
11	Conclusion	162
12	Future Work	163
	List of Figures	164
	Bibliography	169

1 Introduction

According to resolution n° 2005-42 issued by the French Polynesian government on February 4th in 2005, all Tahitian pearls that are exported to foreign countries must have been officially validated as being of sufficient quality. The governmental organization currently in charge of this obligatory control is the *Direction des Ressources Marines et Minières* (DRMM, administration for marine and mineral resources). One of the crucial quality parameters defined in the resolution is the pearls nacre thickness. It is written that the minimal nacre thickness has to be at least 0.8mm, otherwise the pearl cannot be exported. Rejected pearls are to be destroyed by employees of the DRMM.

Currently, the obligatory quality control is done manually by 10 experts for over 7 million pearls that are supposed to be exported annually. As the amount of pearls already exceeds the control capacity of the DRMM, the nacre thickness is not evaluated for each pearl specifically, albeit demanded by the mentioned resolution. Usually a random sample is taken out of a set of pearls from one pearl farmer and if several pearls do not pass the control the rest of the set is controlled as well. Otherwise, the whole set is expected to be generally of sufficient quality. Still, the control procedure has repeatedly been criticized by pearl exporters as being slow. A latency of several weeks between the disposal of pearls at the DRMM and the control result is the rule rather than an exception.

In this part of the thesis the results of research conducted to support an automation of the nacre thickness evaluation with image analysis techniques are presents. In the following section, the manual procedure to measure the nacre thickness, currently realized at the DRMM, is explained. Afterwards, the general inner structure of a pearl is presented to help the reader understand and identify the three crucial regions nacre, nucleus and cavity. The requirements for an automatic measurement procedure defined by the DRMM are presented in section 1.3. In section 1.4 the character of the used training and test images are introduced along with special cases and the results of the human evaluation of the test image pearls. The developed algorithms are briefly introduced in section 1.5 followed by a summary of the results obtained by applying our algorithms to automatically measure the nacre thickness of Tahitian pearls. The internal structure of the main body of Part I will be introduced in section

1.7, followed by the state of the art in regards of automatic nacre thickness measurement of pearls in section 2.

1.1 Manual Nacre Thickness Evaluation

As the nacre thickness depends on the inner structure of a pearl, the DRMM uses X-ray machines for the evaluation purpose. A support with 300 boreholes is filled with pearls (Figure 1 on the right). The support is then placed in an X-ray machine (Figure image on the left, the arrow points at the support in the X-ray machine). As the X-ray gun has a fixed position, the support is moved mechanically to allow the visualization of different pearls. This movement is controlled by the current operator with a joystick (Figure 1 within the red circle). Zooming in and out is done with a second joystick, bringing the support closer to or further away from the X-ray detector. The X-ray image of the current pearl is visualized on a screen (red square in Figure 1).

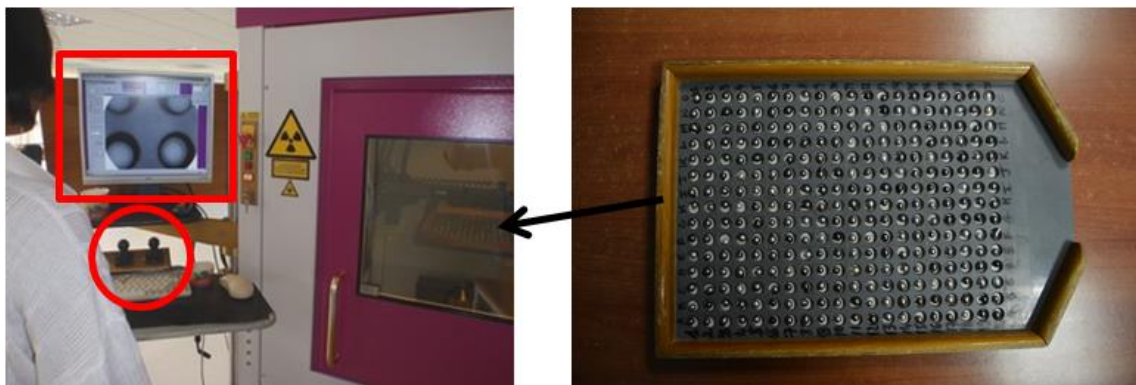


Figure 1: Work station for nacre thickness evaluation at the DRMM (left) and one of the supports in which 300 pearls are placed for X-raying (right).

The general manual evaluation procedure is accordingly. After placing the support in the machine, the operator routes the support so that the pearls in the upper right corner of the support are visualized on the screen. Zooming is usually done so that two pearls can be analyzed at once with the support at the same position (the image in Figure 2 shows the zoom that is usually used). After evaluating the current pearls visually, the support is moved with the joystick so that the next two pearls are shown. The position of pearls that are classified as rejects is noted and they are separated from the other pearls after the evaluation of the whole support.

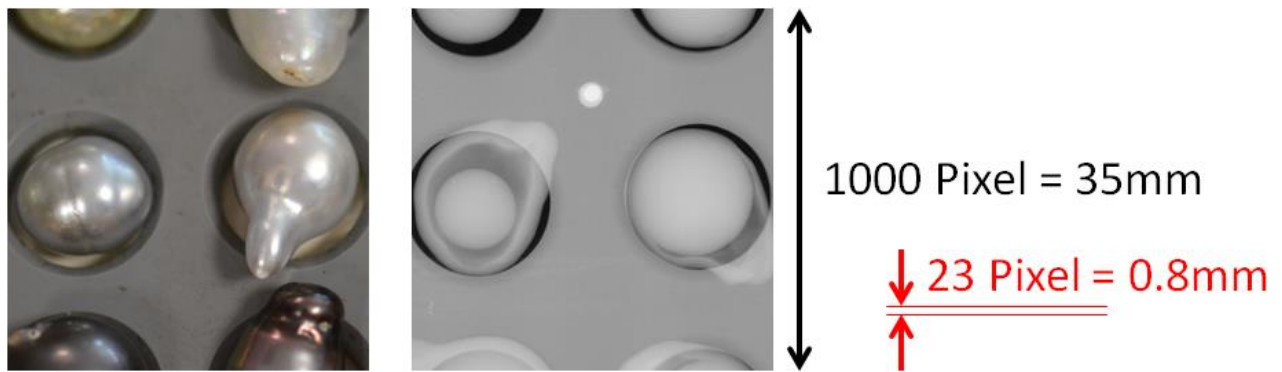


Figure 2: A detail of the support filled with pearls (left) and an X-ray image of Tahitian pearls (right) with a typical zoom used for manual nacre thickness evaluation at the DRMM (pearls of both images do not match).

The manual evaluation of a complete support takes between 5 and 10 minutes. The time needed depends mainly on the nacre configuration of the pearls. While some are obviously either good or rejects, other cases are not clear. The operator has to zoom in manually or in some cases even interrupt the evaluation procedure, take out the support, pick the pearl that is difficult to evaluate, put the pearl separately in the X-ray machine to avoid additional attenuation by the support, zoom in, make a decision, take out the pearl, put in back the support and proceed.

Still in some cases a visual evaluation is not possible. These pearls are deemed as good pearls, as there is no justification for destroying pearls that might have a sufficient nacre thickness, solely because it is not possible to visually evaluate them.

1.2 Pearl Configuration

Analyzing X-ray images of pearls (visually or numerically) means generally to differentiate between three characteristic regions. The regions are visualized in Figure 3 with a mechanically bisected pearl (second image, taken from [KRZ10]) and an X-ray image of a similar pearl (third image). Within the pearl is the nucleus (a blank nucleus is shown in the image on the left), an artificially, out of the shell from a freshwater mollusk formed sphere (marked with number 1). In the X-ray image, the nucleus appears as a circular object within the pearl. The black region of the bisected pearl is the nacre that was secreted by the pearl oyster around the nucleus (marked with number 2). In several cases the nacre does not connect directly to the nucleus. Between nucleus and nacre is accordingly a cavity (marked with number 3). Cavities appear in the X-ray images as darker regions within the pearl.

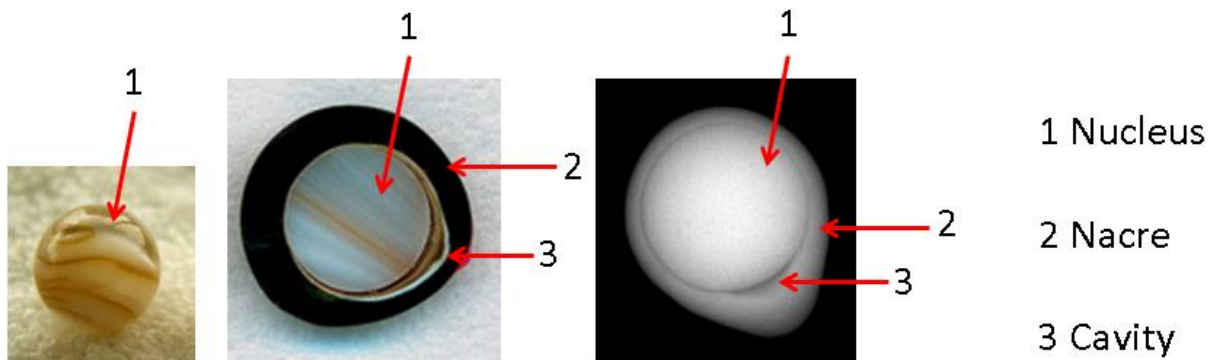


Figure 3: Blank nucleus (left), bisected Tahitian pearl (middle, taken from [KRZ10]) and X-ray image of a Tahitian pearl that is similar to the bisected one (right).

The possibility to visually evaluate the nacre thickness depends on if and how much cavities separate the nacre from the nucleus. Figure 4 shows some possible cases. In the first column, two pearls with a cavity circumferential to the nucleus that are easily evaluable visually can be seen. The second column shows two pearls with a slight cavity around the nucleus. While the pearls of the first column can be evaluated in a glimpse, these cases are still evaluable but need already a closer look. The third column shows two pearls with a non-circumferential cavity. Even though the nucleus is only partially visible, the general contour of the nucleus can be estimated cognitively. The fourth column shows two pearls without any cavity. As their nacre thickness cannot be estimated visually, those pearls pass the current quality control and can be exported.

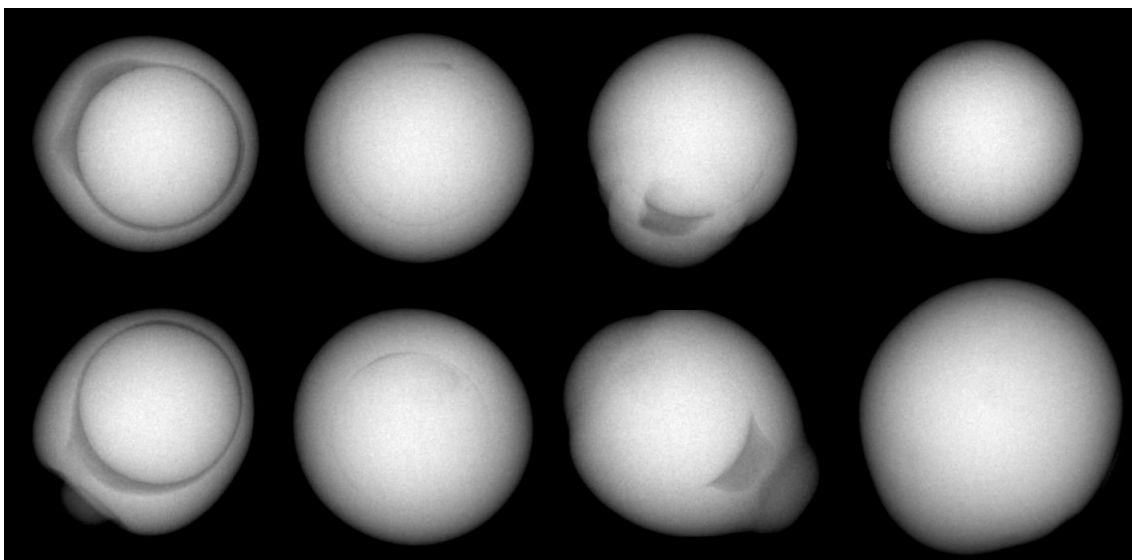


Figure 4: Different nacre configurations of Tahitian pearls.

As pearls are naturally grown gems, the variety of nacre configuration exceeds by far the shown examples. Anyhow, the shown pearls are some typical cases and illustrate the challenges that are faced by the experts at the DRMM currently controlling the nacre thickness of pearls deemed for exportation. In the same way, the examples give a first impression of the challenges of an automatized nacre thickness evaluation.

1.3 Automatizing the Nacre Thickness Evaluation

As for the manual evaluation of the nacre thickness X-ray images are taken anyway, an automation of this process with image processing techniques suggests itself. The general requirements of an automatic evaluation of the images will be stated in the next subsection. Even though not part of this thesis, the later implementation of an automatic image acquisition influences whether or not to address certain image processing challenges. Therefore, the further ongoing of this part of project RAPA will be briefly sketched in section 1.3.2.

1.3.1 General Requirements

General requirements for the automatic measurement were defined by the DRMM. First, the evaluation has to be at least as fast as the human evaluation. A margin was set to 1 second per image, leading to 5 minutes for the evaluation of a support completely filled with 300 pearls. Second, the automatic measurement has to correspond to the general paradigm that in case of doubt the pearl has to pass the quality control. This means for the automatic evaluation that false negative results have to be avoided.

The definition of a reject has to accord to the current evaluation criterion at the DRMM. Even though not stated specifically in the resolution, commonly pearls are rejected if more than 20% of the nacre thickness in regards of the 2-dimesional X-ray profile is lower than $0.8mm$.

1.3.2 Automatic Image Acquisition

The X-ray machines used at the DRMM to radiograph the pearls are equipped with software that allows an automated image acquisition at predefined positions. X-ray images are taken

and stored automatically. This means that together with the known geometry of the support that contains the pearls, the position and size of the boreholes of the support within the images is known. This facilitates their detection. The signal to noise ratio that depends on the internal averaging of the images can be in a certain range predefined. The intensity distribution of the images that depends on the used voltage and current of the X-ray device can be predefined as well. Finally the spatial resolution is set by the distance between the support and the X-ray detector. An automatic detection of these parameters was therefore not analyzed in detail.

Analyzing the influence of all image acquisition parameters on the quality of the resulting X-ray images and to define an automated image acquisition protocol with optimal parameters will be done in a future work. As for this stage of our project it was to evaluate if it is possible to automatically measure the nacre thickness of Tahitian pearls, the parameter configuration used by the employees of the DRMM was used (voltage: 130kV, current 35 μ A, averaging: 8 images per output image).

1.4 Acquired Images

A first set of 100 X-ray images of different pearls was obtained from the DRMM to create suitable image processing algorithms. The spatial image resolution of this first set corresponds to the parameters used by the experts of the DRMM for a visual analysis of the nacre thickness, meaning two pearls per image as shown in Figure 5.

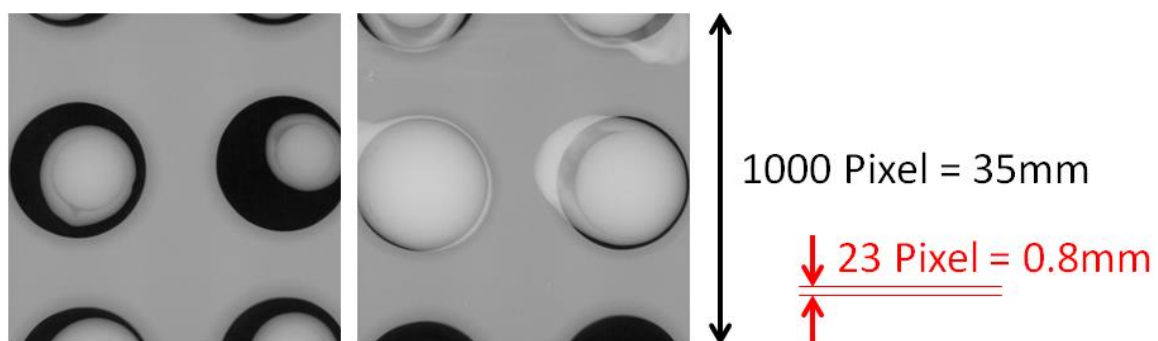


Figure 5: Two images of the set used to create the image processing tools for the automated nacre thickness measurement.

Afterwards a second set of 300 images (a support completely filled with pearls) was obtained along with human evaluation results to test the developed algorithms. For this set the image configuration was adapted so that the images correspond to a later automatic image

acquisition (Figure 6). Only one pearl per image was taken, to avoid that the outer boundary of pearls is cut off as in the images of Figure 5. A slightly higher resolution was obtained by zooming, to increase the precision of the measurement.

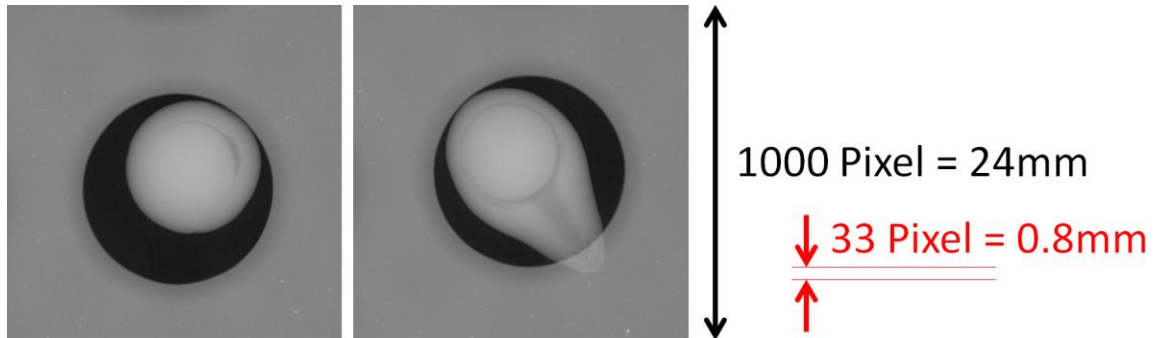


Figure 6: Two images of the set used to test the developed algorithms.

All obtained images have a pixel resolution of 1000x1000 as a fixed size determined by the X-ray detection device of the X-ray machine. The spatial resolution of the images was obtained with X-ray images of normed reference objects (1st set: 1pixel \sim 35 μ m; 2nd set: 1pixel \sim 24 μ m). All images are 16 bit greylevel images of uncompressed TIFF format.

1.4.1 Special Cases

Two of the 300 obtained test images contained keshi pearls (Figure 7). These pearls are formed after the pearl oyster rejected the inserted nucleus. Accordingly, and in contrary to the regular pearls, keshi do not contain a nucleus. The challenge of detecting whether the image contains a regular pearl or a keshi pearl is not part of this work. Therefore these two images were not considered, leaving 298 images to test the proposed algorithms.

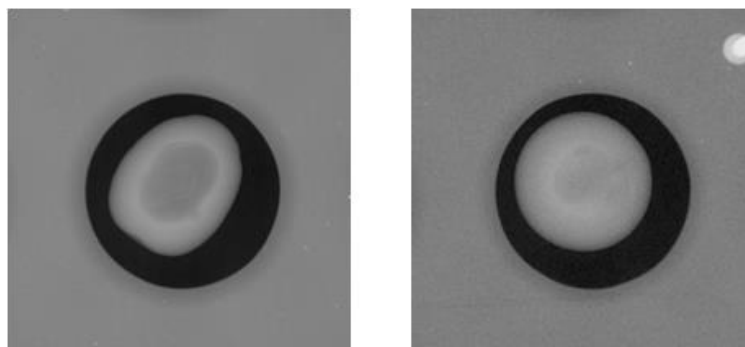


Figure 7: Two keshi pearls that were sorted out of the test image set.

Additionally, several images have an elevated noise level compared to most others. The elevated noise level was a result of the manual registration of the X-ray images before the internal averaging process of the X-raying device had been finished. The difference between regular images and images with elevated noise is shown in Figure 8. The blue graph on the left shows the intensity of the pixels left to the white line of the first X-ray image. The graph on the right shows the image intensity of pixels left to the white line of the second image. As the chosen pixels are in both cases on the relative flat surface of the same support, their intensity distribution corresponds to the noise ratio. The left X-ray image shows a clear noise elevation compared to the right image. This will not happen once the image acquisition is automatized as mentioned in section 1.3.2. Problems caused by elevated noise due to the manual image acquisition are therefore not addressed specifically in the present work.

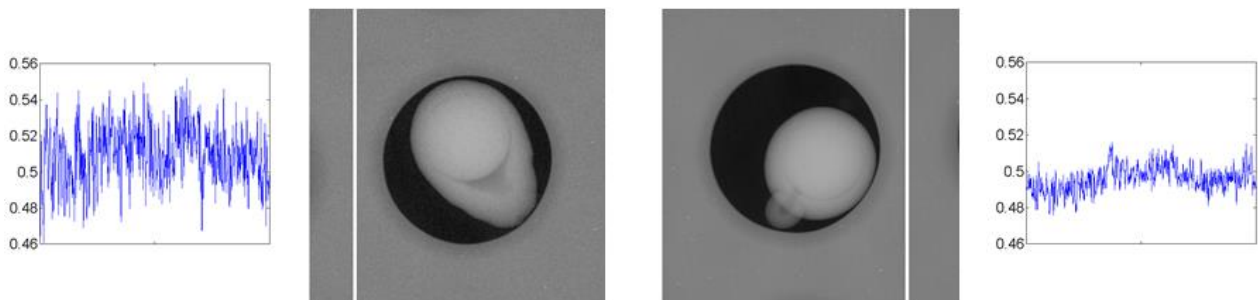


Figure 8: Intensity distribution of the support left to the white lines in the two images shown in the graph next to the respective image.

1.4.2 Human Evaluation

To not disturb the human evaluation routine, the test images were taken prior to the human evaluation. Afterwards an expert of the DRMM evaluated the same pearls according to his daily routine. The results contain the three possible cases ‘good’, ‘reject’ and ‘not evaluable’. Of the whole set of 298 used test images 13 were classified as rejects, 5 as not evaluable and the remaining 280 pearls as good. Three examples of each class are shown in Figure 9. The first row shows examples of rejected pearls, the second row shows pearls that were classified as not evaluable, and the last row shows three examples of pearls classified as good.

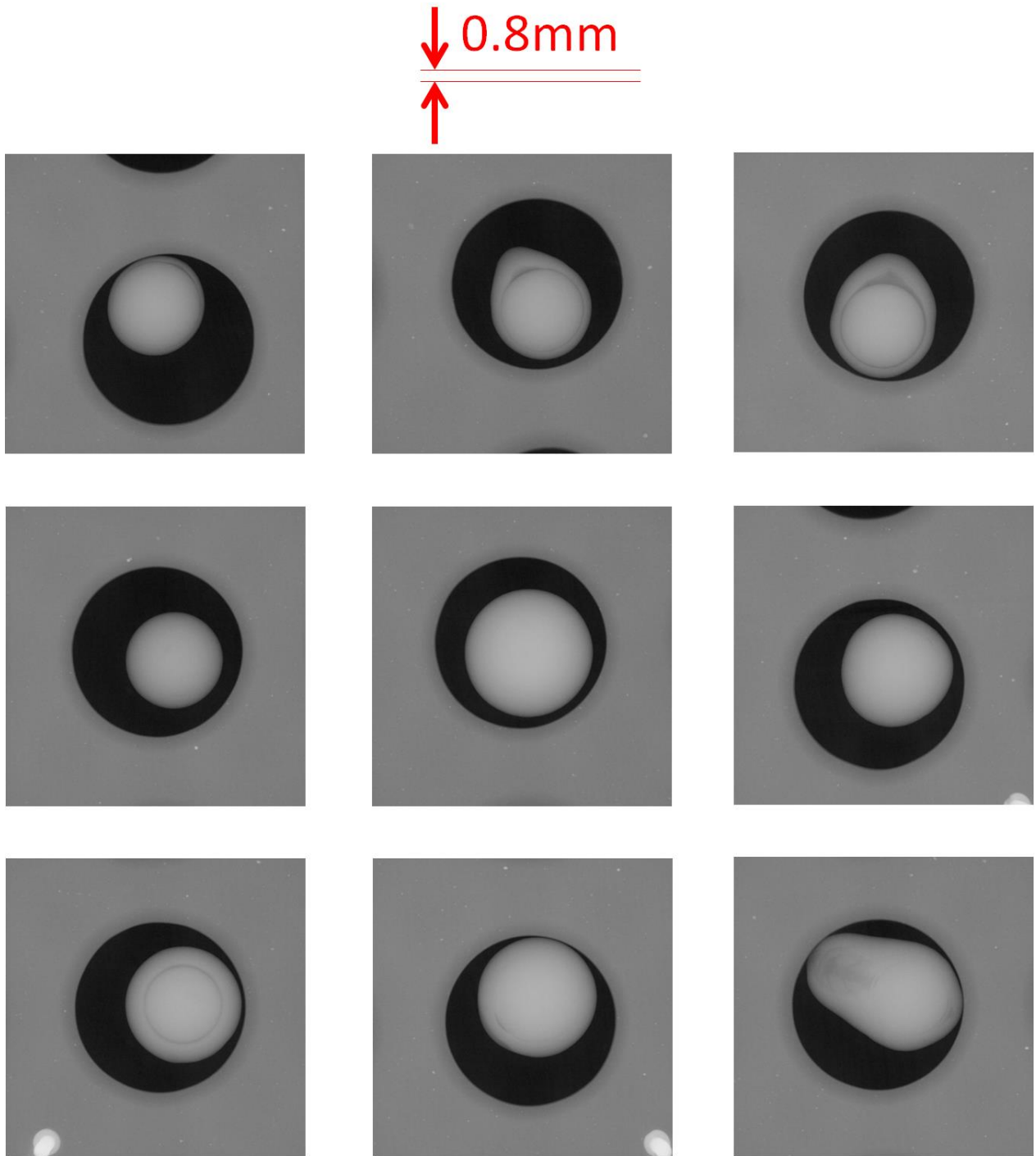


Figure 9: Three types of human evaluation results. First row shows three examples of rejected pearls, second row shows three examples of not evaluable pearls, last row shows three examples of good pearls.

1.5 Image Processing Methodology

At first, a procedure to automatically measure the nacre thickness of Tahitian pearls was developed by dividing the global challenge into 5 sub problems that are addressed chronologically as: (1) segmenting the pearl, (2) detecting the nucleus, (3) detecting cavities, (4) calculating the 2D nacre thickness profile and (5) identifying pearls to reject.

The segmentation chronology was chosen according to the presence of *a priori* information. To segment the pearl from the background, known features (the geometry) of the support in which the pearls are positioned can be used. Furthermore unnecessary background information has to be deleted as soon as possible to decrease the global processing time by cropping the image to the size of the segmented pearl. The nucleus is detected in a second step, as it is known to be an artificially formed sphere and hence to appear within the image as a circular object. Cavities instead occur in a variety of shapes and intensities and furthermore not necessarily occur at all. Hence, its detection was moved to the end of the segmentation process when the segmented image is supposed to contain solely nacre or cavity regions.

1.5.1 Basic Concept

Due to the natural formation of pearls, their shape, size and cavity configuration in general varies. As it was impossible to say to which extend the obtained training images reflect this variety, it was a goal to use algorithms that are as much as possible independent of assumptions corresponding to the named parameters. Thresholding operations were for example generally deemed as not desirable. If applied to image intensity assumptions about the pearl or nacre thickness in direction of the X-ray beam would have to be made. If applied to image gradients assumptions about the pearls or cavity contours would have to be made. Additionally, global operations such as image resizing or Gaussian smoothing were not favored, as they result in a loss of information and blur image acquisition parameters that will be analyzed in a future work.

1.5.2 Pearl Segmentation

To segment the pearl, a model based approach was developed that is based on the geometry of the used support and the physical properties of X-ray attenuation. A synthetic background image is generated according to the current image configuration and both (original and synthetic) are calibrated so that their intensity corresponds to the geometry of the radiographed scene. Due to this calibration, the synthetic image can be mathematically subtracted from the original image, which corresponds to an X-ray image of a pure pearl taken without the support. Resulting artefacts are cleaned with a smoothing filter operation.

The segmentation is hence based on the support configuration and therefore independent of the pearl character.

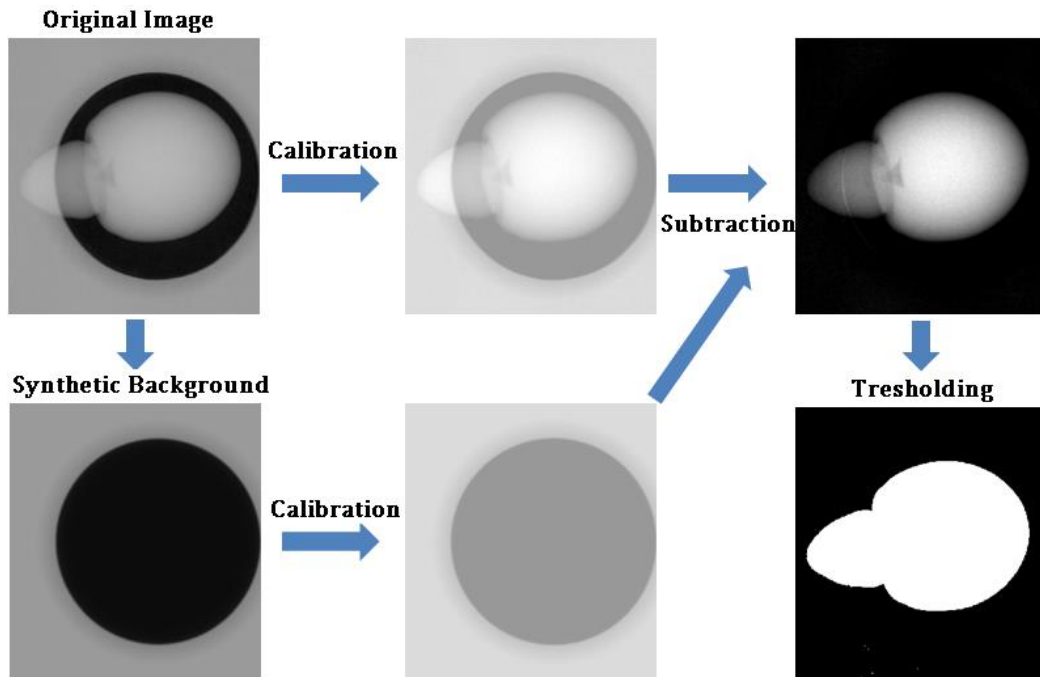


Figure 10: Workflow of the segmentation of the pearl.

1.5.3 Nucleus Detection

As the size of the nucleus is not known prior to the measurement, its radius and center have both to be detected. For this purpose a new heuristic circle detection algorithm was developed. A small circle is initialized around the region of highest image intensity, as after the prior calibration and segmentation it is known to belong to the nucleus (first image in Figure 11). A logical boundary probability is formulated that pushes the circle away from probable nucleus boundary pixels, while its radius is iteratively increased (the blue vectors in Figure 11 are circle pixels with boundary probability 1, the gaps between the vectors are circle pixels with boundary probability 0). If the circle is successfully pushed away from the nucleus boundary at each iteration, it will at one point cover the boundary of the nucleus (third image in Figure 11). The algorithm uses only logical expressions of gradient directions in regards of the current circle center and is hence as well independent of the pearls size or its nacre-nucleus configuration. Additionally, only one center pixel is evaluated per possible radius, making it a fast heuristic approach to comply with the required processing time of 1 second per image.

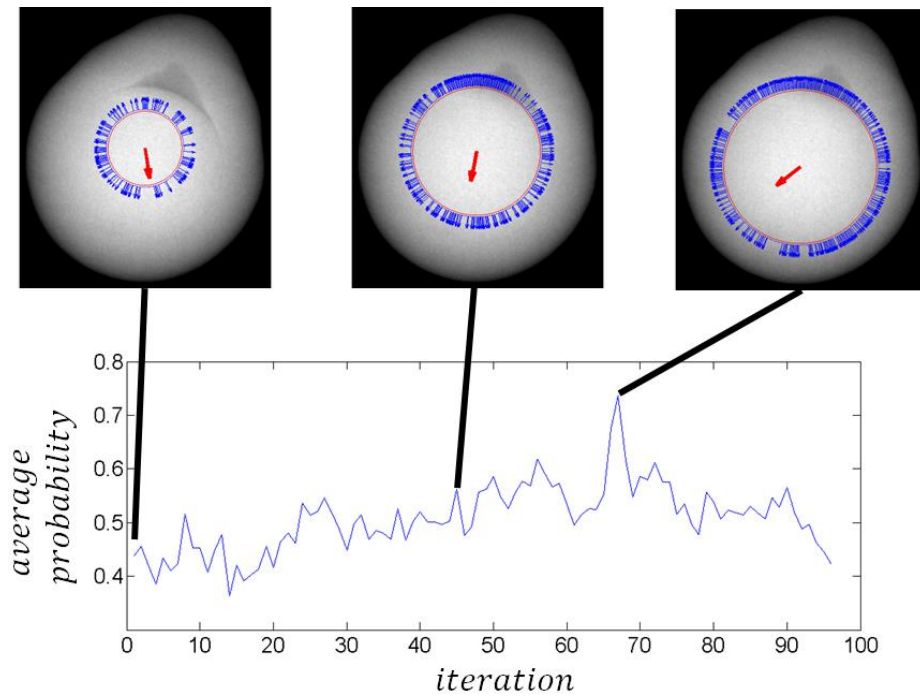


Figure 11: Schema of the developed iterative approach to detect the nucleus.

1.5.4 Cavity Detection

To detect possible cavities, a classical region growing procedure is applied. Seed pixels are the previously obtained outer boundary of the pearl, as it is known to be nacre (second image of Figure 12). According to a simplified physical model, cavity boundaries are defined by local intensity maxima. The region growing is accordingly stopped at local maxima or if the previously detected nucleus is reached (last image of Figure 12).

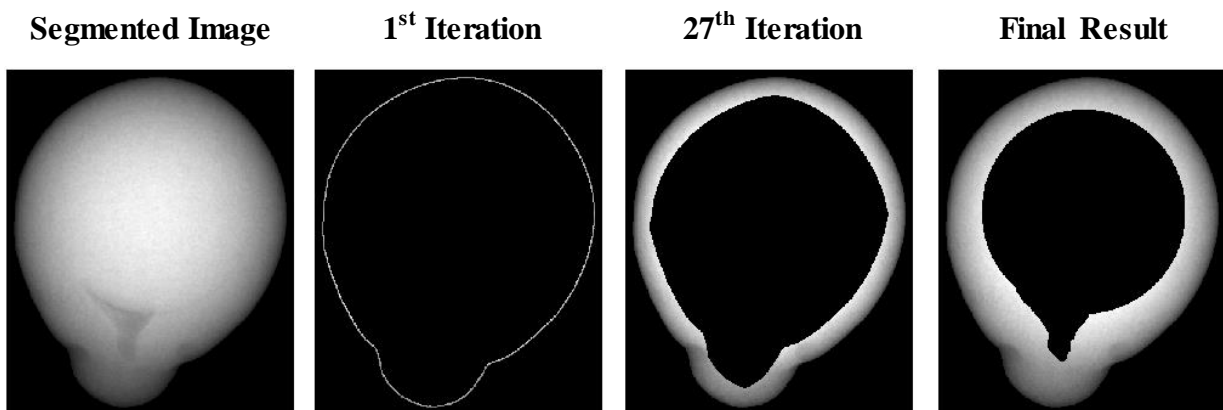


Figure 12: Region growing procedure to detect cavity boundaries.

1.5.5 Nacre Thickness Profile

After the three segmentation steps, all crucial boundaries for the calculation of the nacre thickness profile are determined (Figure 13 on the left). The nacre thickness is measured for each pixel of the obtained outer boundary of the pearl in direction of its inside pointing normal vector (Figure 13 on the bottom right). This procedure corresponds to the current manual nacre thickness evaluation at the DRMM. The result is a vector containing the distance in pixel to either the nacre or the nucleus for each boundary pixel. Together with the spatial resolution of the images the nacre thickness profile can be expressed in mm (Figure 13 on the top right).

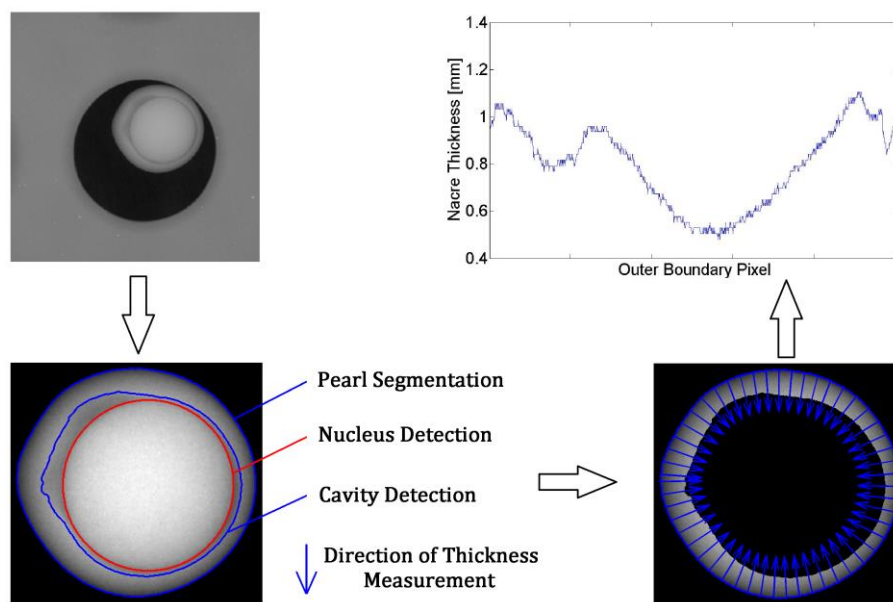


Figure 13: Obtained boundaries after applying the three segmentation steps (left) and schematic representation, of the nacre thickness measurement in direction of the inside pointing normal vectors of the detected outer boundary (blue arrows on the right). The graph on the top right is the obtained nacre thickness profile in mm .

1.5.6 Identification of Rejects and Certainty Value

The procedure currently applied at the DRMM to decide whether to reject a pearl or not is to identify visually if more than 20% of the whole nacre region has a thickness lower than $0.8mm$. The implementation is accordingly. The amount of boundary pixels with a nacre thickness lower than $0.8mm$ is divided by the sum of boundary pixels. This procedure is visualized in Figure 14. The graph on the left shows the calculated nacre thickness for every boundary pixels in mm . The dashed line is the current threshold of $0.8mm$. Every entry of the nacre thickness profile vector is marked in red, as well as the corresponding regions in the X-

ray image of the pearl on the right. The percentage of the nacre region lower than 0.8mm is in the given example 46% which makes the pearl a reject in the current definition of the DRMM.

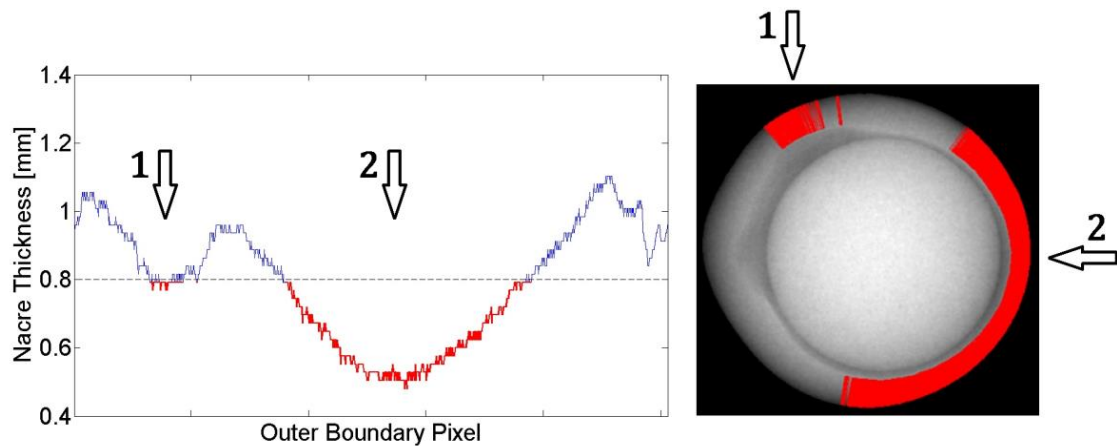


Figure 14: Automatically measured nacre thickness profile of a Tahitian pearl (left). The regions of the profile with a thickness lower than 0.8mm and the corresponding regions of the X-rayed pearl are marked in red

As the automated measurement as well as the general imaging of spherical object results in a discrepancy between detected boundaries and real boundaries, a certainty measurement for the obtained results is proposed. The detected outer boundary is pixel wise shifted along its outside pointing normal vectors which results in a larger nacre thickness measurement. At each iteration, the percentage of the current nacre thickness profile lower than 0.8mm is measured (Figure 15 on the right, the ordinate describes the shift in pixels and the abscissa the percentage of nacre thickness lower than 0.8mm at the corresponding shift.). In the example of Figure 15, less than 20% of the nacre thickness is lower than 0.8mm when the outer boundary is shifted by 9 pixels. It means, the automatic detection of the example pearl as a reject would be false if imprecisions of all segmentation steps and imaging imprecisions resulted in a lower nacre thickness of 9 pixels at every point of the outer boundary.

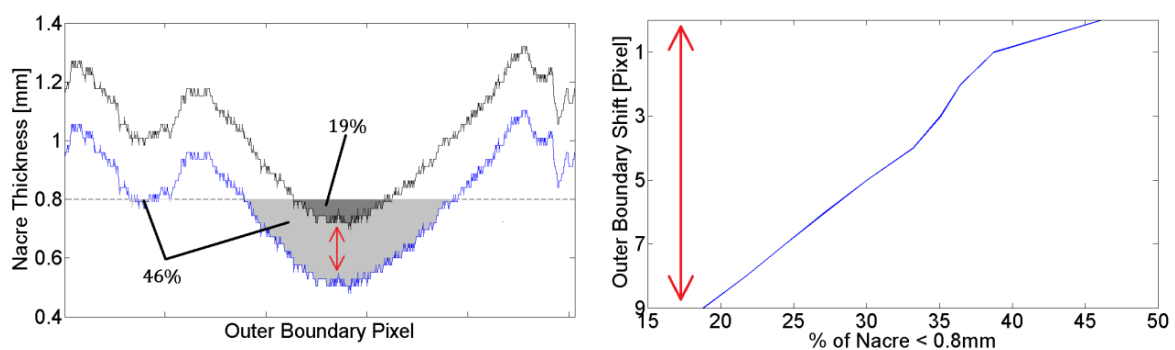


Figure 15: Representation of the certainty calculation. The graph on the left shows the automatically calculated nacre thickness profile in mm blue, and the by 9 pixels shifted profile in black. The graph on the right shows the percentage of nacre thickness lower than 0.8mm at each boundary shift from 0 to 9 pixels.

As the average precision of each segmentation step lies at ~ 1 pixel, pearls automatically detected as rejects with a certainty value lower than 4 pixels might still be considered as good for exportation, according to the paradigm that in case of doubt pearls should not be rejected. However, the certainty value should be seen as a variable that is to be adjusted by the DRMM according to the results of the test phase of the prototype of our algorithm, rather than to be defined by the author.

1.5.7 Used Hard- and Software

All algorithms were programmed and run in Matlab 7.12.0 (R2012a). All tests were run under Windows 7 64 bit on a dual-core Samsung R590 (CPU Intel Core i5 450M / 2.4 GHz) with 4GB RAM. The required processing time of 1 second per image was met with this equipment. Optimization possibilities that require a change of Hard or Software configuration (Multithreading, export to C++, etc.) were not evaluated. Any time a certain processing time is given within the following sections, the measure is based on the processing with the mentioned equipment.

1.6 Automatic Measurement Results

39 pearls with 20% of its nacre thickness lower than 0.8mm were detected. The pearls sorted by descending certainty values can be seen in Figure 16. Red bars correspond to the 13 pearls manually classified as rejects by DRMM experts. Two obvious false rejects due to false nucleus detection occurred. When a self-evaluation of the nucleus detection was applied (will be explained in section 4.4.5) the false rejects could be eliminated. The remaining rejects that were classified as good by the DRMM experts could be validated visually as true automatic classification by visual analysis of the segmentation results. Anyhow, as mentioned earlier, rejects with a low certainty should be filtered out by thresholding the obtained certainty values, as within the region of low certainty, segmentation and imaging imprecision would influence whether a pearl is a reject or not. When a threshold of 4 pixels is applied 16 pearls with automatically detected and visually validated nacre thickness of lower than 0.8mm would pass the control. All pearls with a certainty greater than the last manually rejected pearl (bar 23, certainty of 5 pixels) can instead be seen as human false classifications (the two false rejects of the non-optimized automatic measurement excluded).

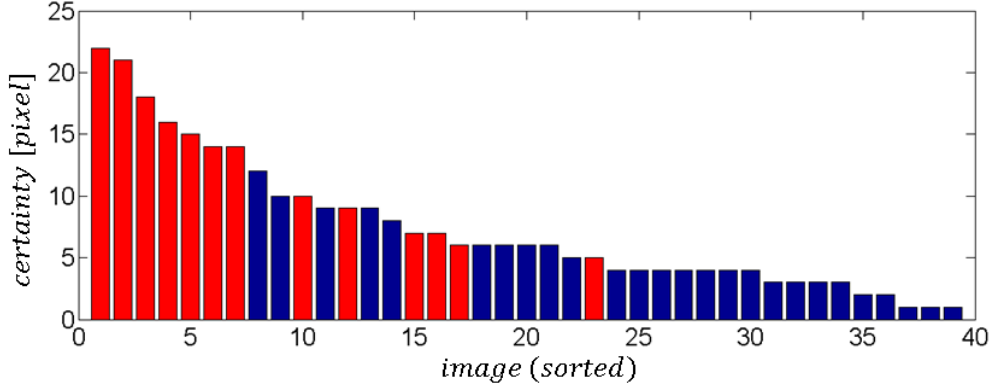


Figure 16: Rejection certainty values of the automated detection of pearls with 20% nacre thickness lower than 0.8mm. Red bars correspond to pearls manually classified as rejects by DRMM experts.

The results show that, first of all, it is generally possible to automatically evaluate the nacre thickness of Tahitian pearls out of X-ray images, despite the large variation of shape and nacre-cavity-nucleus configuration. Secondly, the automatic classification is more reliable as the manual one. This is due to the fact that the experts do not always have enough time to analyze region boundaries in detail, seeing that thousands of pearls have to be controlled on a daily basis. According to the paradigm that in case of doubt the decision has to be made in favor of pearl quality, pearls with a thickness close to 0.8mm might slip through the control.

Another challenge of the manual classification is the estimation if a region that has a thickness lower than 0.8mm corresponds to 20% of the 2D nacre profile. This is specifically for non-round pearls a non-trivial task. Here, the automatic detection has a clear advantage, as the percentage in regards of the complete outer boundary can be calculated precisely.

The average processing time for the complete nacre thickness measurement with the specified equipment is 0.7 seconds per image, which means the requisition of processing an image in less than 1 second was not only met but also some room for precision optimization is left.

1.7 Structure of Part I

After presenting related work in section 2, the implemented algorithms to automatically measure the nacre thickness of Tahitian pearls out of X-ray images will be explained in detail. The presentation of the first three steps, pearl segmentation, nucleus detection and cavity detection (sections 3, 4 and 5) follow a similar methodology. First, the goal of the task is

introduced along with main challenges that appear when classical algorithms are applied. These sections serve the goal to introduce the specific challenges determined by the nature of the Tahitian pearl and the character of the obtained X-ray images. Furthermore, they serve the goal to justify the choice of algorithms used for the automatic measurement. After introducing these challenges, the applied approaches are explained in detail. The results of each segmentation step are presented and the precision is measured independently from the later nacre thickness measurement. In the respective discussion sections the precision of the results is analyzed and optimization possibilities for imprecise detections are presented. Each section ends with a brief conclusion summarizing the presented work. The nacre thickness measurement, based on the obtained region boundaries, is explained in section 6 and the identification of rejects along with the certainty calculation is presented in section 7. In section 8, the results of the automatic nacre thickness measurement are presented. The results are discussed and compared to the manual classification of the experts of the DRMM in section 9. Optimization possibilities are presented with a broader view on the complete measurement. A prototype, developed on the basis of the presented algorithms, that was recently implemented at the DRMM for further validation of the used methods will be briefly introduced in section 10. In section 11, a conclusion in regards of the complete measurement procedure is given followed by a sketch of the further ongoing of project RAPA concerning the automatic nacre thickness measurement of Tahitian pearls.

2 Related Work

Strongly related to this work is the article [LEI09], in which an automated nacre thickness measurement of pearls is proposed. The pearl type is not specified, but the origin of the article suggests that Chinese Freshwater pearls are used. For image acquisition, optical coherence tomography (OCT) is applied. The obtained OCT images are denoised and edge pixels of the outer boundary of the pearl and the nucleus are identified with Canny edge detection and Support Vector Machine respectively. Afterwards the outer boundary of the pearl and the nucleus are obtained by fitting circles to the extracted edge pixels. The automatic nacre thickness measurement is evaluated with 8 manually segmented pearls and reaches 93.6% average accuracy.

While an interesting and straight-forward approach, it is stated clearly in the article that the basic assumption for this approach is that the outer boundary of a pearl can be described by a circle: *‘As a priori knowledge, we suppose that the pearl and nucleus are both spheres, thus, in 2D OCT image, the outer and inner boundaries of nacre are both circles’*. This assumption does not hold for Tahitian pearls, as shape variety is a typical feature. In Figure 17 on the left, an image of the cited article shows the fitted circles in blue that describe the outer boundary of the pearl and the nucleus. The X-ray images of two typical Tahitian pearls on the right show that their outer boundary cannot be described with circles. The approach is further developed in [SUN10] and [LIU13], but still under the condition that the contours of pearl and nucleus can be approximated by circles. Additionally, the occurrence of cavities is not addressed, as they are not typical for Chinese Freshwater Pearls. The approach is hence not applicable to Tahitian pearls.

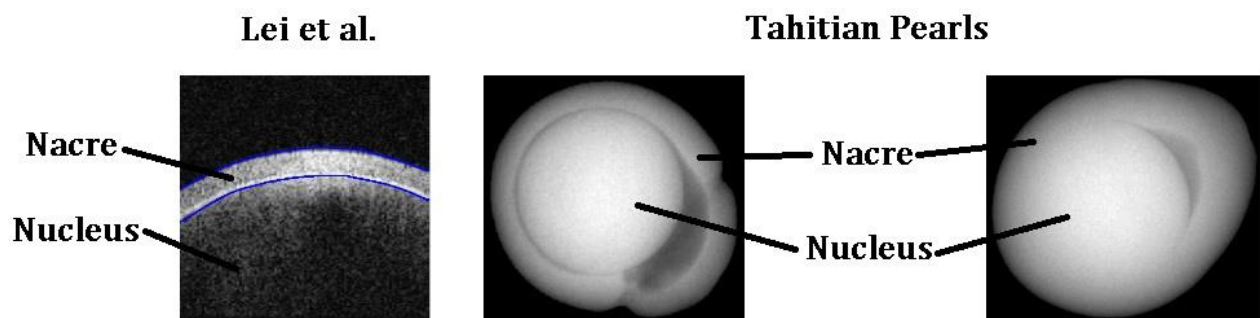


Figure 17: Results of the approach proposed in LEI09 (left) based on the assumption that the pearl boundary can be described by a circle (left). On the right two typical examples of Tahitian pearls are shown for which this assumption does not hold.

To the authors knowledge, the cited articles are the only ones that can be found in the international literature dealing with an automated nacre thickness measurement of pearls.

From a broader point of view, two domains can be related to our work. The first one is the general use of computer vision for quality control in industrial applications [SZA15]. Specifically automated fruit quality control with computer vision applied on X-ray images [ABB99], as it is the automation of quality evaluation of natural products by analyzing their internal structure. Approaches comprise for example automated quality control of apples [SCH96], [SCH97] or wheat kernels [NEE07]. The second domain is medical imaging, in which numerous segmentation approaches applied to X-ray images can be found [STO13]. Anyhow, these domains can only be related to the purely algorithmic parts of each segmentation step of the nacre thickness evaluation and not to the general approach of automatizing the nacre thickness control of Tahitian pearls out of X-ray images. References of related work to those algorithms will hence be given in the corresponding sections.

3 Pearl Segmentation

The first step of our procedure to obtain the nacre thickness profile is to segment the pearl, i.e. to detect the outer boundary of the pearl. The main challenge of this task is the superposition or the adjacency of background gradients and the outer boundary of the pearl. Generally, different approaches can lead to a successful segmentation; the purpose of this study is to define the optimal method in means of processing time and in means of accomplishing the paradigm of avoiding false negative nacre thickness evaluations.

In the next section the possible application of different classical segmentation approaches is analyzed. Main challenges faced when testing these approaches are outlined to illustrate the general character of the X-ray images and why finally a physical-based model approach was chosen to segment the pearls. This approach is explained in detail in section 3.2. The precision of the implemented approach is measured in section 3.3 showing that the chosen method is adequate to segment the pearls from the X-ray images. The results are discussed in section 3.4 along with recommendations of possible improvements. The conclusion follows in section 3.5.

3.1 Main Challenges

In the case of the test images, the general image configuration is rather simple: a background that describes the support, and one object that is the pearl. The main challenge is caused by the non-uniformity of the background and potential superposition of background gradients with the pearls boundary. In Figure 18 one borehole of the support is shown in detail together with its representation in an X-ray image without pearl.

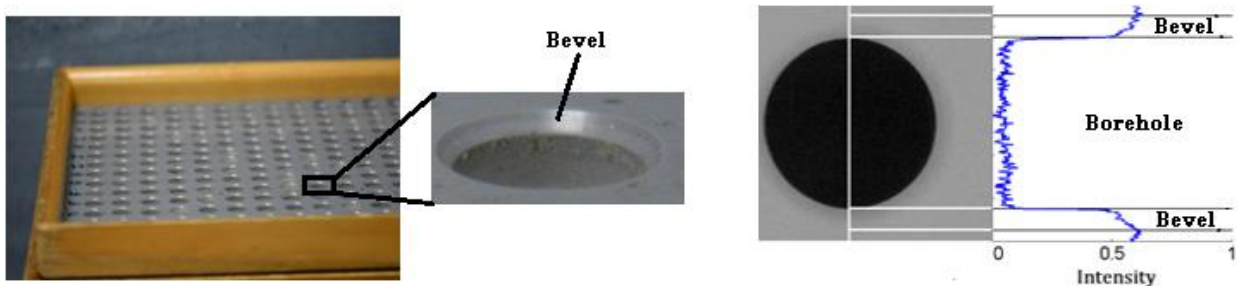


Figure 18: A detail of the support showing a borehole with bevel (left two images). On the right is the according X-ray image with image intensity distribution along the white line through the center of the borehole.

Each borehole contains a bevel to facilitate filling and emptying the support. As a result the X-ray image of a blank borehole contains three regions. First, the borehole as a dark circular area, as it contains less material than the rest of the support. Second, a concentric gradient that describes the bevel. And third, the rest of the support with a more or less uniform light intensity distribution.

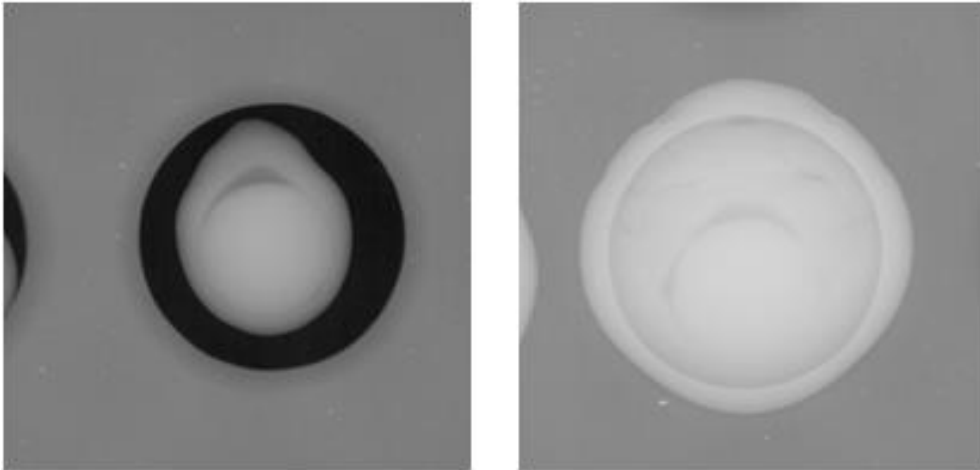


Figure 19: A pearl located completely within the borehole (left) and a pearl surpassing it completely (right).

In the case of a pearl located completely within the borehole (Figure 19 on the left), the pearl can be segmented by deleting the dark borehole region with simple thresholding. In a similar way, pearls that surpass at any point the borehole and its bevel (Figure 19 on the right) can be segmented by deleting the light region of the surface of the support by thresholding. Difficulties arise in case the pearl touches the outer boundary of the borehole or partially surpasses the borehole. An example of the latter is shown in Figure 20.

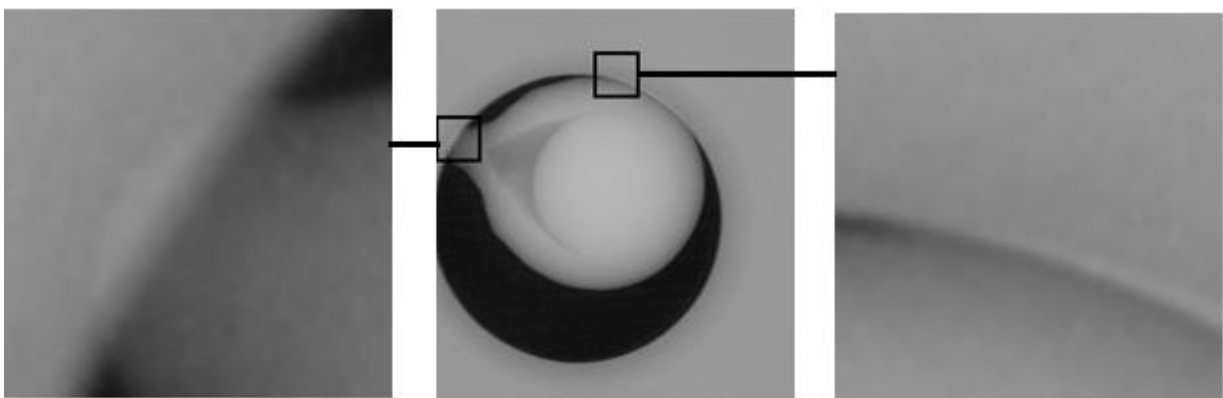


Figure 20: Two details of areas in which the pearls outer boundary lies within the bevel of the borehole.

3.1.1 Region-Based Approach

The idea of region-based approaches is to cluster adjacent pixels that share a certain degree of similarity. A typical example for these approaches is region-growing [ADA94]. Seed pixels are chosen and their adjacent pixels are evaluated if they share the same predefined characteristics. If so, they and the corresponding seed pixels are determined to belong to the same region. Now every adjacent pixel of these regions is again evaluated and in case they share the same homogeneity criterion as well added to the corresponding region, leading to a continuous growing of regions until no adjacent pixel complies with the homogeneity criterion. Applications of this approach applied to X-ray image segmentation can be found for example in [POH01], [PAN07], or [PRA14].

The main challenge when region-based approaches are applied to X-ray images of pearls that partially surpass the borehole is to define a suitable homogeneity criterion. As the background is non-uniform and superposed by the pearl, such a definition based on for example image intensity is difficult (Figure 21). An alternative might be to use gradient information as for example done in [KAU15] for lesion segmentation in medical-ray images, but the strong gradient of the borehole superposed on the pearl would have to be recognized, which means information about gradient directions in regards of a certain reference point would have to be included.

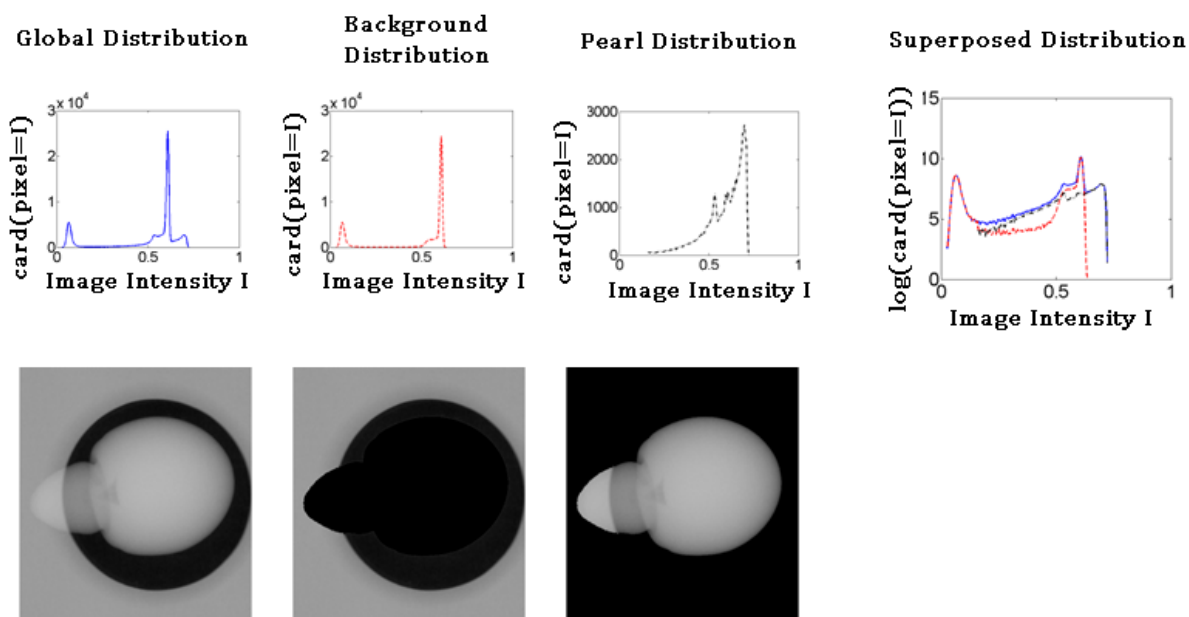


Figure 21: Superposition of intensity distributions of pearl and background.

A more general drawback is that a large number of pixels have to be evaluated iteratively that do not contain useful information of the pearls boundary. Seeing the image size of 1000x1000 pixels and the requirement that the whole measurement has to be done in at least 1 second, region-based approaches are generally not favorable, especially as large parts of the pearls boundary can be detected more easily with edge based approaches.

3.1.2 Edge-Based Approach

The main idea of edge based approaches is that object boundaries are defined by strong image gradient magnitudes. Specifically for the pearl this holds true in many cases as no background or object texture exists. Some basic operators to detect edges are Sobel [SOB68], Prewitt [PRE70], LoG [MAR80] and Canny [CAN86]. Two main difficulties aroused when applying classical edge detection to segment the pearl: cutting of the pearl boundary due to strong superposed borehole gradients and edge shattering due to weak pearl boundaries at the bevel region. Both are visualized in Figure 22 for the application of the Sobel operator with a filter size of 3x3. The image on the left is the original and the image on the right is the original superposed with all detected edges after non-maximum suppression. The upper detail shows the cutting of the pearls boundary due to the strong borehole gradient (number 1) and shattering of edges (non-connected edges) due to the superposition of opposed pearl and bevel gradient (number 2). The second detail shows again cutting due to the borehole gradient (number 1). Additionally, detected false edges with relatively strong magnitude within the pearl region are marked with number 3. This happens due to the spherical form of the pearl and as well for pearls that do not surpass but touch the borehole gradient as in both cases the maximum gradient of the pearls boundary is compensated or superposed by the bevel gradient.

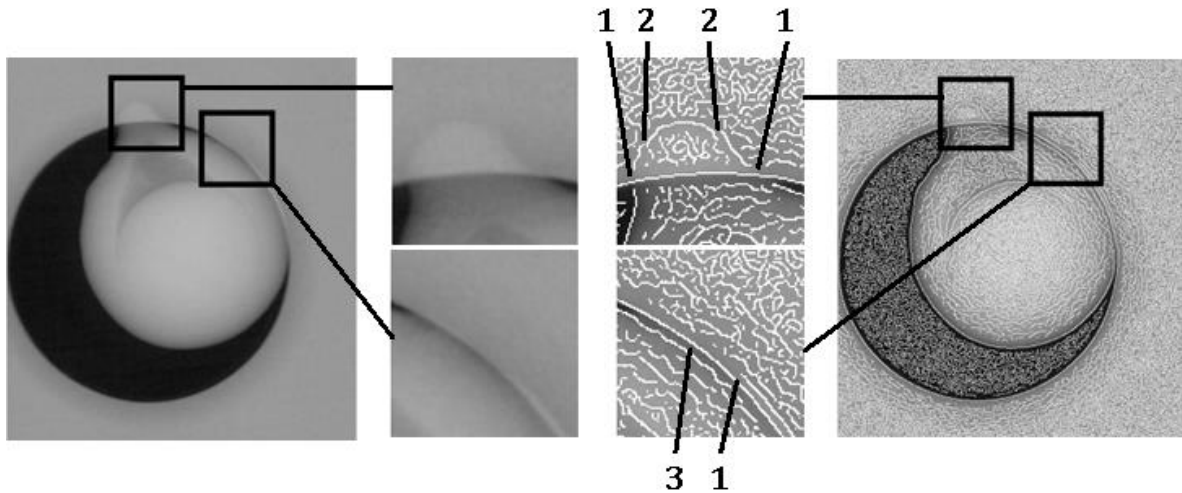


Figure 22: Details of the original X-ray image (left) and of the original image superposed with all edges detected with a 3x3 Sobel operator (right).

The shattering of weak edges could be addressed by applying a larger filter size, but this would increase the cutting of edges due to the strong borehole gradient. Another possibility might be to apply the Canny operator that allows to detect weak edges with a hysteresis method even with a lower filter size, but the operator is too time intense for the required processing (0.7 seconds when applied to the test images of pixel size 1000x1000).

It is not at all impossible to solve the mentioned problems one by one. Anyhow, as each problem has its own reason, these reasons have to be identified and afterwards all edges have to be filtered and connected according to the reason of their shattering. In summary, traditional edge detection does not lead directly to satisfying results; additional steps would have to be added, which at some point conflicts with the general requirement of a complete nacre thickness measurement within 1 second per image.

3.1.3 Active Contours

A method suitable to profit from the partially clear edge gradients while overcoming edge shattering is the active contour approach ‘snakes’ [KAS88]. In this approach an initial curve is iteratively moved over the image until it reaches edges with a predefined condition. The contour of the moving curve is constantly stabilized with an internal energy term that restricts the curve from extensive or craggy deformation. The main advantages of this approach are that the result is a closed curve that might contain pixels with weak or even no boundary information and that its contour corresponds to a predefined degree of smoothness. It is hence

widely used in the related domain of region segmentation in medical images (see [BEC14] for a review on deformable models in medical image segmentation).

As the desired result of segmenting the pearl is a closed and naturally smooth contour the application of snakes seems suitable from a general point of view. Additionally, some general boundary information of the X-ray images can be used. As shown in Figure 23, the gradient directions of the pearls contour point at any point to the inside of the pearl (blue arrows) while the gradient direction of the borehole and its bevel point to the outer borders of the image (red arrows). A simple stopping criterion for an active contour can be formulated accordingly.

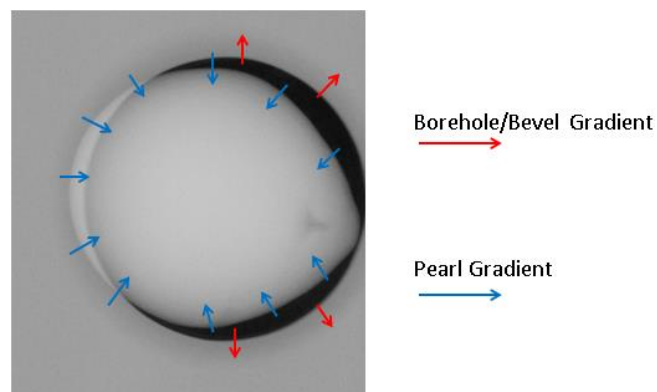


Figure 23: Schema of pearl boundary gradient directions (blue arrows) and borehole and bevel gradient directions (red arrows).

A contour that is initialized at the outer borders of the image will always contain the pearl from the start. If the movement of the curve is a simple constant shrinking that is stopped locally if a point of the curve touches a positive image gradient in direction of the normal vectors of the curve, the contour should after a certain amount of iterations describe the complete outer boundary of the pearl. A simple approach according to [KAS88] with a constant shrinking force and an opposite, positive balloon force for local contour adaption as described in [COH1991] was implemented. With this approach the pearls can generally be segmented, but the trade between processing speed and precision was not ideal. Due to the partially weak boundaries, the step size had to be in a low range (~ 0.1). If the initial boundary length was set to 800 pixels at the image border, average processing time until the contour reached the pearl boundary at any point was 0.7 seconds (first row in Table 1). The average distance between each pixel of the final boundary was 1.6 pixels. To speed up the algorithm, either the initial contour length can be reduced (second row in Table 1) or the step size increased. Increasing the step size resulted in the contour over jumping weak boundary edges,

while decreasing the length of the active contour results in a poor resolution of the resulting boundary. The model-based approach that will be explained in the next sections is not only faster but has additionally the advantage that the superposition of background and pearl gradients can be eliminated, which facilitates all following segmentation steps.

Active Contour Length [pixel]	Average processing time per pearl [sec]	Average pixel distance of final contour [pixel]
800	0.75	1.6
400	0.34	3.0

Table 1: Relation between processing time and precision of final result in regards of the active contour length.

3.1.4 Model Based Approach

The idea of model-based approaches is to use *a priori* knowledge of image or object configuration to segment objects or the background (see for example [CHE05] that describes the use of a femur model in combination with snakes for medical X-ray image segmentation purpose). As the background configuration of the used X-ray images corresponds to the measurable geometry of the support, the requisition of suitable *a priori* knowledge to segment the pearl from the background is generally given. A classical approach would be to create a synthetic background image that describes the current borehole without pearl and to mathematically add out the background by simple subtraction (Figure 24).

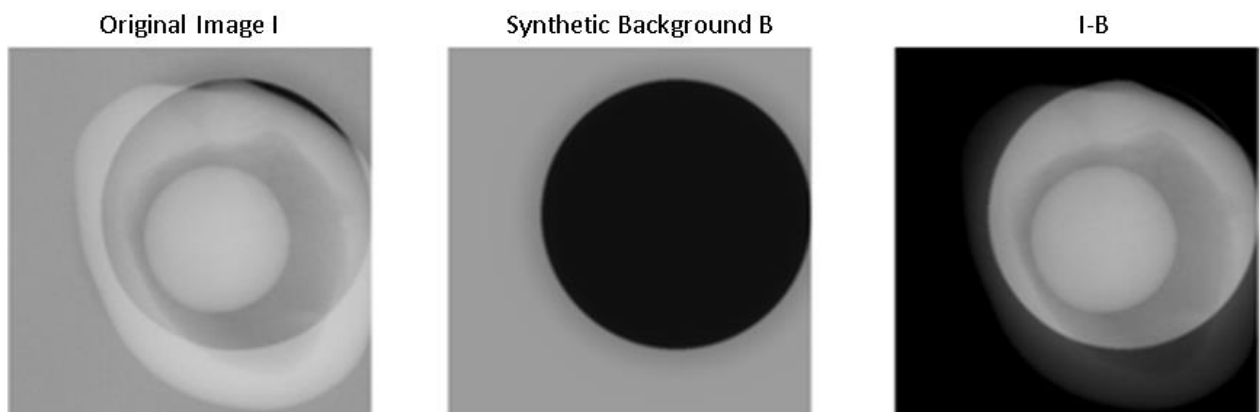


Figure 24: Example of pearl segmentation by subtraction of the synthetic background B from the original image I.

A further improvement of this method can be obtained if the physical properties of X-ray attenuation are used. If the relation between image intensity and X-ray intensity is known, the

attenuation of X-ray intensity caused by the support can be mathematically added out, so that the resulting image corresponds to a theoretical X-ray image of the pearl without the support (Figure 25). The implementation is still straight forward, but has the significant advantage that the general problem of superposed gradients is reduced for all further processing steps. As this approach was deemed the most suitable, its implementation will be explained in detail in the next sections.

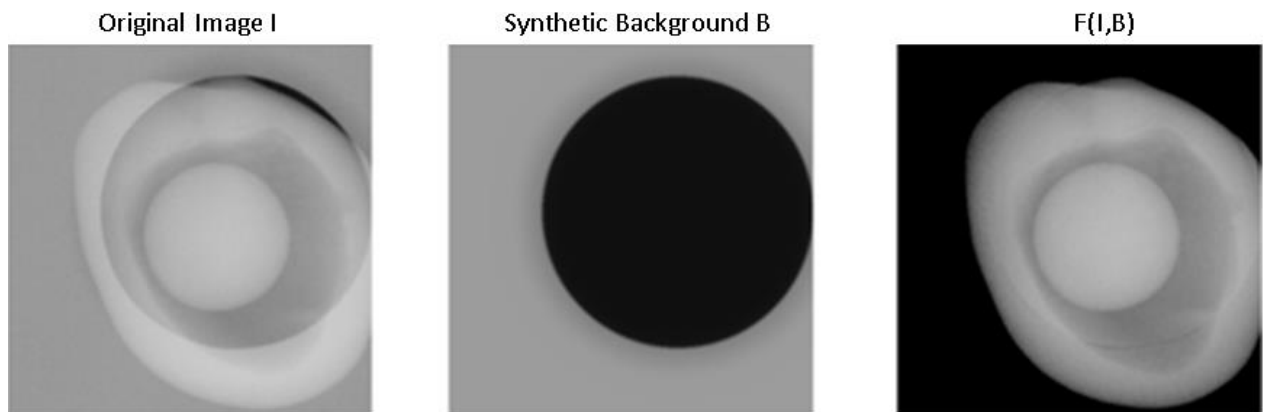


Figure 25: Example of pearl segmentation with a synthetic background in combination with physical properties of X-ray attenuation.

3.2 Implemented Approach

To add out the background based on the physical properties of X-ray attenuation three steps are necessary. First, the image intensity has to be related to the X-ray intensity after the penetration of the support and the pearl. With the obtained function the images can be recalibrated to the X-ray intensity after penetration, which is necessary to mathematically add out the background based on the geometry of the radiographed scene. Second, a synthetic background image has to be created that corresponds to the X-ray intensity of the support without pearl. Afterwards, the background can be added out and potential artefacts have to be deleted.

3.2.1 Image Calibration

Two approaches to obtain the relation between image intensity and physical properties of the radiographed material can be used. The first one is theoretical and starts at the X-ray generator, while the other one is experimental and starts at the output image intensity. For the

first one all physical and numerical parameters along the whole image generation process starting at the X-ray gun have to be known to obtain a formula between initial X-ray intensity and image output. This is not really an option, as even if many parameters are known, the image output can vary depending on parameters that are not considered during the image generation (temperature of the device components, temperature of the radiographed material, air pressure, electronic noise variation, etc.). Additionally, modern X-ray imaging devices are assemblies of components that are manufactured by different companies, making the acquisition of information to reconstruct the whole image generation chain difficult. A shortcut could be made by only considering the conversion between X-ray intensity after the radiographed material and image output; still the mentioned problems stay the same.

The second approach instead is practicable without major effort. A reference image of a known object has to be taken to find a mathematical relation between the objects size and density and the output image intensity. Then each image taken under the same conditions can be recalibrated from image intensity to geometric properties.

For this purpose an X-ray image of a blank nucleus as shown in Figure 26 on the left was used. In a first step the radial intensity distribution was extracted (Figure 26 in the middle) and averaged over 360° (Figure 26 on the right) to decrease possible noise influence. The profile was taken in a radius range that did not include the transition between nucleus boundary and background to avoid transition artefacts).

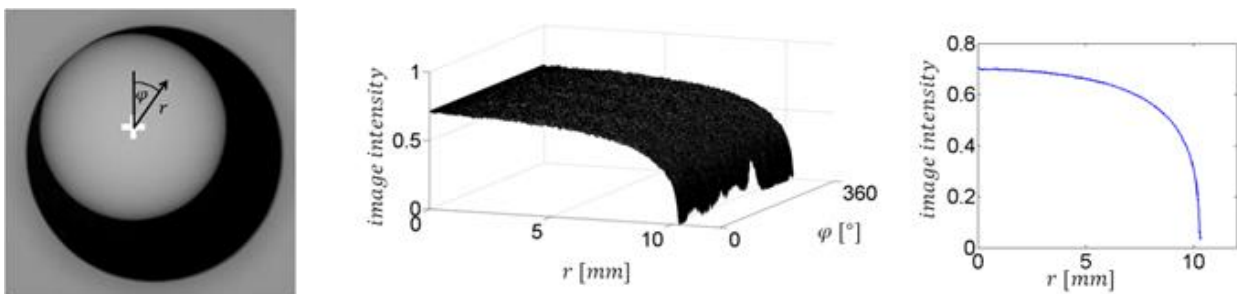


Figure 26: X-ray image of a nucleus (left), its radial intensity profile (middle) and the profile averaged over all angles (right).

A general function that converts the radial intensity profile to a circular function was then estimated experimentally to

$$I'_{r,p} = (1 - I_{r,p})^{-0.4}. \quad (1)$$

In this equation $I_{r,\varphi}$ is the radial intensity profile after averaging and $I'_{r,\varphi}$ the radial intensity that corresponds to a circular object (Figure 27). In a second step the obtained function was calibrated to the measured size of the nucleus as to

$$I''_{r,p} = 12.6I'_{r,p} . \quad (2)$$

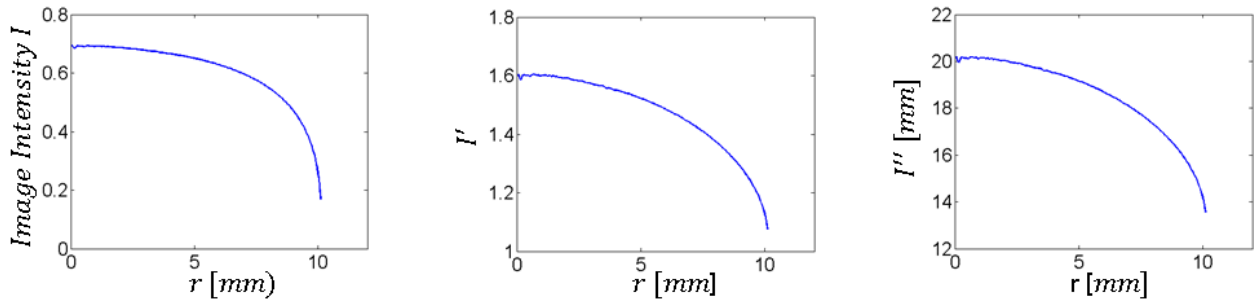


Figure 27: Image calibration process.

The resulting calibration function was validated with 5 nuclei of different size. Additional validation tests were done by calculating a semi 3D nacre thickness profile of near-round pearls. The radius of the nucleus and the outer boundary of the pearl were detected to obtain an average nacre thickness that does not depend on the image intensity (Figure 28 in the middle, radius difference corresponds to 1.23 mm nacre thickness). Out of the calibrated images the nacre thickness at any point of the pearl was calculated as

$$d_i = \sqrt{\left(\frac{I_i}{2}\right)^2 + d_{i,N}^2} - R_N . \quad (3)$$

In this equation I_i is the calibrated image intensity of pixel i , $d_{i,N}$ is the distance of the pixel to the center of the nucleus and R_N the radius of the nucleus. The result corresponds to the 3D nacre thickness profile of one half of the whole pearl (Figure 28 on the right). The results corresponded to the expected constant nacre thickness over the whole surface as well as it corresponded to the actual nacre thickness measured as radial difference between pearl boundary and nucleus.

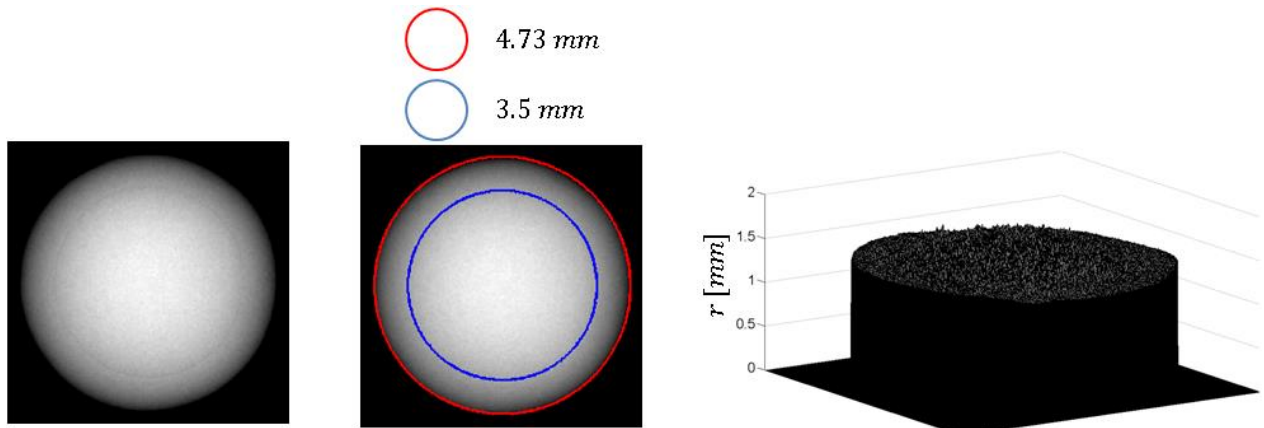


Figure 28: Semi 3D nacre thickness profile (right) for a near-round pearl

3.2.2 Synthetic Background Generation

To create a synthetic background image, the radial intensity distribution of the borehole, its bevel and the rest of the support was obtained directly from the images as shown in Figure 29. The center of the borehole was detected and the radial intensity distribution (Figure 29 in the middle) of areas that were not superposed by the pearl (areas within the white region of the image on the left) averaged over all angles (graph on the right). By rotating the resulting averaged radial intensity function a synthetic background image that corresponds to the original image intensity can be calculated.

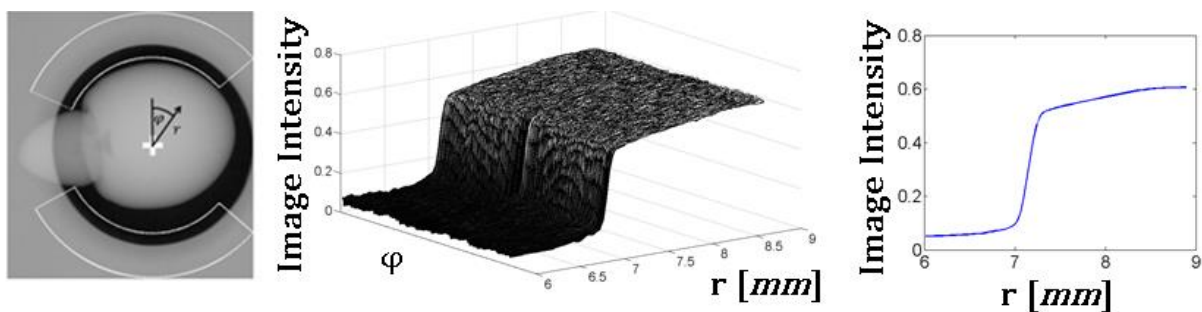


Figure 29: X-ray image with a pearl partially surpassing the borehole (left), the radial intensity profile of the borehole and the profile averaged over all angles (right).

The procedure assumes that the borehole is indeed a rotational symmetric object. This assumption can be evaluated by calculating the standard deviation between the averaged radial intensity distribution and the radial intensity at each angle of the region not superposed by the pearl. The result is shown in Figure 30 in the middle. A large peak appears at the

transition region between borehole and bevel ($\sim 7.14\text{mm}$) while the rest of the graph shows deviations within the noise level.

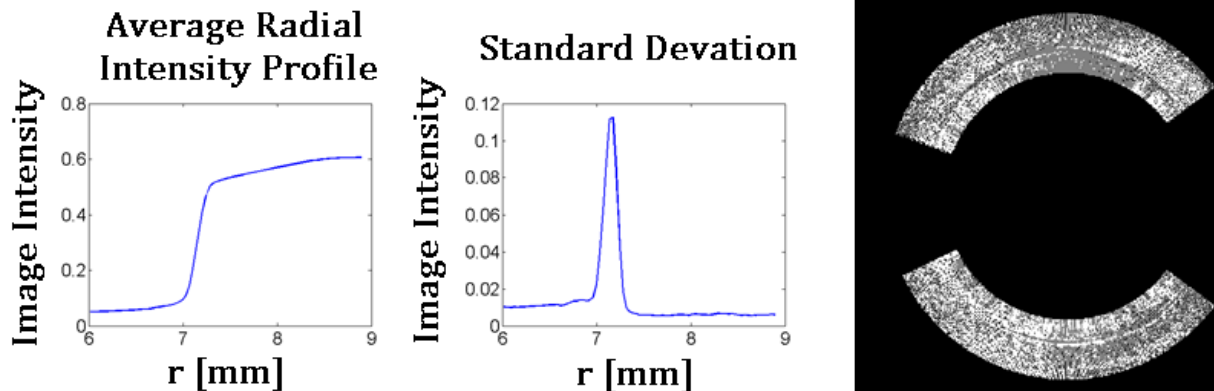


Figure 30: Average radial intensity profile of the borehole (left) its standard deviation (middle) and a visualization of negative (grey) and positive (white) discrepancies to the average profile (right).

Considering an ideally manufactured rotation symmetric borehole that is ideally orthogonal to the X-ray beam, artefacts at this transition region can still be expected due to the approximate character of image generation. This means, even in the ideal case a peak will most likely appear at this transition region as the artefacts caused during image generation are not necessarily distributed symmetrically. Other effects like an imperfect orthogonal alignment between borehole and X-ray beam and imprecise manufacturing or abrasion of the support can be added to the cause. The image on the right of Figure 30 shows all pixels of lower intensity than the average profile in grey and all pixels of higher intensity in white. The more or less random distribution shows that incorrect borehole center detection is not one of the causes, as it would result in a positive deviation on one side and a negative deviation on the other of the bevel contour.

As the assumption that the borehole is rotation symmetric was validated for the set of training images, a general radial intensity profile can be generated that is applicable for all images generated under the same conditions (specifically zoom and initial X-ray intensity). Such a profile would have to be calculated only once prior to the measurement and can then be used for all images of one support. This is not only a faster approach but also necessary for pearls that completely surpass the borehole, as the background intensity cannot be taken out of the image due to the complete superposition of borehole and pearl. For the used images an according general radial profile function was obtained by averaging the averaged radial borehole intensity profiles of 10 images.

3.2.3 Pearl Segmentation

According to the presented methodology, four steps are necessary to segment the pearl in a given image (see Figure 31 for a schema of the workflow). First, the center of the borehole has to be detected. Second, a synthetic background image that corresponds to the position of the borehole of the current image has to be generated. Third, both images have to be calibrated according to the calibration function introduced in section 3.2.1. Finally, as the calibrated images correspond to the material thickness of the radiographed material, the calibrated synthetic image can be subtracted directly from the calibrated original image. Afterwards, the pearl can be segmented by thresholding. Theoretically, the threshold should be zero, but has to be increased by the noise level of the image. In the current implementation this threshold is fixed for all images with the assumption that the noise level should not change for images taken under the same conditions. The threshold is obtained by measuring and averaging the noise level on the flat surface of the support of 10 images.

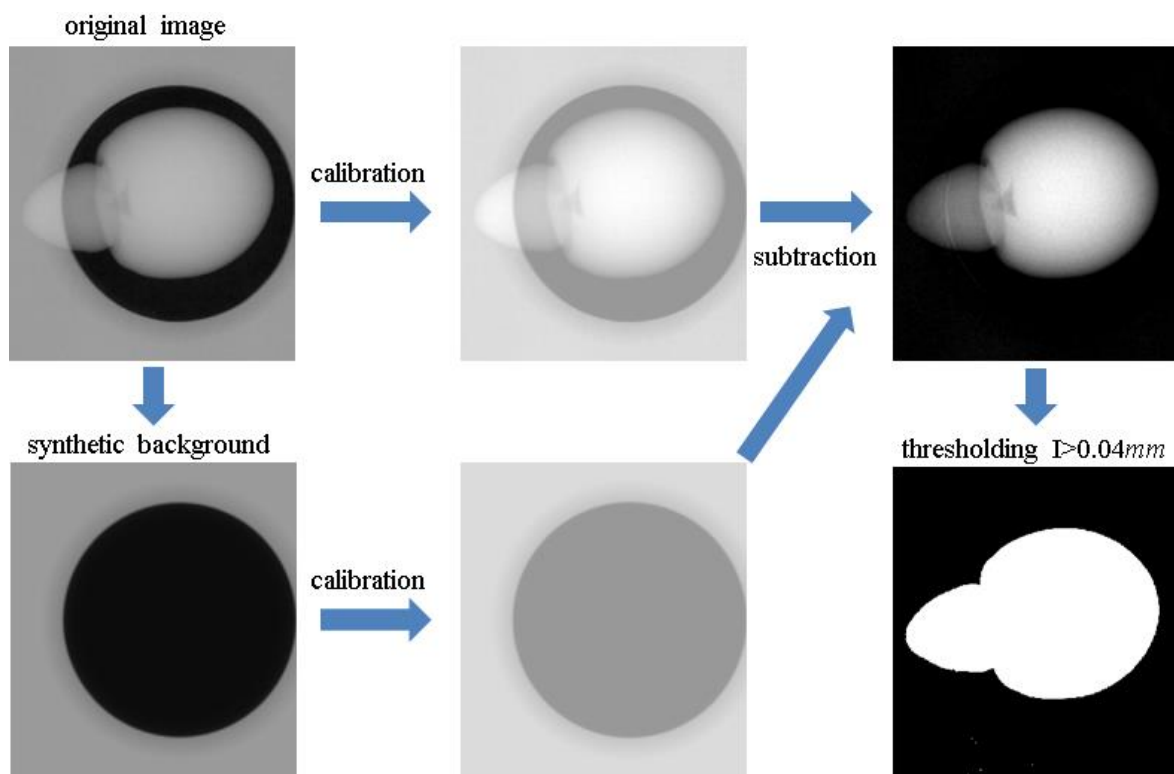


Figure 31: Workflow of the segmentation process

3.2.4 Artefacts

After thresholding the segmented image, three types of artefacts have to be addressed. First, shattered pixels whose intensity exceed the threshold but do not belong to the pearl (Figure 32 marked with 1 in the binary image on the right). Second, artefacts caused by the deviation between ideal synthetic background and real image background at the transition region between borehole and bevel that do not belong to the pearl but are connected to the pearl region (as explained in section 3.2.2; numbered in Figure 32 with 2). And third, artefacts caused by the same reason within the pearl region (numbered with 3).

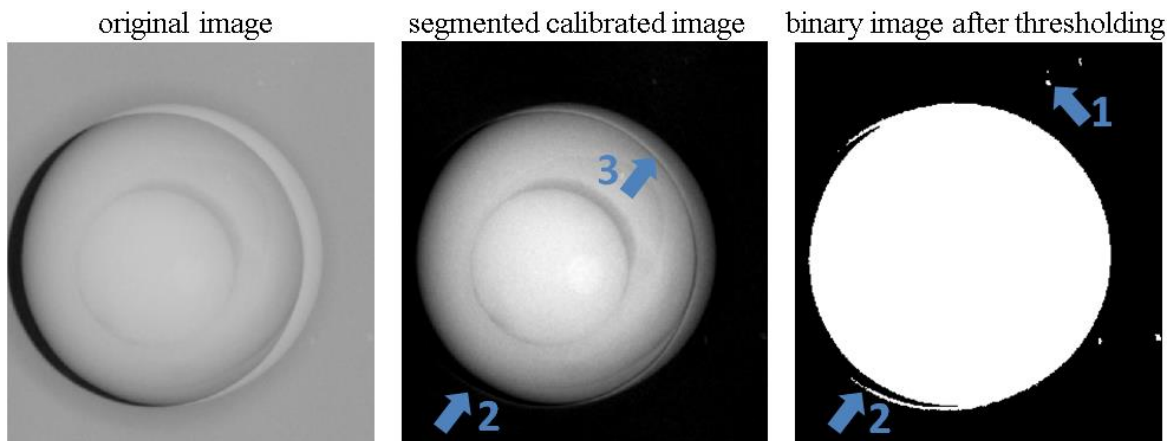


Figure 32: Different types of segmentation artefacts.

The first type, shattered pixels that are likely to be caused by deposits on the surface of the support, can be suppressed by segmenting the largest object of the binary image which is supposed to be the pearl (Figure 33 on the left

For the second and third type, artefacts caused by the deviation between ideal and real background, a single procedure can be applied. As shown in Figure 30 in section 3.2.2 (page 78) the deviation shows a peak at the transition region between borehole and bevel. The affected region of this deviation can be narrowed to -4 to $+4$ pixels in radial direction in regards of the detected borehole center. Those pixels have to be replaced by pixels of intensity that corresponds to the region outside this margin. Accordingly, a smoothing operation leads to a general decrease of intensity for artefacts that do not belong to the pearl but are connected to it (type 2) and an adaption of artefacts within the pearl region to the surrounding pearl intensity (type 3).

The implementation is handled accordingly. First, pixels remaining after the first thresholding within the region of -4 to $+4$ pixels in radial direction of the detected borehole are identified

(Figure 33). Afterwards those pixels are iteratively replaced by the average of their surrounding pixels within a 5x5 neighborhood. A linear filter was preferred to for example a Gaussian filter to not give too much weight to artefact pixels of high intensity. After the filter operation (Figure 34 second image), the largest object of the image containing all remaining pixels greater than the threshold is identified as the pearl (Figure 34 third and fourth image). Please note that the darker region on the bottom right of the pearl is a cavity and not an artefact.

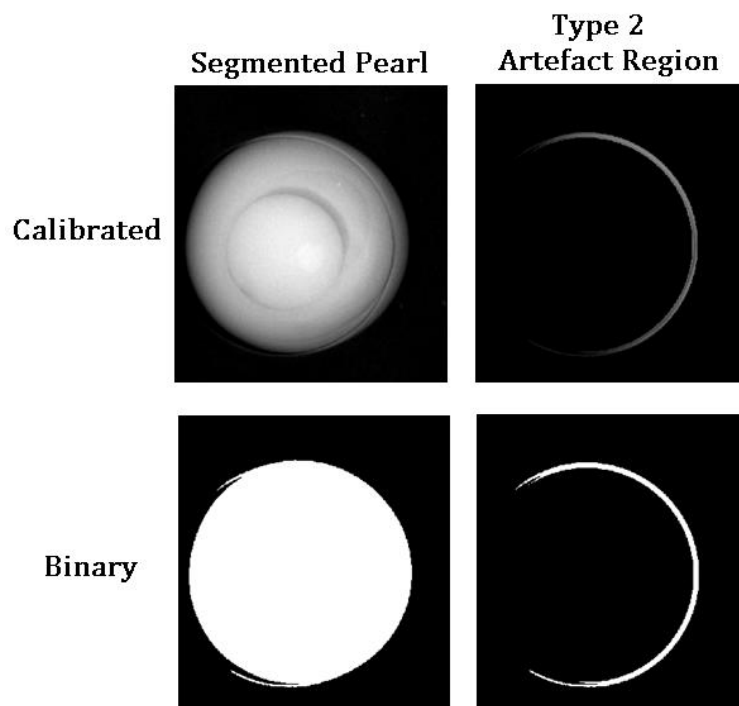


Figure 33: Segmented image and region of artefacts of type 2.

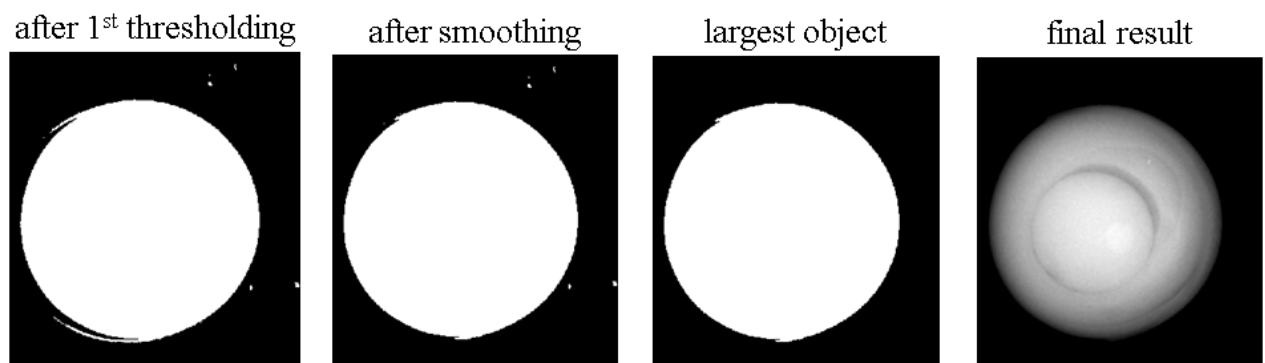


Figure 34: Artefact cleaning procedure.

3.2.5 Summary and Pseudocode

The implementation of the pearl segmentation is according to the previously explained steps the following: An artificial calibrated background image of size 2000x2000 pixels with the spatial resolution of the test images is generated. Afterwards an X-ray image of a pearl is loaded and the center of the borehole is detected. A detail of the generated background image is taken that corresponds to the situation of the detected borehole center in the current image. The current image is calibrated and the obtained background image is subtracted. A threshold of 0.04mm is applied for a first rough segmentation. Afterwards, all remaining pixels within a 4 pixel range around the borehole boundary are identified and iteratively smoothed 10 times with a linear filter of size 5x5. A second time the image is segmented by applying a threshold of 0.04mm. The largest object of the remaining pixels is identified as the pearl.

pseudocode	corresponding section
get calibration function f_c	section 3.2.1
get average radial intensity profile	section 3.2.2
create synthetic background image B	section 3.2.2; 3.2.3
calibrate synthetic background $B' = f_c(B)$	section 3.2.3
for image I_i	
detect borehole center	
get detail of synthetic background B_i'	section 3.2.3
calibrate image $I'_i = f_c(I_i)$	section 3.2.3
delete background $I''_i = I'_i - B_i'$	section 3.2.3
clean artefacts	section 3.2.4
end	

3.3 Precision of Results

The precision of results was first analyzed visually to detect major negative (segmented pearl region too small) or positive (segmented pearl region too large) discrepancies between segmentation result and desired result. Afterwards, a precision measurement based on strong image gradients close to the detected boundary was used to obtain a pixel-based performance evaluation. As unfortunately most pearls of the test image set are located completely within the borehole, all images of the training set in which pearls surpass the borehole (31 images) were used as well to evaluate the precision of the applied algorithm.

3.3.1 Visual Analysis

The largest negative discrepancies between obtained segmentation and desired result for the pearls of the training set surpassing the borehole were observed in two cases in which the pearls outer boundary superposed the bevel of the borehole (Figure 35 on page 84 first two rows, crucial regions marked with 1 and 2), and in one case in which parts of the pearl superposed the upper surface of the support (Figure 35 last row number 3). In all three cases parts of the pearl of lower intensity than the threshold were cut off.

The largest negative discrepancies within the training set were observed in some cases the pearl touches or is close to the borehole boundary (Figure 36 first two rows) and in cases of thin pearl parts on the borehole background (Figure 36 on page 85 third two row).

The largest positive discrepancy within the training set was observed in one case in which parts of the bevel were wrongly identified as pearl (Figure 37 on page 86 first row number 1) and in two similar case within the training set (Figure 37 second and third row number 2 and 3).

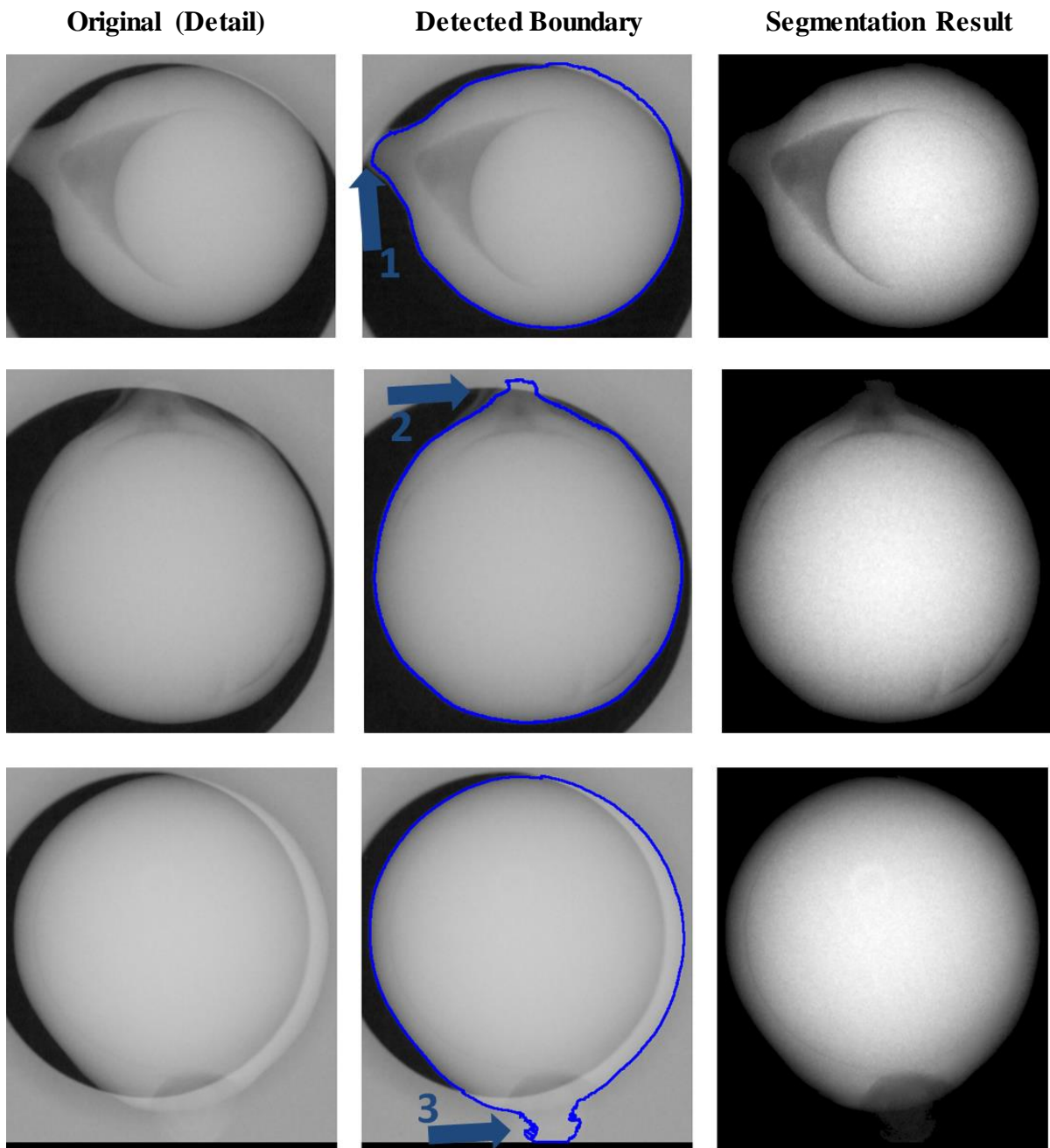


Figure 35: Largest negative discrepancies between segmentation result and desired result of the training set.

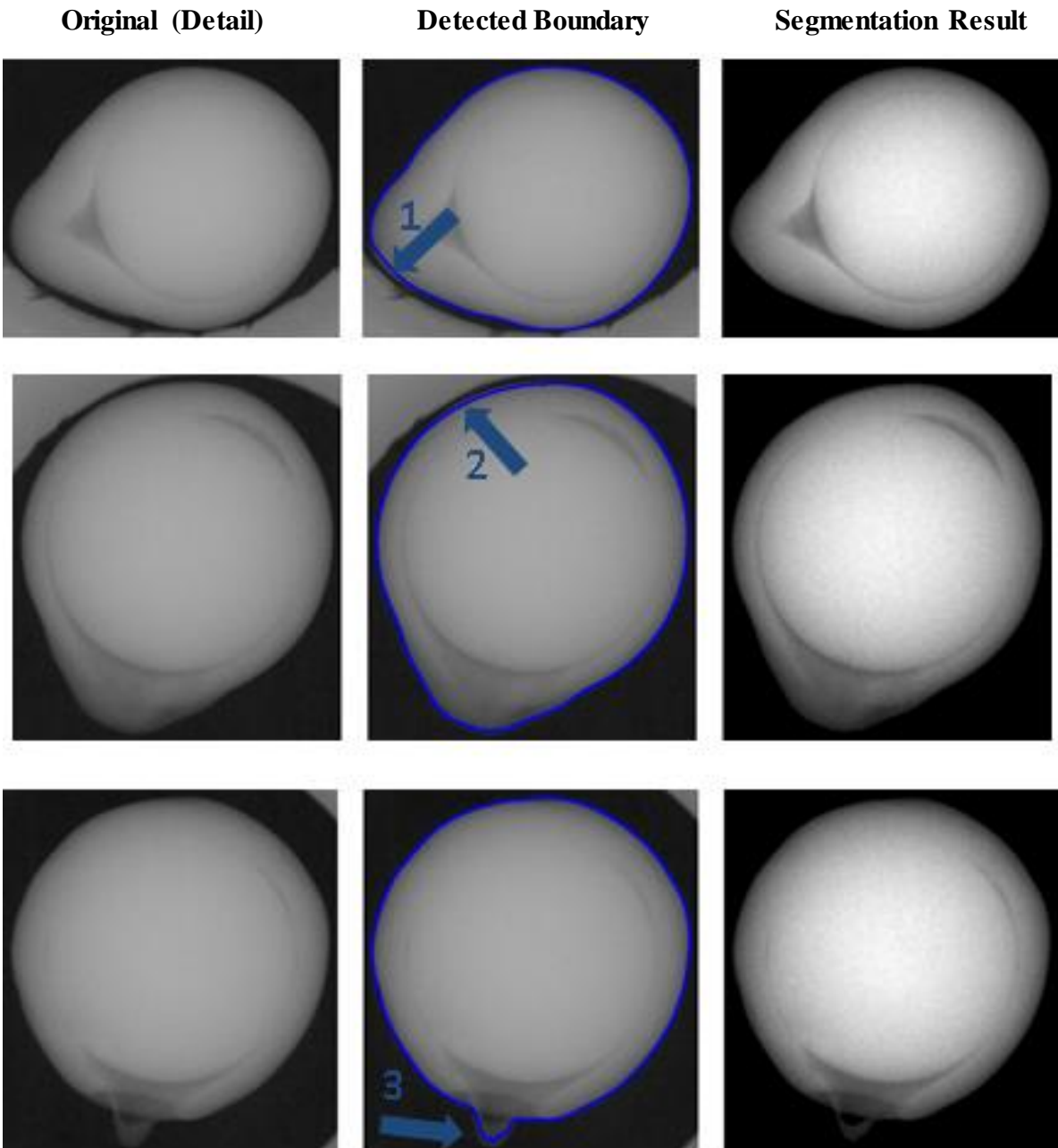


Figure 36: Largest negative discrepancies between segmentation result and desired result of the training set.

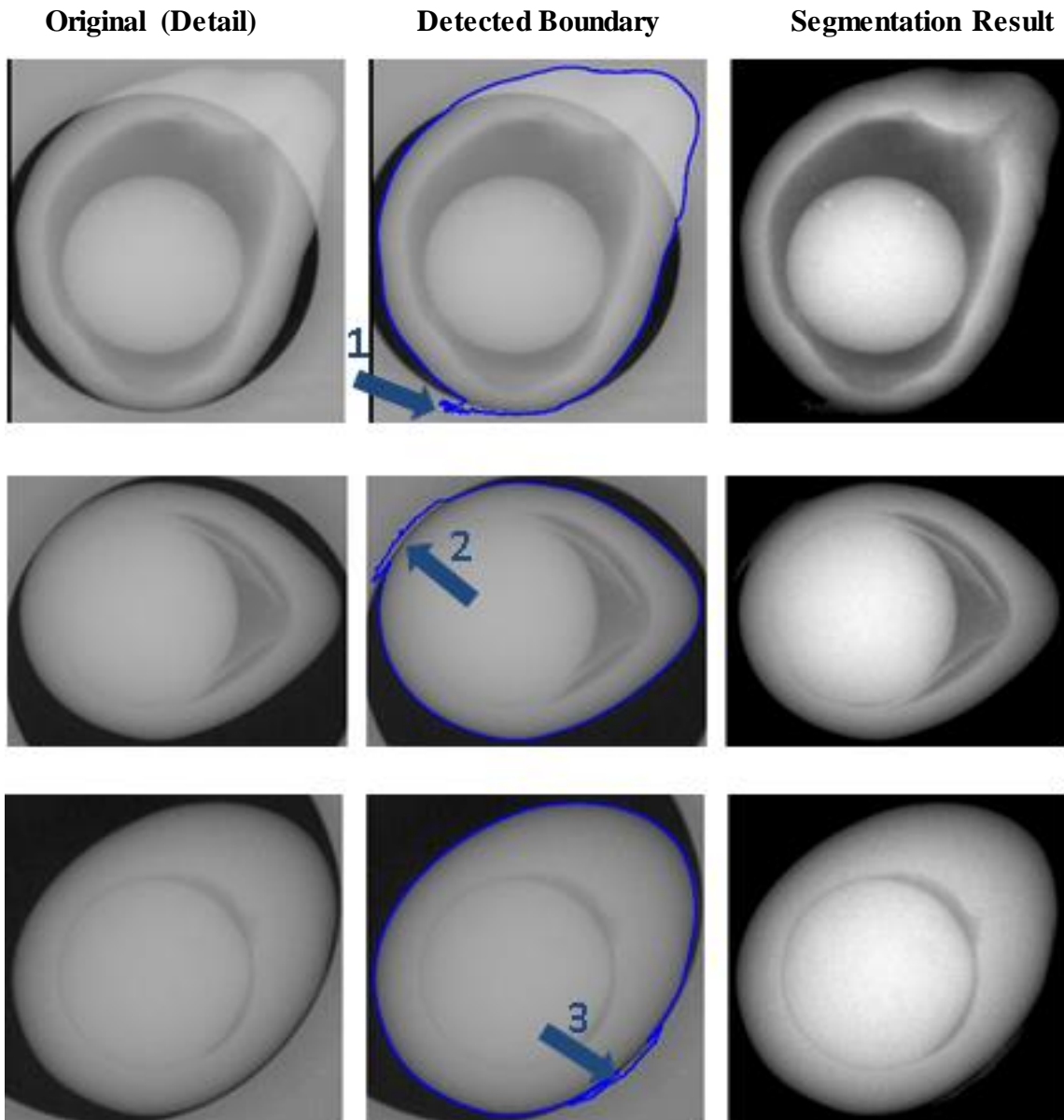


Figure 37: Largest positive discrepancies between segmentation result and desired result.

3.3.2 Precision Measurement

To obtain a numerical precision value on a pixel basis, the following measurement was done. First, the outer boundary of the segmented region (left image of Figure 38 with normal vectors in blue) was smoothed with a regularization matrix to obtain consistent normal vectors (image in the middle of Figure 38 with normal vectors in red). The normal vectors of the smoothed contour were used to evaluate the gradient, starting at each pixel of the non-smoothed detected boundary 15 pixels in positive and 15 pixels in negative normal vector

direction (the image on the right of Figure 38 gives an impression of the evaluation range). The range was chosen empirically, as no larger discrepancies were observed. The strongest gradient in normal vector direction was identified and defined as ‘optimal’ boundary pixel. This assumption is based on the general assumption of edge detection that edge pixels have larger gradients than their neighbors. The distance between each pixel of the boundary obtained by applying our approach and the obtained benchmark boundary at local gradient maxima is used as precision measurement.

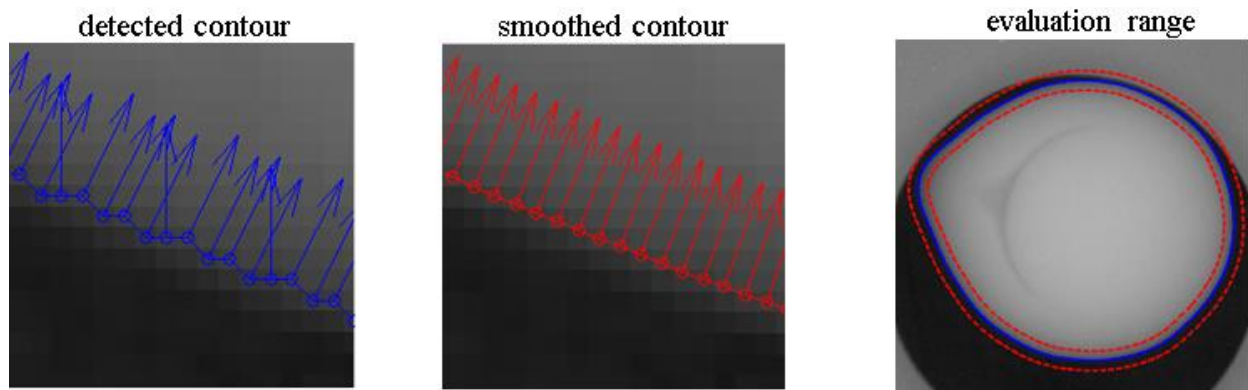


Figure 38: Procedure of the precision measurement.

The average of this distance for the boundary of each of the 298 used test images is shown in Figure 39 on the top (next page, straight blue line) along with the standard deviation of the distance for all pixels of a boundary (dashed black line). The graph can be used for a general performance evaluation of the segmentation process. For an evaluation of the later nacre thickness measurement in regards of false negatives, only negative discrepancies are crucial as they describe boundaries that cut off parts of the pearl and hence lead to a thinner measured nacre thickness as the real one. For this purpose a second average calculation was done in which all positive discrepancies were set to zero. The according graph along with the standard deviation is shown in Figure 39 on the top on the bottom. The three minima at images 21, 91 and 214 in the graph on the bottom of this figure correspond to the three example images shown in Figure 36.

The same procedure was done for the pearls of the training set that surpass the borehole. The according graphs are shown in Figure 40. Here the general deviation from the optimum is shown on the left and the deviation with positive discrepancies set to zero on the right.

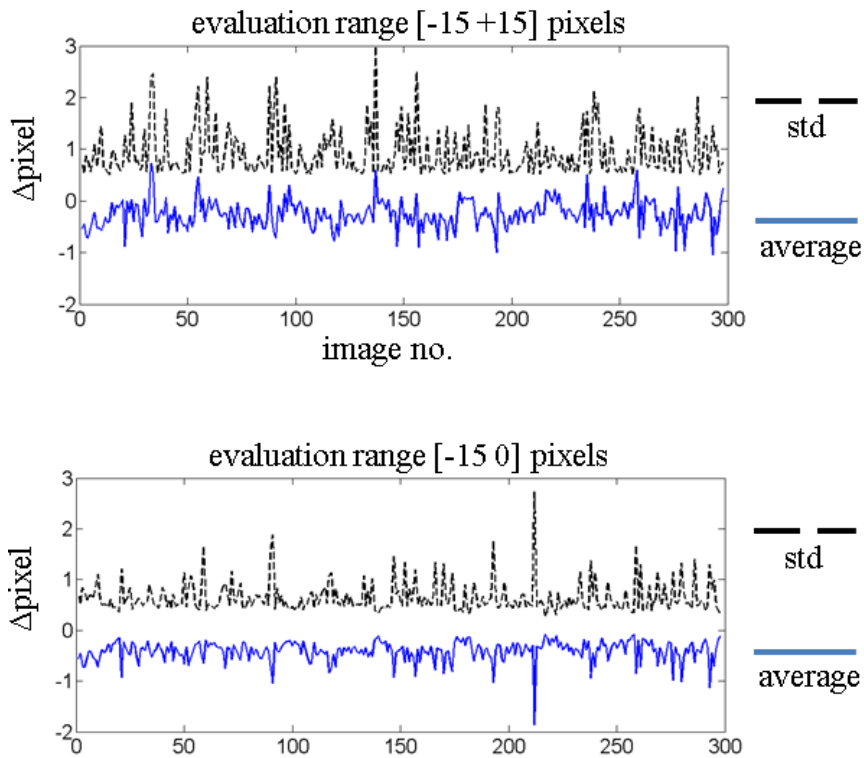


Figure 39: Average deviation from optimal boundary and standard deviation of the detected boundary of each image in a -15 to +15 pixel range (top) and in a range from -15 to 0 pixels (bottom) for the test set.

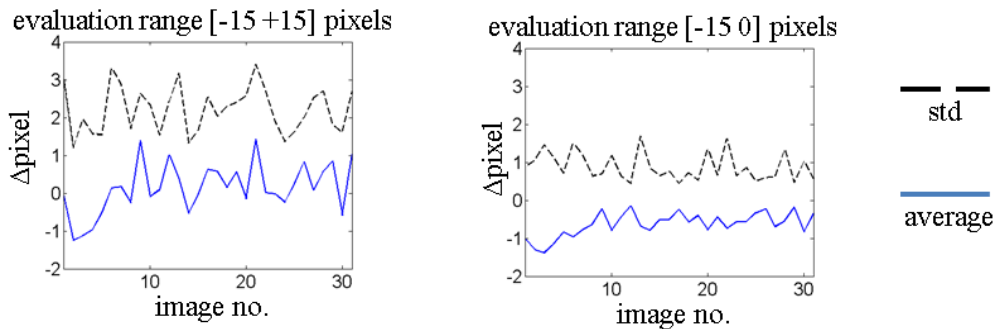


Figure 40: Average deviation from optimal boundary and standard deviation of the detected boundary of each image in a -15 to +15 pixel range (top) and in a range from -15 to 0 pixels (bottom) for pearls of the training set that surpass the borehole.

3.4 Discussion

The detection results are generally deemed as suitable even though discrepancies to the optimal boundary exist. In most of the cases the average discrepancy of all boundary pixels lies between 0 and -1 pixel. Still in some cases local discrepancies are up to 8 pixels large which corresponds in the spatial resolution of the test images to $\sim 0.2\text{mm}$. As the minimal required nacre thickness is currently set to 0.8mm a discrepancy of 8 pixels corresponds to 25% of the rejecting criterion. A positive fact is that larger discrepancies were only observed

at local parts of the whole boundary. As pearls are only rejected if 20% of the nacre thickness is lower than 0.8mm the observed local discrepancies would not necessarily lead to false rejected pearls.

3.4.1 Discrepancy Types

Observed discrepancies between detected and optimal boundary can be divided in two types: threshold-related and model-related. Threshold-related discrepancies occurred when parts of the pearls calibrated image intensity was lower or higher than the applied general threshold. Possible reasons are local variations of support geometry due to imprecise manufacturing or temporary variations of X-ray gun current and voltage or both. An adaptation of the threshold to the corresponding image resulted in a more precise pearl boundary (Figure 41). Accordingly an implementation of a dynamic threshold generation for each image during the segmentation procedure should be considered. It has to be evaluated if the elevated precision justifies the increase in processing time.

Model-related discrepancies were observed for pearls whose outer boundary is close to but does not touch the borehole boundary. Their outer boundary pixels were deleted due to the smoothing process implemented to delete artefacts at the transition region between borehole and bevel (as discussed in section 3.2.4). Examples can be seen in Figure 36 first two rows.

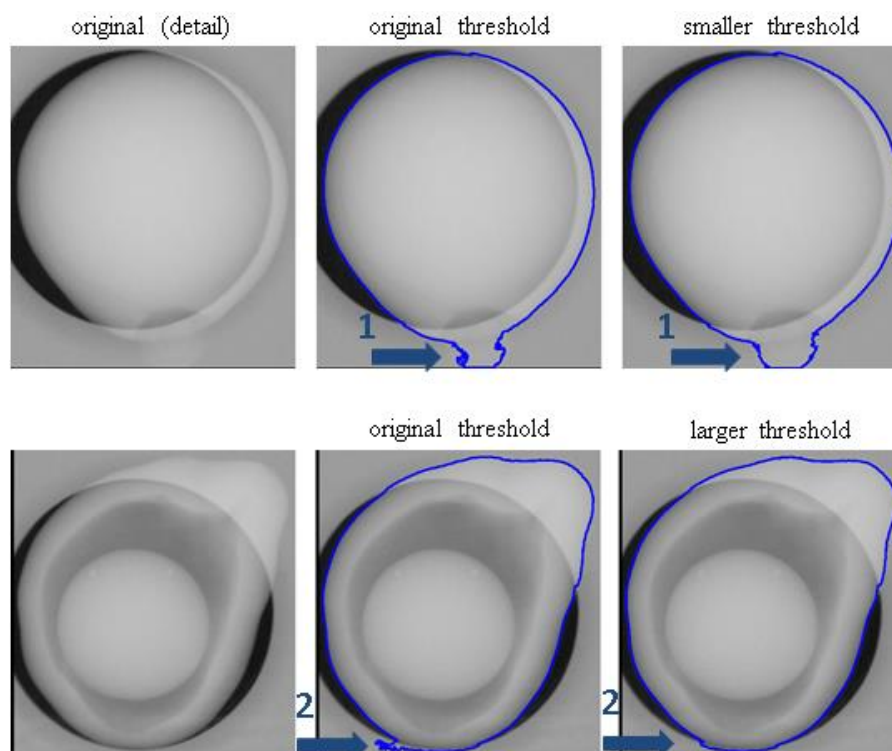


Figure 41: Examples of threshold related artefacts.

3.4.2 Processing Time

The processing time of the executed algorithm was measured for the three sub steps borehole detection, pearl segmentation (includes calibration and subtraction) and artefact cleaning. Figure 42 shows the processing time for each image of the test set. Average processing time for the complete segmentation process is 0.27 seconds for the test images (Figure 43). For comparison the processing time for a simple edge detection without further processing with the Sobel operator (0.1 seconds) and the Canny operator (0.79 seconds) are listed as well.

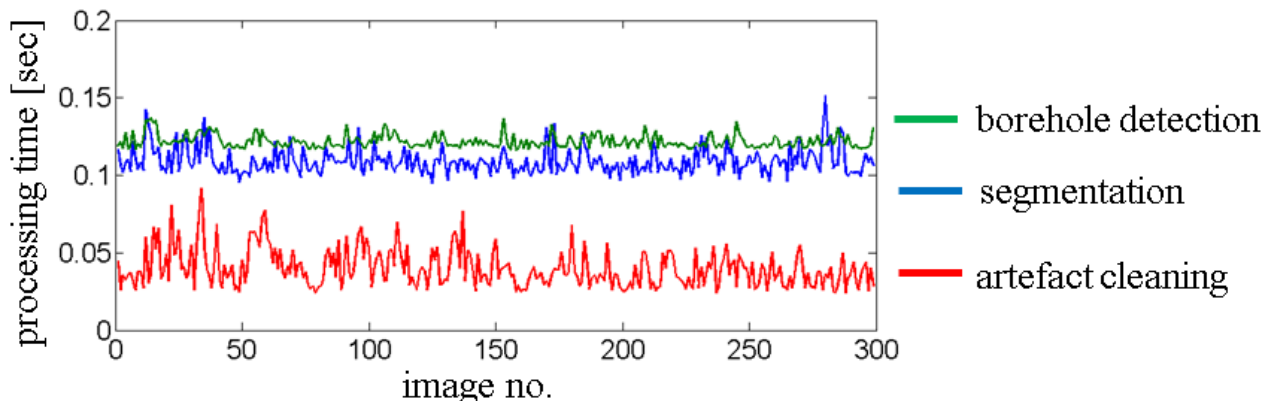


Figure 42: Processing time for the three sub steps of the proposed segmentation algorithm.

Our approach					
Borehole detection	Segmentation	Artefact cleaning	Sobel	Canny	Snake
0.11sec	0.12sec	0.04sec			
Σ	0.27sec		0.1sec	0.79sec	0.65sec

Figure 43: Average processing time in seconds per image for the proposed approach and for standard algorithms.

3.4.3 Optimization Possibilities

As the borehole center is detected anyway, a test if the pearl is located completely within the borehole can be done. If so, the segmentation process can be reduced to the region within the borehole of uniform intensity. For the presented evaluation this was not applied as most of the

pearls of the test set are located within the borehole and an evaluation of such a processing time would implicate a faster processing than to be expected in the average case.

Another optimization can be reached by using resized images of smaller size. After detecting the borehole of the original image, the image could be resized and a synthetic background image according to the resized image can be generated. The pearl of the smaller image can be segmented with the previously proposed procedure and the boundary pixels transferred to and connected within to the original image. In this case the smoothing region and strength to delete artefact would have to be adapted. This would decrease the processing time as most time is caused by the calibration and subtraction of the relative large images of size 1000x1000 pixels.

An increased precision can be obtained if the method used for the precision measurement is applied after the segmentation of the pearl. In a first step the pearl is segmented as proposed. Afterwards the boundary is refined by identifying maximum image gradients in normal vector direction of the previously obtained boundary. To comply with the paradigm that in case of doubt a decision has to be made in favor of pearl quality, those maximum gradients should be identified only outside the detected boundary. An application of this procedure showed that discrepancies caused by the smoothing process can be eliminated. The resulting contour corresponds to the image processing standard that object boundaries are defined by local image gradient maxima.

3.4.4 Background Configuration

The theory of the proposed algorithm is based on the assumption that the boreholes are rotation symmetric. While this assumption was true for the support used to acquire the training images, several boreholes of the support used for acquiring the test images showed major damages (Figure 44).

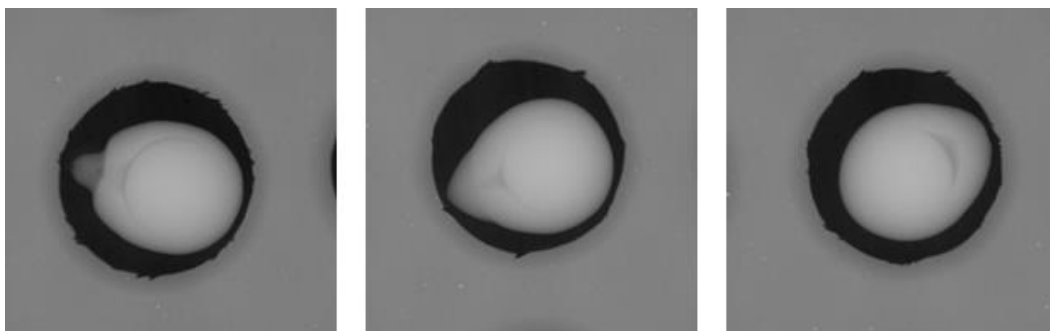


Figure 44: Three examples of damaged boreholes.

Even though this had no negative effect on the segmentation of the test images, as in all these cases pearls were located completely within the damaged boreholes, a combination of surpassing pearls and damaged boreholes might lead to wrong segmentations. For the moment it is not clear how to handle this problem. A dynamic numerical compensation of these damages is difficult, as the dynamic detection of those cases will need major effort (if even possible) in cases the pearl completely surpasses the damaged borehole. As these defects concern only some boreholes on some supports, one possibility is to simply cover those damaged boreholes, so that they are practically 'out of use'. Even though this is the most efficient way to handle this problem on short notice, it has to be assumed that over time all boreholes will suffer from wear and tear (even though the shown examples are most likely damaged by brute force and not by regular use or bad manufacturing). This means for a long term implementation of the presented algorithm: if the deviation between the intensity profile of many boreholes of a support and the ideal profile became significant, the support cannot be used anymore for the automatic measurement and hence has to be replaced with an equivalent new support. If the replacement of damaged supports is not possible, the theoretical basis of the presented model-based approach will become obsolete over time and hence another algorithm has to be used. Out of the tested algorithms the active contour approach 'snakes' has been deemed as the second most suitable to segment the outer boundary of the pearl. This approach does not depend on the geometry of the borehole and can be used for segmentation independently of possible damages. Anyhow, the use of snakes will increase the processing time of both, the segmentation of the outer and the inner boundary of the pearl.

3.4.5 Alternative Support Configuration

Another method to significantly facilitate the pearl segmentation is to generally change the nature of the support. Major difficulties are caused by the superposition of support gradients and the pearl. Support gradients can be avoided by changing the geometry of the support or its material. First tests were conducted by using polystyrene as support material as shown in Figure 45. The resulting image showed no background gradients, which reduces the segmentation process to a simple threshold application. A prototype of a complete support made out of polystyrene is currently in work.



Figure 45: A linear imitation of the borehole geometry with polystyrene and the resulting X-ray image.

3.5 Conclusion

In the previous sections our approach to segment the pearls from the X-ray images was explained. A model based approach was developed that consists of the creation of an artificial background that is subtracted from the original image. Before the subtraction both images are calibrated so that the image intensity corresponds to the actual geometry of the radiographed scene. The resulting image corresponds hence to the geometry of the pearl if radiographed without the used support. The pearl is then segmented by applying a threshold and artefacts are smoothed with an averaging filter operation. The general results of the proposed method correspond with slight exceptions to the optimal boundary. A general discrepancy in a range of -1 and 1 pixel between detected and benchmark boundary has to be considered for the later evaluation of the nacre thickness measurement.

For further processing, the images were cropped to the size of the segmented pearl. As it is of importance to rank the processing time of the following steps, the minimal side length and the maximum side length of the obtained images are shown in Figure 46 in the graph on the top in straight blue and dashed black respectively. The root of the amount of pearl pixels can be seen in the graph on the bottom. The interpretation is that useful information within the segmented and cropped images correspond to a square image of this side length. Average obtained image size is 398x431 pixels and the average root of the amount of pearl pixels is 345. If not stated otherwise the calibrated images will be used for visualization purposes in the following sections, as boundaries appear more clearly compared to the original image configuration.

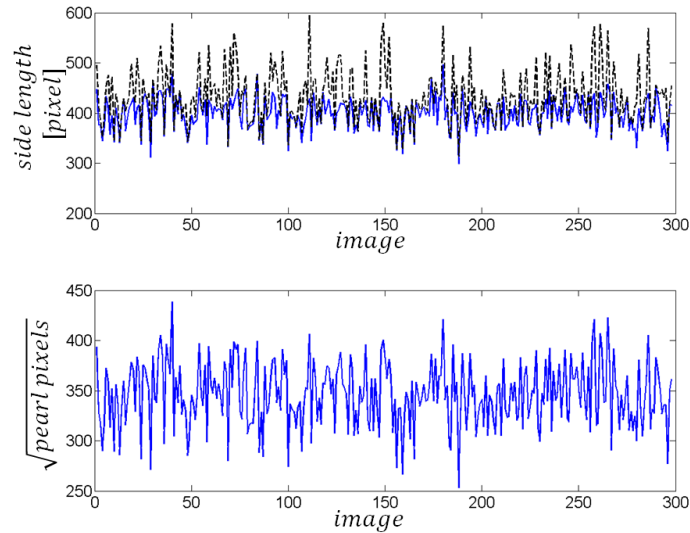


Figure 46: image side length (top) and root of the amount of pearl pixels (bottom) in the segmented and cropped images.

4 Nucleus Detection

The second step of our procedure to obtain the nacre thickness profile is to detect the nucleus. As the nucleus is a spherical object it appears within the X-ray images as a circle. The nucleus detection can hence be seen as classical circle detection. As the size of the nucleus is not known prior to this step, its center as well as its radius has to be detected. General difficulties are caused by the superposition of nacre thickness variation and nucleus, and weak nucleus boundaries.

Main challenges of the detection of the nucleus are illustrated within the next section along with difficulties that arose when classical approaches were applied to this task. Our own developed heuristic circle detection approach is introduced in section 4.2. The precision of results is analyzed visually and compared to a standard brute force approach in section 4.3. The results are discussed and a self-evaluation measurement is proposed in section 4.4. The conclusion follows in section 4.5.

4.1 Main Challenges

The challenge of detecting the nucleus both visually and numerically is determined by if and to what degree the nucleus is surrounded by cavities. In the simplest case a cavity completely surrounds the nucleus (Figure 47 on the left). The more the nacre connects to the nucleus, the more difficult gets the evaluation. The second image in Figure 47 shows an example that is

still evaluable visually, while in the third example the nacre is connected at any point to the nucleus and hence there is no visual evidence of where the nucleus might be. A technical question is if there is any information in the image that allows a numerical detection of the nucleus in those cases. From a physical point of view this is unlikely, as nuclei are made out of pearl shell, which has a similar mineral configuration as the nacre. Hence the attenuation of both is most likely the same. This question will be further addressed in section 4.4.4.

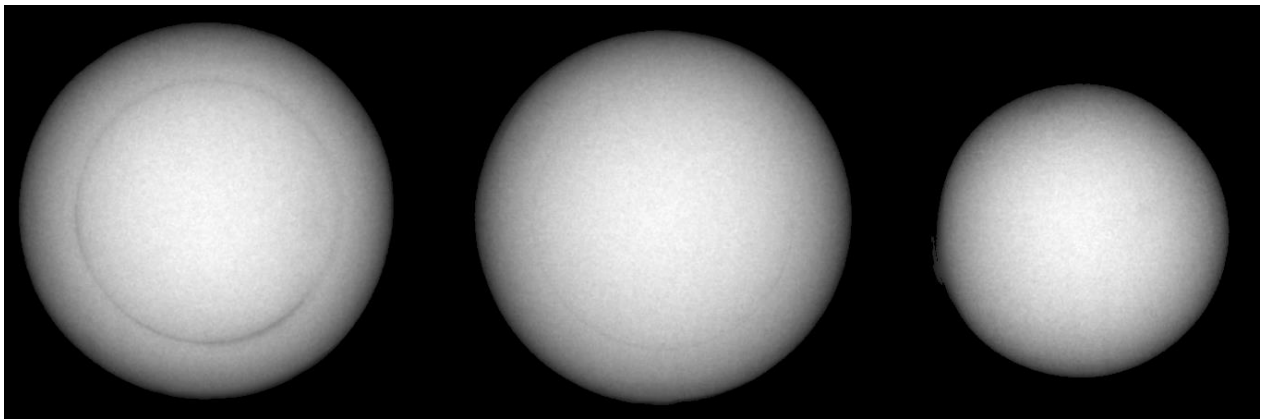


Figure 47: Round pearls with different nucleus visibility

A second challenge from an image processing point of view is caused by only partially visible nuclei. Here the circle detection algorithm has to be capable of detecting the nucleus based on circular arcs (Figure 48).

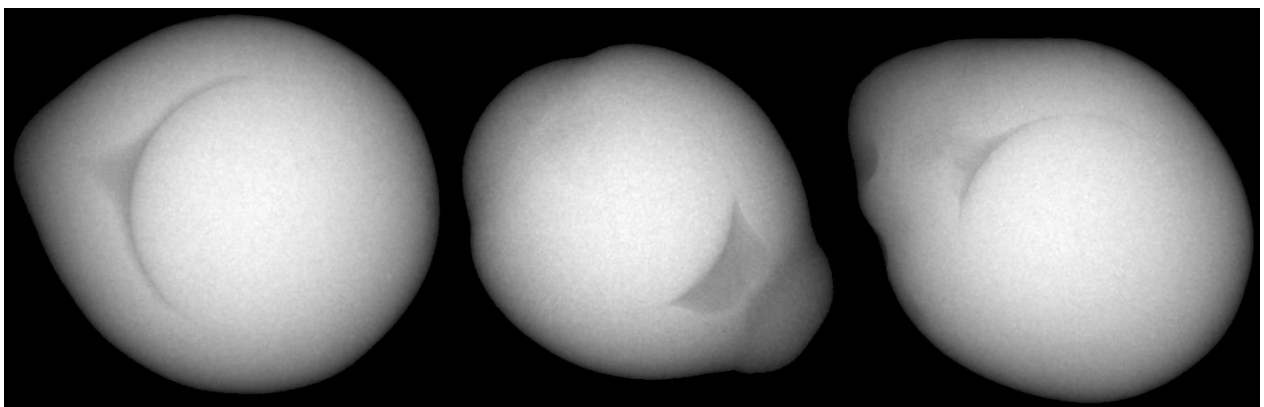


Figure 48: Three example of partially visible nuclei

4.1.1 Model-Based Approach

An intuitive idea might be to create synthetic nuclei profiles, similar to the approach used to segment the pearl. The nucleus is an artificially formed sphere and can with a given radius hence easily be synthetically generated. However, the nacre thickness superposed with the nucleus does not necessarily have to be uniform. In Figure 49 an example of a pearl whose nacre thickness changes in direction of its symmetry axes and perpendicular to the X-ray beam is shown (symmetry axis in direction of both arrows). The image on the left shows the original image and the image on the right shows a surface plot of the image intensity calibrated to *mm*. To apply a model-based approach the nacre contour has to be taken into account. In this case it might be possible to interpolate the symmetric outer contour but for irregular shaped baroque pearls it is not. The example shows further that intensity thresholding, which can be done for round pearls, is not a suitable option as the boundary of the nucleus lies on an inclined plane (which neither has to be the case for baroque pearls, as they have no symmetry axes).

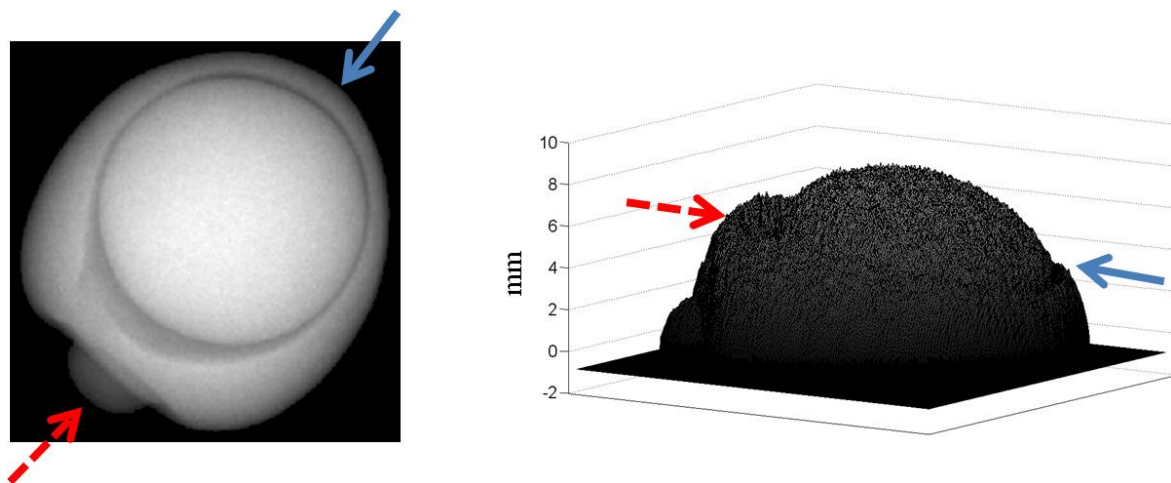


Figure 49: Superposition effect of rotation symmetric nucleus profile and non-rotation symmetric nacre thickness.

4.1.2 Region-Based Approach

A region based approach might be to either start a region growing process at the outer boundary of the pearl of which it is known that it is the pearls nacre or at the region with highest intensity that is likely to be the nucleus and grow until the other region is reached. But cases as shown in Figure 48 cause problems as in a large range no boundary information of nucleus or nacre exist, which means the region will grow over the boundary. Other approaches such as watershed will suffer from the same problems. Thresholding, as

mentioned in the previous section are not applicable, due to the inhomogeneous intensity distribution of nucleus regions superposed with varying nacre thickness.

4.1.3 Edge-Based Approach

Classical edge detection will not yield directly in a segmented nucleus but can be used as pixel preselection step for further processing (such as with the circular Hough transform that will be introduced in the next section). Main drawbacks are caused by the spherical form of the pearl and weak nucleus boundaries in case of small cavities. In Figure 50 the application of the Sobel edge operator to a pearl with weak nucleus boundaries is exemplarily shown. After applying the Sobel operator non-maximum suppression was applied as nucleus edge pixels are supposed to be at local maxima. It can be seen that generally edge pixels at the nucleus boundary remain, but due to the spherical form of the pearl, a large amount of additional edges is still present. Commonly, a thresholding operation would be applied to further eliminate pixels that do not contain boundary information. But as stated earlier, thresholding would mean that assumptions about the general pearl configuration would have an influence on the segmentation process, which is due to the large variety of Tahitian pearls not desired. It means that all remaining pixels would have to be used for further processing.

Due to the large amount of remaining pixels in combination with the unknown nucleus size, approaches based on pixel preselection are not suitable to segment the nucleus of Tahitian pearls. Anyhow, the Sobel operator with non-maximum suppression will be used in combination with the circular Hough transform as benchmark application.

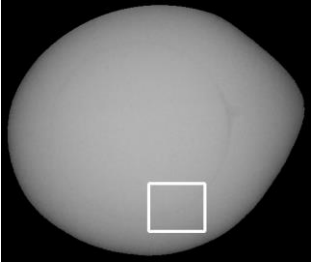

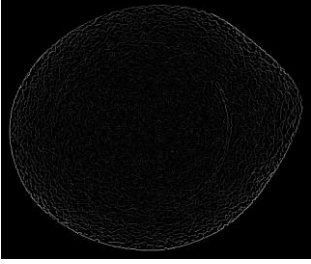

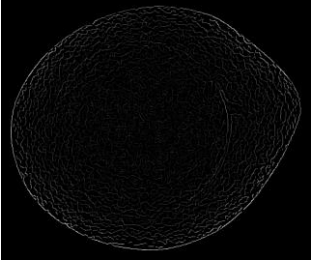

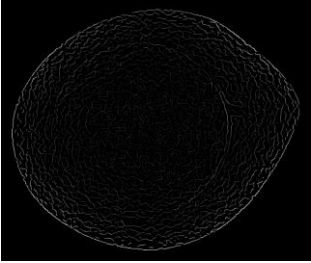

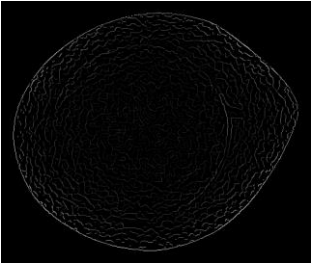
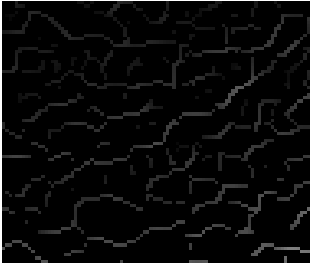
Original	Detail	Sobel Filter Size	Remaining Pixels After Non-Maximum Suppression
		0x0	145208
		3x3	41262
		5x5	32221
		7x7	26678
		9x9	22703

Figure 50: Application of the Sobel operator with different filters size and amount of remaining pixels after non-maximum suppression.

4.1.4 Circular Hough Transform

The circular Hough transform is a brute force algorithm for circle detection in images [DUD72]. Its time intense processing is compensated by its strong detection ability in cases of weak boundary information and/or noise. The basic concept is that all circles with the same radius R of the object to detect, set around boundary pixels, intersect at the center of the object (Figure 51). If the radius R of the object to detect is known a 2D accumulation matrix is generated and for each preselected edge pixel the position in the matrix corresponding to all pixels of a circle with radius R around the preselected pixel is increased by one. For the case shown in Figure 51 the only entry in the accumulation matrix of value three will be at the center of the object to detect, as this is the only point at which all circles around the three edge pixels intersect. If the radius of the object is unknown, a 3D accumulation matrix is generated whose third dimension corresponds to all radii that are to evaluate. For the same example shown in Figure 51 only the level in regards of the third dimension at radius R of the object will have an entry of three. All other values of the accumulation matrix will be smaller.

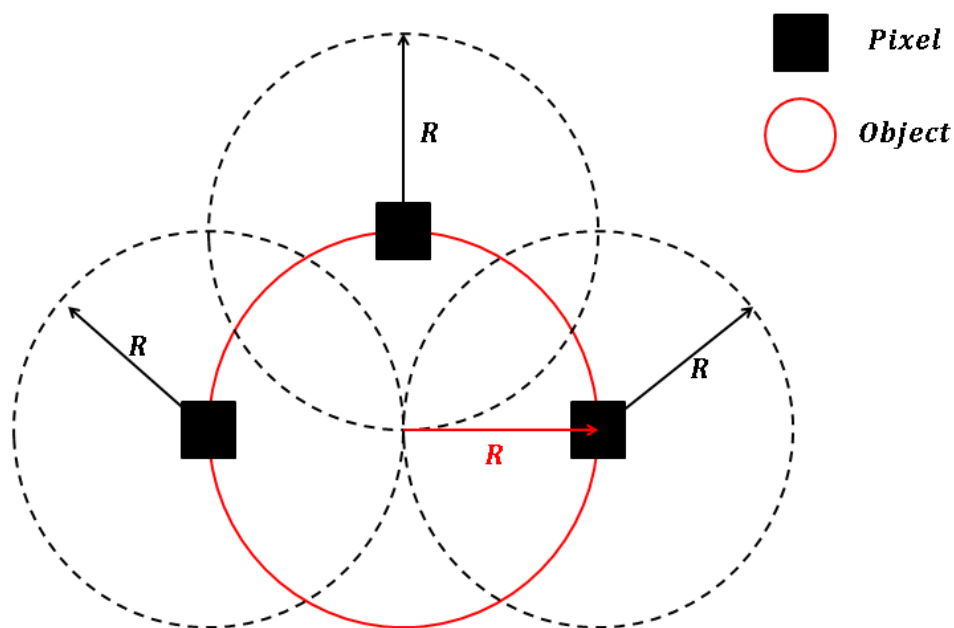


Figure 51: Schema of the basic concept of the circular Hough Transform.

The processing time to detect circles of unknown radii depends on the number of preselected pixels and the number of radii to evaluate. As the radius of the nucleus is prior to the measurement unknown and even the previously shown preselection method leaves a large number of possible edge pixels, this approach is not suitable to detect the nuclei in the required time. Because of its strong detection ability in cases of weak boundary information and noise (which both occur in the X-ray images of pearls) it will be used to evaluate our own

developed circle detection algorithm in section 4.3 and to analyze if a numerical detection of nuclei that are not visible is possible in section 4.4.

4.1.5 Other Circle Detection Approaches

As the circular Hough transform is known to have a high precision but at the cost of time intense processing, several alternatives were and are still developed. The Hough transform itself was developed further to reduce its complexity by keeping its high precision (an overview of approaches can be found in [YUE99]). Still the complexity depends on the detected edge pixels multiplied by the different radii to evaluate. A region based approach can be found in [XU13]. Here the image is binarised by intensity thresholding, a procedure that is, as mentioned, not suitable for pearls with a superposition of nucleus and varying nacre thickness. The gradient direction is used in [LOY02] which not necessarily needs a pixel preselection. But a problem is that at weak nucleus boundaries the local gradients obtained by applying for example the Sobel operator do not necessarily point to the center of the nucleus. Additionally, nucleus edge pixels have to be distributed symmetrically, which causes problems in cases in which the nucleus is partially connected directly to the nacre. Heuristic alternatives are for example given in [AYA06], [DAS10], [CHA11], [CUE12] and [CUE12b], but in all approaches pixel preselection has to be done. As will be shown in the following sections, a heuristic approach can be formulated that do not need such a pixel preselection, while only evaluating the gradient of 1 circle per radius, if *a priori* knowledge of the nucleus geometry is added.

4.2 Our Approach

To detect the nucleus of a segmented pearl we developed a heuristic detection algorithm that is based on the following idea: a circle initialized within a circular object to detect that stays within the object while its radius is iteratively increased will at one iteration cover the outer boundary of the object. The basic concept is to use a suitable definition of the nucleus boundary to prevent the moving circle from surpassing the boundary. Therefore, at each iteration a probability of the circle pixels belonging to the nucleus boundary has to be evaluated. If the probability of some pixels of the circle touching the nucleus boundary is

high, the circle has to be pushed away from this region. Mathematically this movement v at iteration t for a circle of i pixels with outside pointing normal vectors n_i and probability b_i can be formulated as to

$$\vec{v}_t = \sum_{i=1}^i -b_{i,t} \vec{n}_i. \quad (4)$$

The notation corresponds to the schema of Figure 52. Here only four pixels p_1 to p_4 of the moving circle are considered. The probability b_i to belong to the nucleus boundary is for the north and east pixel 1 and for both others zero. The sum of the with the negative probability $-b_i$ weighted normal vectors n_i is a vector that points away from both pixels that are likely to belong to the boundary. A movement of the circle in this direction will hence push it away from the probable boundary.

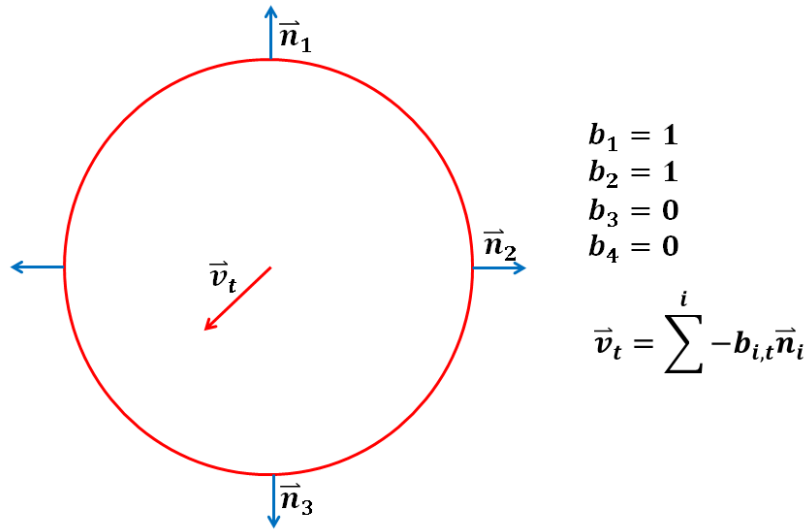


Figure 52: Schema of the idea of our approach.

The crucial steps to obtain an efficient algorithm are to define suitable probability functions (next two subsections) and to calculate a moving direction based on these functions (section 4.2.3). Furthermore, the dynamic parameters of the moving circle, moving speed and radius increment have to be defined (section 4.2.4). As the goal is to find a global maximum whose magnitude is due to the superposition variety of the nacre not known, the algorithm is run until the moving circle touches a background pixel; meanwhile the boundary probability, center and radius of each iteration is stored. Accordingly, the final step is to identify the optimal circle as the one with the maximum boundary probability (section 4.2.5). How to handle artefacts of the segmented pearl at the transition region of the borehole will be

explained in section 4.2.6, followed by a summary of the whole method and the its pseudocode in section 4.2.7.

4.2.1 Intensity Based Probability Function

A simple intensity based probability function can be formulated by using the image intensity I of pixel p_i as probability. The according moving direction becomes at iteration t

$$\vec{v}_{1,t} = \sum^i I(i,t) \vec{n}_i . \quad (5)$$

The effect is shown in Figure 53. Normal vectors of all data points of the red circle, weighted with the corresponding image intensity, are shown in blue. The vector sum (equation 5) is shown in red, pointing, due to the spherical contour of the pearl, to the center of the nucleus.

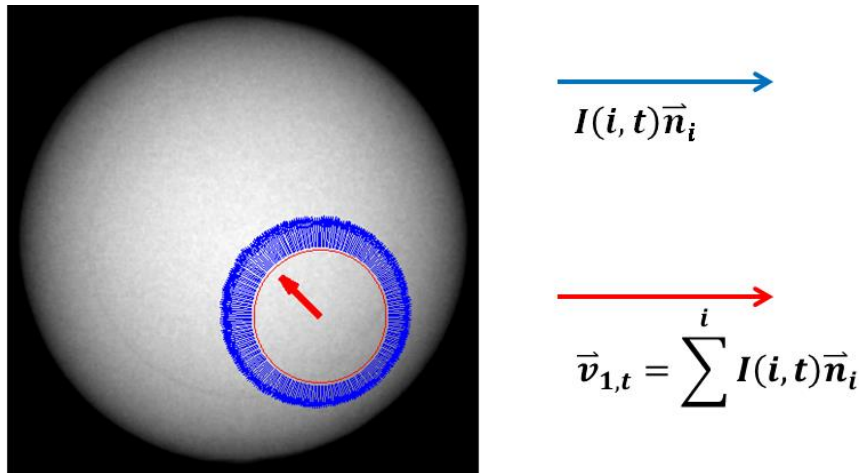


Figure 53: Circle movement defined by intensity based probability

If the circle is moved pixel wise based on Eq. 5 for fifty iterations, the circle center has moved close to the center of the nucleus where it will oscillate around a local equilibrium, due to the point symmetric intensity distribution around the center of the pearl (Figure 54 second image on the top). If now additionally the radius is increased by one pixel at each iteration, the circle keeps its position around the nucleus center and covers the boundary of the nucleus at iteration 129. On the bottom of Figure 54 is the average intensity (corresponds to pearl thickness in mm in the calibrated image) of all circle points at each iteration shown. The profile corresponds approximatively to the average radial intensity profile of the pearl showing a slight inflection at iteration 129 that marks the slight cavity between nucleus and nacre.

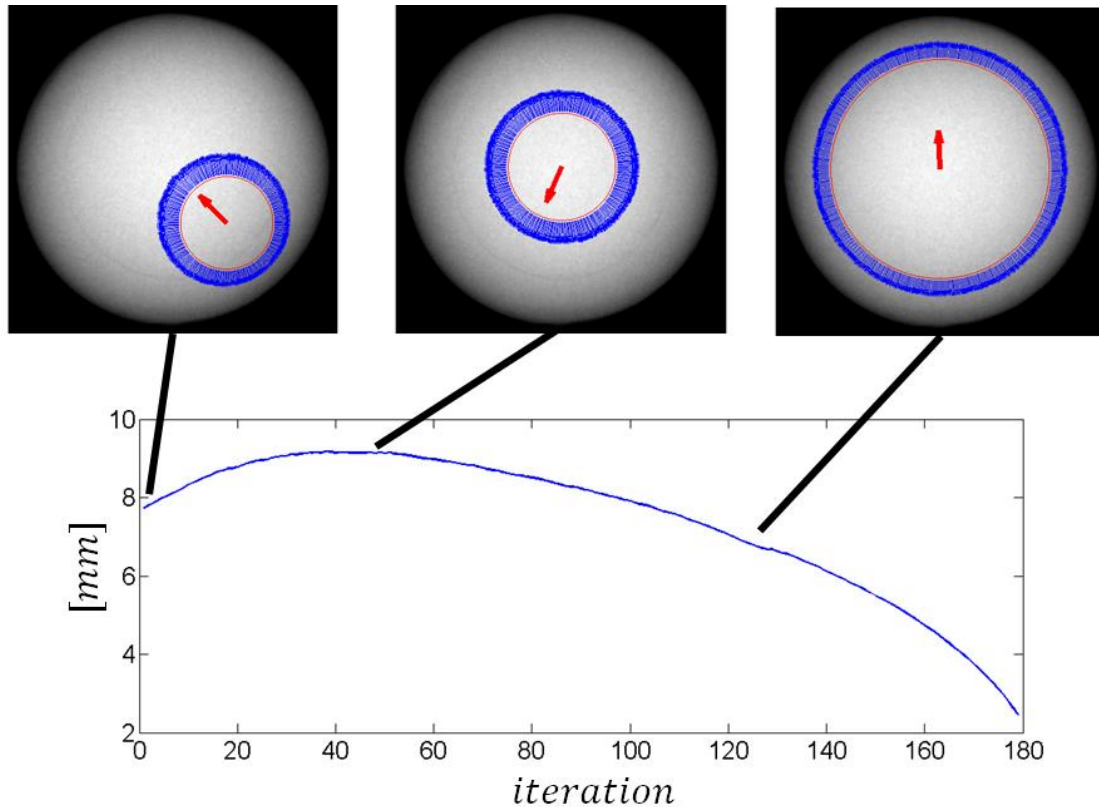


Figure 54: Intensity based movement at three iteration stages

The purely intensity based approach can only be used for round pearls with the nucleus at or close to the center of the pearl, as Eq. 5 results in a steady movement in direction of the region with highest intensity. Still, it illustrates the general idea of the algorithm and the so defined movement will be used as stabilization at iterations where the circle points contain no nucleus boundary information.

4.2.2 Gradient Based Probability Function

For pearls with non-rotational symmetric intensity distribution the previously explained intensity based movement will not succeed, as the nucleus boundary is not of uniform and of lower intensity than the rest of the nucleus. Hence, a more general formulation of boundary probability has to be found. In Figure 55 a schematic representation of the pearl thickness profile in X-ray direction in the case of cavity occurrence is shown. As the nucleus is a circular object and generally the predominant body in means of thickness, the gradient measured from any point within the nucleus will have a local maximum at the nucleus boundary (the same counts for pearls of all shapes under the condition that the nucleus is not connected to the surrounding nacre).

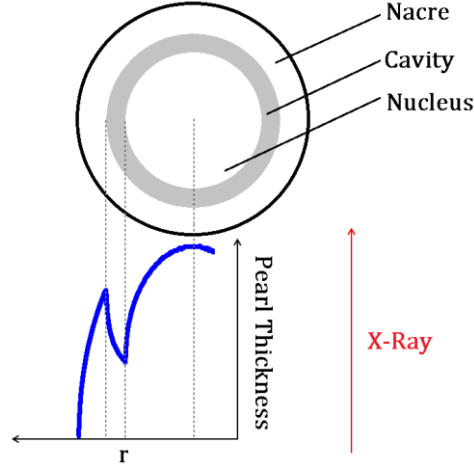


Figure 55: Schematic representation of the pearl thickness profile in X-ray direction in the case of cavity occurrence.

A boundary probability can hence be formulated based on the second derivation of the radial gradient of the moving circle. If $p_{i,t}$ is the i -th circle boundary pixel, n_i its outside pointing normal vector and k a scalar that defines the neighborhood range, the used logical boundary probability for iteration t and image I is

$$b_{i,t} = I(\vec{p}_{i,t} - k\vec{n}_i) - I(\vec{p}_{i,t}) > |I(\vec{p}_{i,t} + k\vec{n}_i) - I(\vec{p}_{i,t})|. \quad (6)$$

This means that at each iteration the gradient of pixel p_i in negative and positive direction of its normal vector has to be calculated (which basically means that the gradient based algorithm consists of three subsequent moving circles). The general idea of using a logical probability function instead of the gradient magnitude is that nucleus boundaries that are barely visible have a gradient magnitude within the range of the image noise level. From a technical point of view, this function can as well be seen as binary pixel selection with locally adapted threshold. The according moving function $v_{x,t}$ is

$$\vec{v}_{x,t} = \sum^i -b_{i,t}\vec{n}_i. \quad (7)$$

The effect of the gradient based moving is shown in Figure 56. The circle is initialized with its center at the region of highest intensity (first image). In this example the radius is increased from the beginning at each iteration by one pixel. The first movements are more or less random, as they are based on the noise distribution of the nucleus region. The moment the

circle touches the nucleus boundary at iteration 47 (second image), the movement is dominated by the large quantity of edge pixels with logical probability 1 (marked with a white arrow) and points away from the boundary. The graph below, containing the average probability of all circle pixels at each iteration, shows a maximum at iteration 67 when the circle covers the boundary of the nucleus.

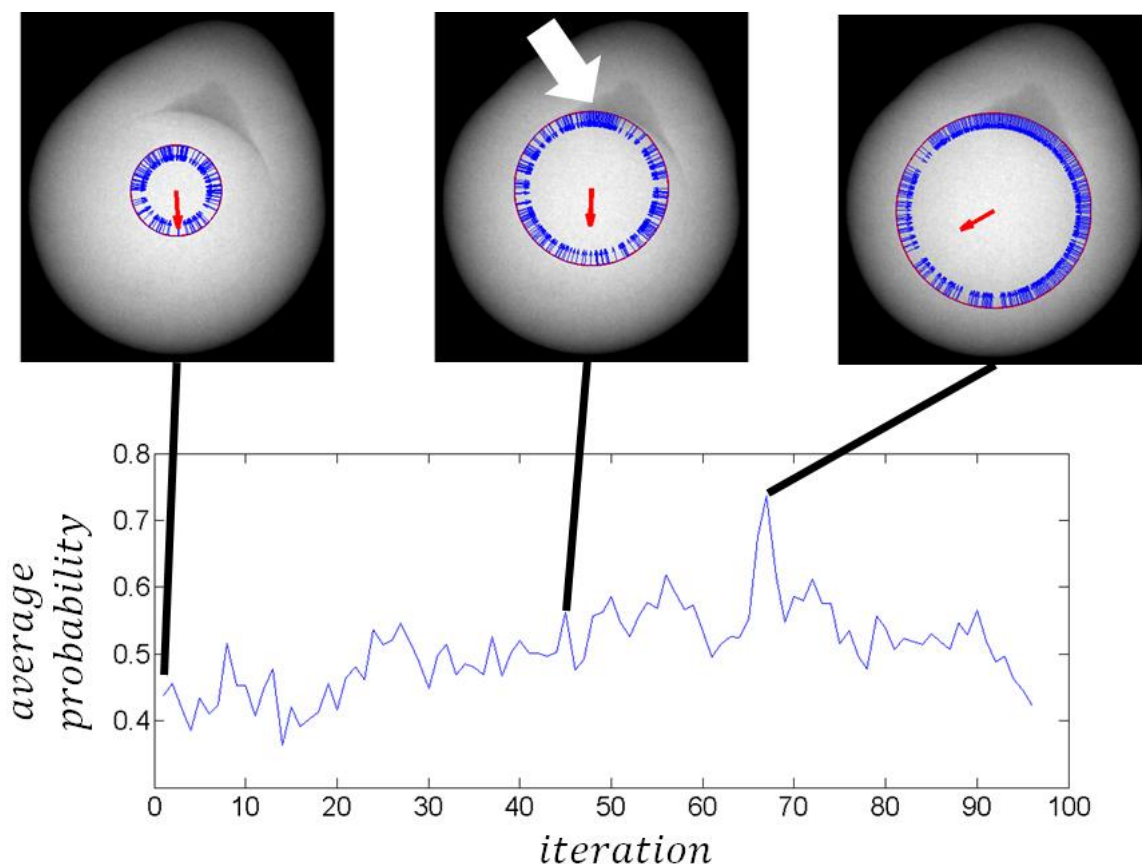


Figure 56: Gradient based movement at three iteration stages

Generally, as long as the circle does not touch the nucleus boundary, its movement when calculated gradient based is determined by the random noise distribution. The possibility exists, that the random movement brings the circle to a region of the nucleus boundary at which no cavity exists, possibly leading to a surpass before its optimal radius is reached. Accordingly it is desirable to know if the moving direction is based on noise, as in such situations an intensity based movement to keep the circle within the nucleus region should be preferred. A possibility of making a decision of whether to move intensity or gradient based will be discussed in the next section.

4.2.3 Moving Direction

To determine whether to move gradient or intensity based a sensitivity analysis of the gradient based moving direction is done according to the following theory: if the gradient based moving direction is a result of circle points touching the outer boundary of the nucleus, the moving direction calculated with every second circle data point starting at an arbitrary circle data point a and with every second circle data point starting at $a+1$ should not vary significantly. Accordingly, two gradient based moving directions are calculated as to

$$\vec{v}_{2,t} = \sum_{l=1.3.5\dots} b_{l,t} \vec{n}_l \quad ; \quad \vec{v}_{3,t} = \sum_{m=2.4.6\dots} b_{m,t} \vec{n}_m \quad . \quad (8)$$

The probability function b for each direction is the logical gradient of the corresponding data point of the corresponding sequence. Afterwards the dot product of both moving directions can be calculated that gives a sensitivity s_t for iteration t ranging from -1 to 1 of how much both vectors differ from each other:

$$s_t = \frac{\vec{v}_{1,t} \cdot \vec{v}_{2,t}}{\|\vec{v}_{1,t}\| \|\vec{v}_{2,t}\|} \quad . \quad (9)$$

An empirical threshold is currently set to 0.7 which corresponds to an angle of ~45 degrees between both calculated moving directions. If the sensitivity is larger than this threshold, it is assumed the gradient based moving direction corresponds to the nucleus boundary and hence the general movement of the circle is done gradient based. In the other case, it is assumed the gradient is caused by noise and hence the circle is moved intensity based to keep it within the nucleus region of high intensity. The effect of applying this sensitivity measurement is shown in Figure 57. The second image in the first row shows a case in which the purely gradient based moving failed, as the circle was pushed over the weak nucleus boundary in the south before reaching the optimal radius. The third image shows a successful detection when gradient and intensity based moving is combined with sensitivity measurement. The second row shows an example in which the purely intensity based moving failed, due to the non-rotational symmetric intensity distribution. Again the combined approach leads to a successful detection (last image third row).

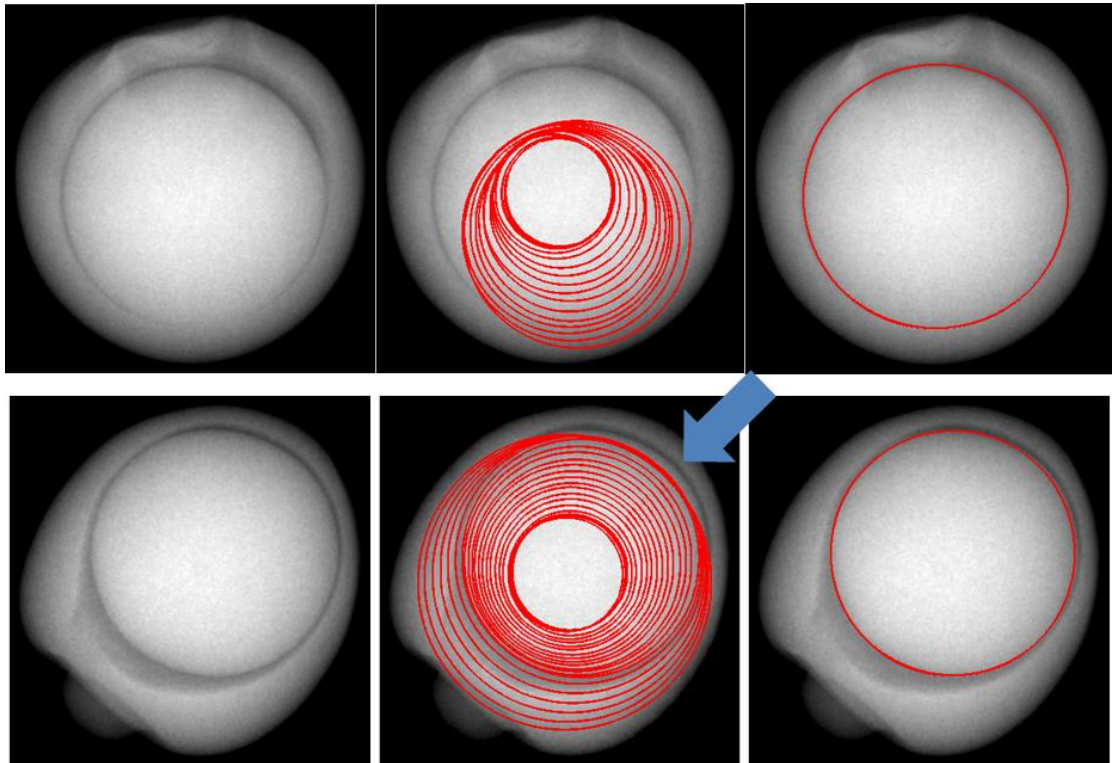


Figure 57: Effect of the implementation of a sensitivity measurement

4.2.4 Moving Speed and Radius Increment

The general relation between moving speed and radius increment, if both actions are executed simultaneously during the run of the algorithm, is shown schematically in Figure 58. In every example the smallest circle is the initial circle, the radius increment is positive and the moving direction is constant at every iteration pointing to the right (meaning the circle region on the left touches the probable boundary). The first example on the left shows three iteration stages for a radius increment R_{inc} equal to the moving speed v_t . The result is an expansion of the circle in moving direction, while the region that is supposed to touch the probable boundary does not move. In the second example the moving speed is lower than the radius increment. Even though the moving direction points to the right (away from the possible boundary) the left side of the circle is moved in opposite direction due to the higher radius increment. In the third example the moving speed is greater than the radius increment resulting in an expansion in moving direction, while the circle region that is supposed to touch the probable boundary is pushed away from it.

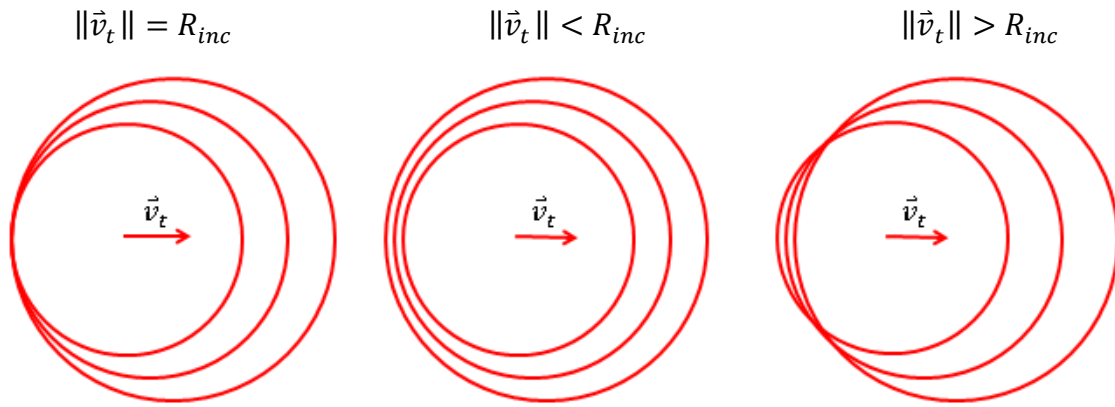


Figure 58: Moving speed in relation to radius increment.

The second example with a radius increment larger than the moving speed is not suitable for the detection, as even if data points of the circle touch the nucleus boundary at a certain iteration, they will surpass it at the next iteration due to the radius increment. This means generally that for a successful detection the moving speed has to be larger or equal to the radius increment. For the current implementation the third variation with a moving speed larger than the radius increment was chosen, as it gives the possibility to correct temporary surpasses due to noise on its own. Empirically set values are a radius increment of 1 pixel and a moving speed of 1.2 pixels. Any larger radius increment would result in a loss of precision, while any lower increment would increase processing time. In this configuration, the theoretical precision of the detected radius is 1 pixel.

4.2.5 Optimum Detection

As mentioned, the algorithm is run until the moving circle touches a background pixel, as prior to the detection, the gradient magnitude of the nucleus boundary is not known. To detect the optimum out of all iterations the average B_t of the gradient based probability function $b_{i,t}$ of all i data points of the circle is calculated for each iteration t and stored along with the current circle center and radius. After the run of the algorithm, the maximum average probability is identified and the corresponding center and radius of this iteration are determined as optimal circle (see Figure 56 the graph on the bottom).

4.2.6 Handling of Segmentation Artefacts

As mentioned in section 3.2.4 artefacts at the transition region between borehole and bevel have to be expected. Even though smoothed, in the current segmentation their probability of

belonging to an edge is set automatically to zero, to not disturb the moving based on artefacts. Unfortunately no pearls with a nucleus boundary surpassing the borehole were within the test or training image set. A validation of this procedure has hence still to be done.

4.2.7 Summery and Pseudocode

The implementation of the proposed algorithm to detect the nucleus is according to the previously explained steps the following. A circle with a radius of 60 pixels (1.4mm) is initialized with its center at the region of highest intensity within the pearl. The image intensity of all data points of the circle as well as the corresponding intensity of pixels in positive and negative radial direction is acquired. Out of the intensities, the probability for each data point to belong to an edge is described with logical values according to equation 6. The average edge probability is stored along with the current radius and center of the circle. A sensitivity measurement is done to evaluate if the circle is likely to touch the nucleus boundary. The sensitivity value is compared to a predefined threshold and the circle is accordingly moved either based on the radial image gradients or based on the intensity of the data points of the current circle. Afterwards, the radius is increased and the next iteration starts with acquiring the image intensity of the new circle data points. The algorithm stops once the circle touches background pixels. Afterwards, the optimal circle is determined by the maximum of the stored average edge probability of each iterations. Empirically set values for all crucial parameters in the current implementation can be seen in Figure 59. The pseudocode of the algorithm is shown in Figure 60.

Parameter	Value
radial gradient neighborhood (k in Eq. 6)	2 pixels
moving speed	1.2 pixels
radius increment	1 pixel
data point sequence for sensitivity measurement	every second pixel
sensitivity threshold	0.7
initial center	region of highest intensity
initial radius	60 pixels (1.4mm)

Figure 59: Values for crucial parameters for the proposed algorithm to detect the nucleus.

Pseudocode	Corresponding section
define initial center \mathbf{M}_t and radius \mathbf{R}_t	
initialize circles $\mathbf{C}_1(\mathbf{R}_t-3, \mathbf{M}_t)$, $\mathbf{C}_2(\mathbf{R}_t, \mathbf{M}_t)$, $\mathbf{C}_3(\mathbf{R}_t+3, \mathbf{M}_t)$	
calculate normal vectors \mathbf{n}_1 of \mathbf{C}_1	
while \mathbf{C}_3 does not contain background pixels	
get image intensity $\mathbf{I}_x = \mathbf{I}(\mathbf{C}_x)$	
calculate probability function $\mathbf{b}(\mathbf{I}_1, \mathbf{I}_2, \mathbf{I}_3)$	sections 4.2.1 & 4.2.2
calculate sensitivity $\mathbf{s}(\mathbf{b})$	section 4.2.3
if $\mathbf{s} > 0.7$	
move gradient based $\mathbf{C}_{x,t} = \mathbf{C}_{x,t} + \mathbf{v}_2 + \mathbf{v}_3$	section 4.2.2
else	
move intensity based $\mathbf{C}_{x,t} = \mathbf{C}_{x,t} + \mathbf{v}_1$	section 4.2.1 &
end	
increase radius of $\mathbf{C}_{x,t}$ by one pixel	section 4.2.4
track $\mathbf{M}_t, \mathbf{R}_t$, average (\mathbf{p}_t)	section 4.2.5
end	
detect optimal circle	section 4.2.5

Figure 60: Pseudocode of the proposed algorithm for the detection of the nucleus. .

4.3 Precision of Results

To evaluate the precision of the proposed algorithm, a brute force circle detection of every image was conducted with the circular Hough transform. Pixel preselection was done by applying the Sobel operator with non-maximum suppression as explained in section 4.1.3. As there is no information about the actual nucleus size within the used pearls, the benchmark results were validated visually. Cases in which a validation was due to invisible nucleus boundary not possible, were treated as correctly detected by the Hough transform in the statistics (three cases, those will be analyzed in the discussion section separately). Afterwards the center and radii of the circles detected with the brute force approach and with our algorithm were compared. The maximum absolute pixel distance between the x- and y-coordinate of both centers was calculated to obtain a pixel based discrepancy. The discrepancies are shown Figure 61 on the top. Discrepancies greater than 5 pixels are set to 5 for a clearer visualization of all results (a 5 pixel discrepancy is here considered as not sufficiently precise, independently of the actual magnitude). The absolute value was taken as the spatial discrepancy was not deemed important for the precision analysis. For the radius instead the signed difference was calculated to evaluate if the detected circle is too small or too big (Figure 61 on the bottom, discrepancies greater than 5 pixels as well set to 5).

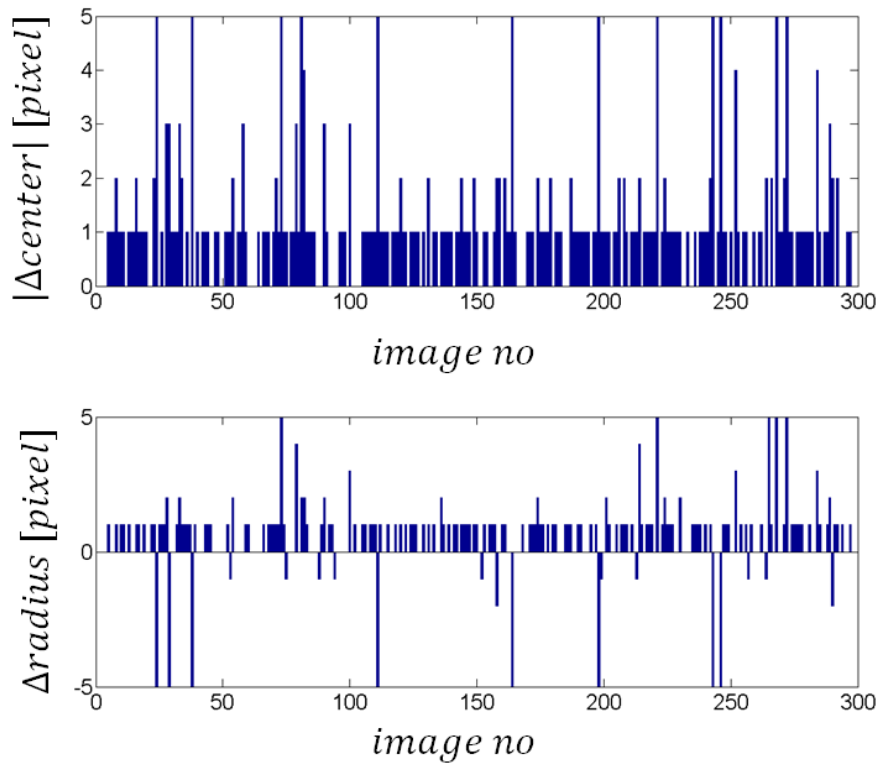


Figure 61: Precision of the proposed algorithm in comparison to a brute force approach. Discrepancies greater than 5 pixels are set to 5 for better clarity.

4.4 Discussion

To give an impression of the impact of the discrepancies, an example of a center and radius discrepancy of 3 pixels each is shown in Figure 62. The circle, detected with our approach, is shown in red and the result of the Hough transform in white.

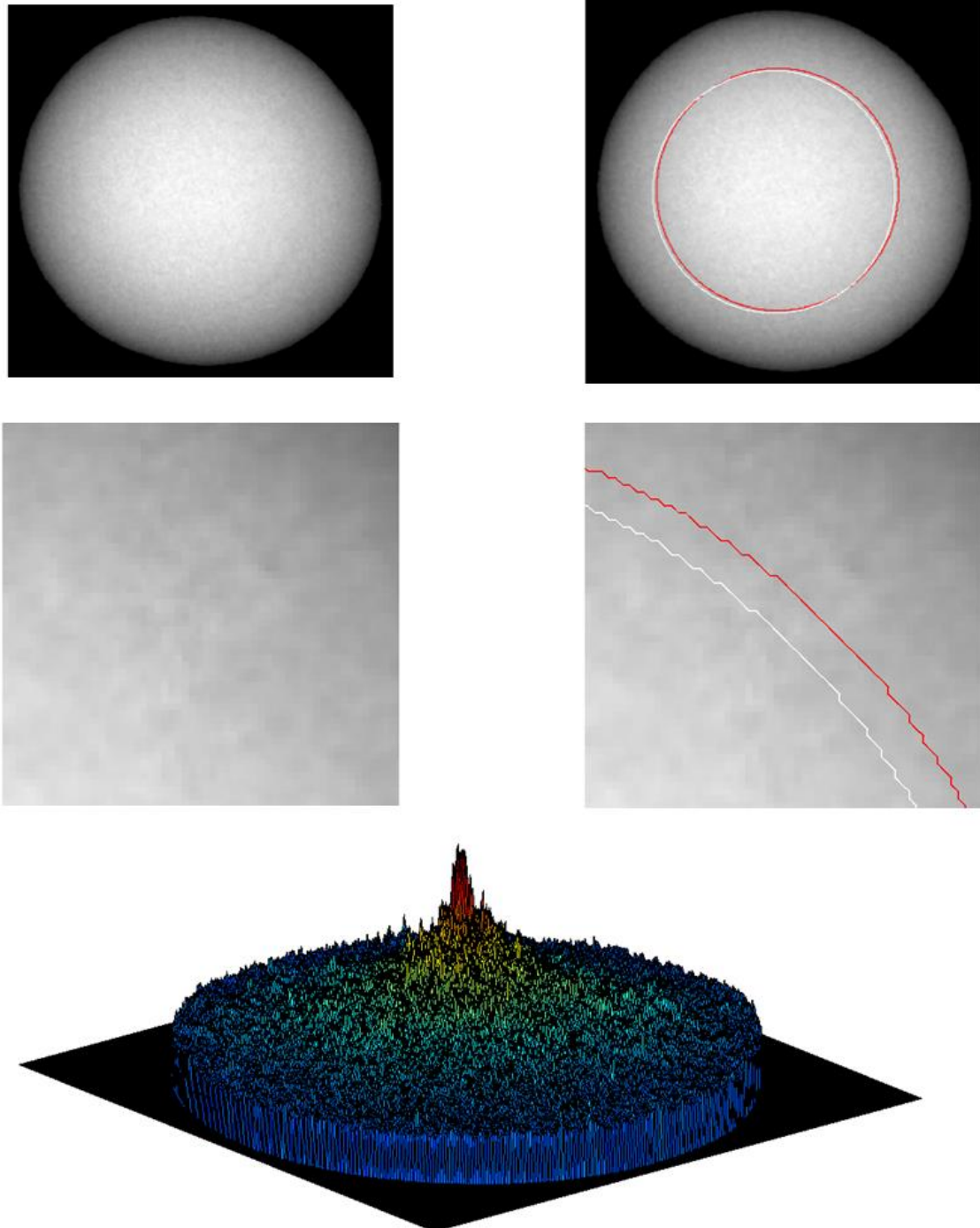


Figure 62: Detected circle with our approach (red) and with the Hough transform (white). The image on the bottom shows the maxima of the accumulation matrix of the Hough transform.

Even though a discrepancy between detected and optimal circle exists, the result of our approach is still adequate from a computer vision point of view, seeing the difficulties caused by the only partially existing nucleus boundary gradients. Additionally, the maxima distribution of the Hough transform for all pixels (shown in Figure 62 on the bottom), out of which the global maximum defines the optimal circle, shows that other candidate circles with a few less circle intersections to the optimal circle exist (next two maxima have 5 intersections less than the optimum). As the visual confirmation is rather difficult, it is possible that even the Hough transform differs, due to noise, in a range of certain pixels from the physical optimum. An exact validation would require an actual measurement of the nucleus size, which is not possible without destroying the pearl (if information of the nucleus size was not registered during its insertion in the pearl oyster). Still the method serves the goal to validate the general theory of our approach. Out of 298 test images, 279 detected nuclei have a maximum radius or center discrepancy of 3 pixels, which equals 94%. This can be seen as adequate result for a heuristic algorithm where a certain discrepancy to the optimum has generally to be expected. The algorithm is based on a moving circle and for the sake of speed the radius is increased after each movement. It means if the circle is two pixels from the optimal center away but only one radius iteration from the optimal radius, a discrepancy will be the result even if the further moving direction will bring the circles center to the optimal one. According to this and based on the signal to noise ratio an absolute discrepancy of 3 pixels for the circle center or the radius might still be considered as suitable result.

Within the 19 cases of absolute discrepancy greater than 3 pixels three general types could be identified: threshold related discrepancies, cavity related discrepancies and (iii) weak boundary related discrepancies.

4.4.1 Threshold Related Discrepancies

12 detection results could be improved by setting the threshold value that defines when to move gradient based or intensity based either to 0 or to 1 (current setting is 0.7 as explained in section 4.2.4). A threshold of 0 gives a larger emphasis on the gradient based movement in comparison to the current implementation. 10 cases could be improved by applying this threshold (5 exemplary cases are shown in Figure 63 on page 115). A threshold of 1 instead means the circle moving is purely based on the intensity distribution of the circle pixels

without gradient information (section 4.2.1). 2 cases could be improved by applying this threshold (Figure 64 on page 116). It shows that in all these 12 cases generally a suitable detection is possible. The problem is that a general adjustment of the threshold does not work as several pearls need an emphasis on either gradient or intensity based movement. A possibility to solve this problem by running the algorithm several times with different thresholds according to the results of a self-evaluation will be presented in section 4.4.5.

4.4.2 Cavity Related Discrepancies

In two cases the nucleus boundary was superposed by a gradient caused by a local cavity in combination with general rather weak boundary gradients (Figure 65 on page 116, blue arrows point at the cavities). Adapting the threshold (thresholds from 0 to 1 in steps of 0.1 were tested) did not lead to improved results. As the superposition region generally deviates from the logic boundary definition those cases have to be detected either automatically and treated specifically or the boundary definition has to be somewhat reformulated. Anyway, two cases might not be sufficient to work on a general solution. The occurrence of those cases will be observed and once a larger set of similar cases is obtained, possible solutions will be investigated.

4.4.3 Weak Boundary Related Discrepancies

The remaining 5 images with a discrepancy greater than 3 pixels contain pearls with no cavities at all (Figure 66 on page 117, first 3 pearls) or only in a very limited region (last two pearl). While the result of the last pearl with a limited cavity region might be still considered as suitable seeing the general lack of boundary information, all other cases show unsuitable results for any threshold configuration. Anyhow, as mentioned earlier, in these cases even the brute force approach has to be evaluated as it is not clear if the bench mark results are a result of invisible but existent nucleus boundary information or just based on noise. This will be done in the following section.

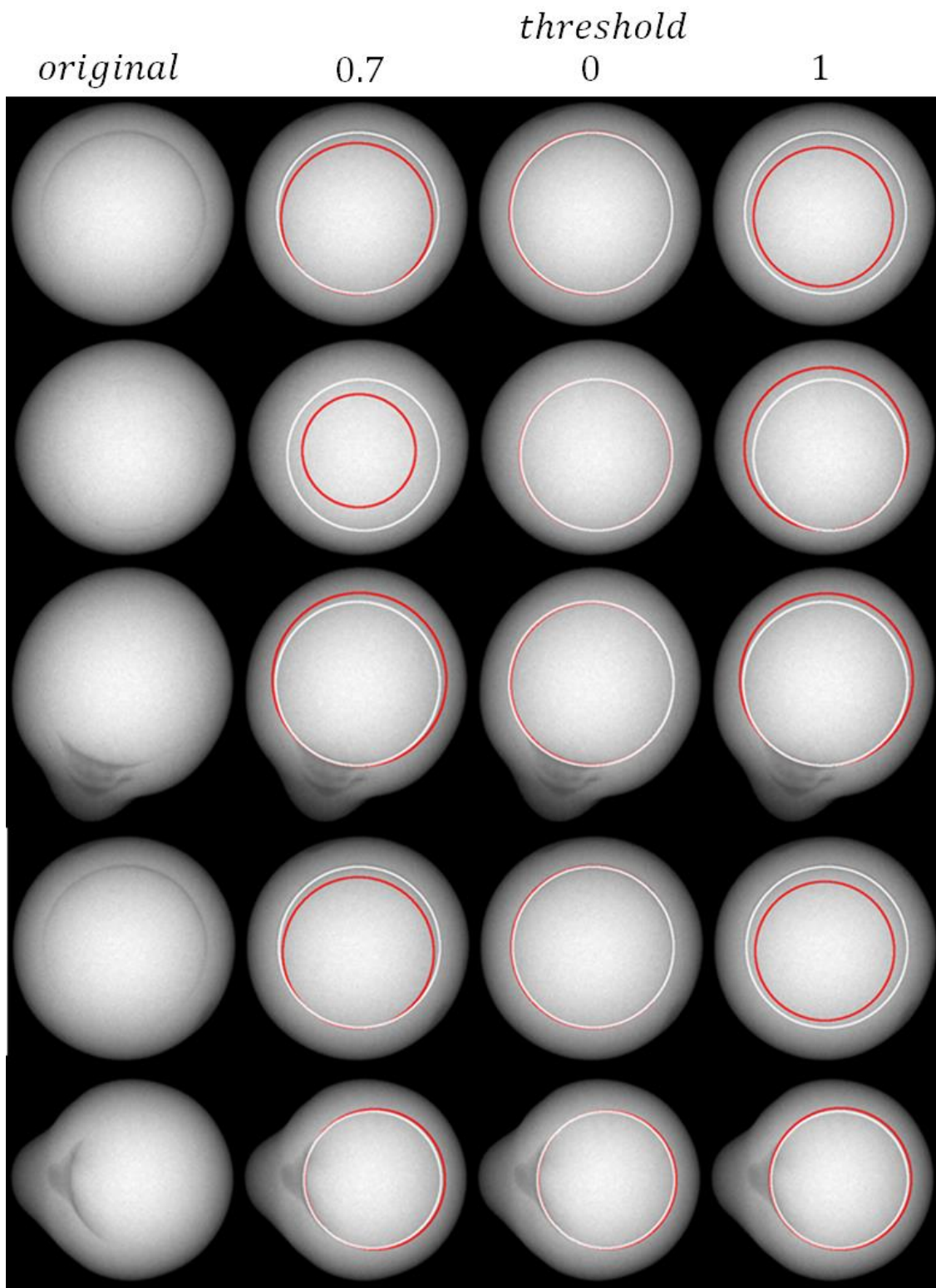


Figure 63: Result improvement by emphasis on gradient based circle movement.

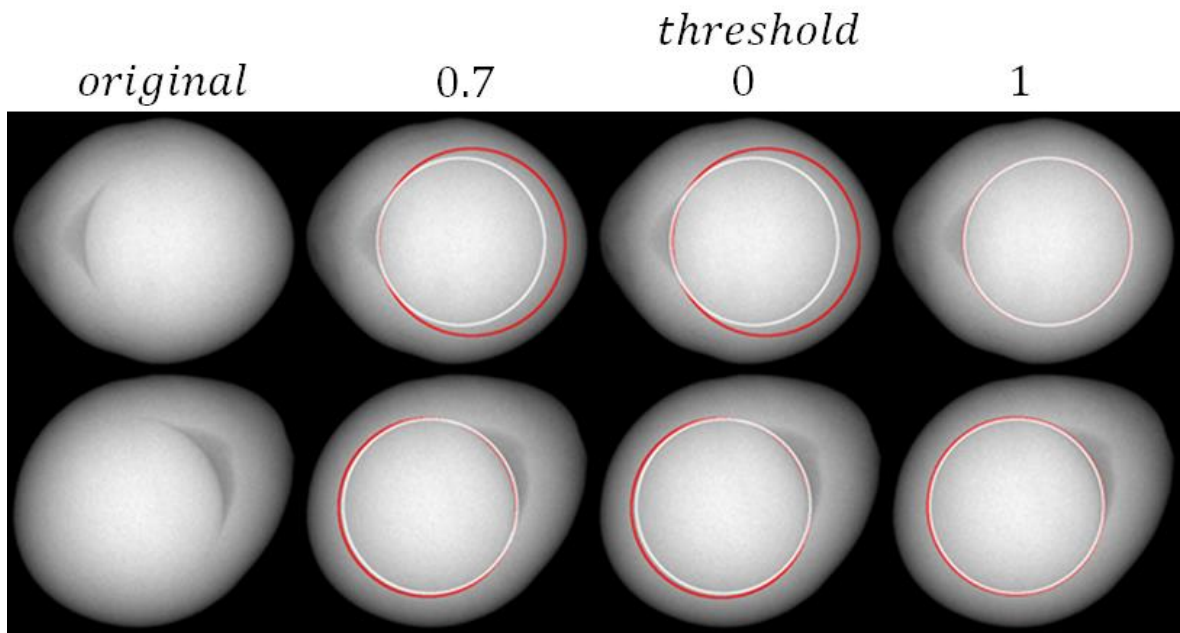


Figure 64: Result improvement by purely intensity based circle movement.

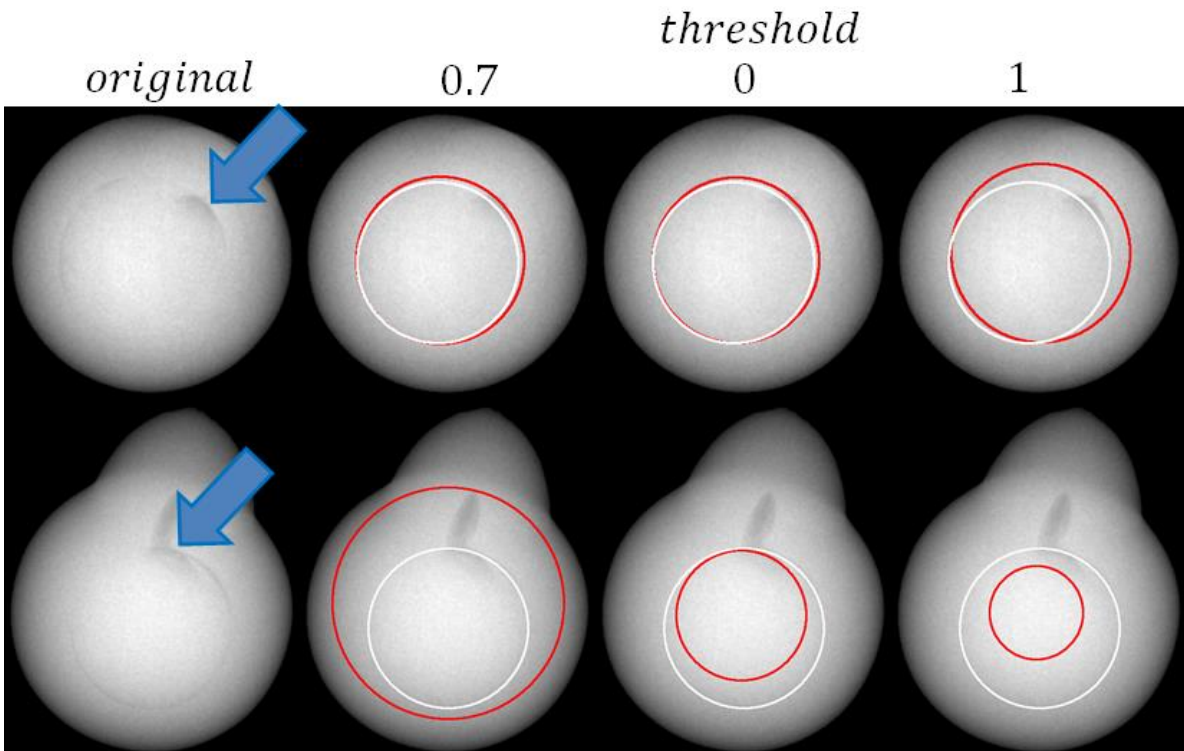


Figure 65: False detection due to superposition of cavity gradient and nucleus boundary.

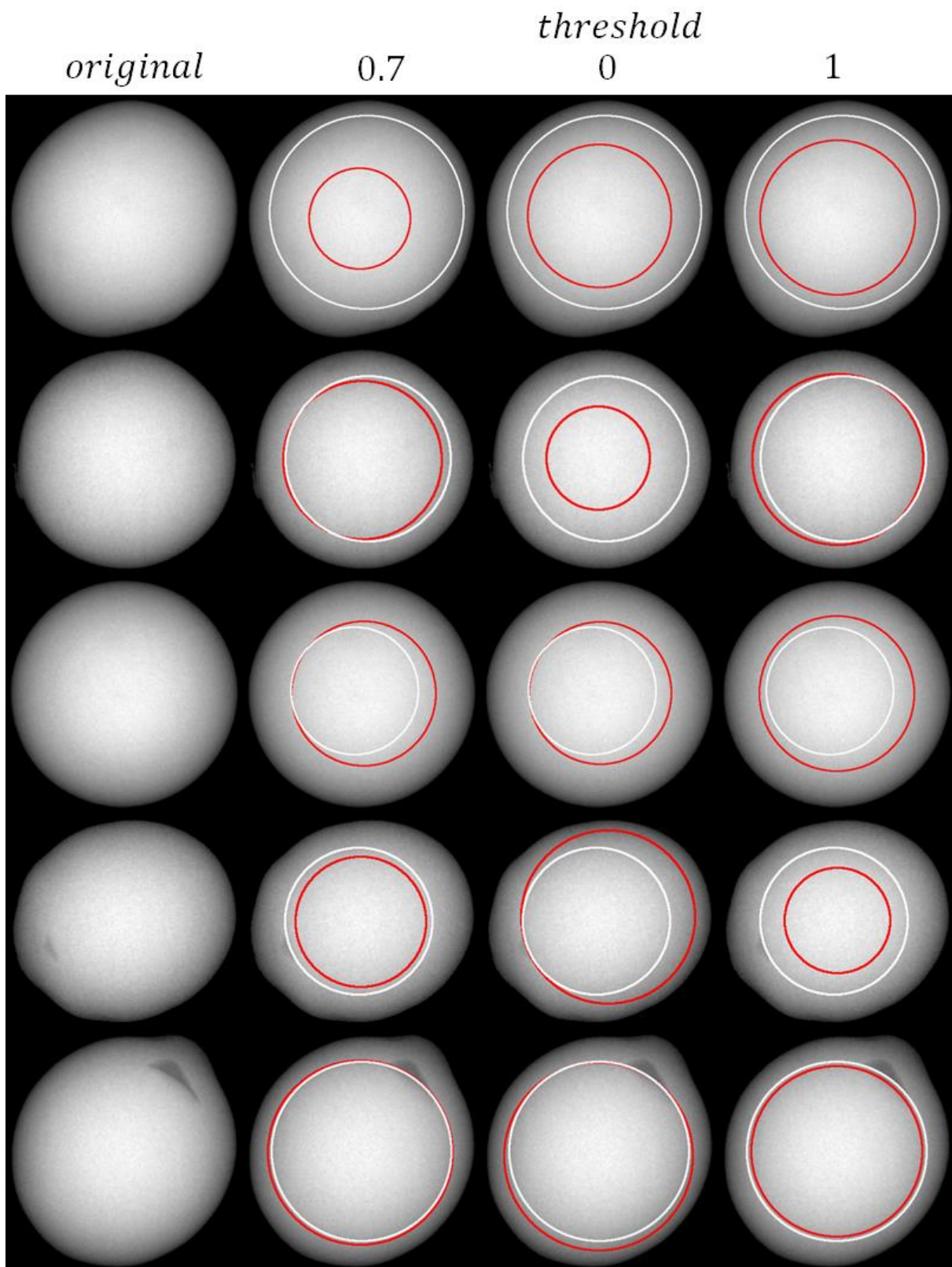


Figure 66: False detection due to weak or no nucleus boundaries.

4.4.4 Nucleus Visibility

Within the human evaluation results 5 pearls were classified as not evaluable as the boundary between nucleus and nacre was not visible. In 2 of these cases, a detailed visual analysis showed boundary gradients that allow a visual confirmation of the correctness of either the brute force result or the result obtained with our algorithm with certainty (Figure 67). The opposite happened in another case that was evaluated by DRMM experts as good, but the author could not find any evidence of boundary gradients (second pearl in Figure 68). A possible reason might be that round pearls tend to roll around within the supports boreholes when the support is mechanically moved. Some pearls show boundary evidence in one position and in another not. Another reason might be that the manual classification of pearls at the DRMM does not allow analyzing pearls for an extensive amount of time, meaning during the daily routine pearls like these might just slip through. Anyway, the two mentioned pearls with boundary evidence will be treated in the further process as evaluable, while the other one classified as good will be treated as not evaluable.

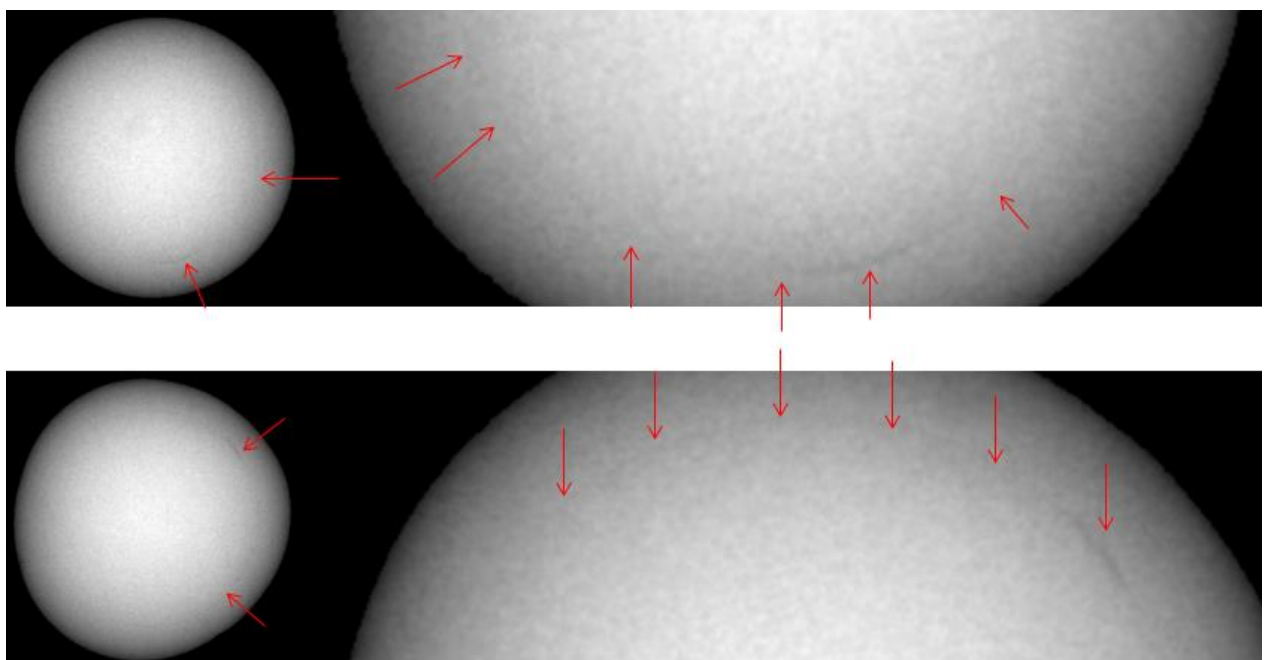


Figure 67: Two pearls classified as not evaluable, but a detailed visual analysis showed boundary evidence. Red arrows point to the regions at which the nucleus boundary is visible.

The question is, if a detection with numerical methods is possible in cases that show no visual evidence of boundary gradients. An analysis of the results of the Hough transform did not show a clear tendency. Generally, the expected result for a visible boundary with clear

gradients is a global maximum of the accumulation matrix at the center of the nucleus at the dimension of the nucleus radius. In Figure 68 on the top is such a pearl with the maxima of the radius dimension of the accumulation matrix on the right. A clear global maximum can be observed at the center of the nucleus.

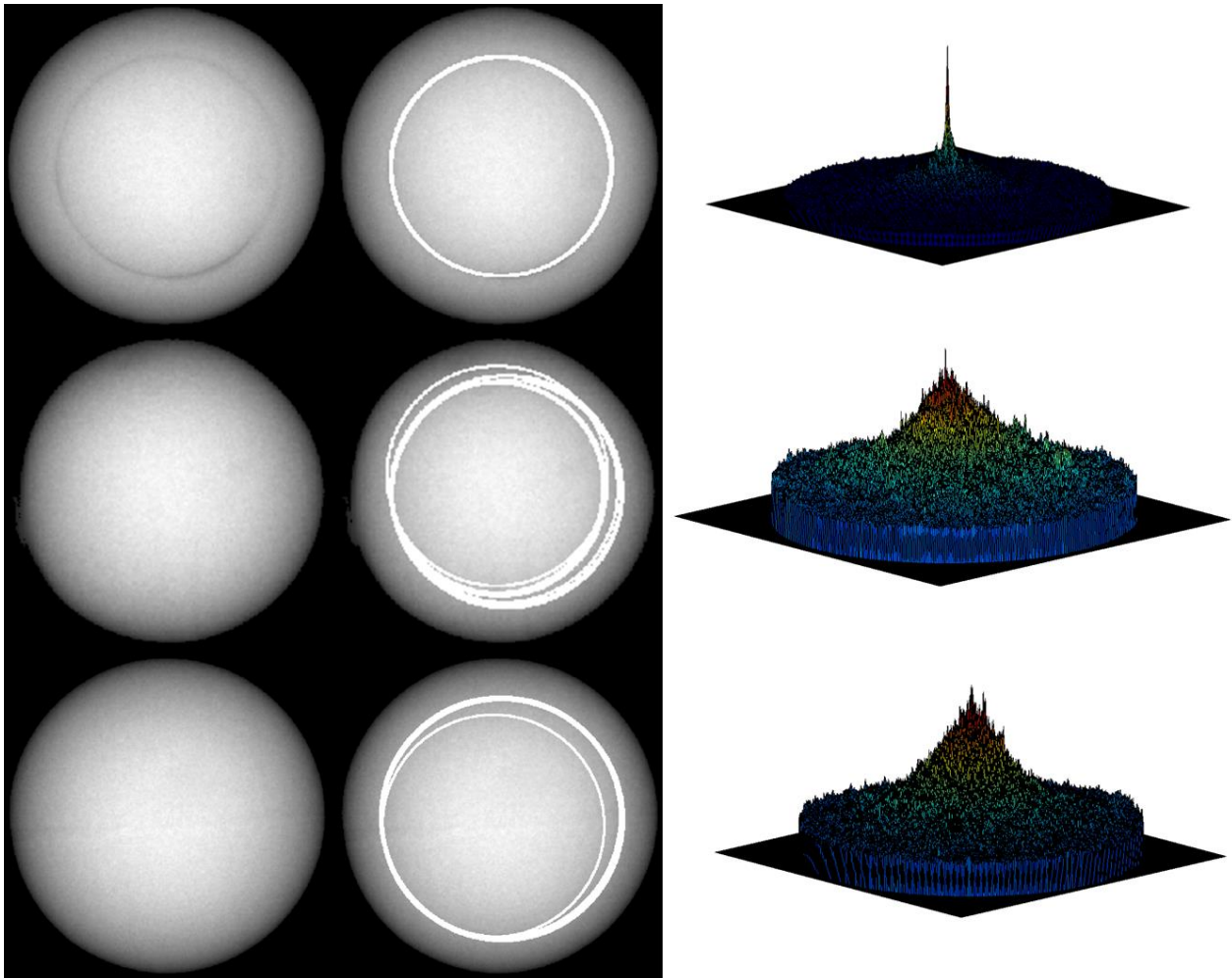


Figure 68: Nuclei of different visibility (left images), together with the first nine circles determined by the nine largest entries of the accumulation matrix of the Hough transform (right).

Additionally high values in the matrix are at all 8 pixels surrounding the optimal center, as those circles still touch larger parts of the nucleus boundary. The second image on the top row of the figure shows a superposition of the circles determined by the 9 largest entries of the accumulation matrix. As expected their centers cover the optimal center and all 8 neighbor pixels. The same procedure applied to the pearl of the second row shows a scattering of the nine circles with a maximum discrepancy of 10 pixels to the radius of the ‘optimal’ circle determined by the global maximum of the accumulation matrix. Even though the maximum is a clear peak, the difference to the next best circle is relatively low considering the general level of the rest of the matrix. Additionally, the cone shaped distribution of large parts of the

accumulation matrix show that the optimum at the center of the pearl might as well be caused by the point symmetric intensity distribution of the round pearl. As there is no visual evidence of the boundary, it is to the moment not possible to say for sure that the circle detected with the Hough transform does indeed identify the nucleus. Another example of a pearl with invisible nucleus shows instead, that, with one exception, the detection might conform to the nucleus boundary (last row of Figure 68). Still, a true confirmation is only possible if the actual size of the nucleus is known. In summary it is not clear if it is generally possible to detect any nucleus of any pearl, at least with the current image quality. To obtain a more precise evaluation, tests with an increased zoom for a better spatial resolution, higher image averaging for less noise and different initial X-ray intensity configurations will be done in a future work.

4.4.5 Self-Evaluation

Based on the previous analysis, a self-evaluation capacity of the algorithm is needed to identify false detections due to the circle not finding an existing optimum or due to the lack of boundary evidence in general.

A possible evaluation value is the maximum of the average probability function B_t that was used to identify the optimal circle out of all iterations. The greater its value the more pixels of the detected circle are likely to contain boundary pixels. The first graph in Figure 69 shows the sorted maxima of all test images that correspond to the boundary probability of the detected circle. The second graph on the bottom shows the detection discrepancy to the benchmark optimum for the corresponding image in pixels. For more clarity, this graph shows the absolute maximum of radius and center discrepancy. Again, discrepancies greater than 5 pixels are set to 5.

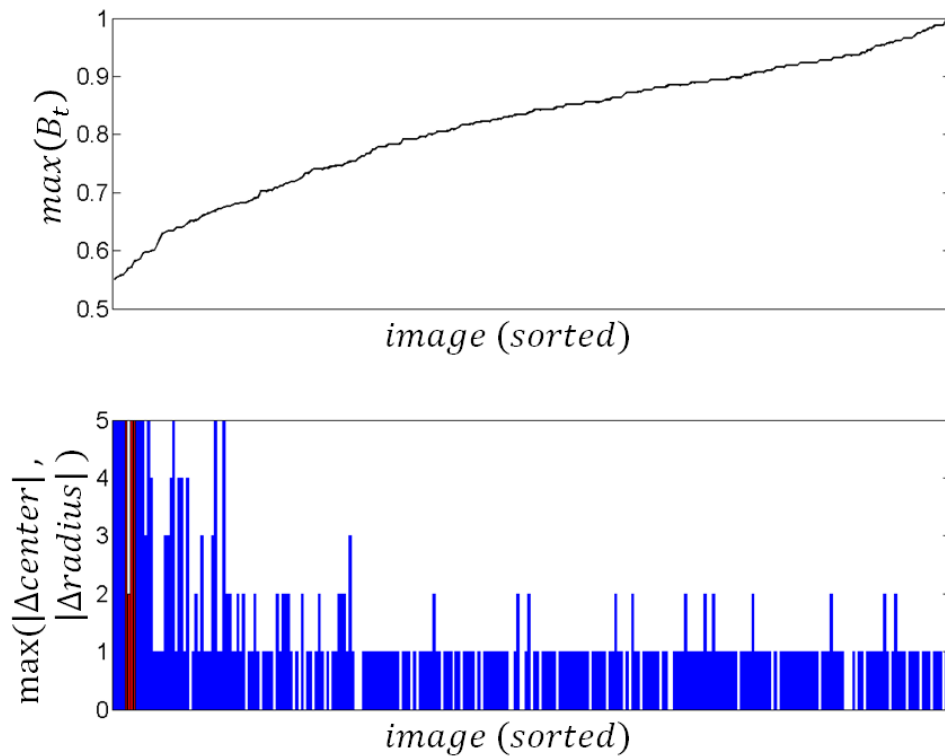


Figure 69: Sorted maximum nucleus boundary probability for all test images (top) and corresponding maximum absolute radius/center discrepancy (bottom, discrepancies greater than 5 pixels are set to 5).

All 19 detection results with a discrepancy greater than 3 pixels can be found within the first 40 images that have a low boundary probability. Additionally, all 4 images of pearls classified as not evaluable (marked in red) can be found within the same range. It means generally the same value can be used to identify uncertain classifications due to weak or no nucleus boundaries or due to an unsuitable algorithm parametrization. A threshold could be set to not evaluate pearls with a detected nucleus boundary probability smaller than 0.65 which would exclude all false detections and all cases that were classified as not evaluable.

A disadvantage of a general threshold is, that within the first 40 images 17 nuclei were detected more or less correctly, even though the general boundary was weak (which causes the low boundary probability). A more suitable method might be to use the threshold to apply an optimized but more therefor more time intense version of the algorithm only to images with a low self-evaluation value. If afterwards the value is still below the threshold, the pearl is classified as good, as the nucleus could not be detected with sufficient certainty. Possibilities of how to improve the algorithm to obtain a more powerful version will be sketched in section 4.4.7.

4.4.6 Processing Time

Average processing time for all 298 used test images is 0.23 seconds per image. The processing time for each image is shown in Figure 70. Generally the processing time is determined by the initial radius of the moving circle and the inner structure and size of the pearl (as the algorithm is stopped once the circle touches background pixels). In the current implementation the initial radius is set to 60 pixels (1.4mm), even though the nucleus sizes detected with the brute force approach are within a range of 100 to 257 pixels (2.4mm to 6.2mm) with an average nucleus radius of 133 pixels (3.2 mm). As the size of the nucleus is prior to the measurement unknown, the smallest possible nucleus has to be considered as minimal margin. Even though smaller nuclei than with a radius of 1.4mm might exist they are to the author's knowledge seldom used. Anyhow, the minimal radius should be implemented as a variable to set by the DRMM experts.

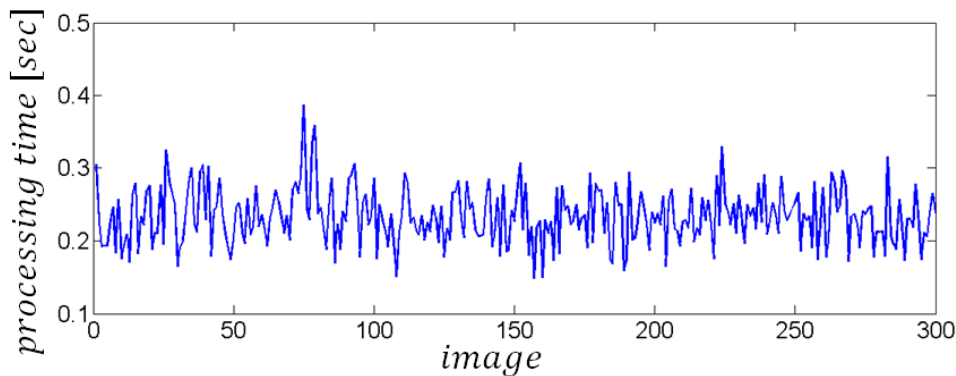


Figure 70: processing time for the detection of the nucleus with our algorithm.

To give an impression of the speed of the proposed algorithm the average processing time for our algorithm, for an application of the Sobel edge detector and for the application of the Canny edge detector are shown in Figure 71. It can be seen that in the same time the Canny algorithm was applied, our algorithm has already final results. As edge detection can only be one first step, the average processing time to obtain the accumulation matrix of the Hough transform with a radius range of 60 to 133 pixels for 100 preselected edges is shown as well (processing time is without edge detection). It can be seen that even if the image information is already reduced to only 100 edge pixels (Figure 71, 100 pixels in red in the pearl image) and the maximum radius is set to the average of detected nuclei (which excludes every nucleus with greater radius), the pure calculation of the accumulation matrix takes already

longer than our algorithm. The fast processing of our algorithm is because for every radius increment only one possible center is evaluated, meaning the processing time depends on the difference between maximum and minimum radius. The processing time of the brute force approach instead depends on the same difference multiplied by the amount of preselected pixels.

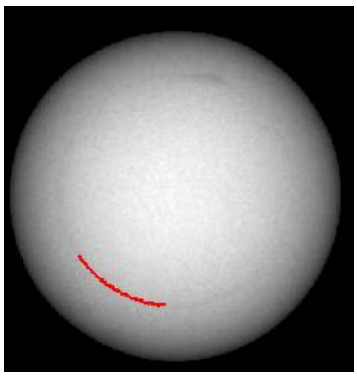
Algorithm	Proposed Approach	Sobel 3x3	Canny 3x3	Hough R=[60 133] Pixel=100	
Average Processing Time	0.23sec	0.04sec	0.29sec	0.29sec	

Figure 71: average processing time per image of our algorithm and standard algorithms. The red region in the image on the right contains 100 pixels. The processing time of the traditional Hough transform with such a small amount of information already exceeds the average processing time of our algorithm.

4.4.7 Optimization Possibilities

Generally all explained circle parameters can be used to adapt or improve the algorithm. In the current implementation the radius is increased after each circle movement. An increment at only every second or third movement for example gives the moving circle the chance to find local maxima (and possibly the global) when it has already reached the optimal radius but is still a few pixels away from the optimal center. The disadvantage is, when applied globally, that incrementing the radius after every second movement doubles the processing time. A dynamic approach of this idea would be to stop or delay the radius increments when the boundary probability is high. A possibility to overcome noise problems is to increase the distance of the radial gradient. Another possibility is to use not only three circles for the radial gradient calculation but five or seven, which would reduce the influence of noise. The optimal parametrization to the nature of the nucleus detection task has yet to be evaluated. The general idea is to run the algorithm in its basic form as presented, as generally the results are deemed good. If the maximum boundary probability is lower than a certain threshold a second run with an improved version is applied.

For a first test an improved version of the algorithm with 7 circles for gradient calculation was developed. If a detection result of the basic algorithm was lower than 0.65, this algorithm was run three times with a sensitivity threshold for gradient or intensity based circle movement of 0, 0.7 and 1. The percentage of detections with an absolute radius or center discrepancy lower than 4 pixels could be increased to 98% (Figure 72) with an increase of average processing time to 0.37 seconds per image. As these results were obtained by adjusting the algorithm to the nature of the test images, they have to be validated with a new set of images.

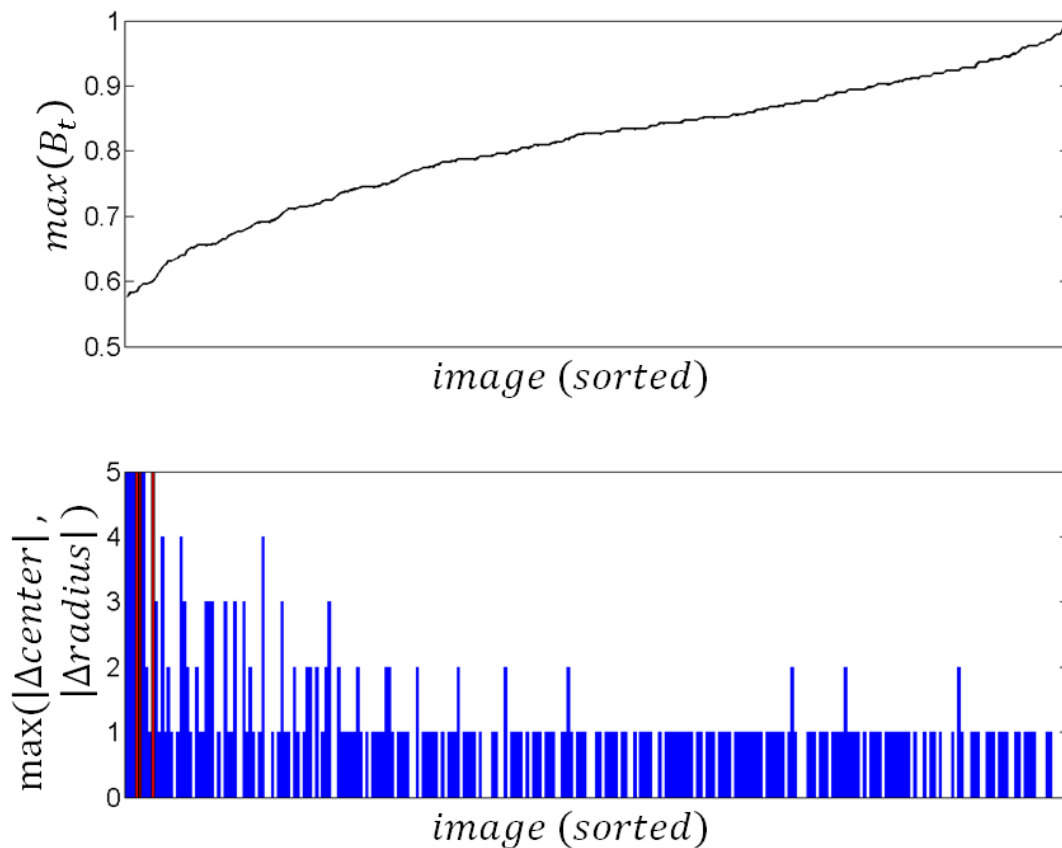


Figure 72: detection results of an improved version of the algorithm.

4.5 Conclusion

Within the precedent sections our own developed algorithm to detect the nucleus within the pearl was presented. The algorithm is a heuristic that is based on the following idea: a circle initialized within a circular object to detect that stays within the object while its radius is iteratively increased will at one iteration cover the outer boundary of the object. A suitable

logic boundary function was proposed that keeps the circle initialized within the nucleus region from surpassing its boundary while its radius is constantly increased. The detection results were compared to the results of a brute force approach, showing detection accuracy of 3 pixels for 94% of the test images. A self-evaluation was proposed that identifies with an according threshold false detections as well as cases that were identified by the experts of the DRMM as not evaluable, due to invisible nucleus boundaries. An improved version was sketched whose application to the test set increased the detection accuracy of 3 pixels to 98% of the test images.

5 Cavity Detection

The third step of our method to obtain the nacre thickness profile is to detect possible cavities within the pearl. Main challenges are caused by the partially weak boundary gradients, as cavities evolve smoothly over a rather larger region, and by the large variety of possible appearances. Additionally, it is still not known how and why cavities formed, which means the formulation of an according model is difficult.

In the next section the main challenges are explained more detailed along with challenges faced when classical algorithms were applied. The chosen region-based approach is explained in section 5.2 and the precision of the results shown in section 5.3. The results are discussed in section 5.4 along with an analysis of the discrepancy between the used simplified cavity model and an intuitive boundary setting based on gradient maxima.

5.1 Main Challenges

While for the segmentation of the pearl known properties of the support were used and for the detection of the nucleus the knowledge of its circular shape, prior assumptions for the detection of cavities are difficult to formulate as until now it is not clear why and how cavities within the pearl are formed. First of all, not every pearl necessarily has to have cavities, as shown within the previous sections. Within those, that contain cavities, different constellations can be observed. One type of cavities is connected to the nucleus and follows the symmetry of the pearls shape, meaning the nacre thickness of the pearl is more or less constant or at least does not change abruptly (first row of Figure 73 on page 127). Other cavity shapes are independent of the pearls shape (first two pearls of the second row of Figure 73). Even additional cavities not connected to the nucleus exist (last two pearls of the second row). Another type can be found within *surgreffé* pearl. Here, instead of nucleus, a complete pearl was inserted in the pearl oyster; the result can be seen as ‘a pearl within a pearl’ (Figure 73 third row). While in all former cases the cavity regions are relatively spacious, here slight cavities that might rather be described geometrically as lines occur. This type of cavities was found as well in regular pearls (not *surgreffé*). Additionally, cases occur in which cavity regions are superposed by shape gradients (Figure 73 fourth row). Even though the boundaries of cavities are in most cases identifiable by humans due to cognitive capacities,

the details shown in Figure 74 (page 128, the images on the right correspond to the region within the black square of the images in the second column) demonstrate a general numerical difficulty caused by partially weak gradients. The magnitude of cavity gradients depends on the nacre thickness gradient of the surrounding nacre. As a naturally formed gem, changes in nacre thickness occur mostly gradually over a larger range rather than abruptly.

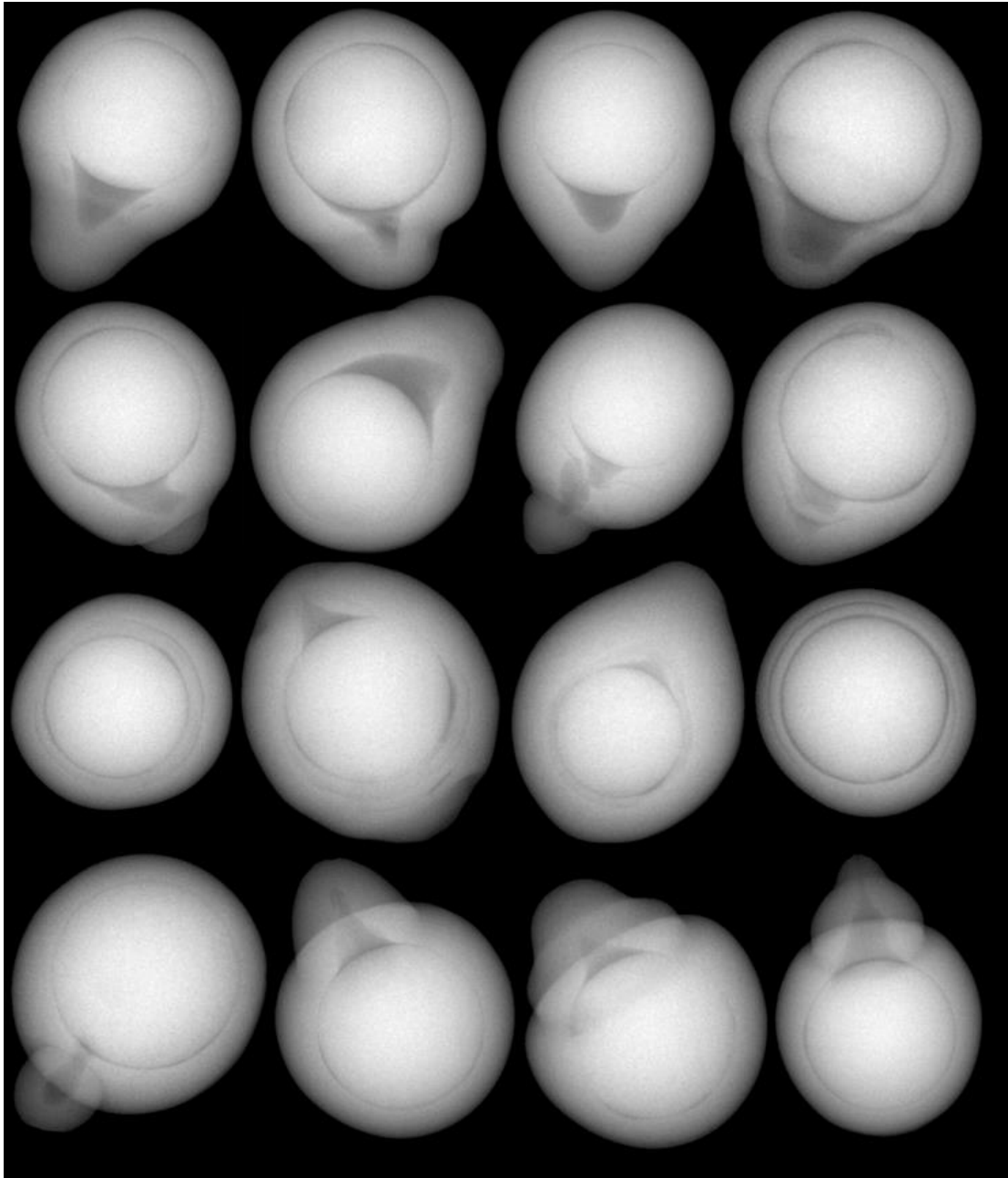


Figure 73: Different cavity formations.

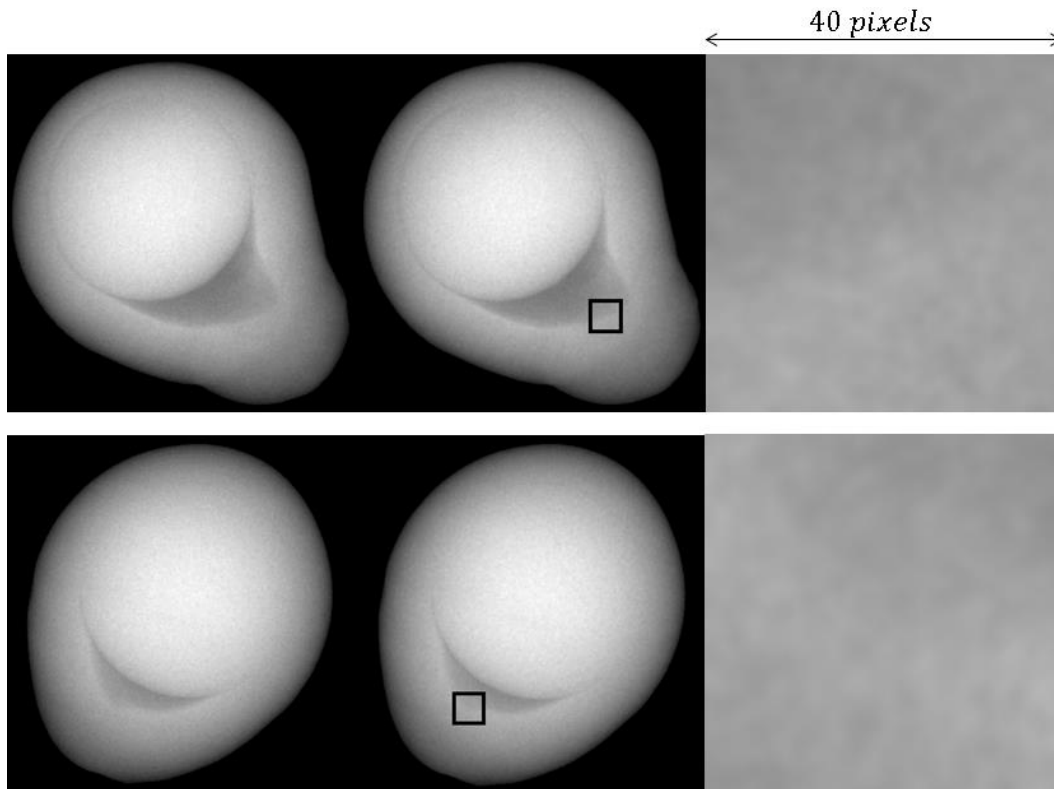


Figure 74: Details of cavities with weak boundary gradients.

5.1.1 Model Based Approach

As previously presented, cavities can appear in a large variety of shapes. Additionally, their intensity distribution within the images depends on the contour of the surrounding nacre, meaning it can vary as much as the form of Tahitian pearls varies. Hence a single model seems to be impossible to fit all cases. An idea might be to identify certain characteristic types and create a model library. To segment the cavity region in a certain image all or the most probable models have to be tested on the image. For the current implementation such an approach is not suitable as it is impossible to say if and to which degree the used training and test images contain typical cases. Anyhow, on a larger scale, such an approach might be worthy not only for the segmentation process, but as well to identify patterns and hence to possibly gain knowledge about how and why cavities are formed. Still, much more images will have to be analyzed for this purpose, meaning a model based approach can only be considered at a later moment of the ongoing project RAPA.

5.1.2 Active Contour

One of the strength of active contours is their ability to approximate boundaries at regions with low or even no boundary information. This is suitable for the partially weak boundaries observed in many cases (two examples were shown in Figure 74). Additionally, the resulting contour of this approach is a smooth curve which corresponded to the naturally smooth contour of the cavities. Anyhow, even though the approximation of boundaries with low or no boundary information seems quite suitable from a technical point of view, it contradicts the paradigm that in cases of doubt any decision has to be in favor of pearl quality. It means if low or no boundary information of cavities occurs, this region should be treated as no cavity to avoid nacre thickness reduction based on a numerical ‘guess’. Therefore, active contour approaches were not deemed suitable for the moment, but might be investigated later when more knowledge about the general structure of cavities is obtained.

5.1.3 Region Based Approach

Prior to the cavity detection the outer boundary of the pearl and the nucleus were already detected. This knowledge can be used for region based approaches. A possibility is to start a region growing process at the detected outer boundary, as those pixels belong in any case to the pearls nacre. The region growing is stopped locally where it touches cavity or nucleus pixels. The challenge is to find a suitable definition of cavity pixels. Pure intensity based approaches cannot be used as the intensity distribution of nacre and cavities depend on the pearls shape and hence vary over the complete pearl region as well as they vary between different pearls. A more suitable approach might be to define a nacre-cavity boundary probability and grow, starting from the outer boundary of the pearl until all neighbor pixels of the region belong either to the detected nucleus or have a high nacre-cavity boundary probability. As the latter are edge pixels, the resulting approach is a hybrid between region and edge based approaches. Therefore, edge based applications will be introduced in the following section before the current implementation that accords to this general idea of using region and edge information will be explained in section 5.2.

5.1.4 Edge Based Approach

The most general description of cavities from an image processing point of view might be that their boundary is defined by local intensity maxima. This means that the derivation of the gradient vector field should have local peaks at cavity boundaries. The direct application of one dimensional second derivative filters such as the LoG operator did not lead to satisfying results mainly due to curved edge lines and range parametrization problems. A more suitable way is to calculate the gradient vector field in a larger neighborhood and afterwards calculate the magnitude of the derivative of the normalized vector field in a small neighborhood (corresponds to the second derivative in gradient direction as proposed in [MAR80]). The process is visualized in Figure 75. Here the Sobel operator was used with different filter sizes (7x7 19x19 and 43x43 pixels) to calculate the gradient vector field (Figure 75 first row and second row for a detail). The magnitude of the derivation of the gradient vector field was afterwards calculated in a one pixel neighborhood (third and fourth row). Two general points can be derived from this example. First, boundary detection using only the gradient magnitude is difficult, mainly because cavities evolve spatially smoothly. Second, a rather large neighborhood function is necessary to obtain a consistent vector field that describes the shape gradient of nacre and cavity without noise interference.

A general edge based procedure to obtain a complete cavity boundary could be to use the active contour approach snakes to connect edges defined by local maxima of the obtained second image derivative. This corresponds to the gradient vector flow approach proposed in [XU97]. Anyhow, as stated earlier, an approach to approximate edges even though no consistent boundary information exists is not preferred due to the paradigm that in case of doubt the decision has to be made in favor of pearl quality. Additionally, a certain stopping criterion would have to be defined with a threshold that separates local intensity maxima due to noise from those caused by cavities. Without further knowledge about cavity configurations such a threshold setting is, as mentioned, for the moment not desired. Still the gradient field can be used for a region growing approach, as will be presented in the next section.

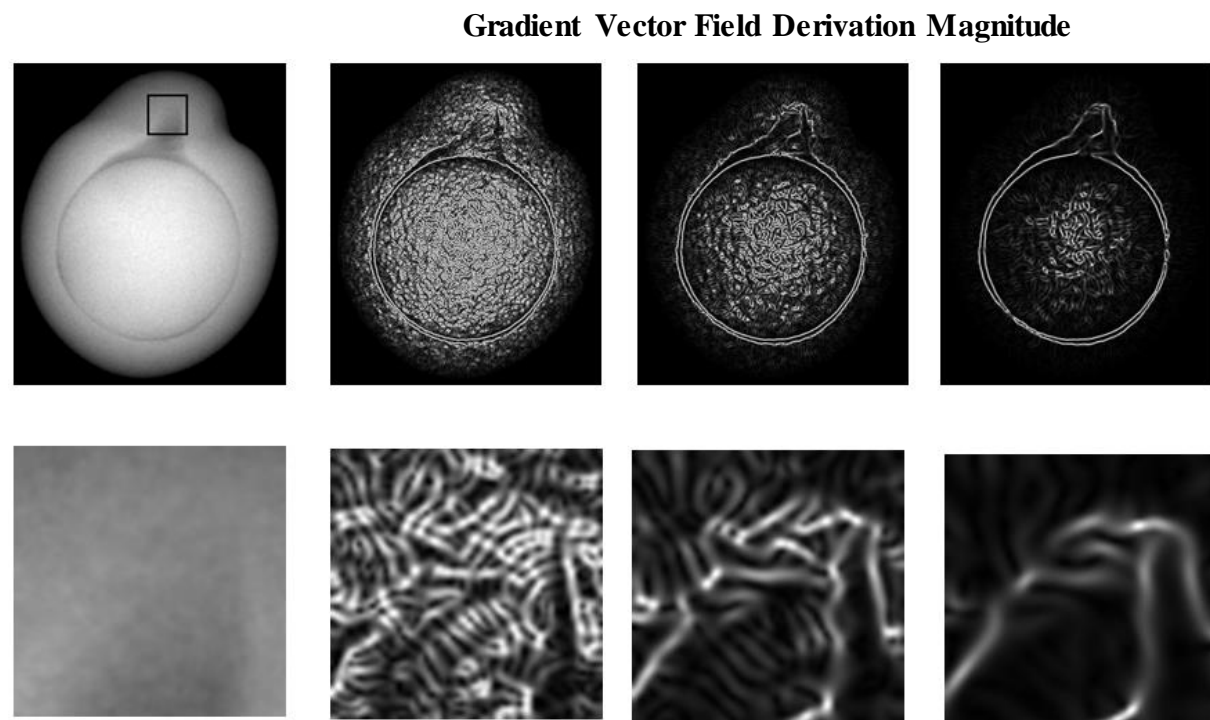
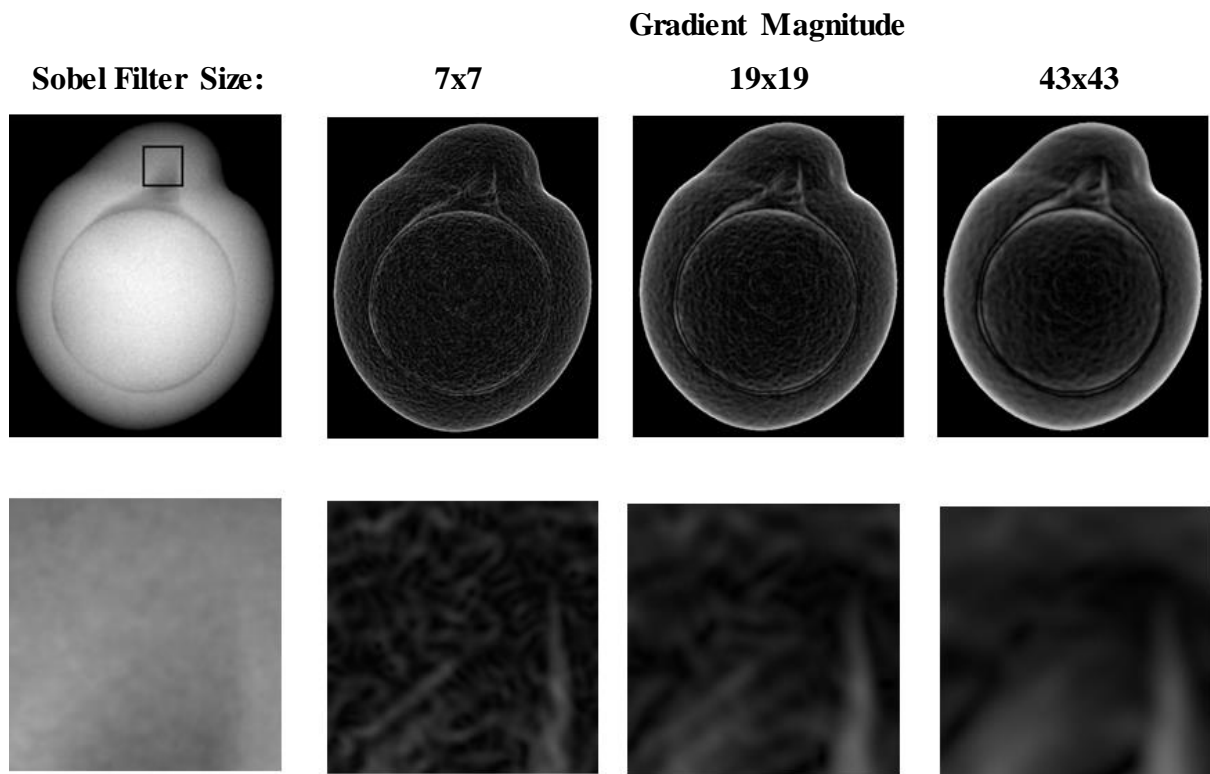


Figure 75: Cavity edge detection with the derivative of the gradient vector field.

5.2 Implemented Approach

The general idea of the implemented approach is to grow a region starting from the outer boundary of the pearl, as it is known to be nacre, and stop at local intensity maxima. As growing criterion, the gradient vector field can be used.

5.2.1 Neighborhood Range and Region Growing Rule

First, the neighborhood range of the applied filter to calculate the image gradient direction has to be defined. In Figure 76, the result of the region growing process for different filter sizes is shown with two example images. It can be seen that when a small filter is applied, the region growing stops even though the pixels adjacent to the region boundary pixels still belong to the nacre. This is due to the fact that the pearl shape gradient gets lower the further pixels lie within the pearls 'body', meaning the shape gradients get more disturbed by noise.

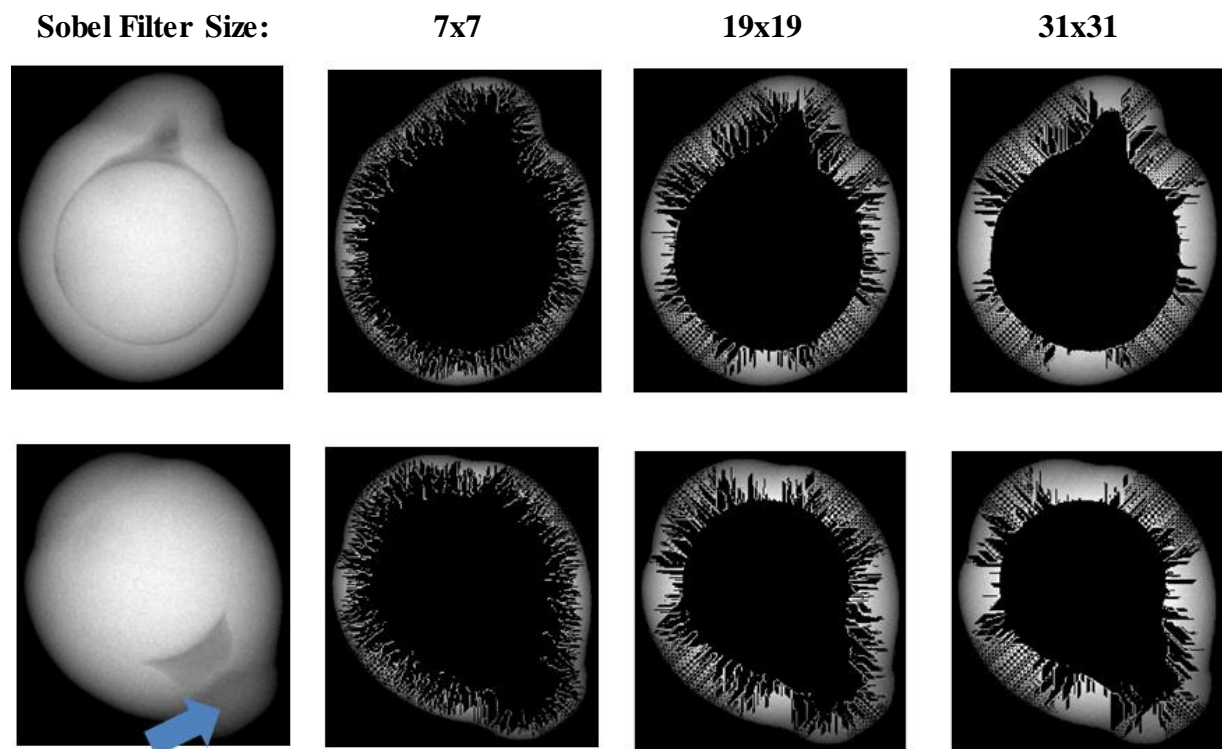


Figure 76: Region growing in gradient direction with different gradient filter size.

A larger filter size helps to overcome this problem (Figure 76). A larger filter size helps furthermore to overcome local intensity maxima caused by the nacre shape without cavity superposition (blue arrow in the first image in the second row). The problem of grooved regions that is caused by gradients in diagonal direction cannot be eliminated with a larger filter size. An application of circular filters diminished this effect, but a more ample growing rule is more efficient.

The effect of not only adding the pixel in gradient direction of a current region boundary pixel but adding its two neighbor pixels as well is shown in Figure 77 (a schema of this growing rule is shown on the right). The effect of grooves due to diagonal shape gradients is completely eliminated. Furthermore the need for a larger filter size to overcome local intensity maxima caused by the pearls shape can be observed more clearly when comparing the second image of the second row (Sobel filter size 19x19 pixels) and the third image (filter size 31x31 pixels). The negative effect of the ample growing rule and the large filter size can be seen in this example as well: cavity boundaries with low local intensity maxima could be over jumped (blue arrow).

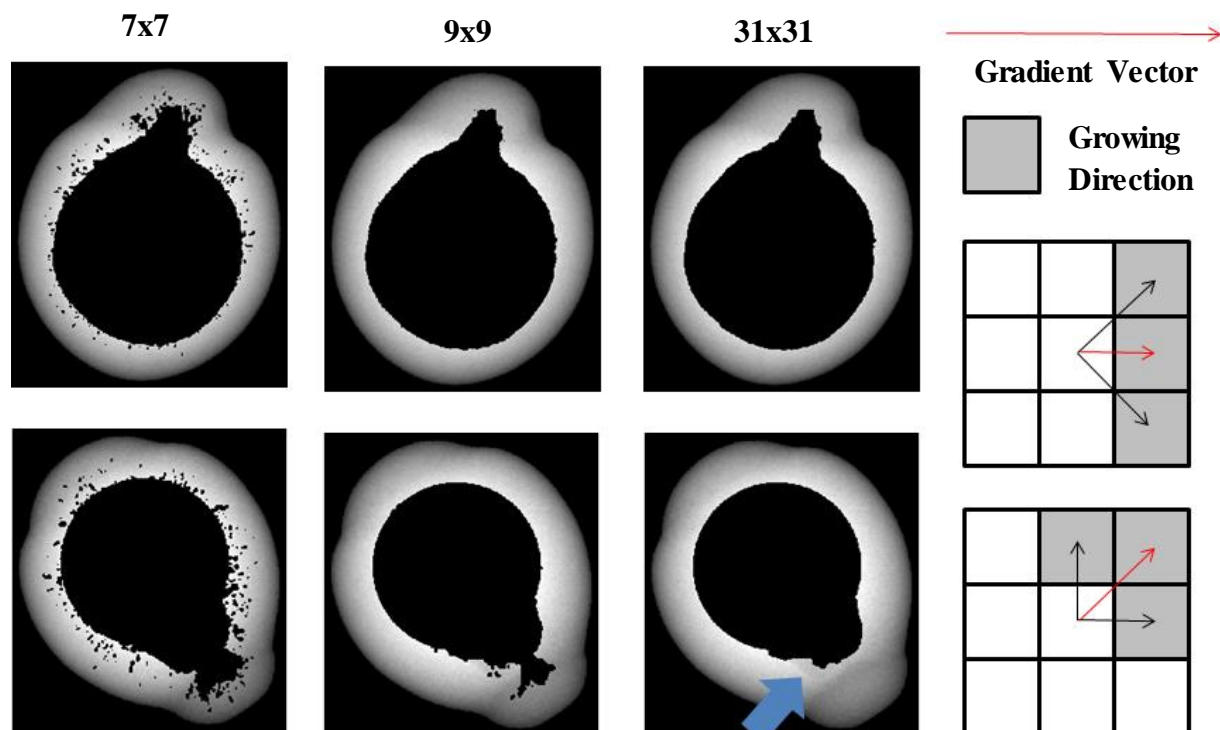


Figure 77: Effect of a more ample region growing rule.

For a first basic implementation this negative effect was willingly condoned for the following reasons. As local shape gradients can show similar characteristics as cavity gradients an analysis of the pearls shape would have to be done for a possible adaptive filter size or growing rule. An analysis of how to do that was postponed to a later time, when more knowledge about the general configuration and character of cavities is obtained. Second, an evaluation of a possible 3 dimensional pearl scan is aimed at in the near future. This means shape information can more easily be obtained than out of a single 2D projection of the pearl. Third, the large filter size can only result in a detection of smaller cavity extent than their real extent, which does not conflict with the general policy that false negative nacre thickness evaluations should be avoided.

5.2.2 Previous Segmentation Artefacts

As explained in section 3.2.4, artefacts along the boundary between borehole and bevel of the support appear after the synthetic background image is subtracted from the original image. These artefacts were treated with a smoothing operation. The effect of not treating the artefact in cases the nacre region is superposed by the borehole gradient can be seen in Figure 78.

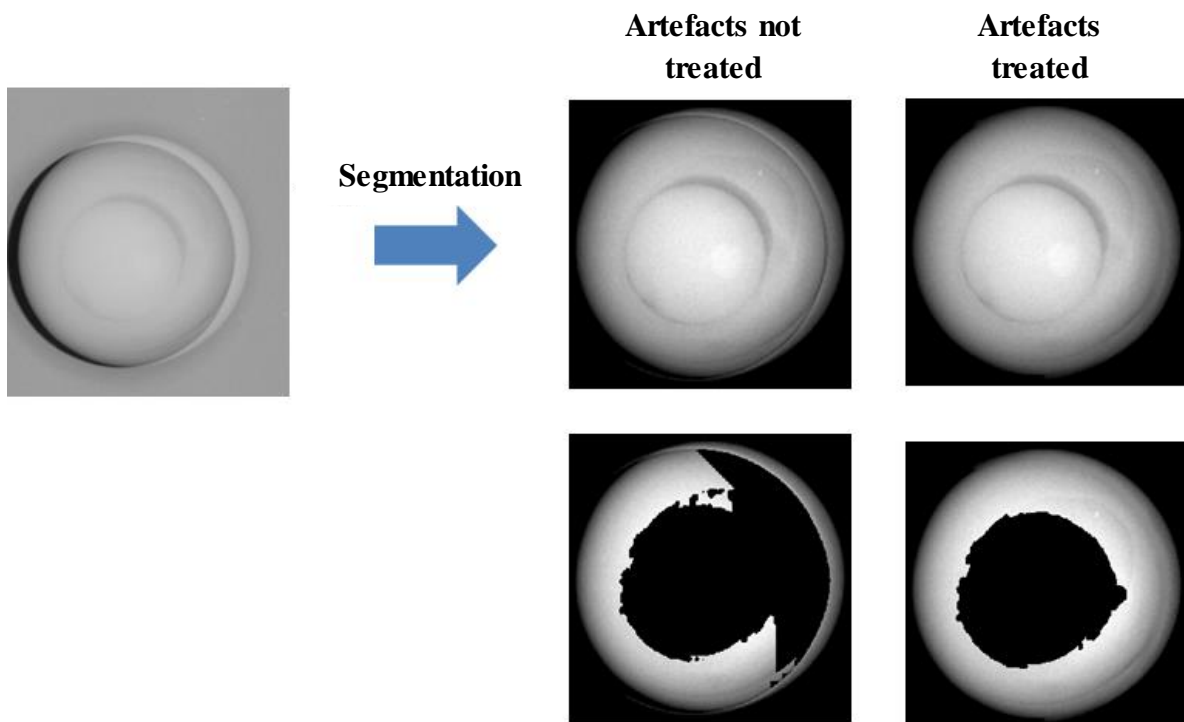


Figure 78: Effect of not treated and treated segmentation artifacts on the region growing process.

It can be seen that the region growing is stopped in a wide area, due to artificial local maxima at the non-treated borehole boundary. The smoothing process overcomes this problem. It has to be said that in several cases the treated region does not exactly approximate the expected nacre shape gradient, but as long as the region growing is not disturbed, this effect has no influence on the nacre thickness measurement.

5.2.3 Pseudocode

Pseudocode
<pre> set region of detected nucleus to -1 calculate gradient direction $\mathbf{g1}=(\mathbf{gx}, \mathbf{gy})$ of pearl pixels calculate $\mathbf{g2}=\mathbf{g1}-45^\circ$, $\mathbf{g3}=\mathbf{g1}+45^\circ$ $\mathbf{b_t}$=outer pearl boundary while $\mathbf{b_{t+1}} \neq \mathbf{b_t}$ Grow for each pixel in $\mathbf{b_t}$ in direction $\mathbf{g1}(\mathbf{b_t}), \mathbf{g2}(\mathbf{b_t}), \mathbf{g3}(\mathbf{b_t})$ Set $\mathbf{b_{t+1}}$=boundary of grown region end </pre>

Figure 79: Pseudocode for the segmentation of cavities.

5.3 Precision of Results

To obtain a numerical precision value the distance between detected boundary pixels and the local intensity maximum in positive and negative outside pointing normal vector direction of the boundary pixel was calculated in a range of -15 to +15 pixels (Figure 80). A positive distance means the detected boundary lies already within the cavity region, while a negative signalizes a detected cavity boundary within the nacre region (meaning the resulting measured nacre thickness will be lower than the actual one). The nucleus region was set to an image intensity of 0 to avoid maxima detection within this region. The average distance to local maxima for the boundary of each image is shown in Figure 81.

A visual analysis of the results showed that cases of larger negative discrepancies occurred in two images with elevated noise (Figure 82 first row). In one case a pearl shape gradient was wrongly identified as cavity (first two images second row of Figure 82). In one case of

multiple cavities the growing region could not reconnect after passing one of the cavities (last two images second row).

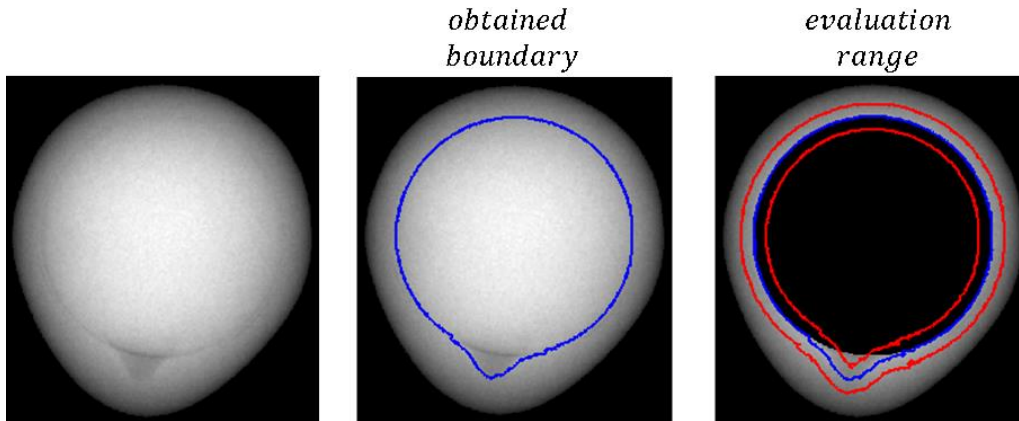


Figure 80: Schema of the precision evaluation range.

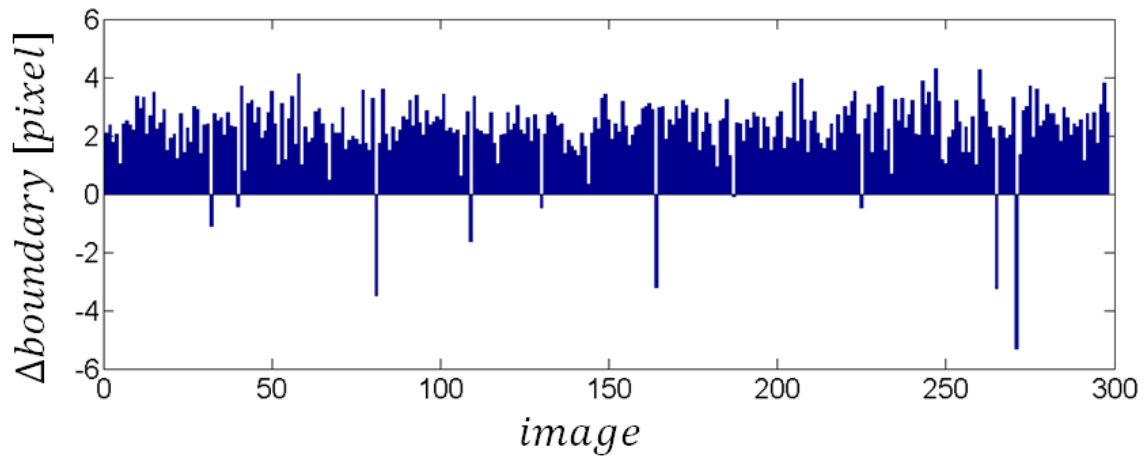


Figure 81: Precision of the detected cavity boundaries.

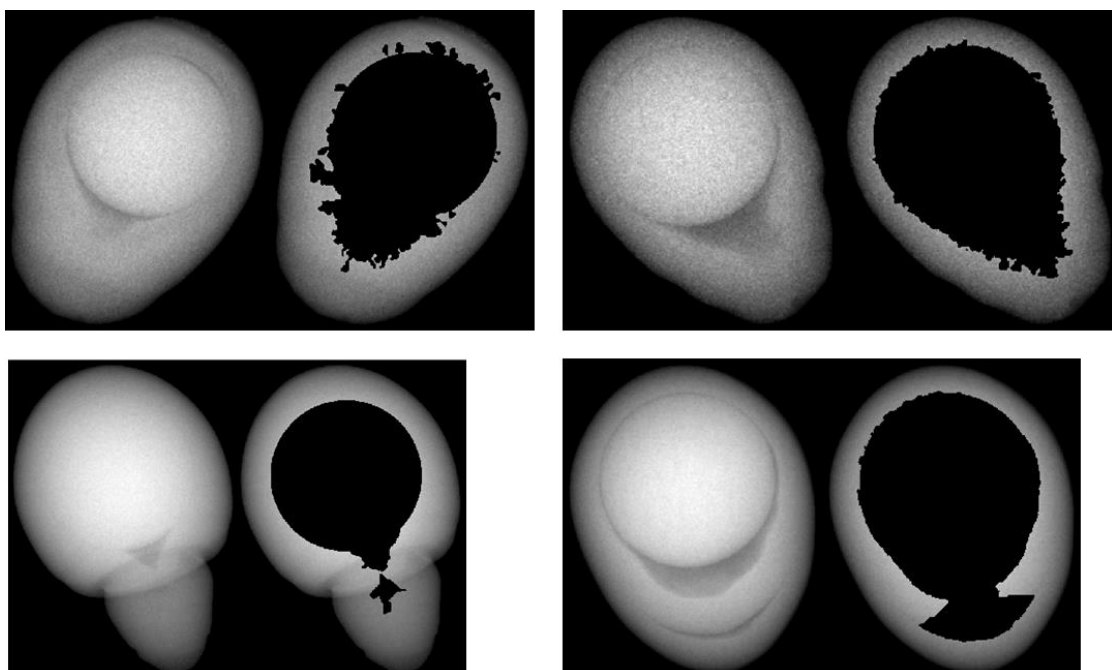


Figure 82: Largest discrepancies according to a visual analysis.

5.4 Discussion

The graph in Figure 81 shows that the general tendency of detection discrepancy is in favor of pearl quality, as almost all pearls have a positive discrepancy. Furthermore is the general discrepancy within a reasonable range of 3 pixels. The nine negative peaks contain the following cases: the two cases of noisy images shown in the previous section, two cases of false nucleus detection (first row of Figure 83) and five cases of ‘surgreffě’ pearls or pearls with a similar nacre cavity boundary characteristic (Figure 83 second to last row). In the cases of false nucleus detection, the applied region growing stopped at local maxima at the nacre nucleus boundary. In these cases, even though the evaluation value is negative, the region growing approach partially compensated the too small detected nuclei as it stopped partially at the nacre nucleus boundary. In all other cases the negative evaluation value is a reason of local maxima caused by the nacre shape after local cavities. It means that in all cases the region growing either stopped correctly at the cavity boundary or surpassed it. That accords to the general idea of the implemented approach.

In general, the visual analysis of the results showed that in only one case a false cavity was detected due to a local intensity maximum caused by the pearls shape (as shown in Figure 82 first images in the second row). False detections due to noise will not be addressed, as the elevated noise level is a result of the manual image acquisition and will not occur once this process is automatized. The case at which the growing region could not reconnect after passing a separated cavity not connected to the nucleus should not have an influence on the nacre thickness measurement, as the not connected region that is technically a false detected cavity lies behind the correctly detected cavity.

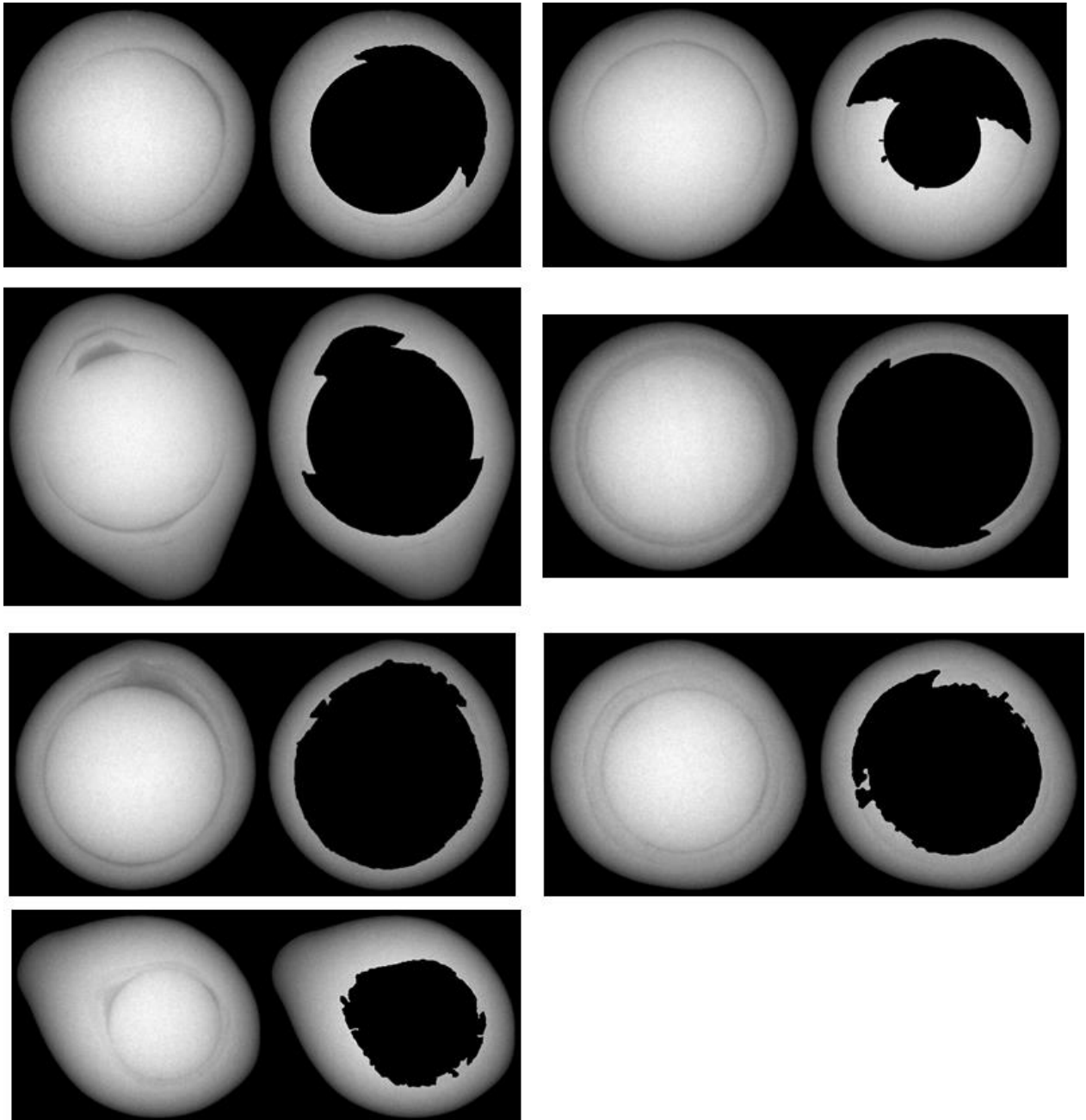


Figure 83: Images with negative precision evaluation value.

5.4.1 Discrepancy to Intuitive Boundary Setting

A more general point to discuss is the assumption that cavity boundaries are defined by local intensity maxima. The first image in Figure 84 shows the boundary of a detected cavity in blue. The second image shows the local intensity maxima calculated in normal vector direction of each boundary pixel (as used for the precision measurement) in red. It can be seen that the detected boundary in blue approximates well those maxima. Anyhow, a human

boundary setting might be more oriented at local gradient maxima. The automatically detected boundary in the region marked in the first image with a blue arrow appears to be several pixels away from an intuitively set cavity boundary. The visualization of local gradient maxima in normal vector direction of the detected boundary (third image in red) correlates better to the intuitive boundary. Anyhow, a pearl with the same shape but without cavity would show a steady increase of intensity (nacre thickness in direction of the X-ray beam) until the nucleus. As soon as the intensity decreases, a local cavity begins. A schema of this relation is shown in Figure 85. The grey region describes material with a cavity. The X-ray beam direction is orthogonal to the viewport. The point of maximum material thickness is situated exactly before the cavity begins. As the image intensity corresponds to material thickness in X-ray beam direction, a decrease in image intensity even though pearl thickness increases means a cavity begins. This means the assumption that cavity boundaries are described by local intensity maxima corresponds to the physical reality but might not correspond to the intuitive boundary setting by employees of the DRMM. If a boundary detection based on human intuition is preferred, a gradient based detection has to be implemented. Anyhow, for the moment the intensity based method will be used, as it corresponds to the physical model. An analysis of the impact on the nacre thickness measurement will be done in section 9.1.

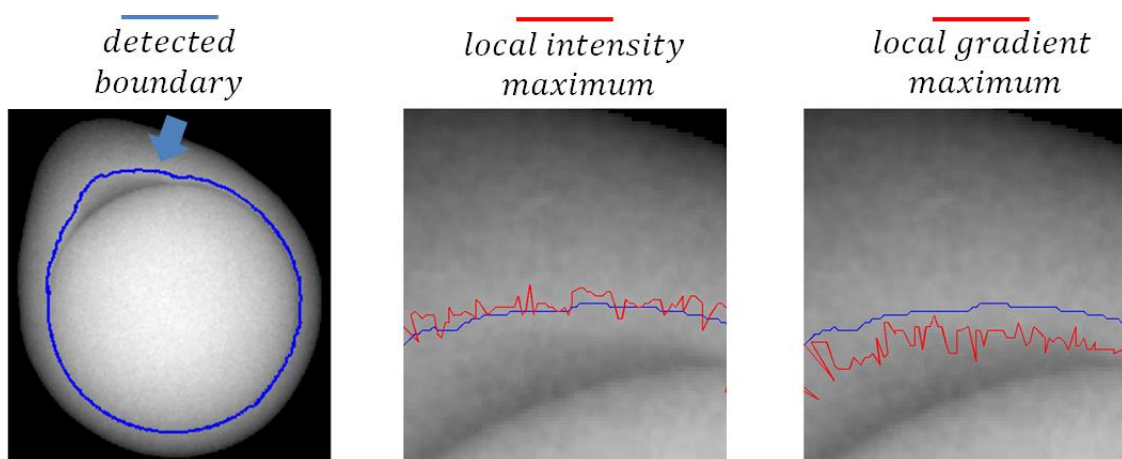


Figure 84: Difference between intensity based and gradient based cavity boundary.

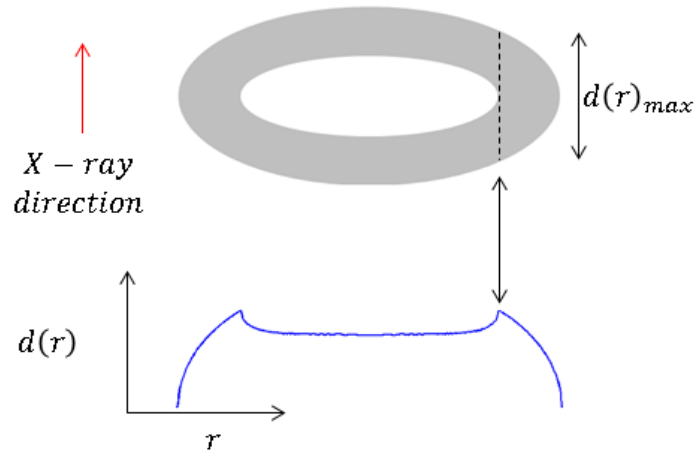


Figure 85: Schematic representation of the thickness profile $d(r)$ of material with cavity (cavity in grey).

5.4.2 Processing Time

The processing time to detect the cavity boundaries as described in the previous sections is shown in Figure 86. The processing time generally depends on the size of the pearl and the cavity configuration. For larger pearls without cavities the region growing process takes longer than for small pearls or pearls with large cavities. The average processing time is 0.15 seconds.

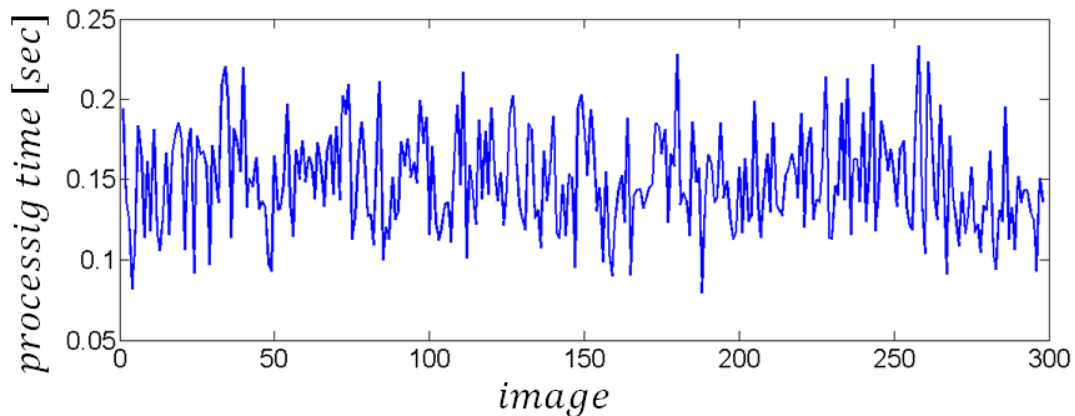


Figure 86: Processing time for the cavity detection for each test image.

5.4.3 Optimization Possibilities

Technically, the region growing process does not have to be done until all region boundary pixels are local maxima. For the decision if a pearl has to be rejected or not it is sufficient to

stop the region growing once every region boundary pixel is further than $0.8mm$ from the outer boundary of the pearl away, as all further regions are not of interest for the rejection criterion. Anyhow, the decrease in processing time is minimal (0.02 seconds). Furthermore, the analysis of the detection result of the complete algorithm might help to gain further knowledge of general nacre configurations.

In the current implementation a fixed filter size for the calculation of image gradients was used for all images. The global precision of results could be increased by implementing a multiscale approach. As adapting the filter size to local image features is a common approach, various techniques can be found in the literature [BAS02], [TUY08]. The challenge is to find an approach that reliably separates the different cavity configuration cases mentioned in section 5.1 (and possibly more). Anyhow, for the moment image acquisition parameters have to be evaluated first (noise reduction, spatial resolution,...), as well as the further ongoing of project RAPA, namely a possible 3D image acquisition has to be decided.

5.5 Conclusion

In the previous section our approach to detect cavities within the pearl was presented. The approach is based on the assumption that cavity boundaries are defined by local intensity maxima. This is due to the fact that the nacre thickness in X-ray beam direction decreases when cavities appear. A region growing process is started at the previously detected outer boundary of the pearl. The region is grown in gradient vector direction of its boundary pixels obtained by applying a Sobel operator on the image. As the gradient vectors around local intensity maxima all point to the maxima, the growing stops at such regions. To avoid false detections due to local intensity maxima caused by noise or the pearls shape a rather large filter size of 31×31 pixels was applied. Accordingly, small or weak cavity boundaries are sometimes not detected. The approach is hence ‘pearl exporter friendly’, as cavities cause a smaller nacre thickness.

6 Nacre Thickness Profile Calculation

After the three segmentation steps, explained in the previous sections, all crucial boundaries for the calculation of the nacre thickness profile are determined (Figure 87 on the left). The nacre thickness is measured for each pixel of the obtained outer boundary of the pearl in direction of its inside pointing normal vector (Figure 87 on the bottom right, nucleus and cavity regions are set to -1). This procedure was chosen as it corresponds to the current manual nacre thickness at the DRMM. Technically, this procedure does not necessarily accord to the real minimal nacre thickness at any point of the boundary (see sketch on the top right of Figure 87). But an absolutely precise measurement can due to the 2 dimensional projection of the X-ray imaging anyway not be guaranteed. Furthermore, a search of the minimal thickness in a 33 pixels radius ($=0.8mm$ in the current spatial resolution) is time intense, as for the certainty measure presented in the next section, not only the boundary pixels of the circle would have to be checked, but all pixels within the circle as well. But, as said, the procedure to measure in direction of the normal vector corresponds to the manual procedure of the DRMM experts and furthermore is not to the disadvantage of the pearl exporters, as a potential discrepancy to the physical minimal nacre thickness will always be positive.

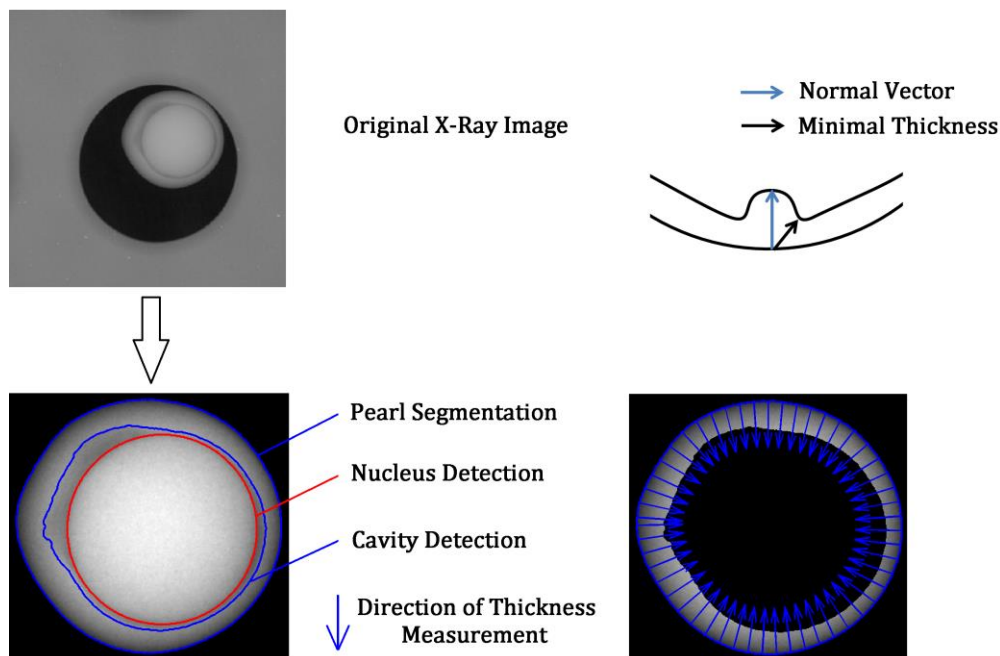


Figure 87: Schematic representation of the nacre thickness measurement in normal vector direction from the detected outer boundary of the pearl.

The measurement is done iteratively for all pixels of the outer boundary in direction, of their inside pointing normal vector. If b_i is a pixel of the outer boundary, n_i its inside pointing normal vector k a natural increment starting at 1, it is checked for each pixel $p_{i,k}$

$$\vec{p}_{i,k} = \vec{p}_i + k\vec{n}_i \quad (10)$$

whether it belongs to the detected nacre region or not. The results are stored in a matrix MC in which the columns contain a Boolean expression for each boundary pixel at a given k describing if pixel $p_{i,k}$ belongs to the nacre region (false) or not (true) (see Figure 89 for the pseudocode). This Matrix will be used for a certainty calculation described in the next section.

The nacre thickness profile in pixels is hence for each boundary pixel i the number of the column with the first non-zero entry (contact with cavity or nucleus). A multiplication with the image resolution results in the nacre thickness profile in mm (Figure 88).

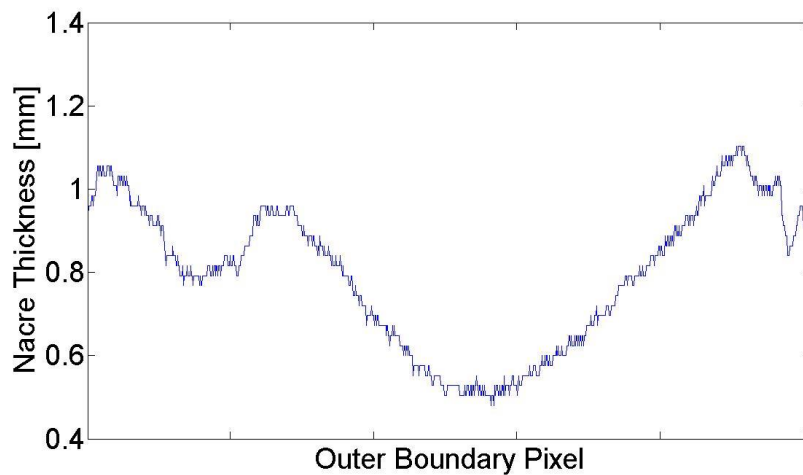


Figure 88: Obtained nacre thickness profile of the pearl shown in Figure 87.

Pseudocode
<pre> set region of detected nucleus and cavities to -1 calculate normal vector \mathbf{n}_i of each pixel \mathbf{b}_i of the outer boundary $\mathbf{k}=1$ while any pixel $\mathbf{b}_i+\mathbf{k}\mathbf{n}_i>0$ $MC(i, \mathbf{k}) = \text{pixel } \mathbf{b}_i+\mathbf{k}\mathbf{n}_i<0$ Set \mathbf{n}_i to zero if pixel $\mathbf{b}_i+\mathbf{k}\mathbf{n}_i=-1$ $\mathbf{k}=\mathbf{k}+1$ end </pre>

Figure 89: Pseudocode for the nacre thickness profile measurement.

7 Certainty Measurement

The procedure currently applied at the DRMM to decide whether to reject a pearl or not is to identify visually if more than 20% of the whole nacre region has a thickness of lower than 0.8mm. According to the current image resolution and the procedure explained in the previous section, the sum of the 33rd column of matrix MC (33 pixels = 0.8mm) divided by the size of the column (the amount of boundary pixels) is the percentage of the 2-dimensional nacre profile with a nacre thickness lower 0.8mm. The graph in Figure 90 on the left shows the calculated nacre thickness for every boundary pixel of the pearl of the previous example. The dashed line is the current threshold of 0.8mm. Every entry of the nacre thickness profile lower than 0.8mm is marked in red, as well as the corresponding regions in the X-ray image of the pearl on the right. The percentage of the nacre region lower than 0.8mm corresponds to ~46% which makes the pearl a reject in the current definition of the DRMM.

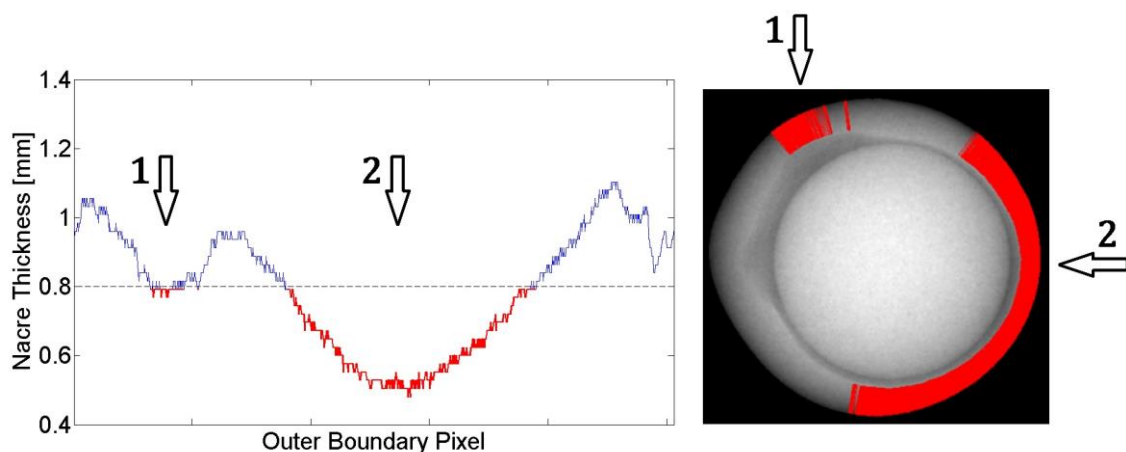


Figure 90: Automatically measured nacre thickness profile of a Tahitian pearl (left). The regions of the profile with a thickness lower than 0.8mm and the corresponding regions of the X-rayed pearl are marked in red.

As the automated measurement as well as the general imaging of spherical object results in a discrepancy between detected boundaries and real boundaries, a certainty measurement for the obtained results is proposed.

The sum of the k -th column of matrix MC divided by the amount of boundary pixels corresponds to the percentage of nacre regions lower than 0.8mm if the outer boundary is shifted by k pixels in direction of its outside pointing normal vectors. The identification of the column at which a pearl detected as a reject, has a percentage lower than 20% gives a scalar value in pixels of the certainty of the measurement. This procedure is visualized in Figure 91. The graph on the left shows the obtained nacre thickness profile of the previous figure in blue,

and a hypothetical profile shifted by 9 pixels that would result in a detection of a pearl to be exported in black. It means the automatic detection of the example pearl as a reject would be false if the imprecision of all segmentation steps and imaging imprecisions resulted in a lower nacre thickness of 9 pixels at every point of the detected outer boundary. The graph on the right shows the sum of the k -th column of matrix MC divided by the amount of boundary pixels, which corresponds to the percentage of nacre being lower than 0.8mm when the boundary is shifted by k pixels.

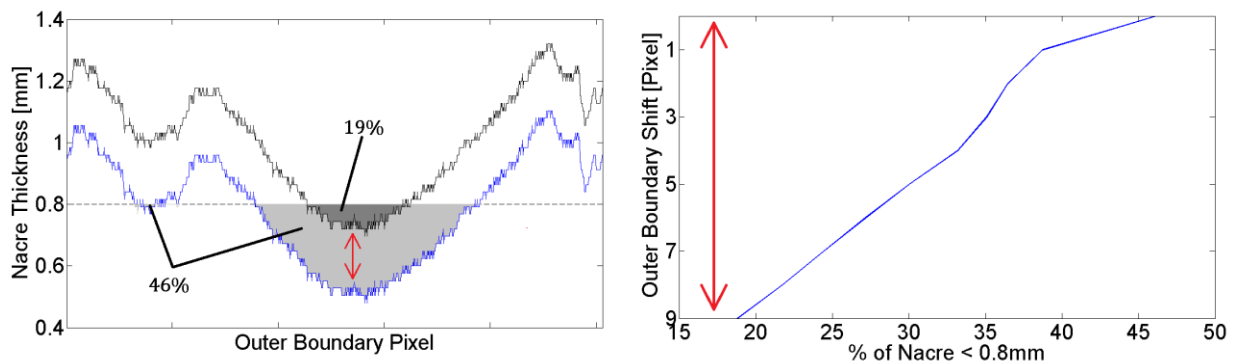


Figure 91: Representation of the calculated certainty value.

As the average precision of all segmentation steps within a range of -2 to 2 pixel, pearls automatically detected as rejects with a certainty value lower than 4 pixels might still be considered as good for exportation, according to the paradigm that in case of doubt pearls should not be rejected. However, the certainty value should be seen as a variable that is to be adjusted by the DRMM according to the results of the test phase of the prototype of our algorithm, rather than to be defined by the author.

8 Results

All test images were processed as described in the previous sections, without any of the proposed optimizations. The bar plot in Figure 92 on the top shows the sorted certainty values for pearls with at least 20% of automatically measured nacre thickness lower than $0.8mm$. Red bars mark the 13 pearls classified by experts of the DRMM as to reject. Within the sorted results, the last pearl classified by the experts as to reject has a certainty of 5 pixels and is situated at position 23. This means that if a threshold for the certainty value is set to 5, every pearl classified by experts of the DRMM as to reject is as well classified as to reject by the proposed automatic measurement. With such a threshold 10 pearls classified by the experts as good, would be rejected by the automatic measurement.

To identify false rejects due to imprecise segmentations of the proposed algorithm, a second measurement was done with optimized outer boundary and nucleus detection. The outer boundary detected with our approach was refined with the benchmark method used for the precision measurement (section 3.3.2). Larger image gradients only outside the detected boundary were identified and the boundary adjusted accordingly. This means that the optimized boundary always results in a nacre thickness equal or larger than the originally detected one but corresponds to standard assumption that object boundaries are defined by gradient maxima. For the nucleus the results of the brute force approach used to measure the precision of our algorithm were taken (sections 4.1.3, 4.1.4 and 4.3). Cavity boundaries were refined by identifying intensity maxima inside the detected boundary as done for the precision measurement explained in section 5.3 (an analysis of the difference between intensity based and gradient based cavity detection in regards of the nacre thickness measurement will be discussed in section 9.1). The optimized version is hence a ‘best case’ benchmark detection in means of nacre thickness. The certainty value for the nacre thickness measurement of this optimized version is shown in Figure 92 on the bottom. The certainty difference in pixels between proposed and optimized version is shown in Figure 93. The dashed black line marks a certainty difference of -2 pixels.

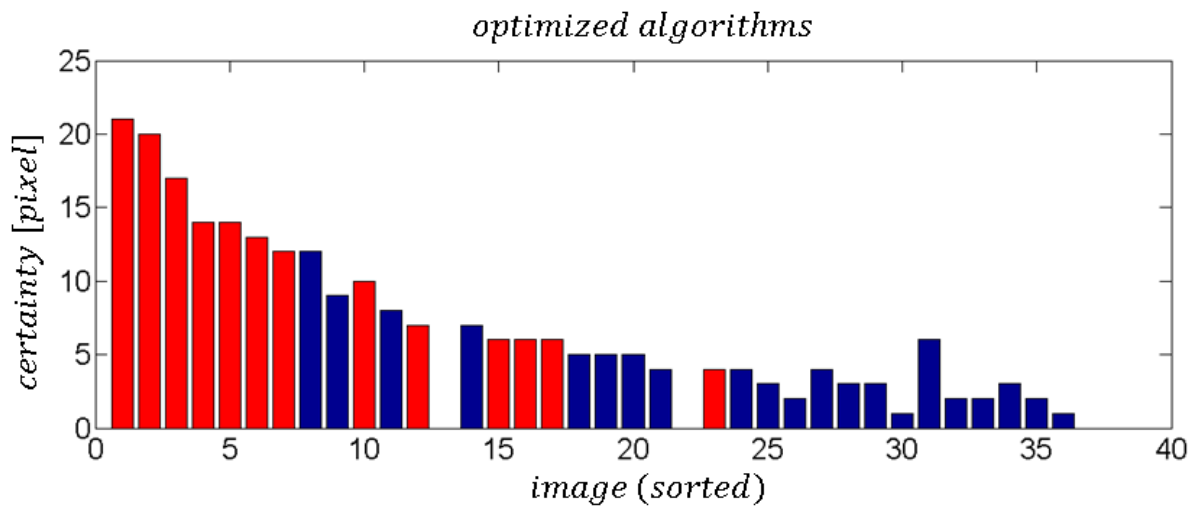
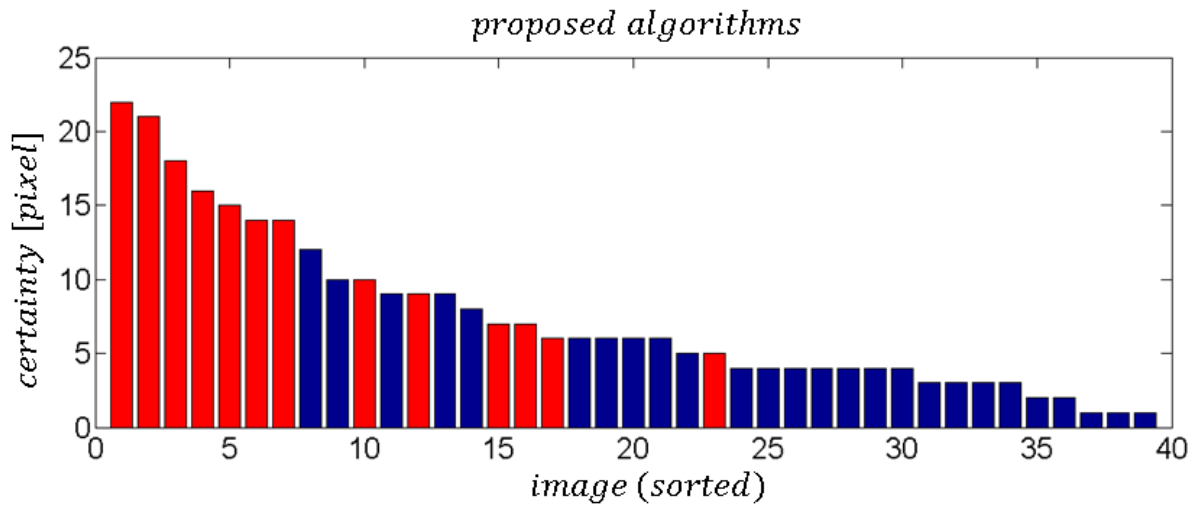


Figure 92: Certainty value for pearls detected as to reject with the proposed algorithms (top) and with an optimized (bottom). Pearls classified manually as to reject by experts of the DRMM are marked in red.

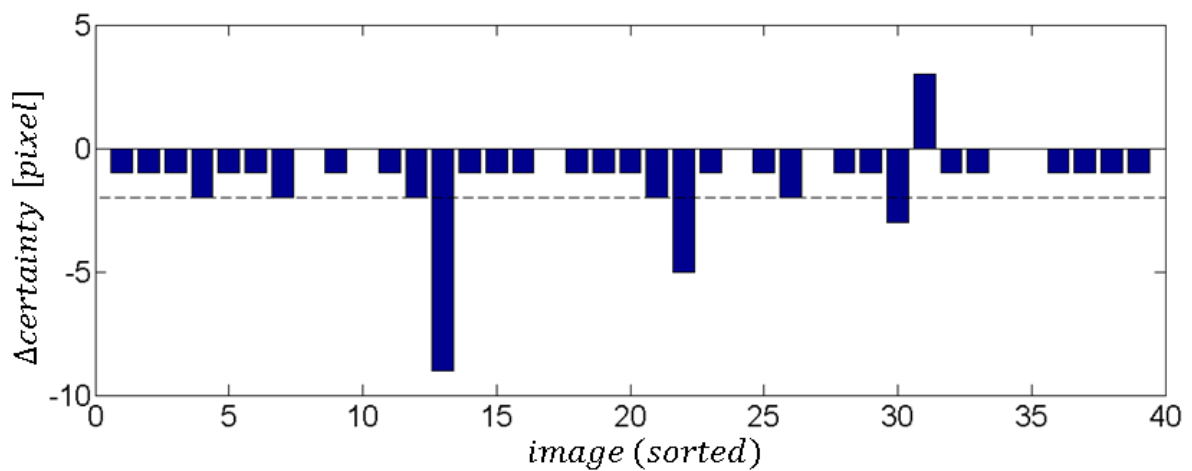


Figure 93: Certainty difference between proposed and optimized version of the nacre thickness measurement.

9 Discussion

Two pearls classified as to reject by the proposed algorithm are classified as good with the benchmark version (bars 13 and 22 in Figure 92). The results of both versions for both images are shown in Figure 94 (page 149). The first column shows a detail of the original image containing the pearl. The second column shows the detected outer boundary and cavity boundary in blue and the detected nucleus in black. The third column shows regions with a detected nacre thickness lower than $0.8mm$ in red. The yellow regions in the last image are regions with a nacre thickness lower than $0.8mm$ but all together do represent less than 20% in regards of the whole outer boundary. In both cases imprecise nucleus detection led to a thinner detected nacre thickness. The examples illustrate again the importance of a self-evaluation of the nucleus detection to either improve the automatic detection or to classify pearls that have a low self-evaluation value as exportable.

The contrary of a pearl with higher rejection certainty when the optimized version was applied is shown in Figure 95 (page 150 first two rows, corresponds to bar 31 in Figure 92). Again the discrepancy is caused by different nucleus detection. In the optimized version the nucleus is positioned two pixels more to the west and has a 2 pixels larger radius. As a result a slightly smaller region has a nacre thickness lower than $0.8mm$ but the certainty value is greater as all pearl boundary pixels in the west are closer to the nucleus. If a threshold is set to a certainty value of 5 pixels, the proposed version results in a good pearl while the optimized version results in a reject. The example shows that even small detection imprecisions have an impact on the general classification. Specifically for round pearls with a general nacre thickness close to $0.8mm$ as a nucleus displacement affects the nacre thickness measurement of the complete boundary.

The third and fourth row in Figure 95 show the impact of imprecise outer boundary detection (corresponds to bar 30 in Figure 92). Due to the smoothing process to delete segmentation artefacts, parts of the nacre in the south of the pearl are cut off. As a result, a larger nacre region has a thickness lower than $0.8mm$. If the outer boundary is detected correctly, the certainty value decreases from 4 pixels to 1. All other results show no larger discrepancies between boundary detections of the proposed and the optimized version. In the following two sections it will be clarified if the discrepancy between human and numeric classification is based on the intensity based cavity boundary assumption or caused by human misclassification.

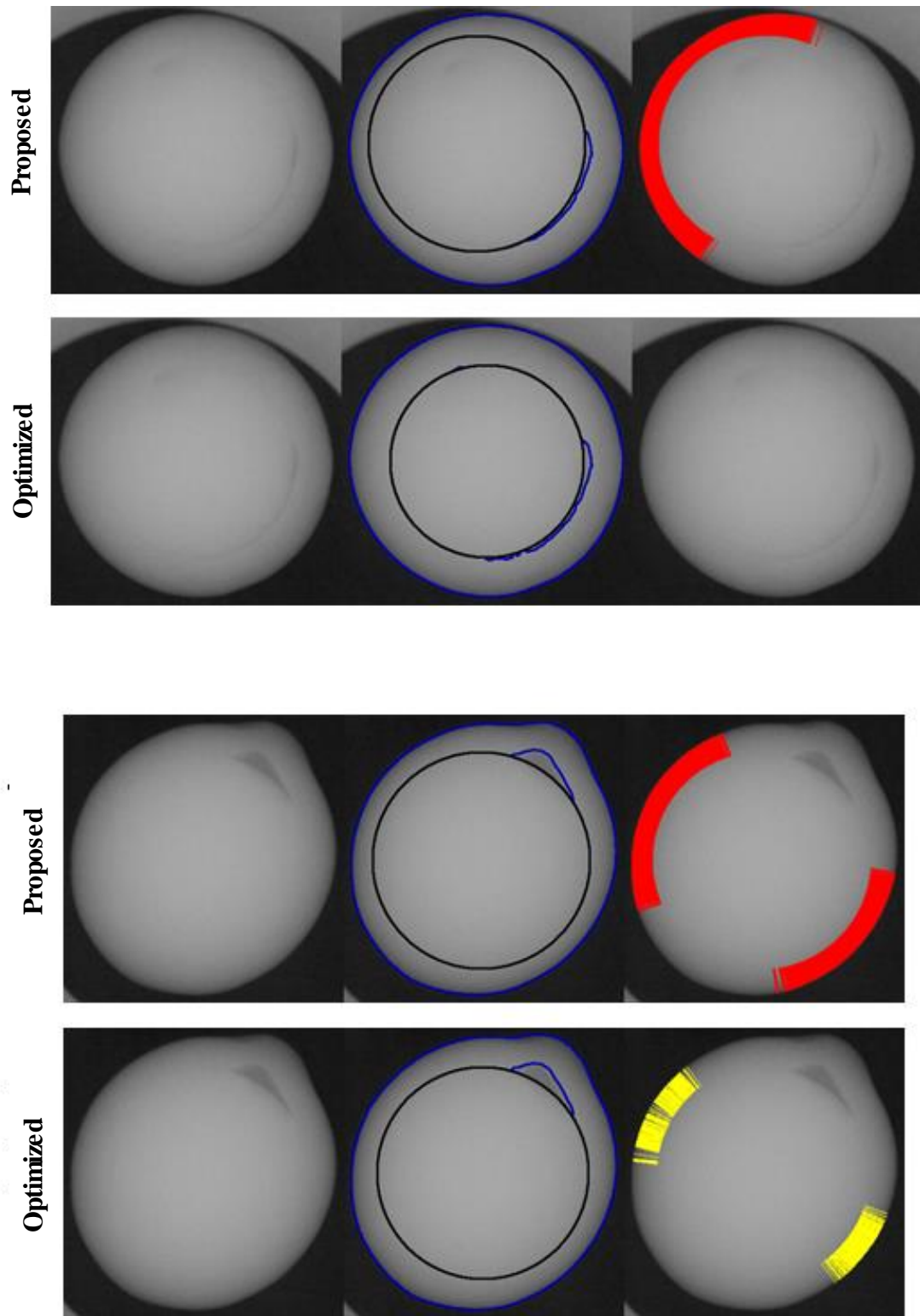


Figure 94: False rejects obtained with the proposed classification.

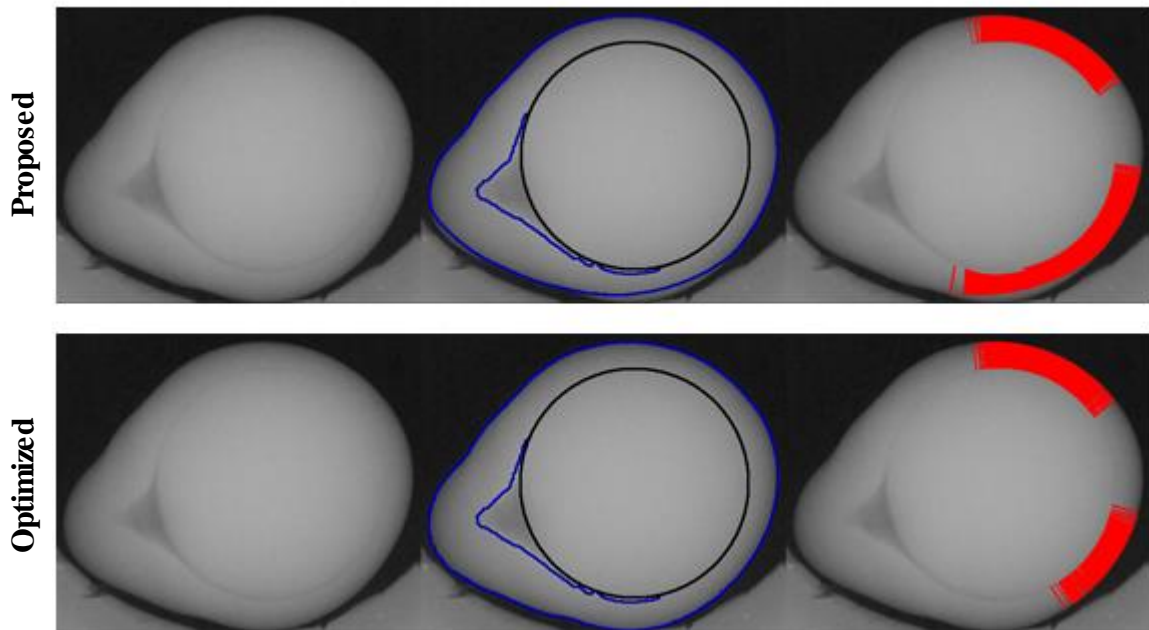
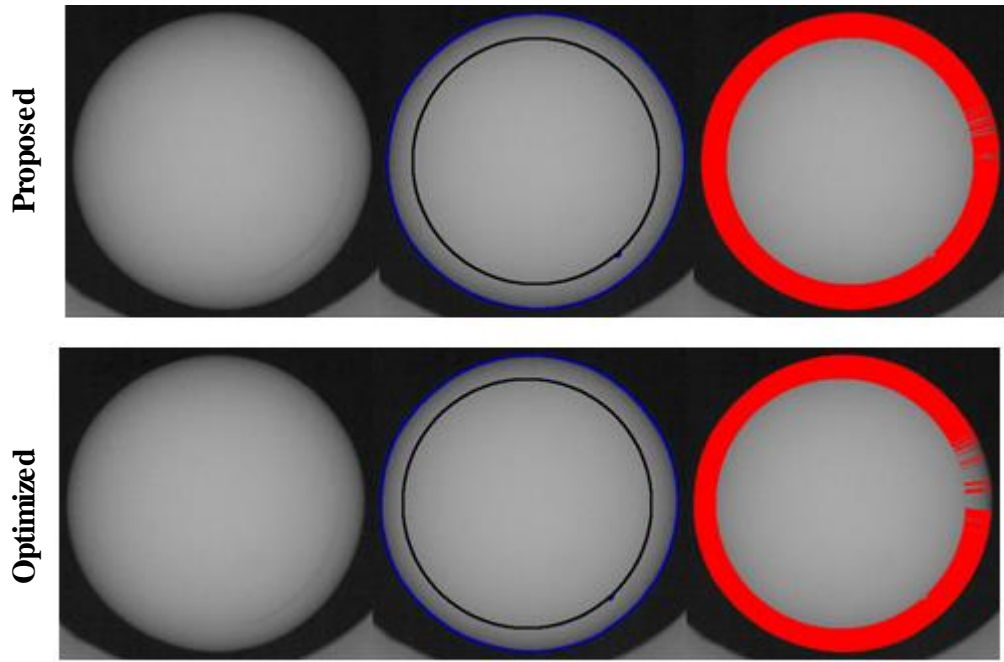


Figure 95: Pearls classified as rejects but with different certainty between proposed and optimized algorithms.

9.1 Intensity vs Gradient Based Cavity Detection

To evaluate if the discrepancy between pearls classified automatically as rejects but evaluated as good by experts of the DRMM is caused by the assumption that cavity boundaries are defined by local intensity maxima, a gradient based cavity boundary refinement was done. The strongest image gradients along the inside pointing normal vectors of the intensity based and optimized boundary were identified and the boundary adapted accordingly (see section 5.4.1 and Figure 84). This means, the so calculated nacre thickness will always be equal or larger than with the intensity based cavity detection. The outer boundary and the nucleus were detected with the previously mentioned benchmark version, to reduce the influence of segmentation imprecisions. The results were compared to the results obtained with the same benchmark version with intensity based cavity detection (corresponds to the bar plot on the bottom of Figure 92). In Figure 96 the certainty values for the gradient based cavity detection are shown on the top (the order still corresponds to the results of the proposed version). The difference of certainty values to the intensity based version are shown on the bottom.

It can be seen that several pearls show a decreased certainty value. But still, if a threshold is set at the value of the pearl at bar 23 to include all pearls that are manually classified as rejects, 9 other pearls are classified automatically as to reject in contrary to the human classification. It is hence to clarify if those pearls might be misclassified during the expert evaluation or if the even benchmark methods meet their limit. Before this analysis is done in the next section, it has to be said that the comparison between intensity based and gradient based cavity detection was done to exclude the conceptual difference as a unique reason for the discrepancy between human and numerical classification. As stated before, the intensity based method corresponds to the physical model of cavities and should to the author's opinion be preferred to the gradient based one. Anyhow, the model is an assumption. For a proof pearls would have to be cut. This is not an option for pearls deemed for exportation, but the DRMM owns pearls from its own production that cannot be exported as it would lead to a conflict of interest. The permission to cut some of those was granted by the DRMM so that in the near future a validation of the cavity model will be done.

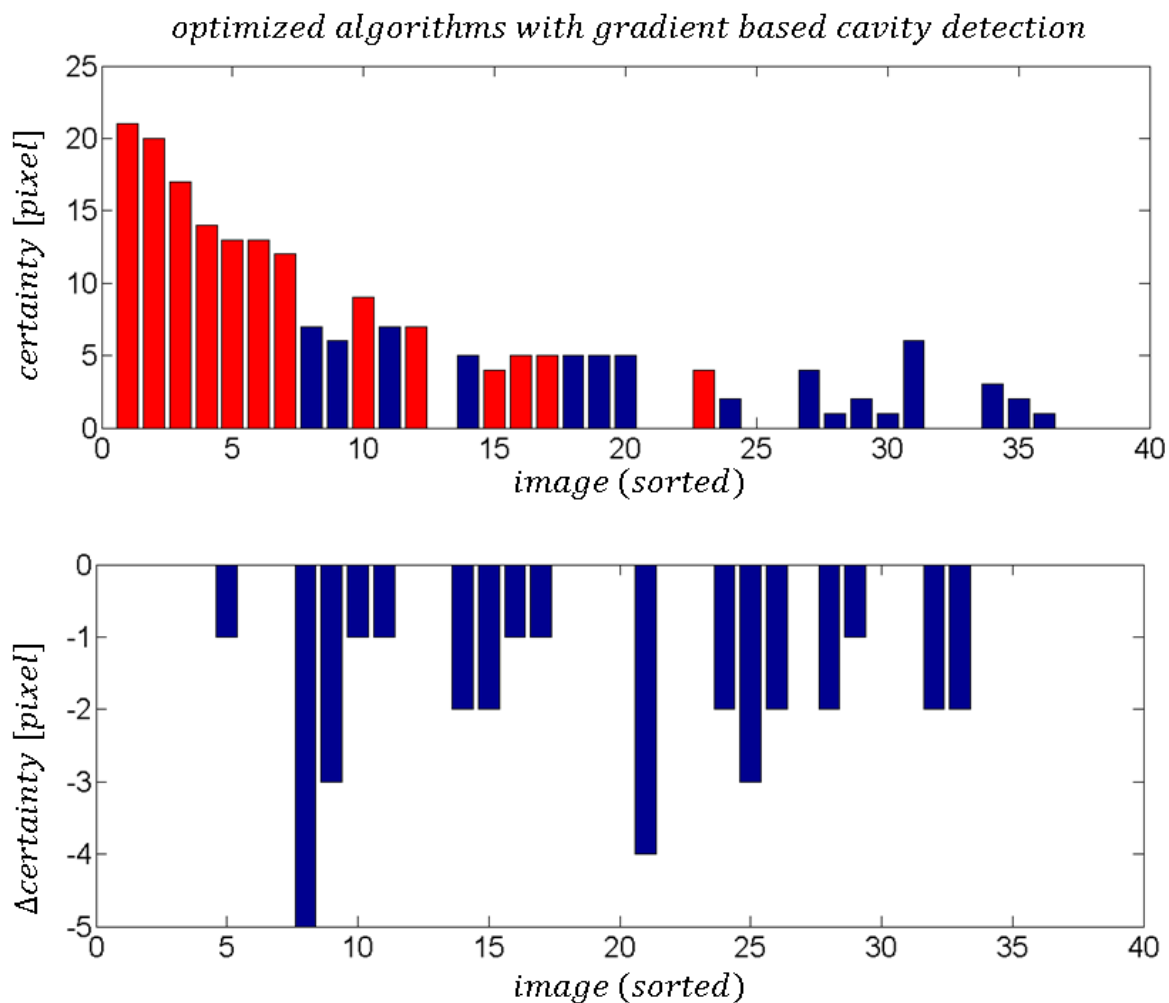


Figure 96: Certainty values for the optimized version with gradient based cavity detection (top) and difference to the optimized version with intensity based cavity detection (bottom).

9.2 Manual vs Numerical Rejection

To compare cases manually classified as good but automatically as reject, the results of the benchmark version with intensity based cavity detection will be used. In Figure 97 (page 155) different pearls are shown with the original X-ray image intensity in the first column. The numbers on the images correspond to the bar plots of the previous figures. Red numbers mark pearls classified by DRMM experts and by the automatic measurement as rejects, while blue numbers correspond to pearls classified automatically as rejects but as good by DRMM experts. The second column shows the segmented and calibrated image. The white dashed line in the images marks a distance of 0.8mm to the outer boundary. Cavities or a nucleus region that lies between the outer boundary and the white line correspond accordingly to

regions with a nacre thickness lower than $0.8mm$. The third column shows automatically detected outer and cavity boundaries in blue and the detected nucleus in black. In the fourth column pearl regions with an automatically detected nacre thickness lower than $0.8mm$ are colored in red. The first row shows the pearl with the largest rejection certainty. The nacre thickness is at any point clearly lower than the required $0.8mm$. The second row shows the pearl that corresponds to bar number 7 in the previous plots, one position before the first pearl classified manually as good but as a reject by the automatic measurement. Here as well the nacre thickness is at any point lower than the required $0.8mm$, another case of a rather obvious reject. The third and fourth rows show the first two pearls classified automatically as reject in contrary to the expert classification. In both cases it can be visually validated that larger regions of cavity boundaries lie outside the white line that marks the $0.8mm$ margin. Even with the gradient based cavity boundary refinement both pearls still are classified as rejects. While pearl number 8 (third row) is a rather obvious human misclassification, pearl number 9 illustrates the challenge of a manual classification when the nacre thickness lies close to $0.8mm$. In such cases the operator has not always enough time to analyze the boundaries in detail and instead judges intuitively. The next pearl (last row) is again a pearl manually as well as automatically classified as rejects.

Figure 98 (page 156) shows three reject examples that correspond to bars 18 to 20 with a certainty of 6 pixels in the proposed and 5 pixels in the optimized measurement. The first two examples illustrate a general challenge concerning the manual classification. It is likely that a DRMM expert recognizes that certain nacre regions of both pearls are smaller than $0.8mm$. The challenge is to estimate if those regions correspond to 20% of the complete boundary. Specifically for non-round pearls this is a non-trivial task. In those cases the automatic measurement has a clear advantage, as the percentage can be calculated quite precisely. The third row shows a pearl with nacre thickness close to $0.8mm$. Again a case that is difficult to estimate visually. The detail on the bottom shows that the nucleus or cavity boundary is still several pixels from the $0.8mm$ margin and hence the results are correct automatic classifications.

In Figure 99 (page 157) three reject examples with a certainty of 4 pixels are shown including the one manually classified as reject with the lowest certainty of all manually rejected pearls. Again a visual analysis showed that those pearls manually classified as good are correctly

detected as rejects with the automatic measurement. This means if a threshold for the certainty value is set to 4 pixels, all 13 manually rejected pearls can be identified along with 11 pearls manually classified as good but correctly classified as reject with the optimized automatic measurement.

9.3 Summary

The analysis of classification results obtained with the optimized version of the proposed measurement procedure showed that it is generally possible to automatically identify pearls that were manually classified as rejects. Additionally, several pearls that were manually classified as good were correctly detected as rejects, meaning the automatic measurement shows a higher degree of reliability. With the optimized version no false rejects due to false segmentation occurred. The application of the non-optimized measurement showed generally similar results but contained two false rejects due to false nucleus detection. The implementation of a self-evaluation after the nucleus detection is hence of importance to avoid false rejects.

As the X-ray images are a numerical approximation of the pearls, an automatic measurement even if highly optimized will always be associated with a certain degree of uncertainty. Additionally, the requirement of a maximum processing time of 1 second per image will at one point lead to a sacrifice of precision for processing speed. A suitable threshold for the proposed certainty value has accordingly to be defined. For the implementation of the non-optimized measurement as proposed a threshold that includes all manually rejected pearls can be set to 4 pixels. Anyhow, a general recommendation for such a threshold might be premature as the proposed algorithms will be further optimized and a possible threshold has to be adapted accordingly. Additionally, an analysis of imaging parameters and their influence on image quality will be done. A different image quality will likely result in a different certainty distribution which again will require an adaption of the threshold.

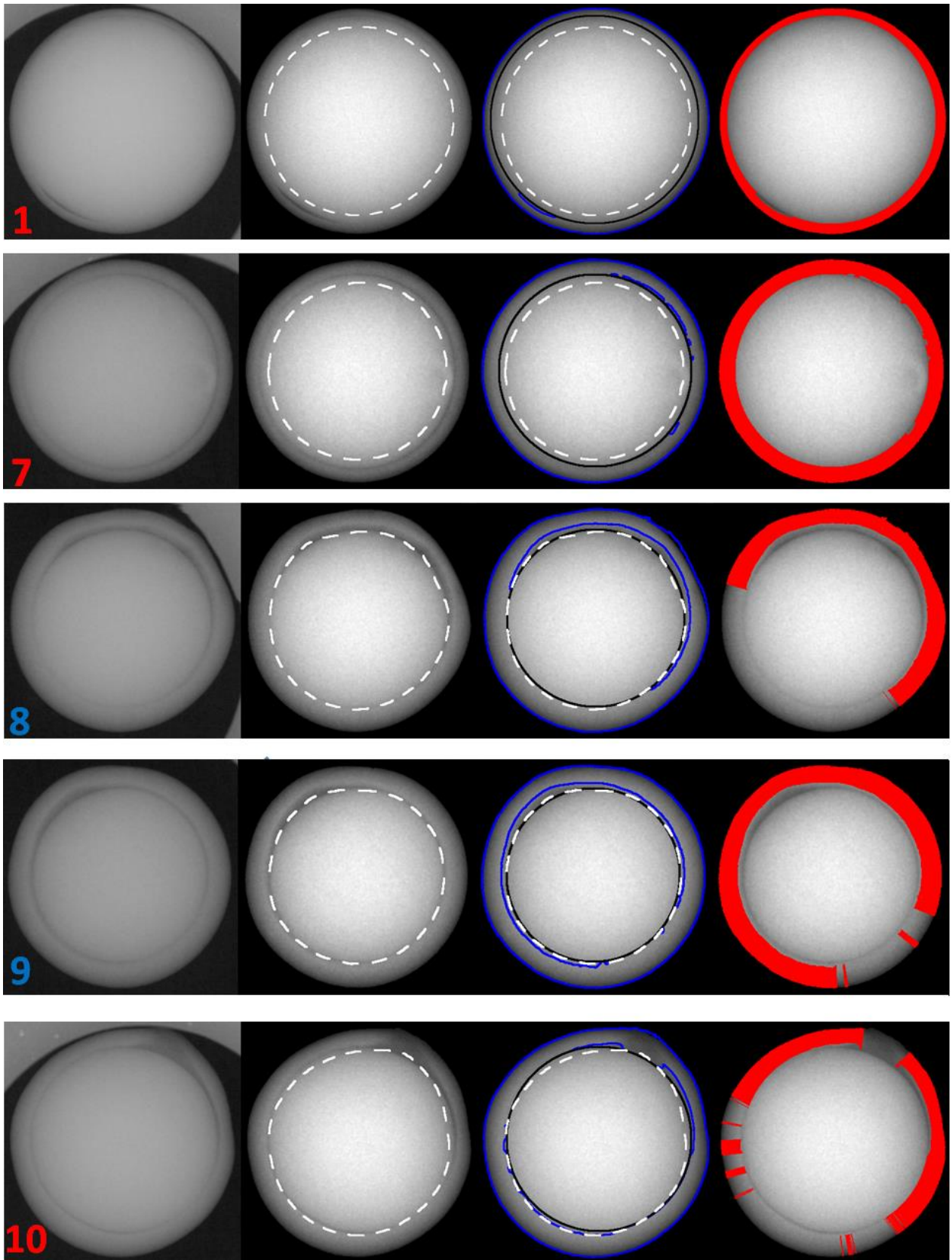


Figure 97: Automatic classification results. The numbers in the image corresponds to the bar plot in the previous Figures. Red numbers show pearls classified as rejects by DRMM experts.

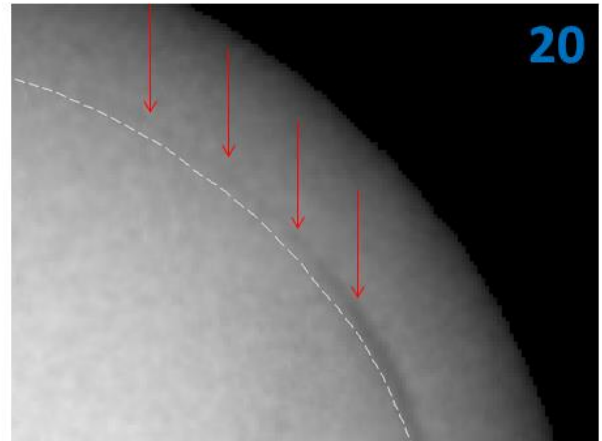
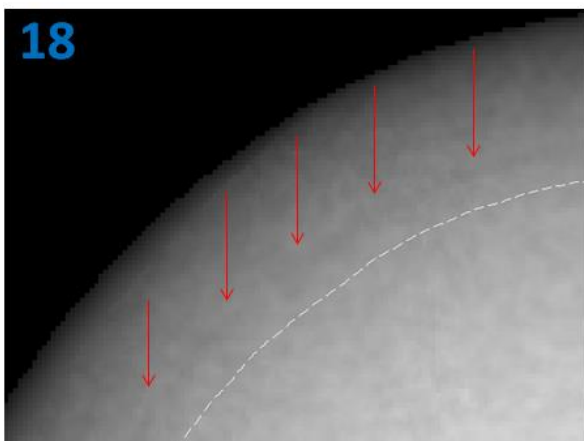
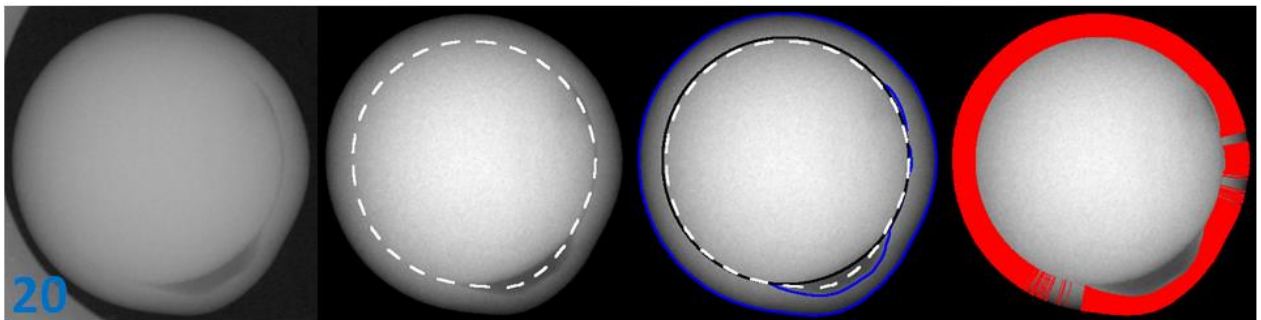
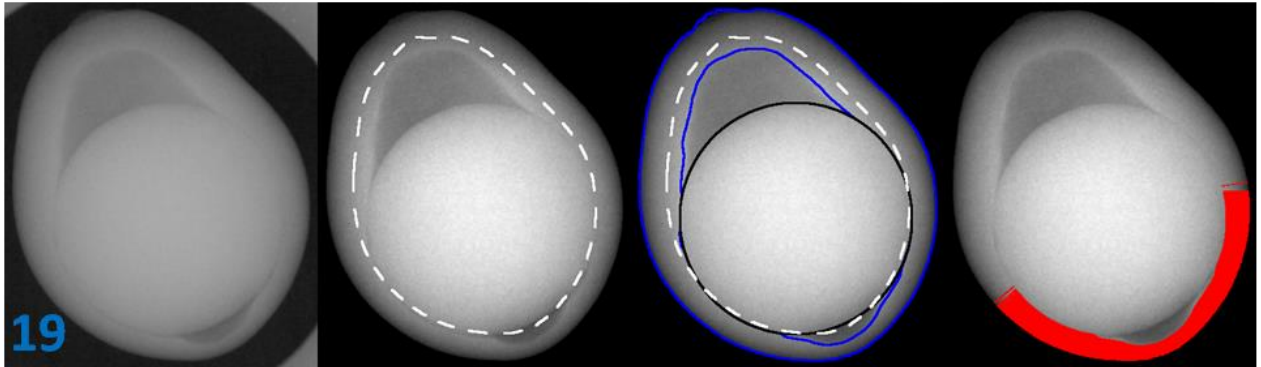
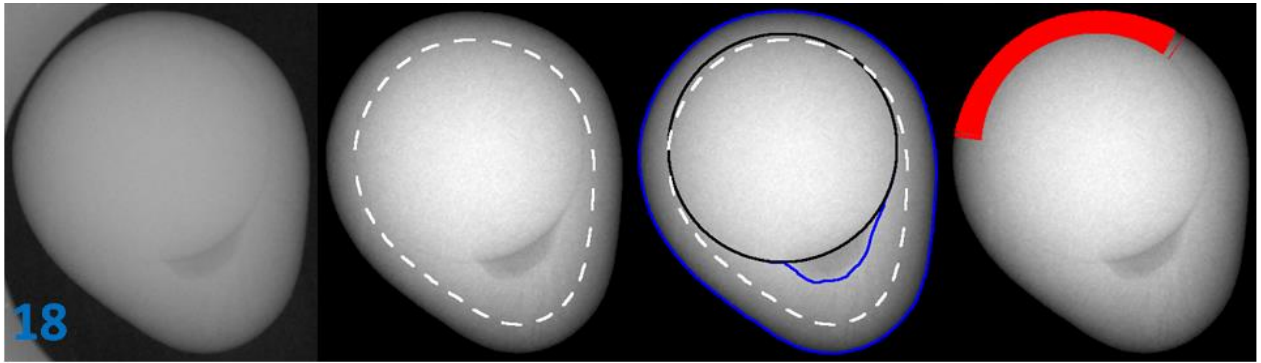


Figure 98: Further cases manually classified as good but as rejects by the automatic measurement. The red arrows point at regions with nacre thickness visibly lower than 0.8mm.

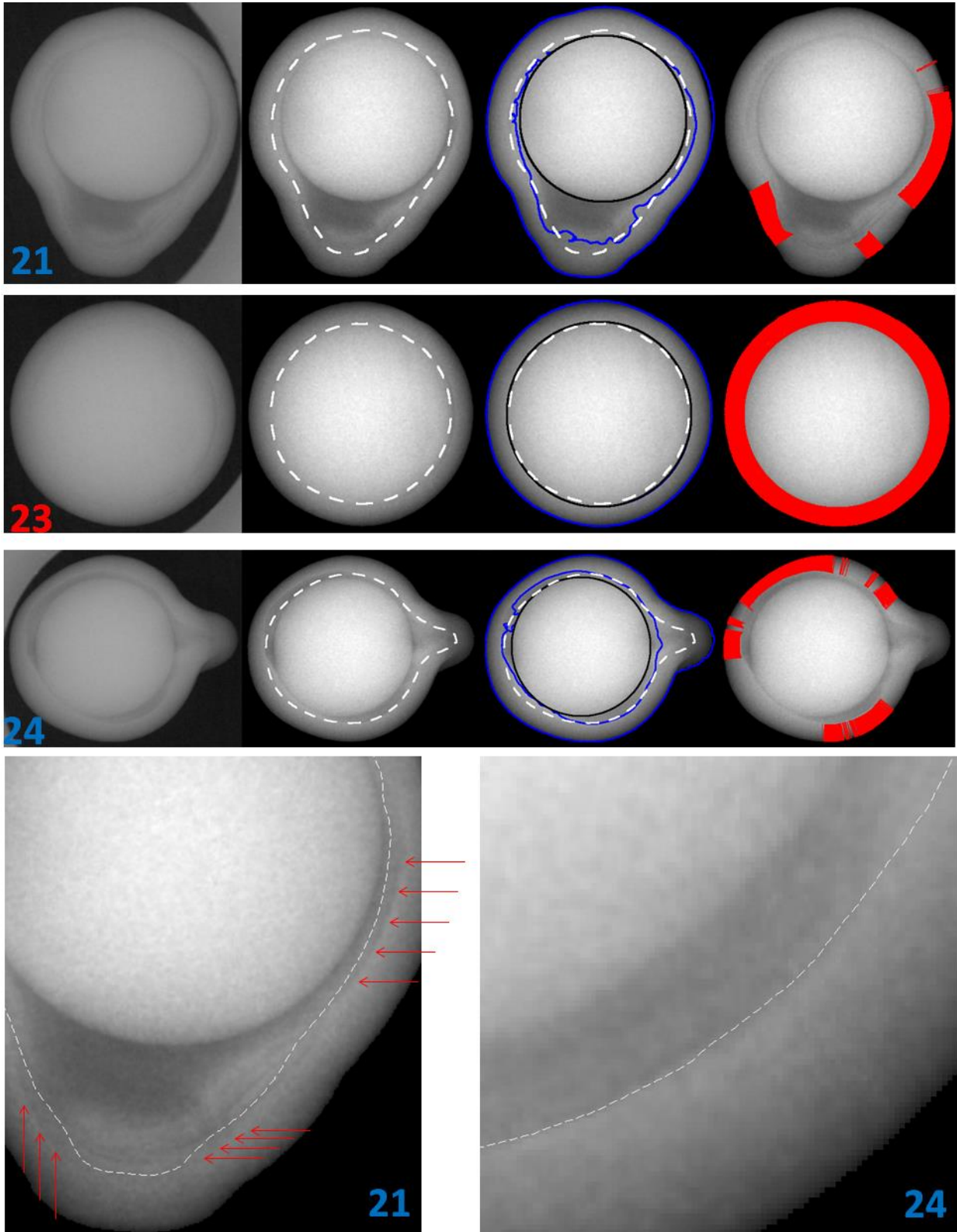


Figure 99: Reject pearls with a certainty of 4 pixels when the optimized measurement is applied. The red arrows point at regions with nacre thickness visibly lower than 0.8mm.

9.4 Processing Time

The processing time for each of the 3 segmentation steps (pearl segmentation, nucleus detection and cavity detection) and the processing time for the remaining steps (nacre profile calculation, classification and certainty calculation are measured together) together with the complete processing time is shown in Figure 100. Variabilities are caused by different pearl sizes and different nacre cavity configurations. The average processing time for the complete measurement is 0.7 seconds per image. This means the general requirement of a maximum processing time of 1 second per image is met. Additionally, possible optimizations can be added without surpassing the required processing time.

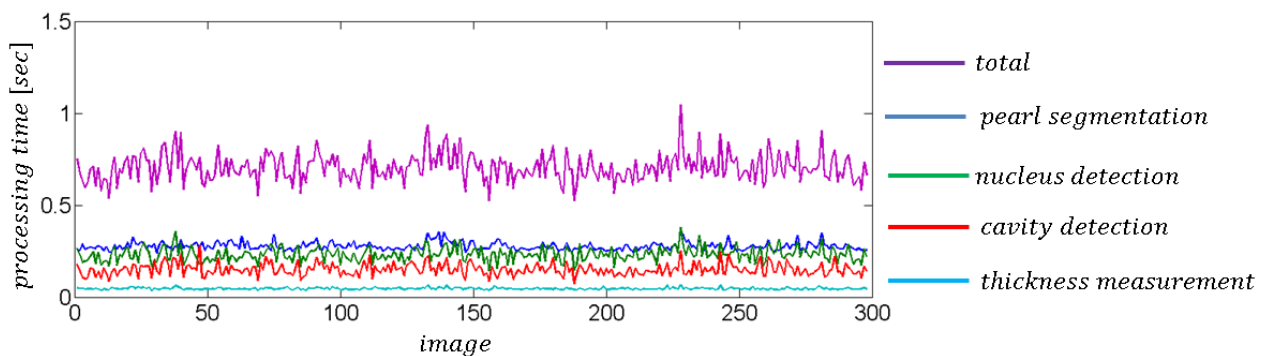


Figure 100: Processing time of the four processing steps and the total processing time for each test image.

processing step	pearl segmentation	nucleus detection	cavity detection	nacre thickness measurement	total
average processing time per image	0.27sec	0.23sec	0.15sec	0.05sec	0.7sec

Figure 101: Average processing time per image for the four processing steps and total processing time per image.

9.5 Optimization Possibilities

A priority should be to evaluate the possibilities of changing the support configuration as proposed in section 3.4.5. If the support material is partially replaced by polystyrene the background will be of uniform intensity. The pearl segmentation can hence be done by a single thresholding operation. This would not only reduce segmentation imprecisions but

leave more time for an improved nucleus and cavity detection. Second priority should be to improve the nucleus detection as both false rejects in the non-optimized version of the nacre thickness measurement are caused by false nucleus detections. The application of a self-evaluation after the nucleus detection together with additional treatment of detected nuclei with low boundary probability as proposed in section 4.4.5 eliminates those false detections. This procedure should hence be further investigated and validated with a new set of images. Concerning the method to detect cavities, an improvement might be possible by applying multiscale gradient calculation as mentioned in section 5.4.3. But, as the current approach is rather ‘pearl exporter friendly’ this would likely lead to an elevated amount of rejected pearls. Even if correctly measured, a significant elevation of rejected pearls could at one point become a ‘political’ issue, as the quality control is not meant to exclude as much pearls as possible from exportation rather than to regularize the market. An improvement of the cavity detection has hence to be reconciled with the control policies of the DRMM, as an application of the algorithm as proposed already leads to almost the double amount of rejected pearls in comparison to the human classification.

10 Prototype

For the purpose of further validating the presented method to automatically measure the nacre thickness, a prototype with a graphical user interface was developed (Figure 102, the functionality of numbered items is listed in Figure 103). The prototype was recently installed on the computer of an X-ray machine at the DRMM. The program runs independently from the image acquisition. This means images have to be taken prior to the measurement and stored in one folder. Afterwards the program is run and all images of the folder are processed. The results for each image are displayed and have to be validated by an operator of the DRMM. In case of a false boundary detection the operator has the possibility to manually measure the nacre thickness with a tool that corresponds to the software used for the current manual nacre thickness measurement. If this function is chosen the current image and the false detection results are stored automatically in a separate folder for further analysis. Images with pearls that are not visually evaluable can be identified so by the operator. Those images are stored as well automatically in another folder for further analysis. The minimal nacre thickness of the current pearl is displayed in *mm* as well as the percentage of the nacre with thickness greater or lower than 0.8mm . The automatic measurement results are visualized in two displays. One contains the original image with all detected boundaries for visual validation. The second one contains a visualization of the nacre profile with nacre regions thicker than 0.8mm shown in green and regions thinner than 0.8mm in red. After the evaluation of the complete folder all images of this folder can be deleted, as the storage of thousands of images per day would cause storage problems at a certain point. The two folders with false classifications and not evaluable pearls instead will be the basis for future improvements of the algorithms.

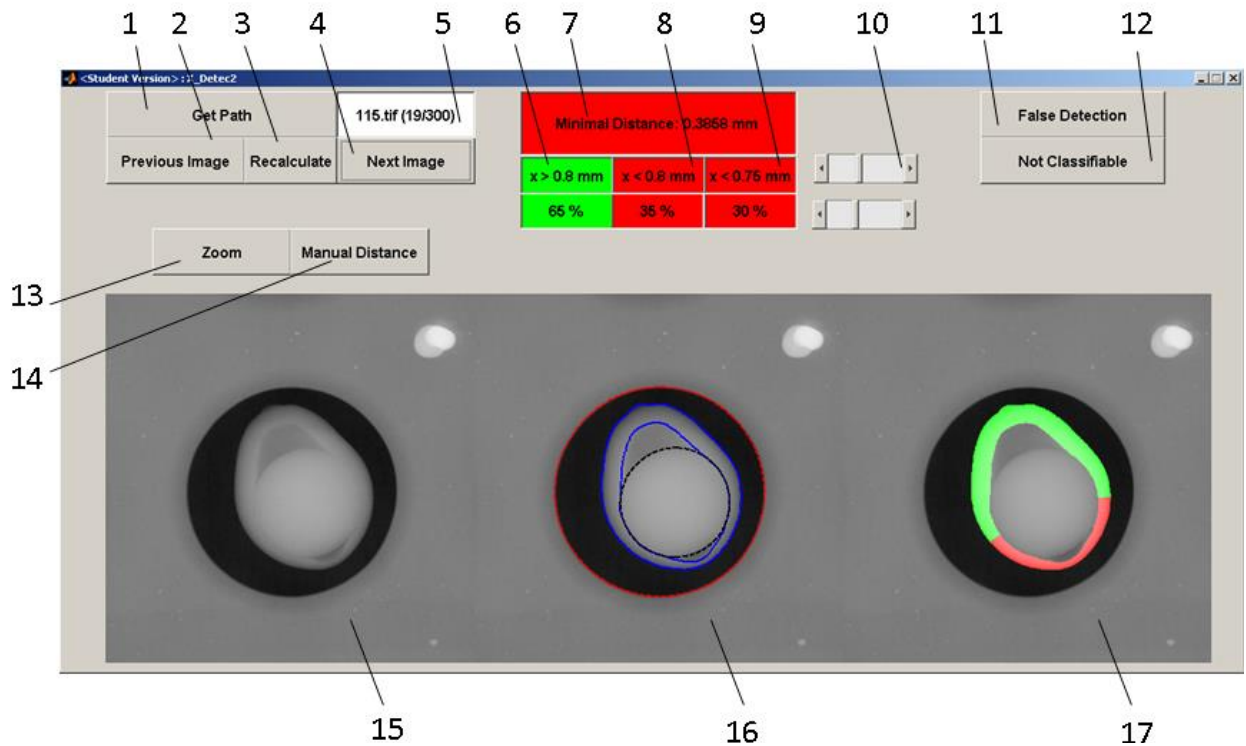


Figure 102: GUI of the prototype currently implemented at the DRMM.

item	function
1	choose image folder
2	process previous image
3	recalculate current image
4	process next image
5	current image name
6	display percentage of nacre with thickness greater 0.8mm
7	display minimal nacre thickness
8	display percentage of nacre with thickness lower 0.8mm
9	display percentage of nacre with thickness lower 0.75mm
10	controller to adjust minimal required nacre thickness in case of change
11	registration of false detections
12	registration of images that are not evaluable visually
13	zoom function for each displayed image
14	tool for manual nacre thickness measurement
15	display original image
16	display detected boundaries
17	display visualization of nacre thickness profile

Figure 103: Functionality of GUI (numbers correspond to Figure 102).

11 Conclusion

In the previous sections, a method to automatically measure the nacre thickness of Tahitian pearls out of X-ray images was presented. The developed approach was tested with a set of 298 X-ray images and the results compared to the manual classification of experts. It could be shown that it is possible to numerically evaluate the nacre thickness of Tahitian pearls out of X-ray images. The requisition of a maximum processing time of 1 second per image was met. The average processing time is at 0.7 seconds which leaves room for possible optimizations.

A general challenge is the large variety of pearl shapes, nuclei sizes and cavity configurations of Tahitian pearls. To address this challenge, the proposed algorithms use as little assumptions about pearl parameters as possible. For the pearl segmentation, only information of the support geometry is used. The nucleus detection is achieved by using logical gradient direction functions. For the cavity detection, the gradient direction is used to obtain boundaries at local intensity maxima. Accordingly, the algorithms are independent of the pearls size or the nacre thickness in direction of the X-ray beam and potential superposition of cavities.

Negative boundary discrepancies that led to a thinner nacre thickness are mainly caused by the smoothing process to delete artefacts caused by the pearl segmentation and false nucleus detections. Here only two false nucleus detections had a significant influence on the general pearl classification. Optimization possibilities were proposed that, when applied, reduced the amount of two false rejects to zero.

Several pearls were manually classified by the experts of the DRMM as good but as rejects by the automatic measurement. A visual analysis showed that the automatic classification is correct.

In general it can be stated that an automatic nacre thickness measurement is suitable to accelerate the obligatory quality control of Tahitian pearls deemed for exportation as well as it is more reliable in means of accuracy compared to the human evaluation.

12 Future Work

As mentioned, a real validation of the numeric nacre thickness measurement can only be done by cutting the measured pearls and compare the detected boundaries to the real internal pearl profile. As the permission to do so with some of the pearls owned by the DRMM was granted, such an analysis will be done in the near future. Additionally, the proposed optimization possibilities will be further investigated and tested with new sets of X-ray images.

While the presented work concerned the processing of X-ray images of Tahitian pearls, next steps for a complete automatization of the nacre thickness measurement concern as well the image acquisition. Possibilities of an automatized image acquisition of a complete support have to be investigated on-site at the DRMM and the suitability of a support with alternative material configuration has to be tested. Additionally the parametrization of the image acquisition has to be analyzed. Parameters of interests are the initial X-ray intensity and its influence on the image structure and quality and the internal image averaging for noise reduction and its influence on the image acquisition speed. Afterwards the possibilities of how to integrate the proposed image processing into an automated image acquisition process have to be investigated.

On a longer term a 3-dimensional nacre thickness profile measurement is aimed at. Here, the technical possibilities of rotating the pearls within the X-ray machine to acquire X-ray images at different angles have to be analyzed. Afterwards, suitable algorithms to reconstruct the 3-dimensional pearl profile out of the acquired images have to be developed. Finally, the technical possibilities to route the pearls into the X-ray machines and to automatically sort them after the numeric nacre thickness measurement have to be analyzed.

List of Figures

Figure 1: Work station for nacre thickness evaluation at the DRMM (left) and one of the supports in which 300 pearls are placed for X-raying (right).	49
Figure 2: A detail of the support filled with pearls (left) and an X-ray image of Tahitian pearls (right) with a typical zoom used for manual nacre thickness evaluation at the DRMM (pearls of both images do not match).....	50
Figure 3: Blank nucleus (left), bisected Tahitian pearl (middle, KRZ2010) and X-ray image of a Tahitian pearl that is similar to the bisected one (right).	51
Figure 4: Different nacre configurations of Tahitian pearls.	51
Figure 5: Two images of the set used to create the image processing tools for the automated nacre thickness evaluation.....	53
Figure 6: Two images of the set used to test the developed algorithms.	54
Figure 7: Two keshi pearls that were sorted out of the test image set.....	54
Figure 8: Intensity distribution of the support left to the white lines in the two images shown in the graph next to the respective image.	55
Figure 9: Three types of human evaluation results. First row shows three examples of rejected pearls, second row shows three examples of not evaluable pearls, last row shows three examples of good pearls.	56
Figure 10: Workflow of the segmentation of the pearl.	58
Figure 11: Schema of the developed iterative approach to detect the nucleus.	59
Figure 12: Region growing procedure to detect cavity boundaries.	59
Figure 13: Obtained boundaries after applying the three segmentation steps (left) and schematic representation, of the nacre thickness measurement in direction of the inside pointing normal vectors of the detected outer boundary (blue arrows on the right). The graph on the top right is the obtained nacre thickness profile in <i>mm</i>	60
Figure 14: Automatically measured nacre thickness profile of a Tahitian pearl (left). The regions of the profile with a thickness lower than 0.8mm and the corresponding regions of the X-rayed pearl are marked in red	61
Figure 15: Representation of the certainty calculation. The graph on the left shows the automatically calculated nacre thickness profile in <i>mm</i> blue, and the by 9 pixels shifted profile in black. The graph on the right shows the percentage of nacre thickness lower than 0.8mm at each boundary shift from 0 to 9 pixels.....	61
Figure 16: Rejection certainty values of the automated detection of pearls with 20% nacre thickness lower than 0.8mm. Red bars correspond to pearls manually classified as rejects by DRMM experts.	63

Figure 17: Results of the approach proposed in LEI09 (left) based on the assumption that the pearl boundary can be described by a circle (left). On the right two typical examples of Tahitian pearls are shown for which this assumption does not hold.	65
Figure 18: A detail of the support showing a borehole with bevel (left two images). On the right is the according X-ray image with image intensity distribution along the white line through the center of the borehole.	67
Figure 19: A pearl located completely within the borehole (left) and a pearl surpassing it completely (right).	68
Figure 20: Two details of areas in which the pearls outer boundary lies within the bevel of the borehole.	68
Figure 21: Superposition of intensity distributions of pearl and background.	69
Figure 22: Details of the original X-ray image (left) and of the original image superposed with all edges detected with a 3x3 Sobel operator (right).	71
Figure 23: Schema of pearl boundary gradient directions (blue arrows) and borehole and bevel gradient directions (red arrows).	72
Figure 24: Example of pearl segmentation by subtraction of the synthetic background B from the original image I.	73
Figure 25: Example of pearl segmentation with a synthetic background in combination with physical properties of X-ray attenuation.	74
Figure 26: X-ray image of a nucleus (left), its radial intensity profile (middle) and the profile averaged over all angles (right).	75
Figure 27: Image calibration process.	76
Figure 28: Semi 3D nacre thickness profile (right) for a near-round pearl.	77
Figure 29: X-ray image with a pearl partially surpassing the borehole (left), the radial intensity profile of the borehole and the profile averaged over all angles (right). ...	77
Figure 30: Average radial intensity profile of the borehole (left) its standard deviation (middle) and a visualization of negative (grey) and positive (white) discrepancies to the average profile (right).	78
Figure 31: Workflow of the segmentation process.	79
Figure 32: Different types of segmentation artefacts.	80
Figure 33: Segmented image and region of artefacts.	81
Figure 34: Artefact cleaning procedure.	81
Figure 35: Largest negative discrepancies between segmentation result and desired result of the training set.	84
Figure 36: Largest negative discrepancies between segmentation result and desired result of the training set.	85
Figure 37: Largest positive discrepancies between segmentation result and desired result.	86

Figure 38: Procedure of the precision measurement.	87
Figure 39: Average deviation from optimal boundary and standard deviation of the detected boundary of each image in a -15 to +15 pixel range (top) and in a range from -15 to 0 pixels (bottom) for the test set.	88
Figure 40: Average deviation from optimal boundary and standard deviation of the detected boundary of each image in a -15 to +15 pixel range (top) and in a range from -15 to 0 pixels (bottom) for pearls of the training set that surpass the borehole.	88
Figure 41: Examples of threshold related artefacts.	89
Figure 42: Processing time for the three sub steps of the proposed segmentation algorithm. .	90
Figure 43: Average processing time in seconds per image for the proposed approach and for standard algorithms.	90
Figure 44: Three examples of damaged boreholes.	91
Figure 45: A linear imitation of the borehole geometry with polystyrene and the resulting X-ray image.	93
Figure 46: image side length (top) and root of the amount of pearl pixels (bottom) in the segmented and cropped images.	94
Figure 47: Round pearls with different nucleus visibility	95
Figure 48: Three example of partially visible nuclei.....	95
Figure 49: Superposition effect of rotation symmetric nucleus profile and non-rotation symmetric nacre thickness.....	96
Figure 50: Application of the Sobel operator with different filters size and amount of remaining pixels after non-maximum suppression.....	98
Figure 51: Schema of the basic concept of the circular Hough Transform.....	99
Figure 52: Schema of the idea of our approach.....	101
Figure 53: Circle movement defined by intensity based probability	102
Figure 54: Intensity based movement at three iteration stages.....	103
Figure 55: Schematic representation of the pearl thickness profile in X-ray direction in the case of cavity occurrence.....	104
Figure 56: Gradient based movement at three iteration stages.....	105
Figure 57: Effect of the implementation of a sensitivity measurement.....	107
Figure 58: Moving in relation to radius increment.....	108
Figure 59: Values for crucial parameters for the proposed algorithm to detect the nucleus. .	109
Figure 60: Pseudocode of the proposed algorithm for the detection of the nucleus. .	110
Figure 61: Precision of the proposed algorithm in comparison to a brute force approach. Discrepancies greater than 5 pixels are set to 5 for better clarity.....	111

Figure 62: Detected circle with our approach (red) and with the Hough transform (white). The image on the bottom shows the maxima of the accumulation matrix of the Hough transform.....	112
Figure 63: Result improvement by emphasis on gradient based circle movement.	115
Figure 64: Result improvement by purely intensity based circle movement.	116
Figure 65: False detection due to superposition of cavity gradient and nucleus boundary. ...	116
Figure 66: False detection due to weak or no nucleus boundaries.	117
Figure 67: Two pearls classified as not evaluable, but a detailed visual analysis showed boundary evidence. Red arrows point to the regions at which the nucleus boundary is visible.	118
Figure 68: Nuclei of different visibility (left images), together with the first nine circles determined by the nine largest entries of the accumulation matrix of the Hough transform (right).	119
Figure 69: Sorted maximum nucleus boundary probability for all test images (top) and corresponding maximum absolute radius/center discrepancy (bottom, discrepancies greater than 5 pixels are set to 5).	121
Figure 70: processing time for the detection of the nucleus with our algorithm.	122
Figure 71: average processing time per image of our algorithm and standard algorithms. The red region in the image on the right contains 100 pixels. The processing time of the traditional Hough transform with such a small amount of information already exceeds the average processing time of our algorithm.	123
Figure 72: detection results of an improved version of the algorithm.	124
Figure 73: Different cavity formations.	127
Figure 74: Details of cavities with weak boundary gradients.	128
Figure 75: Cavity edge detection with the derivative of the gradient vector field.	131
Figure 76: Region growing in gradient direction with different gradient filter size.	132
Figure 77: Effect of a more ample region growing rule.	133
Figure 78: Effect of not treated and treated segmentation artifacts on the region growing process.	134
Figure 79: Pseudocode for the segmentation of cavities.	135
Figure 80: Schema of the precision evaluation range.	136
Figure 81: Precision of the detected cavity boundaries.	136
Figure 82: Largest discrepancies according to a visual analysis.	136
Figure 83: Images with negative precision evaluation value.	138
Figure 84: Difference between intensity based and gradient based cavity boundary.	139

Figure 85: Schematic representation of the thickness profile $d(r)$ of material with cavity (cavity in grey).	140
Figure 86: Processing time for the cavity detection for each test image.	140
Figure 87: Schematic representation of the nacre thickness measurement in normal vector direction from the detected outer boundary of the pearl.	142
Figure 88: Obtained nacre thickness profile of the pearl shown in Figure 87.	143
Figure 89: Pseudocode for the nacre thickness profile measurement.	143
Figure 90: Automatically measured nacre thickness profile of a Tahitian pearl (left). The regions of the profile with a thickness lower than 0.8mm and the corresponding regions of the X-rayed pearl are marked in red.	144
Figure 91: Representation of the calculated certainty value.	145
Figure 92: Certainty value for pearls detected as to reject with the proposed algorithms (top) and with an optimized (bottom). Pearls classified manually as to reject by experts of the DRMM are marked in red.	147
Figure 93: Certainty difference between proposed and optimized version of the nacre thickness measurement.	147
Figure 94: False rejects obtained with the proposed classification.	149
Figure 95: Pearls classified as rejects but with different certainty between proposed and optimized algorithms.	150
Figure 96: Certainty values for the optimized version with gradient based cavity detection (top) and difference to the optimized version with intensity based cavity detection (bottom).	152
Figure 97: Automatic classification results. The numbers in the image corresponds to the bar plot in the previous Figures. Red numbers show pearls classified as rejects by DRMM experts.	155
Figure 98: Further cases manually classified as good but as rejects by the automatic measurement. The red arrows point at regions with nacre thickness visibly lower than 0.8mm.	156
Figure 99: Reject pearls with a certainty of 4 pixels when the optimized measurement is applied. The red arrows point at regions with nacre thickness visibly lower than 0.8mm.	157
Figure 100: Processing time of the four processing steps and the total processing time for each test image.	158
Figure 101: Average processing time per image for the four processing steps and total processing time per image.	158
Figure 102: GUI of the prototype currently implemented at the DRMM.	161
Figure 103: Functionality of GUI (numbers correspond to Figure 102).	161

Bibliography

- ABB99 Abbott, J. A. (1999). *Quality measurement of fruits and vegetables*. *Postharvest Biology and Technology*, 15(3), 207-225.
- ADA94 Adams, R., & Bischof, L. (1994). *Seeded region growing*. *IEEE Transactions on pattern analysis and machine intelligence*, 16(6), 641-647
- AYA06 Ayala-Ramirez, V., Garcia-Capulin, C. H., Perez-Garcia, A., & Sanchez-Yanez, R. E. (2006). *Circle detection on images using genetic algorithms*. *Pattern Recognition Letters*, 27(6), 652-657
- BAS02 Basu, M. (2002). *Gaussian-based edge-detection methods-a survey*. *IEEE Transactions on Systems, Man, and Cybernetics, Part C*, 32(3), 252-260.
- BEC14 Becker, M., & Magnenat-Thalmann, N. (2014). *Deformable models in medical image segmentation* (pp. 81-106). Springer London.
- CAN86 Canny, J. (1986). *A computational approach to edge detection*. *Pattern Analysis and Machine Intelligence, IEEE Transactions on*, (6), 679-698.
- CHA11 Chattopadhyay, K., Basu, J., & Konar, A. (2011). *An efficient circle detection scheme in digital images using ant system algorithm*. arXiv preprint arXiv:1106.0962.
- CHE05 Chen, Y., Ee, X., Leow, W. K., & Howe, T. S. (2005). *Automatic extraction of femur contours from hip x-ray images*. In *Computer Vision for Biomedical Image Applications* (pp. 200-209). Springer Berlin Heidelberg.
- COH91 Cohen, L. D. (1991). *On active contour models and balloons*. *CVGIP: Image understanding*, 53(2), 211-218.
- CUE12 Cuevas, E., Oliva, D., Zaldivar, D., Pérez-Cisneros, M., & Sossa, H. (2012). *Circle detection using electro-magnetism optimization*. *Information Sciences*, 182(1), 40-55.
- CUE12b Cuevas, E., Osuna-Enciso, V., Wario, F., Zaldívar, D., & Pérez-Cisneros, M. (2012). *Automatic multiple circle detection based on artificial immune systems*. *Expert Systems with Applications*, 39(1), 713-722.
- DAS10 Dasgupta, S., Das, S., Biswas, A., & Abraham, A. (2010). *Automatic circle detection on digital images with an adaptive bacterial foraging algorithm*. *Soft Computing*, 14(11), 1151-1164
- DUD72 Duda, R. O., & Hart, P. E. (1972). *Use of the Hough transformation to detect lines and curves in pictures*. *Communications of the ACM*, 15(1), 11-15.
- KAS88 Kass, M., Witkin, A., & Terzopoulos, D. (1988). *Snakes: Active contour models*. *International journal of computer vision*, 1(4), 321-331

- KAU15 Kaur, N., & Jindal, G. (2013). *A survey of K means Clustering with modified gradient magnitude region growing technique for lesion segmentation*. International Journal of Innovations in Engineering and Technology (IJJET), 2(2).
- KRZ10 Krzemnicki, M. S., Friess, S. D., Chalus, P., Hänni, H. A., & Karampelas, S. (2010). *X-ray computed microtomography: distinguishing natural pearls from beaded and non-beaded cultured pearls*. Gems and Gemology, 46(2), 128.
- LEI09 Lei, M., Sun, Y., Wang, D., & Li, P. (2009). *Automated thickness measurements of pearl from optical coherence tomography images*. In Hybrid Intelligent Systems, 2009. HIS'09. Ninth International Conference on (Vol. 1, pp. 247-251). IEEE.
- LIU13 Liu, J., Tian, X. L., & Sun, Y. K. (2013). *Pearl Thickness Measurements from Optical Coherence Tomography Images*. In Applied Mechanics and Materials (Vol. 421, pp. 415-420).
- LOY02 Loy, G., & Zelinsky, A. (2002, May). *A fast radial symmetry transform for detecting points of interest*. In European Conference on Computer Vision (pp. 358-368). Springer Berlin Heidelberg.
- MAR80 Marr, D., & Hildreth, E. (1980). *Theory of edge detection*. Proceedings of the Royal Society of London B: Biological Sciences, 207(1167), 187-217.
- NEE07 Neethirajan, S., Jayas, D. S., & White, N. D. G. (2007). *Detection of sprouted wheat kernels using soft X-ray image analysis*. Journal of Food Engineering, 81(3), 509-513.
- PAN07 Pan, Z., & Lu, J. (2007). *A Bayes-based region-growing algorithm for medical image segmentation*. Computing in Science & Engineering, 9(4), 32-38
- POH01 Pohle, R., & Toennies, K. D. (2001). *Segmentation of medical images using adaptive region growing*. In Medical Imaging 2001 (pp. 1337-1346). International Society for Optics and Photonics.
- PRA14 Pratondo, A., Ong, S. H., & Chui, C. K. (2014). *Region Growing for Medical Image Segmentation Using a Modified Multiple-seed Approach on a Multi-core CPU Computer*. In The 15th International Conference on Biomedical Engineering (pp. 112-115). Springer International Publishing.
- PRE70 Prewitt, J. M. (1970). *Object enhancement and extraction*. Picture processing and Psychopictorics, 10(1), 15-19.
- SCH96 Schatzki, T. F., Haff, R. P., Young, R., Can, I., Le, L. C., & Toyofuku, N. (1996, December). *Defect detection in apples by means of x-ray imaging*. In Photonics East'96 (pp. 176-185). International Society for Optics and Photonics.

- SCH97 Schatzki, T. F., Haff, R. P., Young, R., Can, I., Le, L. C., & Toyofuku, N. (1997). *Defect detection in apples by means of X-ray imaging*. Transactions of the ASAE, 40(5), 1407-1415
- SOB68 Sobel, I. (1968). *An Isotropic 3x3 Image Gradient Operator*. Presentation at Stanford A.I. Project 1968 02/2014
- STO13 Stolojescu-Crişan, C., & Holban, Ş. (2013). *A comparison of X-Ray image segmentation techniques*. Advances in Electrical and Computer Engineering Engineering, 13(3).
- SUN10 Sun, Y., & Lei, M. (2010). *Automated thickness measurements of nacre from optical coherence tomography using polar transform and probability density projection*. In Intelligent Signal Processing and Communication Systems (ISPACS), 2010 International Symposium on (pp. 1-4). IEEE.
- SZA15 Szafarczyk, M. (Ed.). (2012). *Automatic supervision in manufacturing*. Springer Science & Business Media.
- TUY08 Tuytelaars, T., & Mikolajczyk, K. (2008). *Local invariant feature detectors: a survey*. Foundations and Trends® in Computer Graphics and Vision, 3(3), 177-280.
- XU13 Xu, G., Li, X., Su, J., Zhao, J., & Pan, H. (2013). *Circle recognition and parameter measurement methods with the similarity constraint on the slope curve of the tangent lines to a contour*. Optik-International Journal for Light and Electron Optics, 124(16), 2463-2467.
- XU97 Xu, C., & Prince, J. L. (1997). *Gradient vector flow: A new external force for snakes*. In Computer Vision and Pattern Recognition, 1997. Proceedings., 1997 IEEE Computer Society Conference on (pp. 66-71). IEEE.
- YUE99 Yuen, H. K., Princen, J., Illingworth, J., & Kittler, J. (1990). *Comparative study of Hough transform methods for circle finding*. Image and vision computing, 8(1), 71-77.

Part II

Color Classification

Content

1	Introduction	175
1.1	Manual Classification	175
1.2	Data Acquisition	177
1.3	Theoretical Work on Normalized <i>rgb</i> Histograms	178
1.4	Experiments	178
1.5	Results	179
1.6	Structure of Part II	181
2	Related Work	182
3	On Normalized <i>rgb</i> Histogram Binning	184
3.1	The Normalized <i>rgb</i> Color Space	185
3.2	Histogram Calculation	186
3.2.1	One-Dimensional Data Distribution	186
3.2.2	Multidimensional Data Distributions	189
3.3	Standard Application	191
3.4	Formalizing Normalized <i>rgb</i> Histogram Calculation	194
3.5	Topology of the Normalized <i>rgb</i> Color Space	199
3.6	Summary	202
4	Data Acquisition	204
4.1	Image Acquisition and Preprocessing	204
4.2	Human Classification	206
5	Classification Method	210
5.1	Data Set Splitting	211
5.2	Feature Configuration	213
5.3	ANN Configuration	217
5.4	Training and Evaluation Values	218
5.4.1	Qualitative Analysis	220
5.4.2	Quantitative Analysis	220
5.5	Summary	220
6	Results and Discussion	222
6.1	Qualitative Analysis	222
6.1.1	Channel Redundancy	222
6.1.2	Influence of Histogram Orientation per Agent	223
6.1.3	Influence of Histogram Orientation per Color Class	225
6.1.4	Equidistant Binning vs Topological Binning	229
6.1.5	Summary	231
6.2	Quantitative Analysis	231
6.2.1	Accuracy Range	232
6.2.2	Generalization Capabilities	234
6.2.3	Preliminary Maximum Classification Results	235

7 Conclusion	236
8 Future Work.....	238
List of Figures	239
Bibliography.....	242

1 Introduction

The Tahitian pearl is a natural gem that is cultivated in black-lip pearl oysters (*Pinctada margaritifera*) in the lagoons of French Polynesia. Compared to other famous pearls sold on the international market, such as the Japanese Akoya pearl or the Chinese Freshwater pearl that appear mostly in white or yellow tones, the Tahitian pearl comes in a large variety of colors. Typical hues that might appear solely or in combination are blue, green, yellow, white, turquoise or rose. Additionally, any shade of gray from pure white to pure black (as well as black and white together, see bottom left in Figure 1) can appear, as well as the intensity of hues themselves can vary between for example light blue and dark blue. This variety is one of the unique and desired features of Tahitian pearls.

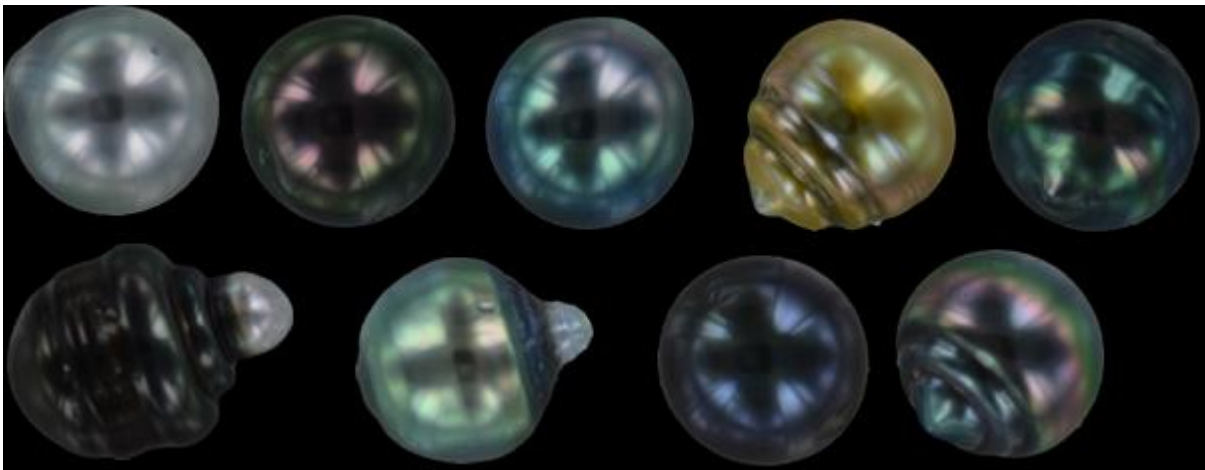


Figure 1: Tahitian Pearls of different and partially multiple colors.

1.1 Manual Classification

The color variety causes several challenges when it comes to classifying pearls according to their color. A classification is generally needed for multiple reasons. The first reason is that the price of each pearl depends, besides other quality parameters such as its form, size and luster, on its color. Pure bright blue pearls or pearls with a bright rose overtone are more seldom than for example greenish or gray pearls and therefore more expensive. Accordingly each time a pearl is sold, a certain kind of color classification is necessary to estimate its price.

A second reason is that jewelry made out of pearls with similar colors is esthetically appealing. Earrings are made almost exclusively with pearls of similar color. A whole set of

jewelry (earrings, necklace and bracelet) with all pearls of similar color can be sold for a higher price than if each item contained pearls of similar colors but differing from those of the other items. Accordingly, a set of pure pearls of similar color can be more expensive when sold as whole, as if they were sold separately. It means here, a classification is made not only based on the appearance of a single pearl but as well based on color similarity.

A third reason concerns research projects conducted in French Polynesia aiming to find correlations between pearl cultivation parameters and pearl quality. The goal is to understand why a certain pearl has a certain appearance; and if it is known to possibly influence the cultivation procedure to increase the production of high-valued pearls. To mathematically relate the color of a pearl to its cultivation parameters, its color has to be somehow classified as well.

Currently, the color classification of Tahitian pearls for whatever purpose is done manually by simply looking at a pearl, meaning based on the perception of the beholder and inspection conditions (light sources, view angle, etc.). It is accordingly possible that a pearl sold in one place might have a different price from a very similar pearl sold in another place. Especially for non-experts, this purely perceptual price generation is difficult to comprehend, which causes uncertainties not favorable for this very important business branch. Furthermore, a subjective classification as basis for the mentioned correlation analysis between cultivation parameters and pearl quality is questionable.

In summary, color classification of Tahitian pearls is absolutely necessary for trading and processing pearls as well as to gain further knowledge on the pearl formation itself. But a subjective classification based on the perception of the beholder and inspection conditions is not ideal. The goal of our project is accordingly to create a method suitable to classify the color of a pearl on a more objective basis while still relating to the human perception. The general approach is to use color images of pearls, taken under fixed acquisition parameters, and classify extracted color features with an Artificial Neural Network (ANN). The main focus of our work is on determining suitable color features. The main idea is that the more precise the features describe the pearls color in respect of human perception, the better the resulting classification results.

1.2 Data Acquisition

Color images of 150 Tahitian pearls, each photographed from 3 different view angles, were obtained. All images were taken with a NIKON D-7000 with AF-S NIKKOR 18-55mm objective. All images have a pixel resolution of 6000x4000 pixels and are of uncompressed TIFF format. All 150 pearls were classified in 8 predefined color classes by 7 different employees of IFREMER that work in research projects concerning the cultivation of Tahitian pearls and the nature of their genesis. The 8 predefined classes are eggplant (dark purple), white, blue, champagne (cream), gray, yellow, peacock and green (7 examples assigned by majority vote of all 7 agents for 7 classes are shown in Figure 2).

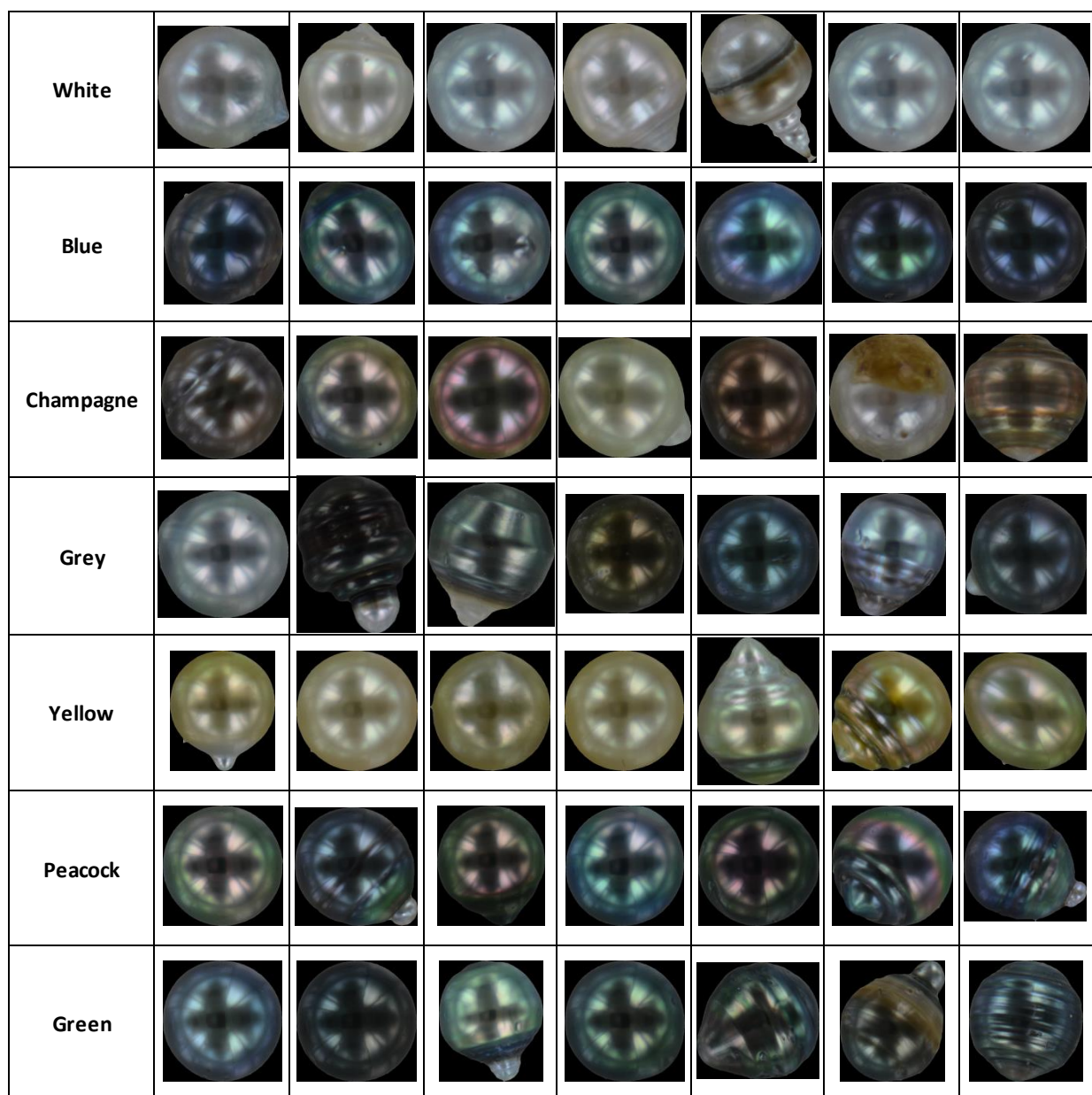


Figure 2: Example images for 7 of the 8 used color classes.

1.3 Theoretical Work on Normalized *rgb* Histograms

In color image processing based on human color perception, the normalized *rgb* color space is often applied, as it combines the human perceptual color model with the biological model of color processing in the human retina. In many approaches, the normalized *rgb* color space is used in combination with histogram binning. The choice of which color channels are binned, or more generally, which histogram orientation is applied, is made either based on empirical observations or even based on false mathematical assumptions.

One of the main contributions of this part of the thesis is the formalization of normalized *rgb* histogram calculation. The choice of which chromatic index to bin, is reduced to a single parameter, namely the perceptual parameter Hue. In contrary to the few histogram orientations that are used in the literature, the derived formula shows that theoretically infinite possibilities of chromatic index generation exist, which means the possibilities of feature generation with normalized *rgb* histogram binning are theoretically infinite. To explore the huge range of new possibilities, extensive experiments were conducted by using different histogram orientations for feature generation to classify Tahitian pearls based on human perception with Artificial Neural Networks. Additionally, a binning strategy that respects the topology of the normalized *rgb* color space is proposed and its application included in the experiments.

1.4 Experiments

As a major focus of this work lies on feature generation, not only the majority vote of all 7 human classifications was used, but the separate votes of each of the 7 agents that classified the pearls (Figure 3). Based on our theoretical work and the formalization of normalized *rgb* histogram binning, separate histograms of 180 different Hues are calculated for equidistant binning and for a binning adapted to the topology of the normalized *rgb* color space each. ANNs are trained tested and validated for each of the 7 agents as well as for the majority vote of all agents for all 320 different feature generation strategies. The results are analyzed under two different aspects. A qualitative analysis is done to explore if and to which extend histogram orientation and topological binning effect the result of color object classification with ANN. A quantitative analysis is done to estimate if and in which range of accuracy Tahitian pearls can be classified artificially based on their perceived color.

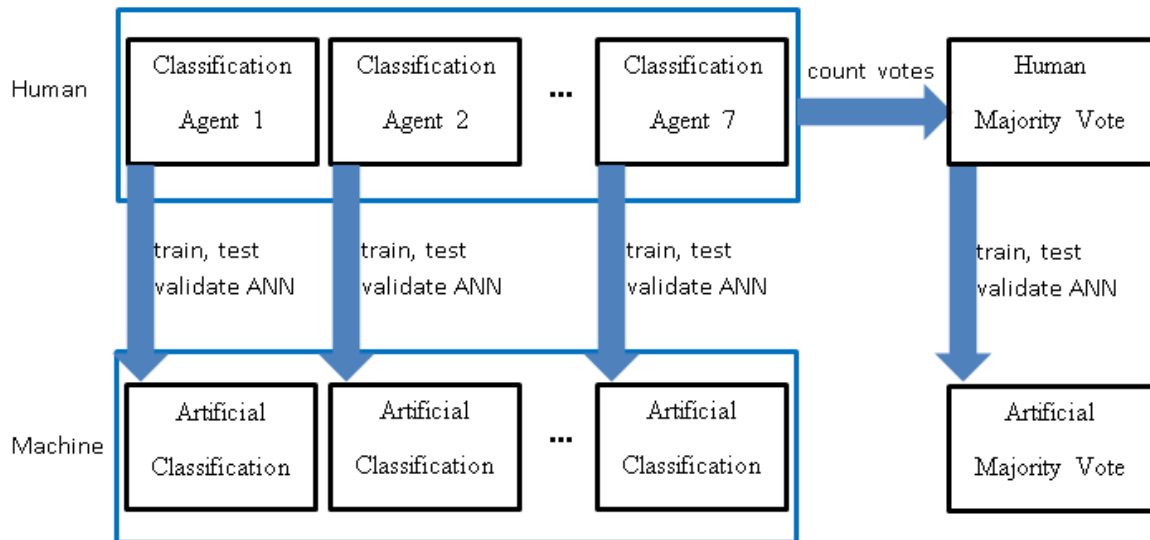


Figure 3: Workflow of the experimental classification procedure.

1.5 Results

The results of experiments show that normalized *rgb* histogram orientation has a significant impact on the global performance of ANN based color object classification. A classification rate variance between feature vectors calculated based on different chromatic indices of up to 20% were observed for certain human classifications (Figure 4). A variance of at least 15% was observed for each of the 8 human classifications.

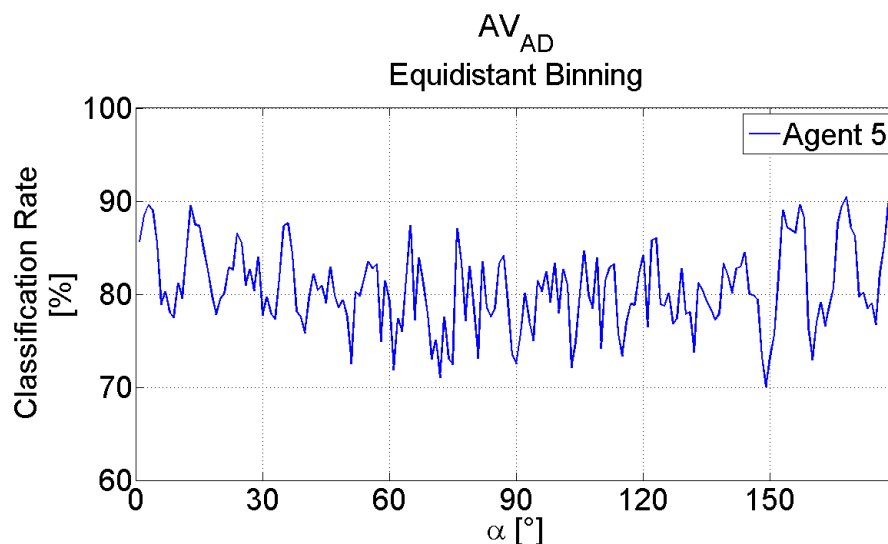


Figure 4: Variance of global classification rate depending on the used histogram orientation.

The results show further that the classification accuracy of each class (here pearl color classes) depends on the used chromatic index. A classification rate variance between different feature vectors of up to 100% was observed for certain classes (Figure 5).

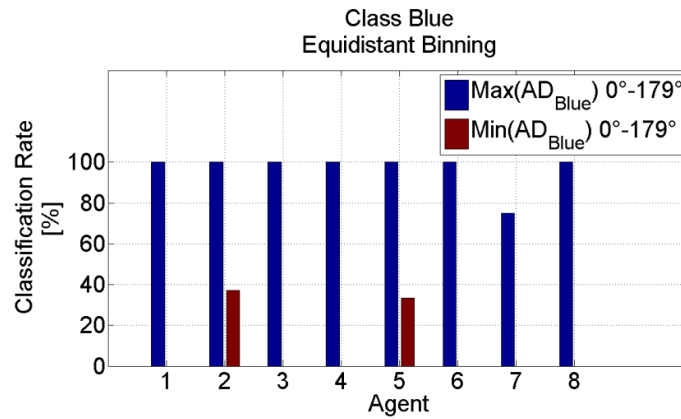


Figure 5: Minimum and maximum classification rate for the color class 'Blue' over the whole range of tested feature vectors for each human classification.

The results show that the descriptive power of a given chromatic index generally depends on the data distribution it is supposed to describe. The use of only a few chromatic indices in the literature and especially the use of the same index for different applications stand in sharp contrast to the results of our experiments.

The application of the proposed topological binning had in tendency a positive effect on the global classification rate when compared to the standard equidistant binning. For certain human classifications the difference was significant with variations of up to 18% (Figure 6). As this was not the case for all human classifications, no general recommendation of which binning strategy should be applied can be given. But seeing the partially large difference, topological binning should at least be considered for a given application.

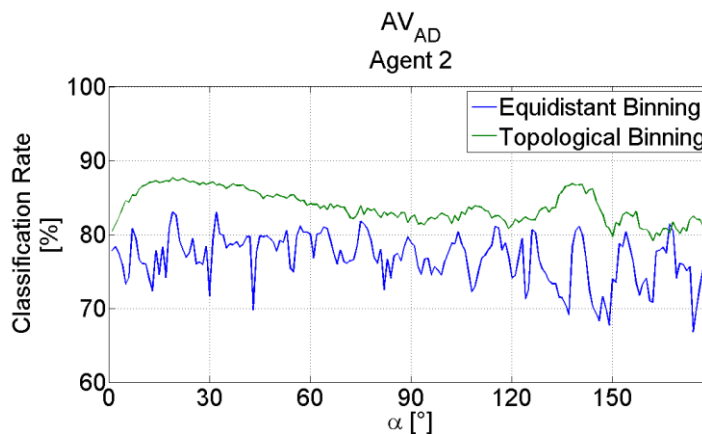


Figure 6: Difference of topological and equidistant binning over all tested feature vectors for 1 human classification.

The quantitative results showed that it is generally feasible to classify Tahitian pearls based on their perceived color. Classification rates of over 84% for training data and over 79% for test data were reached for all human classifications (Figure 7). The classification rate of validation data instead showed larger variance between different human classifications. A major reason for this lack of generalization ability might be that the total amount of 150 pearls might not be sufficient, seeing the wide range of different colors and color combinations that appear on different Tahitian pearls. Still, an average classification rate of 76% for validation data was reached.

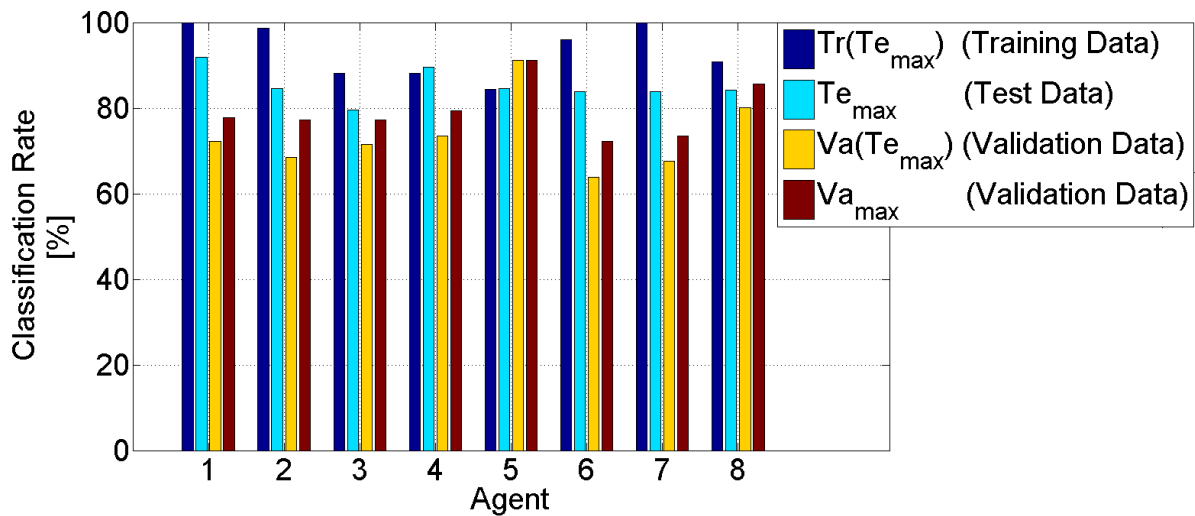


Figure 7: Preliminary optimal results for the artificial classification based on 8 human classifications.

1.6 Structure of Part II

In section 2, related work to this part of the thesis is presented. The main focus lies on related research concerning the color classification of pearls. In section 3, the normalized *rgb* space and histogram binning are introduced. A formalization of normalized *rgb* histogram binning is derived in the RGB geometry and the topology of the normalized *rgb* color space in relation to histogram binning is analyzed. The image acquisition and preprocessing is specified in section 4 along with an analysis of the human classification of the used 150 Tahitian pearls. The design of experiments is presented in section 5 by specifying the used ANN topology, the data splitting methods and the feature vector variation. The results of the experiments are shown in section 6 and analyzed qualitatively and quantitatively. A conclusion is given in section 7 followed by a sketch of future work in section 8.

2 Related Work

The use of a monochrome camera with different filters to obtain images sensitive to specific wavelength bands are used to classify the pearls color according to human perception is proposed in [NAG94]. 100 pearl samples are graded by experts in 10 classes ranging from white to cream. An Artificial Neural Network (ANN) is used to identify wavelength bands that allow a maximum correlation between human and artificial classification. Therefore, an ANN is trained with all images, and bands with a small influence on the classification result are removed iteratively. The optimal classification is reached with 9 filters with a classification success of 91% for the training data and 71% for the test data. This approach has the advantage of covering a larger area of the pearls surface when compared to the use of a spectrometer. Additionally, the instrumentation is generally cheaper.

An approach to quantize pearl color and luster with UV-visible spectroscopy is presented in [MAM10]. The obtained spectra of 8 Indonesian South Sea Pearls are evaluated visually and a correlation between peaks and pearl color is assessed intuitively. It is concluded that UV-visible spectroscopy can be a useful tool to quantitatively assess the quality of a pearl. The approach is developed further in [AGA12] and [AGA15]. Here the UV-visible spectra of 28 pearls of 4 different types (Akoya, South Sea, Freshwater and Tahitian pearls) are measured. Artificial Neural Networks are used to automatically assess parameters such as donor oyster condition and type, breeding oyster type, pearl color, luster, surface quality, form and potential pearl treatment. The results indicate an impressively successful classification for every parameter, but the trained networks were validated with only four pearls, one pearl for each pearl type. The general suitability of this method has to be confirmed with a larger set of pearls, as some correlations are not intuitive. The classification of surface quality for example is somewhat astonishing. Grades include the number of surface defects and their concentration over the complete pearl surface. But the spectra are measured at only two areas on the pearls surface, each of less than 1 *mm* diameter. The results suggest that the overall surface quality is encoded in any point of the pearl surface, which does not correspond to the partially local character of surface defects [CUI15]. If a further validation holds, the necessity to develop a 3D data acquisition device for pearl evaluation, as is part of our current work, as well as of other research groups [TAN14] [CAO10], could be omitted.

A ‘traditional’ approach with RGB color image acquisition for pearl color classification is presented in [TIA09]. First, the original RGB images are transposed to the HSV color space. Then, median filtering is applied and areas containing reflections are segmented by thresholding the Value channel. For the remaining region the averages of Hue and Saturation channels are calculated separately. The average Hue of each pearl is used as feature for an ANN classification into three classes red, purple and white (again the pearl type is not specified but the papers origin and the shown images suggest Chinese Freshwater Pearls). Afterward, the average Saturation of pearls of the same Hue class are classified with fuzzy C-means in four unspecified classes A-D. Even though the approach is straight-forward, averaging Hue and Saturation is not applicable to Tahitian pearls, as one specific feature is the appearance of multiple colors on the same pearl. Furthermore, the illumination component is not considered, a feature that is vital for the color classification of Tahitian pearls.

Even though the topic of pearl classification is quite specific, the general goal of classifying an object based on its perceived color is the same as in numerous applications, such as color object recognition in robotics [SUN03], plant, fruit and food characterization [HER16], [AVI15], [PED06], [ROS04], face recognition [LI13] or even color object segmentation based on human perception, if the segmentation process is formulated as classification problem [HAS16]. One of the very first questions when it comes to color object classification is which color space to use; a question without general answer, as every space has its specific advantages and disadvantages (see [CHE01] table 2 for a brief comparative listing of 7 commonly used spaces). For the purpose of classifying Tahitian pearls based on their perceived color we use the normalized *rgb* color space. Related work that includes similar strategies on non-pearl related applications will be referenced in the course of developing the theoretical basis of our approach in the next section.

3 On Normalized *rgb* Histogram Binning

The RGB color space was invented by James Clark Maxwell to mathematically describe visible colors. His work is based mainly on the trichromatic theory proposed by Thomas Young and Hermann von Helmholtz. This theory (which was confirmed later) states that within the human retina, three different types of cones are mainly responsible for color vision. Each one of the three types is sensitive to light of different wavelength, namely light that appears red, green or blue. The theory implies that every visible color can be described as a combination of red, green and blue in a certain kind of proportional relation and magnitude. The RGB color space was created, according to this model, as a three dimensional Euclidean space spanned by the axes red, green and blue in which visible colors are described by a three dimensional vector containing the three primary colors red, green and blue at different magnitudes.

While the RGB color model is based on the human processing of color, it does not correspond to the human color perception. Humans do not described colors as a certain mix of the three primary colors red, green and blue, but with parameters such as Hue, Saturation and Intensity. Based on these perceptive parameters, a mathematical formulation of three perceptive color spaces was proposed in [JOB79]. All spaces are mathematically derived from the RGB color space. The basic concept is that Hue is described as an angle, while Saturation and Intensity (or other illumination parameters) are linear parameters. The proposed spaces are rotational symmetric around the Intensity axis, while the rotation profile is determined by the mathematical definition of Saturation. As the transformation from the RGB color space to the proposed perceptual spaces is non-linear, the additive concept of the RGB space that corresponds to the human biological processing of color is hence abandoned. A possibility to combine the perceptual and the biological model is the normalized *rgb* color space. Here, the concept of separating achromatic (Value) from chromatic information (Hue, Saturation) of the perceptual model is applied within the linear RGB geometry. It is hence an interesting approach that is generally applied often in computer vision, but its possibilities are exploited only poorly, as will be shown in the next subsections.

3.1 The Normalized *rgb* Color Space

In the definition of the HS color spaces as proposed in [JOB79], Hue and Saturation of an RGB vector do not change when shifted along a line through origin and the normal vector itself. A separation of achromatic and chromatic components in this definition can hence be reached by normalizing an RGB vector with the sum of its entries as to

$$\begin{bmatrix} r \\ g \\ b \end{bmatrix} = \begin{bmatrix} R \\ G \\ B \end{bmatrix} / (R + G + B) . \quad (1)$$

The normalization results in a shift of an RGB vector along a line through origin and the vector itself to a plane with normal $[1 \ 1 \ 1]$ going through point $[1/3 \ 1/3 \ 1/3]$ (Figure 8). The plane is cut by the borders of the RGB cube into an equilateral triangle, often referred to as chromatic triangle or Maxwell triangle [WYS00]. The normalized *rgb* vectors contain all chromatic information in the definition of the HS spaces, while the proportional relation of its entries, one of the basic concepts of the RGB color model, is preserved.

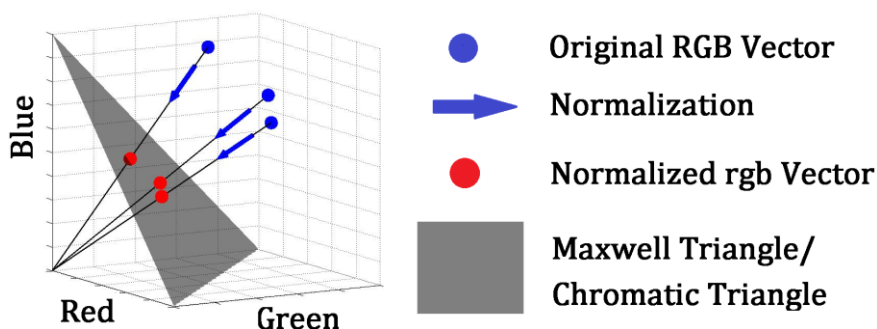


Figure 8: Schema of RGB vector normalization.

As all normalized *rgb* vectors lie on the same plane, a dimensionality reduction can be done by rotating the plane as shown in Figure 8. The rotated triangle can be seen as a barycentric coordinate system, meaning the proportional relations of the entries of a normalized *rgb* vector are still preserved. All mathematical operations on normalized *rgb* vectors that will be presented in the coming subsections can be done either in the RGB space or in the 2-dimensional representation. In Figure 8 the example of a division of the Maxwell triangle with planes that corresponds to a division of the 2D representation with lines is given, an identity that will be used often in the coming sections. Numerically, it is more convenient to apply all operations in the RGB space as the data does not have to be rotated. For visualization purposes instead, the 2D representation is more convenient. In the coming subsections both will be used for illustration purposes, while calculations are done in the RGB space.

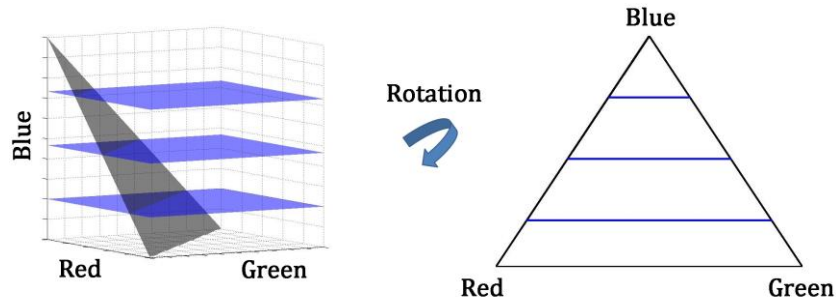


Figure 9: The Maxwell triangle in the RGB space and its 2-dimensional representation after rotation. A division of the Maxwell triangle with planes (left) is equivalent to a division of the 2-dimensional triangle with lines (right).

3.2 Histogram Calculation

By calculating a histogram of a given x -dimensional data distribution, the data is divided in domains and the frequency of data occurrence in every domain is counted [BRU02] (in this thesis only histograms with non-overlapping bins are considered, see [THA02] for other types). With a suitable choice of domain indices, histogram calculation can be seen as mapping an x -dimensional data distribution D with a mapping function F to vector h_F in which every element j is the frequency of occurrences in D that are mapped by F to the same domain j :

$$\vec{h}_{F,j} = \text{card}(d \in D : F(d) = j). \quad (2)$$

3.2.1 One-Dimensional Data Distribution

The procedure for binning a 1-dimensional data distribution in 5 equidistant bins is shown in Figure 10 by an exemplary normalized r -channel binning. The image on the top left shows a hypothetical data distribution in the RGB space (every possible permutation of RGB values in a range of 0 to 10). The RGB vectors are normalized according to Eq. 1 (top right image). On the bottom left is the absolute occurrence of the data of the normalized r -Channel (a 1-dimensional data distribution). The histogram binning is done by dividing the whole data distribution in 5 equidistant intervals ('bins', black dashed lines in the graph on the bottom right). The histogram vector is described by the absolute occurrence of data in each bin (bottom left).

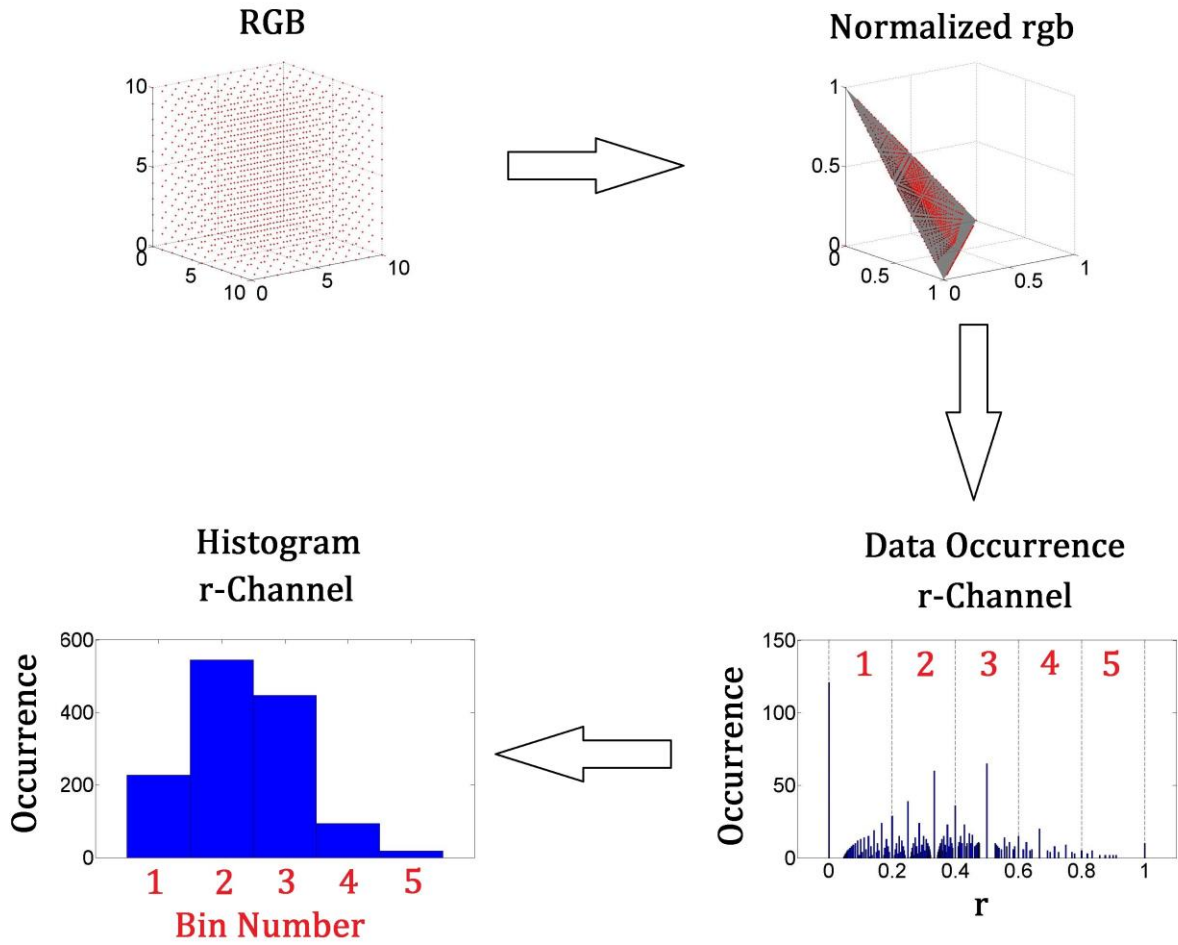


Figure 10: Schema of binning the r -channel of a normalized rgb data distribution in a histogram of 5 equidistant bins.

In image processing, the histogram of an image is typically divided by the sum of all data points that are binned, as to

$$\vec{h}'_{F,j} = \frac{\vec{h}_{F,j}}{\text{card}(D)} \quad (3)$$

to obtain the relative frequency in regards of the cardinality of the data set.

Histogram binning has two essential features making it a suitable tool for image analysis. First, the size of the histogram is determined by the mapping function. This means, the same mapping function applied to images (or image regions) of different size, results in histograms of the same size that can be directly mathematically compared or used as feature vectors for further processing (ANN, etc..). Second, if Eq. 3 is applied, the influence of absolute data occurrence variation between different images or image regions is eliminated. Both features

and its simple implementation make histogram binning one of the major tools or maybe “*the major statistical tool for normalizing and requantizing an image*” [WIL00].

In the example shown in Figure 10, the r -channel was binned in 5 equidistant bins. The same result is obtained, when the binning is done directly in the RGB space by describing the index to be binned as a dot product as to

$$r = \begin{bmatrix} r \\ g \\ b \end{bmatrix} \cdot \begin{bmatrix} 1 \\ 0 \\ 0 \end{bmatrix}. \quad (4)$$

This means, the bins can be described as domains in the RGB space that are separated by equidistant parallel planes with normal vectors $[1 \ 0 \ 0]'$ (second image in Figure 11).

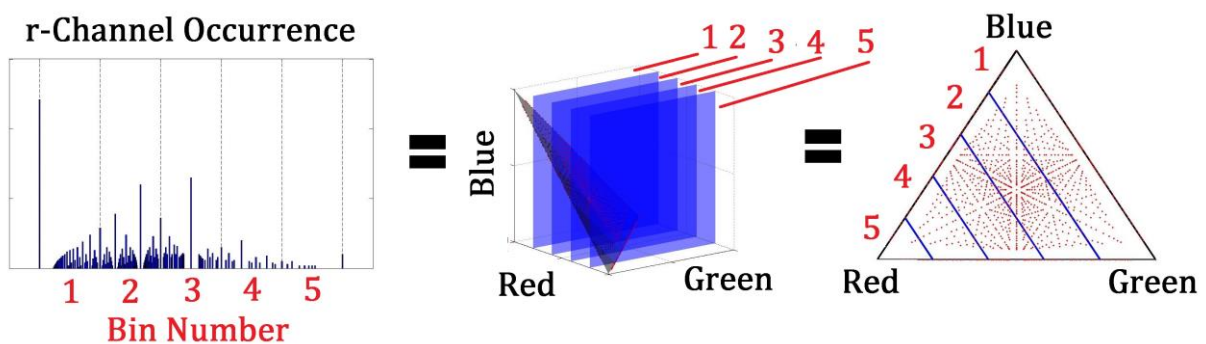


Figure 11: Equivalency between r -channel binning by using scalars in the r -channel (left), planes in the RGB space (middle) and lines in the rotated Maxwell triangle.

As every plane intersects the Maxwell triangle in a line, the binning can as well be done in the rotated Maxwell triangle with lines parallel to the blue-green axis. Please note, that even though the binning is applied in spaces of greater dimension than 1, it is still only the 1-dimensional distribution of the r -channel binned. The method serves, as mentioned, the goal to introduce the equivalency of binning in the RGB space and in the rotated Maxwell triangle. It is necessary to understand the concept of this relation and its visualization for all the sections to come.

3.2.2 Multidimensional Data Distributions

In the case of multidimensional data distributions, two methods to generate histograms are typically applied: Concatenated 1-dimensional histograms, each one of the type shown in the previous section, or histograms based on mapping functions with several input variables. Both approaches will be introduced with a 2-dimensional data distribution described by the rg -channels of the example given in the previous section (Figure 10). This is no loss of generality, but done for the purpose of accustoming the reader to the geometrical equivalency between normalized rgb vectors in the RGB space and in the rotated Maxwell triangle.

In the concatenated case, histograms of each channel are calculated and concatenated as schematically shown in Figure 12.

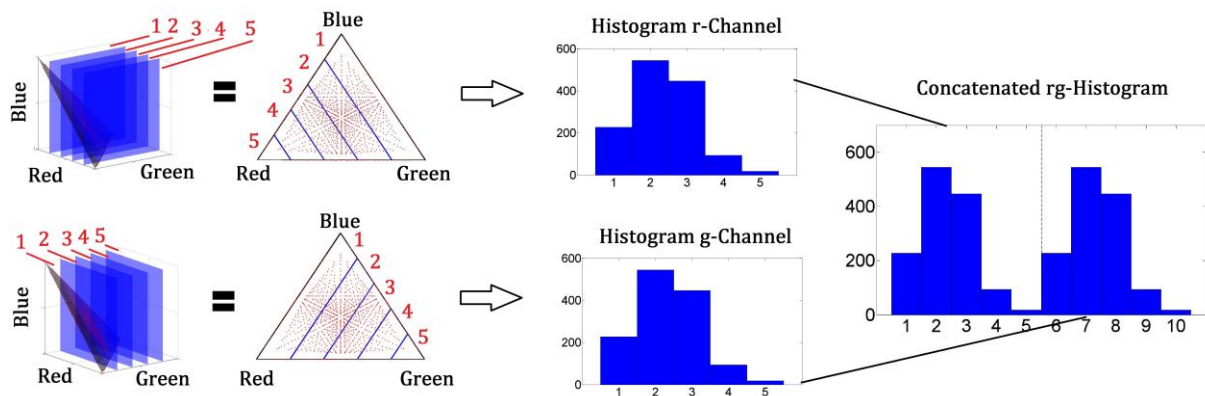


Figure 12: Concatenated rg -Histogram (right) obtained by concatenating the two independent r - and g -histograms.

Here, the g -channel binning in the RGB space is, equivalently to the r -channel binning, done based on the dot product

$$g = \begin{bmatrix} r \\ g \\ b \end{bmatrix} \cdot \begin{bmatrix} 0 \\ 1 \\ 0 \end{bmatrix}. \quad (5)$$

which means bins are described by regions between equidistant planes with normal $[0 \ 1 \ 0]$. Again, binning in the Maxwell triangle can be done with lines that correspond to the intersection lines of these planes with the triangle. The two separate histograms are afterwards concatenated.

The second typical histogram application in image processing, in case the correlation between color channels shall be considered, is to calculate the corresponding bin number for a given

color vector based on all its entries. This can either be done with an according mapping function with multiple arguments, or by combining the bin numbers of previously calculated histograms of each channel. The latter is shown in Figure 13. First, the bin number $bin_{r,i}$ of a r -histogram for each vector i is calculated (top left), as well as the bin number $bin_{g,i}$ of the g -histogram (top right). Both can for example be combined as to

$$bin_{rg,i} = bin_{r,i} + (bin_{g,i} - 1)N_r. \quad (6)$$

in which N_r is the number of bins of the r -histogram.

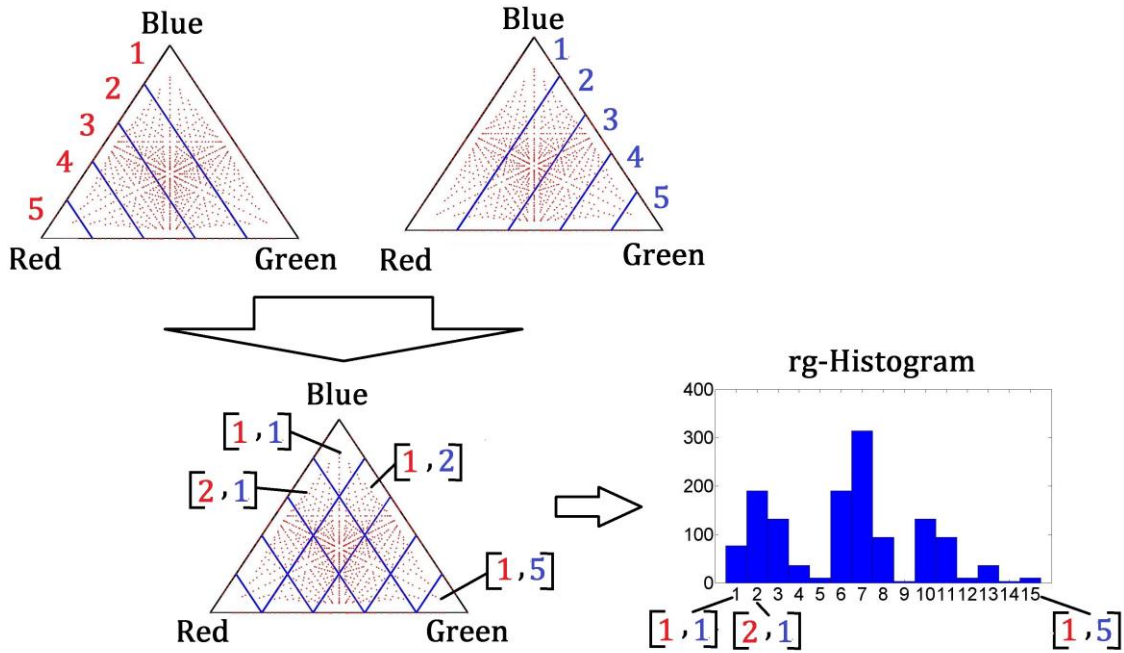


Figure 13: rg -histogram generation as a division of the rotated Maxwell triangle in rhombs.

Finally, the rg -histogram h_{rg} with bin numbers j can be calculated as to

$$\vec{h}_{rg,j} = \text{card}(bin_{rg,i} = j). \quad (7)$$

The corresponding regions in the Maxwell triangle are rhombs (Figure 13 bottom) defined by lines of the r -histogram bins and the g -histogram bins. The equivalent procedure in the RGB space is a division of the space by planes with normal $[1\ 0\ 0]$ or $[0\ 1\ 0]$ into cubes (Figure 14, it can be seen why the rotated Maxwell triangle is the better choice, when it comes to visualization of multidimensional data binning).

Before concluding this section, a remark on a misinterpretation of the final bin number, when multidimensional normalized rgb histogram binning is applied, shall be given. In some

articles it is stated that n bins are used for r and b channel each, which resulted in a maximum feature length (number of bins in the multidimensional histogram) of nxn [SOR03], [YAN95], [CER17]. If the binning is formulated in the RGB space (Figure 14), it can be seen that the whole 3-dimensional RGB space is divided in nxn bins, but the Maxwell triangle is only separated by one part of the bins. This can as well be seen in the rotated Maxwell triangle (Figure 13). Here, the triangle is separated by 5 bins for the r -channel and 5 bins for the g -channel but the amount of multidimensional bins is 15 and not 25, as not every 1-dimensional r -bin overlaps with all of the 1-dimensional g -bins and vice-versa.

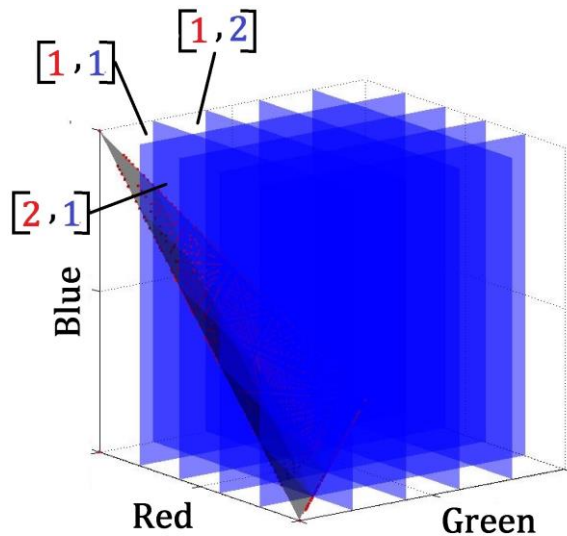


Figure 14: rg -binning in the RGB space.

3.3 Standard Application

The normalized rgb color space is used in the literature either included in novel approaches, or as benchmark. Applications comprise for example vehicle color recognition [CHE14], food inspection [DU05], [FON14], skin detection [LEE02], [HAS15], color texture analysis [MAE04] or object tracking [WAN08]. In many cases (all cited articles), histogram binning is applied to the normalized rgb vectors to reduce data complexity and to obtain consistent feature vectors. Out of literally infinite possibilities of histogram orientation, only a few are used in standard applications. The few that are used are chosen either based on empirical observations, or even on a false mathematical assumption.

In [YAN95], [CHE01], [VEZ03], [DU05], [KAK07], [BUS08], [SAN10] and [ZHU13] it is stated that only the r and g channel of the normalized rgb vectors have to be used, as the sum of r , g and b is 1, and hence the blue channel contains redundant information. Based on this

argument, histogram binning is applied only on the r and b channel in [YAN95], [DU05], [SAN10] and [ZHU13]. Clearly, the sum of a normalized rgb vector is 1, as it is an RGB vector projected to a plane with normal $[1\ 1\ 1]$ going through $[1\ 0\ 0]$. But histogram binning is a nonlinear operation, meaning channel redundancy does not imply histogram redundancy.

In Figure 15 rg -binning (top row) and gb -binning (bottom row) is done for two different hypothetical data sets (left and right column). The red dots represent data points (normalized rgb vectors).

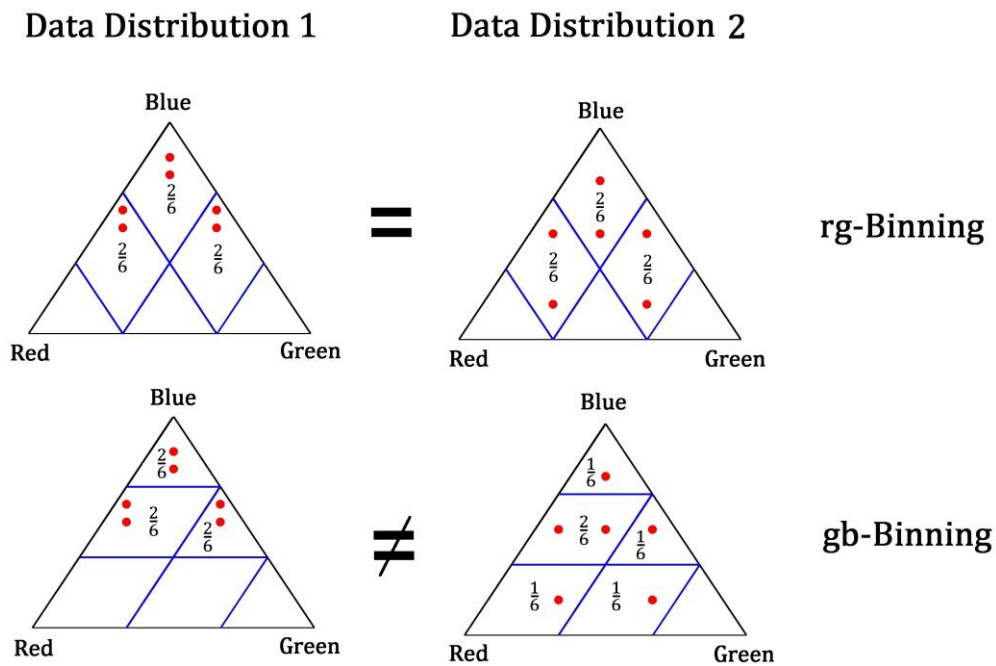


Figure 15: Two different data distributions (first column and second column) resulting in the same histogram distribution when binned with rg channels (first row) but different histogram distribution when binned with gb channels (second row).

If for the data distribution of the left column a 2-dimensional rg histogram with 3 bins per channel is calculated, 3 histogram entries are non-zero, each representing $\sim 33\%$ of the data (top left). The same rg histogram is obtained for the 2nd data distribution (top right). For a gb binning of the two data distributions instead (bottom row) two different histograms are obtained. It means, there is no bijective relation between rg and gb histograms. The example holds as well if concatenated histograms out of 1D channel histograms are used. More generally, if only one or two 1D histograms or one 2D histogram of normalized rgb channels without the actual data distribution is given, it is impossible to mathematically generate the histograms of the remaining channels or channel combinations:

$$r + g = 1 - b$$

$$H(r) + H(g) \neq_n 1 - H(b) \quad (8)$$

$$H(r, g) \neq_n H(g, b) \neq_n H(r, b).$$

Accordingly, the argument to use rg binning because the sum of the entries of a normalized rgb vector is 1, as used in the cited articles, is mathematically wrong.

However, this does not mean that any other binning strategy would necessarily lead to better results as those shown in the cited papers. In [YAN95], [VEZ03] and [KAK07] for example, rg histogram binning is applied to detect human skin in images. Rg -binning is chosen based on the false redundancy assumption. The same binning strategy for skin detection is used in [HAS15] but here it is argued that the rg histogram was chosen because skin regions contain only small amounts of blue; an empirical but true assumption. In [SOR03] it is argued that the ‘*sensitivity of most cameras in blue are small*’ and therefor rg binning was used. It is hence possible that rg binning for skin detection is the optimal choice. But it does not mean that it is ideal for vehicle color detection [CHE14], color texture analysis [MAE04], [CER17] object recognition [WAN08], or any other application. Anyhow, probably based on the successful application of rg -binning for skin detection in combination with the spread false assumption of histogram redundancy, in all the just cited articles, r and g channels are used exclusively without any argument why they were chosen, as if there was not even a choice. A first indicator that the success of rg -binning is data dependent can be found in [GRO06]. Here, rg -histogram binning (chosen based on the false histogram redundancy assumption) is applied as benchmark for building recognition to the ZUBUD database. A classification success of 92% is reached. Afterwards, the same approach is applied to a custom database containing buildings of the University of Amsterdam. The classification result for rg -binning dropped to 24%.

The hypothesis that different applications might need different chromatic descriptors can be derived theoretically from the example given in Figure 15 on the right column. If the red dots are seen as features, each one independently vital for a given application, the gb histogram (bottom right) represents the data more detailed (hence better) than the rg histogram (top right). For the data distribution on the left instead, there is no difference between rg and gb binning. It means the ideal histogram is completely data dependent. This assumption is further bolstered by published approaches successfully using empirically defined linear combinations

of the rgb channels for histogram calculation such as the chromatic indices $r-g$, $g-b$, or $1.4r-g$ [BAT00], [MEY11], [GOL12].

If the 2D representations of the histograms based on the indices are visualized (Figure 16), it becomes clear that every possible histogram orientation of the normalized rgb color space can be defined by a single parameter, namely an angle that corresponds to the human perceptive parameter Hue. Normalized rgb histogram binning can hence be formalized, which might help to find suitable histograms for a given application.

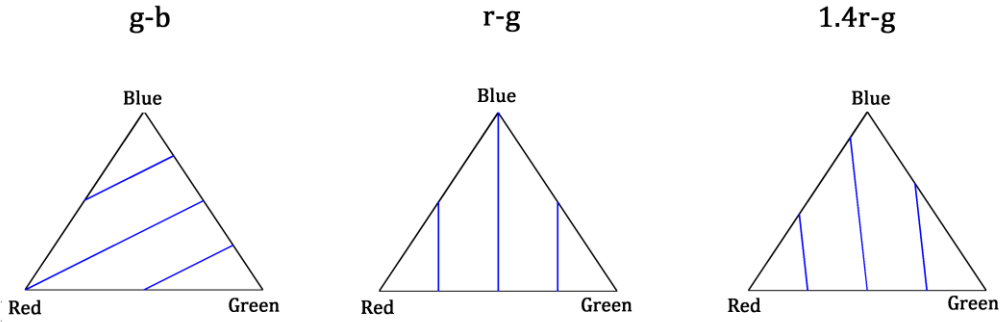


Figure 16: Alternative chromatic indices used in the literature and their histograms in the 2D chromatic triangle.

3.4 Formalizing Normalized rgb Histogram Calculation

All chromatic indices described as linear combinations of normalized rgb color channels can be seen as dot product of a normalized rgb vector and a 3-dimensional vector:

$$r = \begin{bmatrix} 1 \\ 0 \\ 0 \end{bmatrix} \cdot \begin{bmatrix} r \\ g \\ b \end{bmatrix}; \quad g - b = \begin{bmatrix} 0 \\ 1 \\ -1 \end{bmatrix} \cdot \begin{bmatrix} r \\ g \\ b \end{bmatrix}; \quad 1.4r - g = \begin{bmatrix} 1.4 \\ -1 \\ 0 \end{bmatrix} \cdot \begin{bmatrix} r \\ g \\ b \end{bmatrix}. \quad (9)$$

Hence, each index can be seen as a scaled distance measurement between a normalized rgb vector and a plane with a normal described by the chromatic index going through point $[0 \ 0 \ 0]$ (scaled as the indices found in the literature are usually not normalized by its l_2 -norm). As the normalized rgb vectors lie all on a plane (the Maxwell triangle), an equivalent distance measurement to a given index can be done with a transformed index described by a vector whose element sum is zero.

For a given chromatic index described as a vector p , the scaled distance d , as described above, can be written as dot product between vector p and the normalized rgb vector:

$$d = \begin{bmatrix} p_1 \\ p_2 \\ p_3 \end{bmatrix} \cdot \begin{bmatrix} r \\ g \\ b \end{bmatrix}. \quad (10)$$

Transforming vector p so that the sum of its entries equals zero means shifting it to a plane through origin with normal $[1 \ 1 \ 1]$. The so obtained scaled distance d_2 is

$$d_2 = \left(\begin{bmatrix} p_1 \\ p_2 \\ p_3 \end{bmatrix} - \frac{(p_1 + p_2 + p_3)}{3} \right) \cdot \begin{bmatrix} r \\ g \\ b \end{bmatrix} \quad (11)$$

which can be written as

$$d_2 = \left(\begin{bmatrix} p_1 \\ p_2 \\ p_3 \end{bmatrix} \right) \cdot \begin{bmatrix} r \\ g \\ b \end{bmatrix} - \frac{(p_1 + p_2 + p_3)}{3} (r + g + b). \quad (12)$$

As the sum of a normalized rgb vector is 1, the relation between distance d obtained by the original index and distance d_2 obtained by shifting the original index to a plane through origin with normal $[1 \ 1 \ 1]$ is

$$d_2 + \frac{(p_1 + p_2 + p_3)}{3} = d. \quad (13)$$

It means shifting vector p to a plane through origin with normal $[1 \ 1 \ 1]$ results in a linear shift of the distance obtained with the original chromatic index. Accordingly, a histogram calculated with the original index can as well be obtained by using the shifted index, if the binning strategy is adapted accordingly. In other words, every histogram calculated with an index that is described by a linear combination of rgb channels, can as well be calculated with a vector n whose sum of elements equals 0:

$$d_n = n_1 r + n_2 g + n_3 b \quad \text{with} \quad n_1 + n_2 + n_3 = 0 \quad (14)$$

The so far expressed relations are visualized in Figure 17. On the top left, a plane is shown that corresponds to a hypothetical chromatic index $g+3b$. On the bottom is the equivalent line in the rotated Maxwell triangle shown. This configuration corresponds to a binning in 2 equidistant bins over the whole normalized rgb space. On the top right is the plane with a normal that results when the original normal described by the hypothetical index is shifted to a plane through origin with normal $[1 \ 1 \ 1]$ shown.

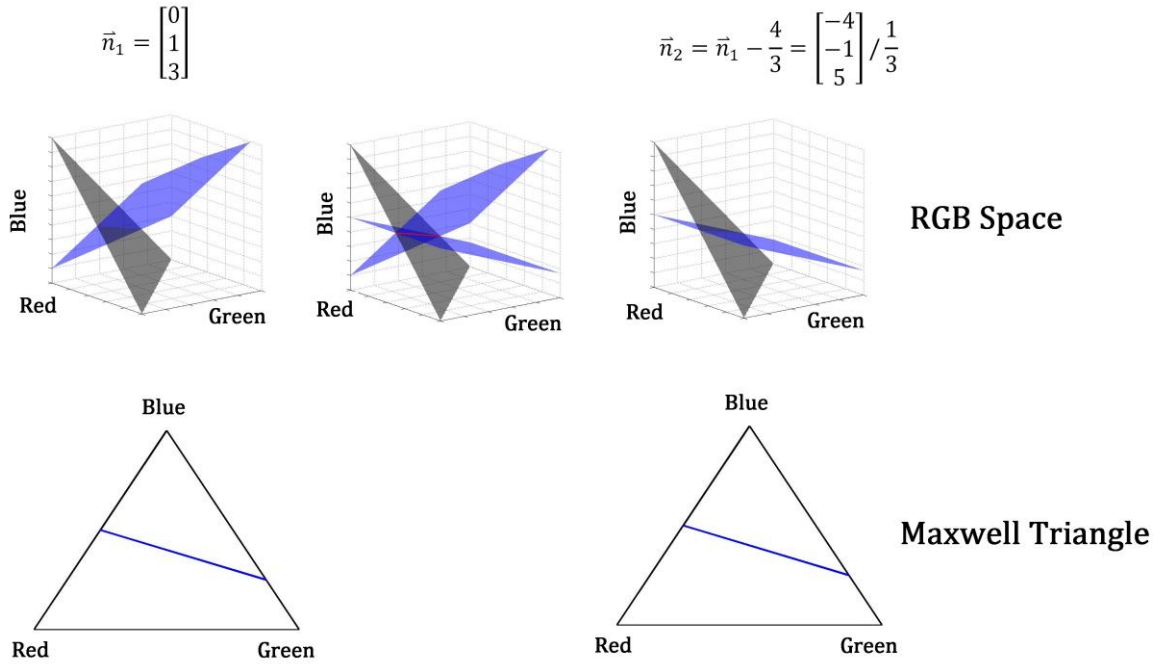


Figure 17: The same *rgb* histogram with 2 bins obtained with two ‘different’ chromatic indices.

A binning into 2 equidistant bins over the whole triangle based on the shifted index is identical with the first. The general orientation of the histogram does not change, as the orientation of the intersection lines of the planes with the Maxwell triangle are not influenced by a shift of an index to a plane through origin with normal $[1 \ 1 \ 1]$ (Figure 17 in the middle; this identity could as well be used to prove the shown relations).

By now it has been shown that any chromatic index that is a linear combination of *rgb* channels can be expressed as well by a 3-dimensional vector whose sum of elements is zero, meaning a vector on a plane through origin with normal $[1 \ 1 \ 1]$. As the sum of elements of vector n is zero, all n are perpendicular to the achromatic axis if the condition that vector n is normalized with the l_2 -norm is added (a scaling that does not change the general character of the histogram), each vector n can be expressed by a vector n_0 rotated around the achromatic axis by a certain angle α .

$$\vec{n}_\alpha = \bar{R}_{\alpha, [1 \ 1 \ 1]} \vec{n}_0. \tag{15}$$

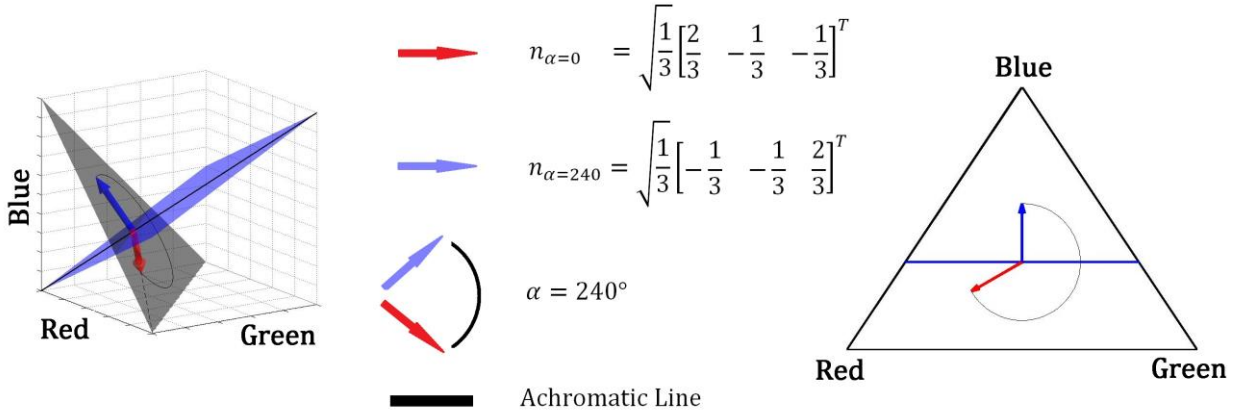


Figure 18: Normal vector and corresponding plane obtained by rotating n_0 by 240° (left) and corresponding representation in the rotated Maxwell triangle (right).

In this equation R is the 3-dimensional rotation matrix. If the initial vector n_0 is pointing in the direction of the red-axis, and the rotation is counterclockwise in respect to the rotated Maxwell triangle, any normal vector complying with Eq.14 n_α can be expressed as

$$\vec{n}_\alpha = \sqrt{\frac{2}{3}} \begin{bmatrix} \cos(\alpha) \\ \cos(\alpha - 120^\circ) \\ \cos(\alpha + 120^\circ) \end{bmatrix} \quad (16)$$

which can be obtained by expanding Eq. 15 and simplifying the trigonometric terms. The rotation is visualized in Figure 18 for rotating n_0 by 240 degrees.

With Eq. 16 any normalized rgb histogram orientation is reduced to a single parameter α . As this parameter describes a rotation around the achromatic axis it corresponds to the human perceptual parameter Hue in the definition of the HS spaces. By inserting Eq. 16 in Eq. 14, any chromatic index that is described as a linear combination of rgb channels can now be expressed as

$$d_\alpha = \sqrt{\frac{2}{3}} (\cos(\alpha) r + \cos(\alpha - 120^\circ) g + \cos(\alpha + 120^\circ) b) \quad (17)$$

which is the distance of an rgb vector to a plane through origin and perpendicular to a certain Hue described by α .

As the sum of a normalized rgb vector is 1, Eq. 17 can be simplified to

$$d_\alpha = -\sqrt{\frac{2}{3}} \cos(\alpha) - \sqrt{2} (g \sin(\alpha - 60) - b \sin(\alpha + 60)). \quad (18)$$

Please note that this is how one can make use of the redundancy of the *rgb* color channels without neglecting any channel. The obtained distance d_α is the mathematical distance to the plane defined by α . As scaling and shifting can be compensated by adapting the binning strategy, Eq. 18 can be further simplified by substituting

$$d_{H,\alpha} = \frac{d_\alpha}{\sqrt{2}} + \frac{1}{\sqrt{3}} \cos(\alpha). \quad (19)$$

Inserted in Eq. 18, a chromatic index based on a certain Hue can be calculated with the very compact equation

$$d_{H,\alpha} = -(g \sin(\alpha - 60) - b \sin(\alpha + 60)). \quad (20)$$

As all chromatic indices described as linear combinations of the *rgb* channels can be expressed by α , this equation is the formalization of chromatic indices based on the human perceptual parameter Hue.

For the actual binning, in the case bins over the whole range for a given α are used, the minimum and the maximum of this range have to be calculated. As the minimum and maximum are described by two of the three vertices of the Maxwell triangle they can be calculated as to

$$\min_{d_{H,\alpha}} = \min(0, -\sin(\alpha - 60), \sin(\alpha + 60)) \quad (21)$$

$$\max_{d_{H,\alpha}} = \max(0, -\sin(\alpha - 60), \sin(\alpha + 60)). \quad (22)$$

A last remark, before concluding this section concerns the rotated Maxwell triangle. All previous proofs can be derived as well from the 2-dimensional rotated Maxwell triangle. The author decided to stay in the RGB geometry, to illustrate that normalizing RGB vectors by its sum is the application of the human perceptual color model within the RGB geometry. Anyway, it was on several occasions of advantage to visualize data and histograms within the 2-dimensional rotated Maxwell triangle. For the interested reader, the conversion of a normalized *rgb* vector to the rotated Maxwell triangle geometry (derived from the conversion between Euclidean and barycentric coordinates) can be calculated as

$$\begin{bmatrix} x \\ y \end{bmatrix} = \begin{bmatrix} \frac{h}{\sqrt{3}}(g - r) \\ h\left(\frac{2}{3} - r - g\right) \end{bmatrix}. \quad (23)$$

In this equation h describes the height (scaling) of the rotated Maxwell triangle. When set to 1, a chromatic index based on a certain Hue α can be written as

$$\mathbf{d}_{H,\alpha} = -x \cos(30^\circ + \alpha) - y \sin(30^\circ + \alpha) \quad (24)$$

with minimum and maximum at two of the three vertices of the rotated triangle

$$\begin{bmatrix} x_{red} \\ y_{red} \end{bmatrix} = \begin{bmatrix} -\frac{1}{\sqrt{3}} \\ 1 \\ -\frac{1}{3} \end{bmatrix}, \quad \begin{bmatrix} x_{green} \\ y_{green} \end{bmatrix} = \begin{bmatrix} \frac{1}{\sqrt{3}} \\ 1 \\ -\frac{1}{3} \end{bmatrix}, \quad \begin{bmatrix} x_{blue} \\ y_{blue} \end{bmatrix} = \begin{bmatrix} 0 \\ 2 \\ \frac{2}{3} \end{bmatrix}. \quad (25)$$

3.5 Topology of the Normalized *rgb* Color Space

The projection of the discrete RGB space to the Maxwell triangle results in a topology with two features that are theoretically relevant for normalized *rgb* histogram binning: a non-uniform spatial distribution of data points, and a variance in maximum possible occurrence of different RGB vectors with the same normalized coordinates. This property is generally known to affect image processing operations such as segmentation [KEN76] and has been analyzed within the HSV geometry in [ROM12]. Here, it will be analyzed in the context of normalized *rgb* histogram binning.

In Figure 19 the distance between unique sorted normalized b values of an 8 bit RGB space (every permutation of R, G, and B in a range of 0 to 255) is shown. It can be seen that the distance between subsequent normalized b values is not uniformly distributed. In consequence, if the channel is binned with equidistant bins, the frequency of unique b values might vary between different bins.

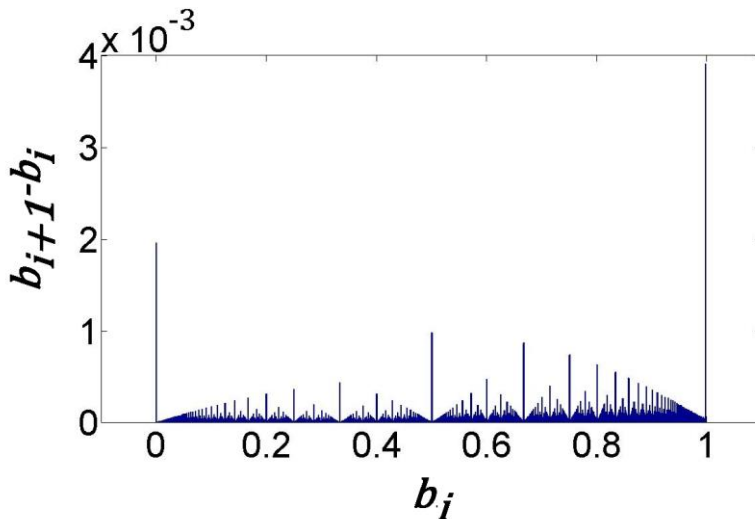


Figure 19: Non-uniform distance between subsequent normalized b -values, calculated for all possible b values of the RGB space.

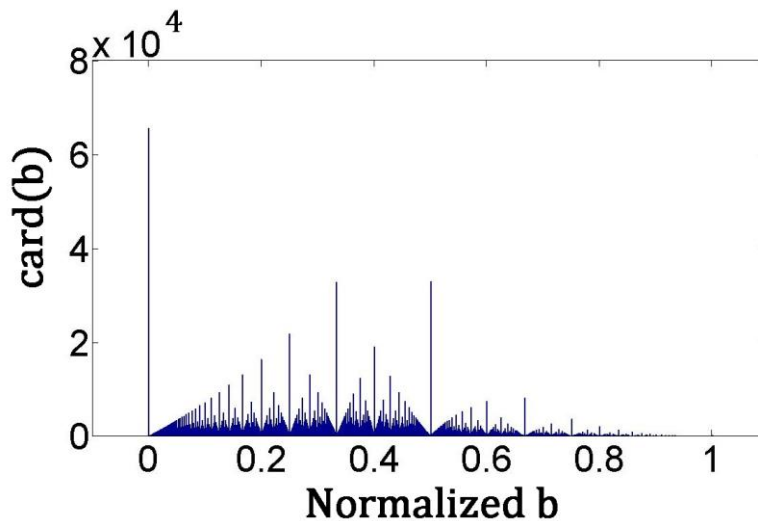


Figure 20: Non-uniform occurrence frequency of unique b values, calculated for all possible b values of the RGB space.

In Figure 20, the occurrence frequency of unique normalized b values of an 8 bit RGB space is shown. Here as well, the frequency is distributed non-uniformly. This is due to the discrete character of the RGB space and the definition of the normalized rgb space as projection of RGB vectors along lines through origin. The achromatic axis for example contains 256 different RGB vectors that are all projected to the same coordinate on the Maxwell triangle, while the line through origin and the RGB vector $[1\ 1\ 255]$ contains no other discrete vector within the range of an 8 bit RGB space. Hence, its normalized coordinate has an occurrence frequency of 1. The non-uniform occurrence frequency results as well in a non-uniform occurrence frequency in equidistant bins.

This non-uniformity, when all possible normalized b values of the 8 bit RGB space are binned with 16 equidistant bins, is shown in Figure 21 on the left.

As it has so far not been shown if and to which extend these non-uniformities affect normalized rgb histogram binning when used for color classification with ANN, an analysis of this effect was included in the classification experiments. For this purpose the same experiments were conducted with the typically used equidistant binning and with topological binning. The term ‘topological binning’ will be used in all coming section for bins that contain more or less the same amount of normalized RGB values if the whole 8 bit RGB space is normalized and binned (more or less as the occurrence frequency of normalized coordinates vary and hence an exact uniform division is not always possible). The distribution in each of the 16 bins for topological binning of all b values of the normalized RGB space are shown in Figure 21 on the right. The different bin boundaries for topological and equidistant binning for the same data are shown in Figure 22.

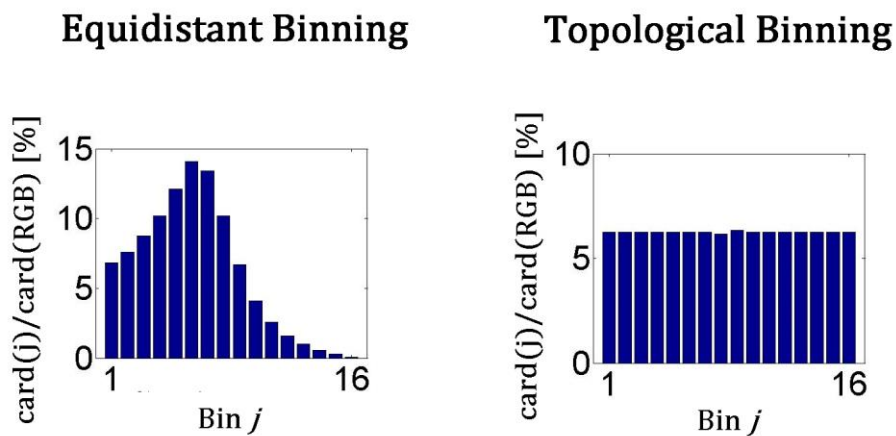


Figure 21: Occurrence frequency for equidistant (left) and topological binning (right) of all possible b values of the 8 bit RGB space in 16 bins.

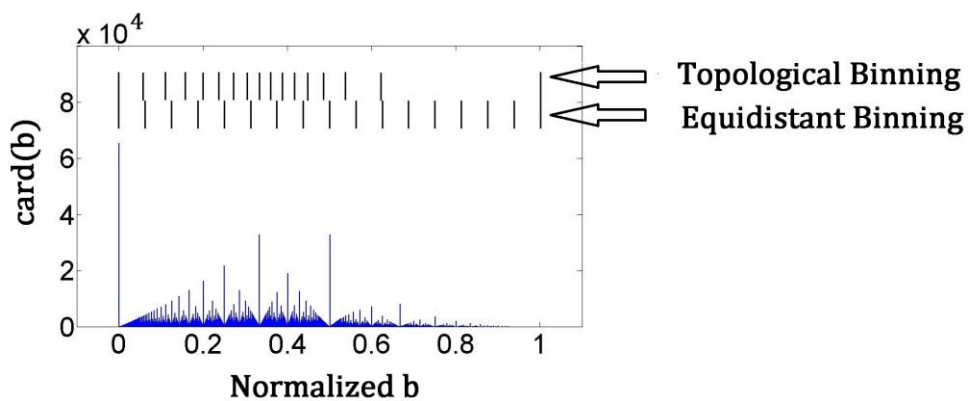


Figure 22: Different bin boundaries for equidistant and topological binning of the normalized b channel with 16 bins.

The occurrence frequency in bins subject to histogram orientation is a complex number theoretical problem to which no general formula exists (approximations are given in [KEN76] and [ROM12] for some cases). The bin boundaries for topological binning subject of histogram orientation were therefore calculated by brute force for all of the 180 different used histograms (Hue between 0° and 179° with a 1° increment; will be specified in section 5.2).

3.6 Summary

In the previous sections the concept of normalized *rgb* histogram binning has been introduced. It has been shown that *rgb* histogram binning is used in a wide range of color image processing applications, but the general concept as well as the relation to the RGB geometry and the perceptual HS geometry seems to be partially unclear. Additionally, *rgb* histogram binning is applied only to a handful of chromatic indices and their choice is justified either empirically or based on a false mathematical assumption.

A hypothesis was postulated that the descriptive power of a given chromatic index depends on the actual data distribution of a given application. In analogy, it might be possible that an optimal index exists for a given application.

A formalization of *rgb* histogram binning was developed, showing that any chromatic index that is described by a linear combination of normalized *rgb* channels can be expressed by a single parameter, namely the human perceptual parameter Hue. The formalization might help to find suitable mathematical tools to identify optimal chromatic indices for a given application.

The formalization was done in regards of *rgb* histogram binning but the main conclusion that any chromatic index can be expressed by the human perceptual parameter Hue might be useful for any other method that is applied to chromatic indices (as for example *rg*-SIFT for local feature detection in images [BRO11])

In regards of *rgb* histogram binning it can be stated that in contrary to the limited choice of chromatic indices and their combination found in the literature, the possibilities of which chromatic indices to use and how many different indices in combination is theoretically unlimited.

To explore if and to which extend histogram orientation has an influence on color object classification, 180 different orientations over the whole range of the normalized *rgb* color

space will be applied to classify the color of Tahitian pearls with Artificial Neural Networks. Additionally, the effect of considering the normalized *rgb* topology with topological binning on the classification will be analyzed.

4 Data Acquisition

150 Tahitian pearls, provided by the Centre IFREMER du Pacifique (the French Polynesian department of the French oceanographic institution Institut français de recherche pour l'exploitation de la mer), were used in this study. All 150 pearls were classified in 8 predefined color classes by 7 different employees of IFREMER that work in research projects concerning the cultivation of Tahitian pearls and the nature of their genesis (in the following, they will be referred to as ‘agents’, details on color classes and the human classification will follow in section 4.2). The pearls were farmed at the same location, and no prior sorting was done, meaning not all pearls are of commercial value, as they may contain surface defects, poor luster, etc. This procedure was chosen because the corresponding research projects at IFREMER aim at finding correlations between pearl quality and cultivation parameters. Therefore, all available quality types have to be used.

4.1 Image Acquisition and Preprocessing

All images were taken with a NIKON D-7000 with AF-S NIKKOR 18-55mm objective. To guarantee the same acquisition parameters for all pearls the device PackshotCreator was used (Figure 23 on the left). The device is a closed acquisition environment with fixed illumination parameters and fixed camera position. The original RGB images were of size 6000x4000 pixels and in uncompressed .tif format. To obtain as much surface information as possible, each pearl was photographed at three different positions (Figure 23 on the top and on the bottom). The segmented images of the same pearl at three different view angles in Figure 23 show the necessity of capturing the whole surface, as the color distribution can vary over the surface.

For every pearl, the RGB vectors of the complete pearl region of all three images were stored as a vector containing unique RGB values and the amount of occurrence. This means that first, no spatial information of color regions on the pearls surface were used, as the goal is to classify the pearl based on its global appearance independently of the color distribution on the surface. Second, no prior segmentation of surface regions was applied. In [TIA09] for example, reflections were segmented based on the argument that they do not contain pearl color information. According to the used images shown in the paper, this might be true. For Tahitian pearls instead it is known that reflections contain vital information, especially for

multicolored pearls where secondary colors appear in reflection areas (compare Figure 23 on the bottom right). In general, it was the approach to use as less preprocessing as possible for the following reasons. First, it is not known which regions or parameters are essential for the human color evaluation, meaning for the moment all available color information is used. And second, every preprocessing would need a certain parametrization, which has an influence on the whole following classification procedure. As the focus of this works lies on color feature generation, it was the goal to reduce or fix all remaining parameters.

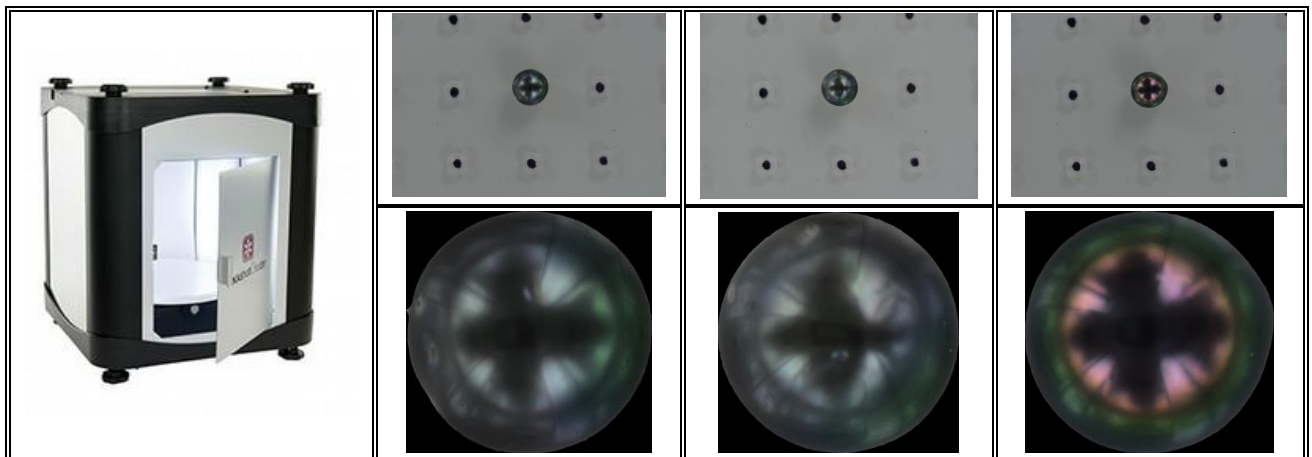


Figure 23: The device PackshotCreator (left) used for image acquisition, original images of one pearl captured from three different view angles (top), and the corresponding segmented pearl (bottom).

In summary, for feature calculation and classification, only the stored RGB values and the frequency of their occurrence in all three images of a pearl were used. Average amount of pixels per pearl (all three images) is $\sim 10^6$ and average amount of unique RGB vectors per pearl is $\sim 4 \cdot 10^4$ (Figure 24, 1 pixel length $\sim 12.3 \mu m$).

For the conducted experiments it was assumed that the acquired images represent the character of pearls as perceived by humans under ideal inspection conditions. An adaption of image acquisition parameters will be done, if necessary, in a future work.

	Pixels per pearl (all 3 images) [pixels]	Unique RGB vectors (all 3 images) [-]	Pearl surface per image (average of all 3 images) [mm ²]	Pearl diameter per image (average of all 3 images) [mm]
min	$\sim 7.1 \cdot 10^5$	$\sim 7.0 \cdot 10^3$	~ 36.1	~ 6.8
average	$\sim 1.1 \cdot 10^6$	$\sim 3.6 \cdot 10^4$	~ 54.4	~ 8.3
max	$\sim 2.5 \cdot 10^6$	$\sim 1.1 \cdot 10^5$	~ 126.3	~ 12.7

Figure 24: Statistical image values after segmentation.

4.2 Human Classification

The 8 color classes in which the pearls had to be classified by the 7 agents were predefined as eggplant (dark purple), white, blue, champagne (cream), gray, yellow, peacock and green (see pearls assigned by majority vote to 7 of the 8 classes in Figure 25). While 7 classes are defined by a single color, peacock is a class that is commonly used for Tahitian pearls containing several colors, but mainly green, blue, turquoise and almost always reddish or rose overtones. An additional option for pearls that subjectively do not correspond to any of the mentioned classes was given, but was used only three times and never reached a majority vote.

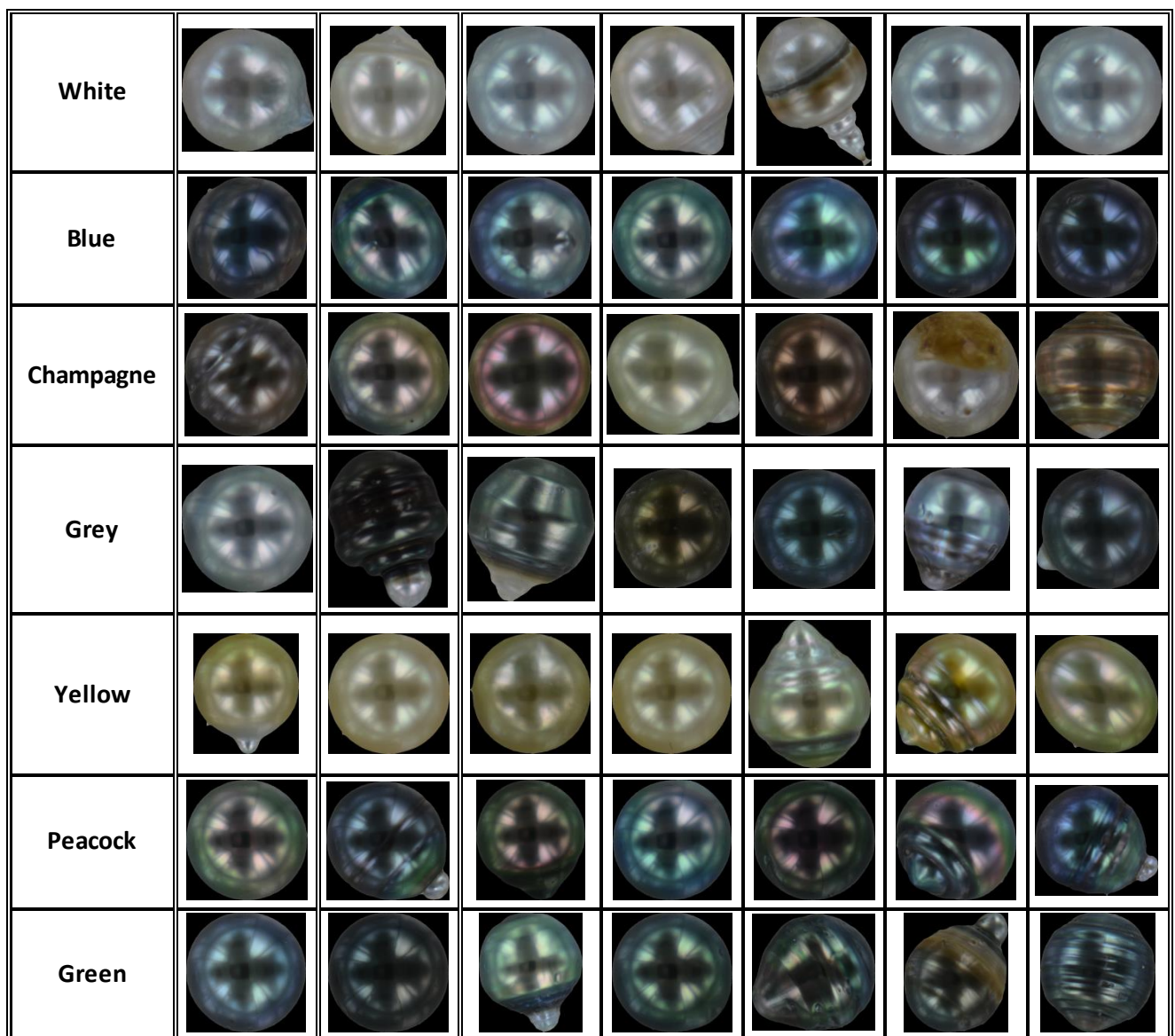


Figure 25: Pearls classified by majority vote of all 7 agents in the 7 classes of the first column.

To give the reader an impression of the influence of perception on the human classification of Tahitian pearls, the magnitude of the majority vote for each of the 150 pearls is shown in Figure 26 on the top, along with the amount of different classes assigned to the same pearl on the bottom (each bar corresponds to 1 pearl). First thing to note is that only 37 pearls were assigned to the same class by all 7 agents (~25%, all bars with magnitude 7 in the top graph, and at the corresponding position with an amount of assigned classes of 1 in the bottom graph). This is due to the general subjective nature of color perception, as well as due to the multicolored character of Tahitian pearls. Within classes ‘Aubergine’, ‘Blue’ and ‘Yellow’, not a single pearl was assigned unanimously. For 9 pearls there was not even a majority (same amount of votes for different classes, in both graphs at the position ‘Mixed’), with up to 5 different class assignments to the same pearl. Without going further into details, the main message to take to the following sections is that the human classification that will be used to train an ANN is highly subjective with a large variance between classifications of different agents.

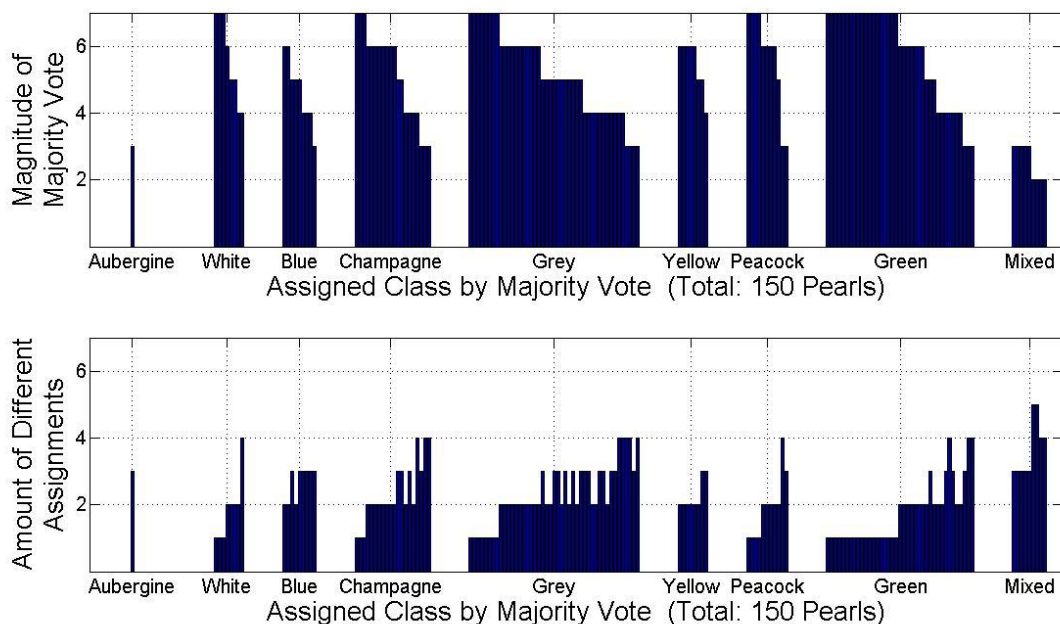


Figure 26: Distribution of majority votes (top) and amount of different class assignments (bottom) for 150 Tahitian pearls classified by 7 agents.

A second point to mention is the class population. Generally, the shown population reflects in large parts the state of Tahitian pearl cultivation. Greenish pearls and pearls with minor saturated colors (class ‘Green’ and ‘Grey’) are the larger parts of a harvest. White and yellow pearls are not typical and not very valuable due to the high production and quality of pearls

with similar colors in Japan and China. Blue and Peacock instead are unique but relatively seldom (compared to a whole harvest) features of Tahitian pearls and can achieve, assuming the remaining quality parameters are accordingly, high prices on the market. The only thing that does not fit is that only one pearl was assigned to the class ‘Aubergine’. Generally, this color is a typical one, and on the local and international market many pearls are sold by this definition. Three possible reasons might be the cause: First, illumination conditions have a large influence on the perceived color, especially secondary tones that appear as result of reflection and refraction of the incoming light by the multiple crystalline layers of nacre [NAG97]. An improper illumination might result in an increased perception of gray pearls, which would correspond to the elevated population of this class (even though it is generally a typical class). A second reason might be that the harvest did not contain pearls with aubergine colors and the classification is accordingly. A third reason might be, that the definition of a class is as well a subjective manner, meaning not only the perceived color of a pearl is biased by the perception of the observer but the class definition as such as well.

On the one hand, when analyzing visually the acquired images of pearls that were classified by majority vote as ‘Gray’, one can observe many different overtones such as green, blue, rose, and even aubergine (in the authors perception). This might point to improper illumination conditions. On the other hand, 28 of all votes (of all agents for all pearls) are class ‘Aubergine’, but only once it was a majority vote. This points to the difference in perception and against the possibility that the harvest did not contain ‘Aubergine’ pearls. Most likely, illumination and perception combined are the reasons for the low population of class ‘Aubergine’.

Based on the visual analysis summarized in the precedent paragraphs it was decided to not only use the majority vote of all 7 agents to create an artificial classification but to include the separate classification of each agent. This is mainly for the reason, that at first, a suitable feature vector that describes the color of a pearl based on human perception has to be defined. If using the majority vote, the variance of perception between different agents, as well as the ‘distribution of perception’ (as seven agents might not be representative) play a role. When using the classification of each agent separately, it is at least more likely that the votes of one agent are consistent. As the main focus of this work lies on feature generation, it gives as well the possibility to analyze if there are specific features for each agent (see Figure 27 for a work flow diagram).

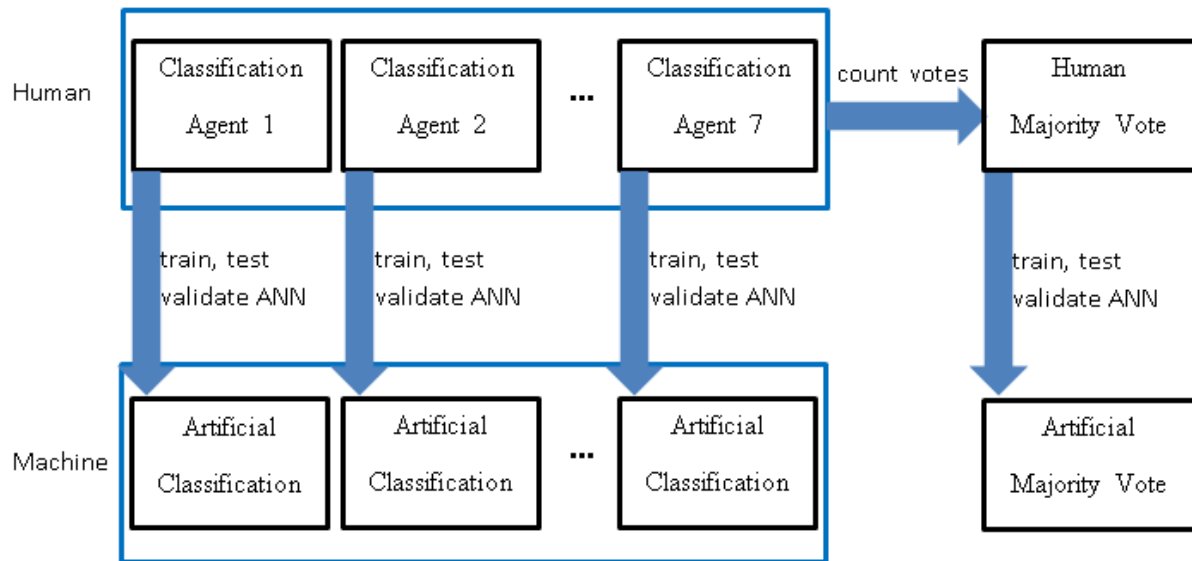


Figure 27: Workflow of the conducted experiments.

5 Classification Method

Our general methodology to classify the color of Tahitian pearls is to generate features by normalized *rgb* histogram binning and train an Artificial Neural Network based on the obtained feature vectors and their class labels obtained by the human classification. ANN were chosen, as they are one of the most powerful tools for supervised multiclass classification and hence widely applied in computer vision [EGM02]. The ANN type used for our experiments is a feed-forward ANN with error backpropagation and one hidden layer. The concept will be briefly introduced, for a detailed description of this and other types of ANN the reader is referred to [CLA09], [HAY05], or [IZE08].

An Artificial Neural Network consists of interconnected neurons organized in different layers. Along the connections information is passed from one neuron to another. Each neuron has an activation function that defines how to react to incoming information. The topology of the network used for our experiments is shown schematically in Figure 28. On the left is the input layer with a number of neurons that is defined by the size of the feature vector used to describe an object (here the color of a pearl). All neurons of the input layer are connected to all neurons of the hidden layer. The incoming information at each neuron of the hidden layer is the weighted sum of the input neurons (weighted sum of features). This sum is transformed and passed to every neuron of the output layer according to the used activation function. The number of neurons in the output layer is determined by the number of classes (here the predefined color classes).

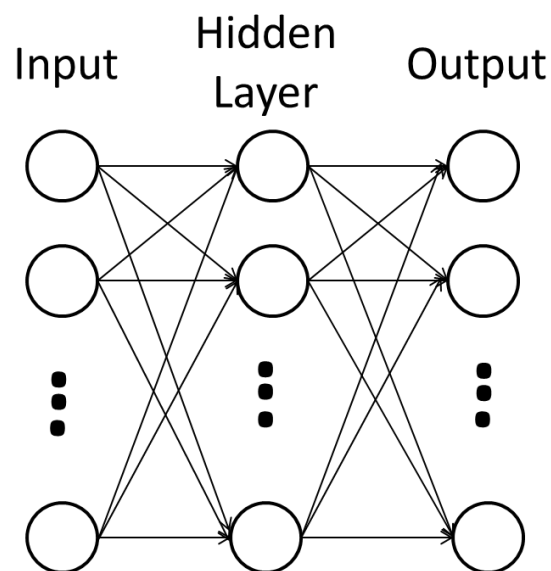


Figure 28: Topology of a feed-forward neural network with one hidden layer.

The incoming information at each neuron in the output layer is the weighted sum of the outputs of the neurons of the hidden layer. The weighted sum is as well processed with the chosen activation function. The values of the output neurons, after the information starting at the input neurons is processed through the whole network, is compared to the desired output (class label of the current feature vector). The error between output and class label is passed through the network in opposite direction and the weights are adapted to minimize the error (Figure 29). Now, the feature vector is again presented to the network, the information is processed and the weights again adapted. The process of iterative, error dependent weight adaption to minimize the output error is called learning.

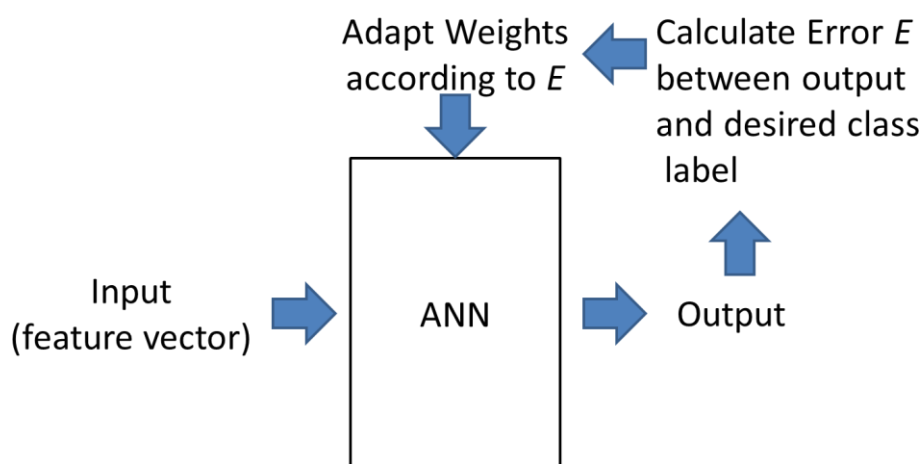


Figure 29: Schema of the learning procedure of ANN by weight adaption.

5.1 Data Set Splitting

To develop a suitable ANN model, the available data set is typically split in three subsets: training set, test set and validation set. The training set is used to train a given network by repeatedly feeding the feature vectors of the training set into the network. At each iteration, the error between network output and humanly assigned class labels is calculated (prediction error) and the network adapted so that the error is continuously minimized. As ANN tend to overfit, the test set is used to identify the optimal state of a learning network in means of generalization (the ability of classifying unseen data correctly). As the test data has no influence on the training procedure, it simulates the performance of the network on unseen data. This procedure is shown in Figure 30. The blue line corresponds to the prediction error of the training data and the green line to the prediction error of the test data. While the

training error decreases continuously, the test error, after initial decrease, stagnates and even increases. The optimal state of the learning network in means of generalization is hence defined by the minimum of the prediction error of the test set.

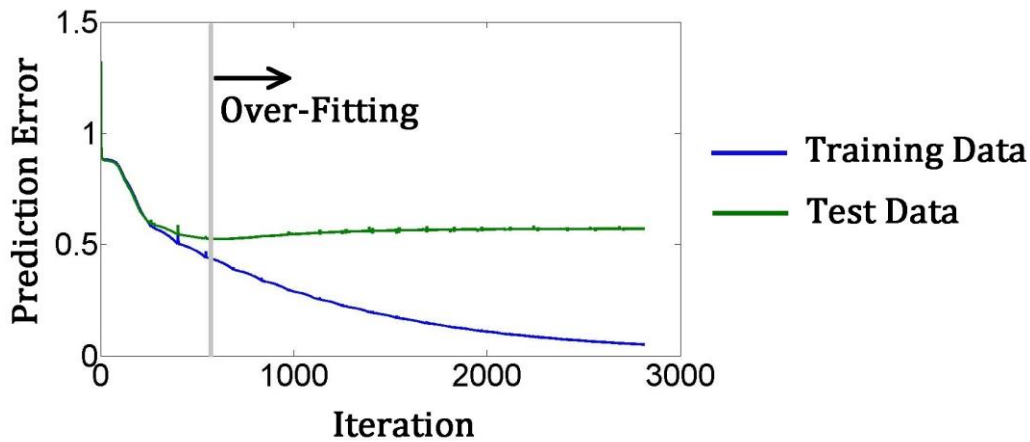


Figure 30: The effect of over-fitting during the ANN learning procedure.

To identify a suitable ANN model, different models are trained with the training data set and the minimal prediction error of the test set of each model is compared. The optimal model is identified by the absolute minimum of the test set prediction errors. As the chosen model is likely to be biased by the test set data, the validation set that has been used neither for training nor for model selection is used to validate the generalization capabilities of the chosen model.

It has been shown that the method used to split the original data in three subsets has a major influence on the generalization capability of the network [REI10], [WU12]. While more or less uniformly distributed data can be split randomly, this method is not suitable for Tahitian pearls. As within one color class pearls with different color occur (see Figure 25, especially classes gray, champagne and peacock), a deterministic method has to be applied to ensure that in each of the three data sets the color variance of each class is equally represented.

For this purpose the DUPLEX method was applied, to ensure an optimal data representation in each of the three subsets [REI10], [WU12], [KEN69]. As in this approach the original data set is split based on mutual Euclidian distances, feature vectors for each pearl have to be already calculated. As one of the main goals of our work is to analyze a large variety of different feature vectors but the data split is supposed to be done only once prior to model selection or comparison for a given human classification, a feature definition that is unbiased to the ones used in the experiments has to be determined. It was decided to use a multidimensional histogram of all three normalized *rgb*-channels together with the Intensity

channel. Binning was done with 16 bins per channel. The data set was split in 50% training data, 25% test data and 25% validation data. No further tests or adaptations of this splitting configuration in means of histogram channels, bins, etc. were done, as any change might bias the split in one way or the other.

It has to be stated that the use of three data sets assumes that each state within a class occurs at least three times. Due to the variety of Tahitian pearls, this cannot be guaranteed for all classes. Still, it was decided to use three data sets (3-fold cross-validation) as it is applied standardly, proven methods for data splitting exist and it is much faster than exhaustive methods as for example leave-one-out cross-validation. For the latter one each experiment would have to be done 150 times which was, seeing that all performed tests take together several days of calculation, not realizable. Anyway, once the choice of histogram orientations is narrowed, exhaustive cross-validation might be more suitable for ANN performance verification in regards of classifying the color of Tahitian pearls.

5.2 Feature Configuration

Based on the formalization of normalized *rgb* histogram binning, general parameters for feature generation are: number of different histogram orientations (amount of chromatic indices), type of histograms (concatenated, multidimensional or hybrid), orientation of each histogram, binning strategy per histogram and number of bins per histogram. As one of the main question is if and to which extend the histogram orientation has an influence on the classification, it was decided to evaluate histogram orientations over the whole range of 0° to 179° (the remaining 180° are redundant), with an increment of 1° . To evaluate the influence of the topology of the normalized *rgb* space, two binning strategies were applied: equidistant binning and topological binning (section 3.5).

As shown in section 3.3, in many papers the *r*- and *g*-channel are used exclusively and based on the argument of channel redundancy (or even without any argument). It has been shown that the argument is mathematically incorrect. To evaluate the discrepancy between the standard choice of *r*- and *g*-channel and the remaining two channel combinations, two chromatic indices are used for feature generation, both defined by a Hue with a difference of 120° . As the pearl color classes contain the classes ‘white’ and ‘gray’, an achromatic value has to be considered as well. Here, the Intensity, the sum of elements of an original RGB vector was chosen. The intensity is subject to similar non-uniform effects due to the discrete

character of the RGB space as those mentioned in section 3.5. When topological binning is tested, all two chromatic values as well as the intensity channel are binned with adapted non-equidistant boundaries.

The number of bins per histogram was empirically set to 16 bins over the whole normalized *rgb* space range for all generated histograms and all test series. The parameter was fixed to exclude its influence on the variation analysis of histogram orientation and binning strategy (equidistant and topological).

6 possibilities to combine the three chosen values to bin exist. The least computationally expensive is to concatenate the histograms of each value, while the most computationally expensive is to generate a non-concatenated histogram out of the 3-dimensional data distribution of *r*-, *g*- and Intensity channel (*I*). Here, computationally expensive does not only concern the histogram generation but the whole classification procedure, as the complexity of each ANN training iteration depends on the number of features. For the moment, the concatenated combination of multidimensional *rI* histogram and multidimensional *gI* histogram was chosen. This was done for the reason that the color of Tahitian pearls is typically assessed with a Hue and an intensity value combined (e.g. dark blue with light green overtones). Anyhow, other possibilities will be considered in a future work.

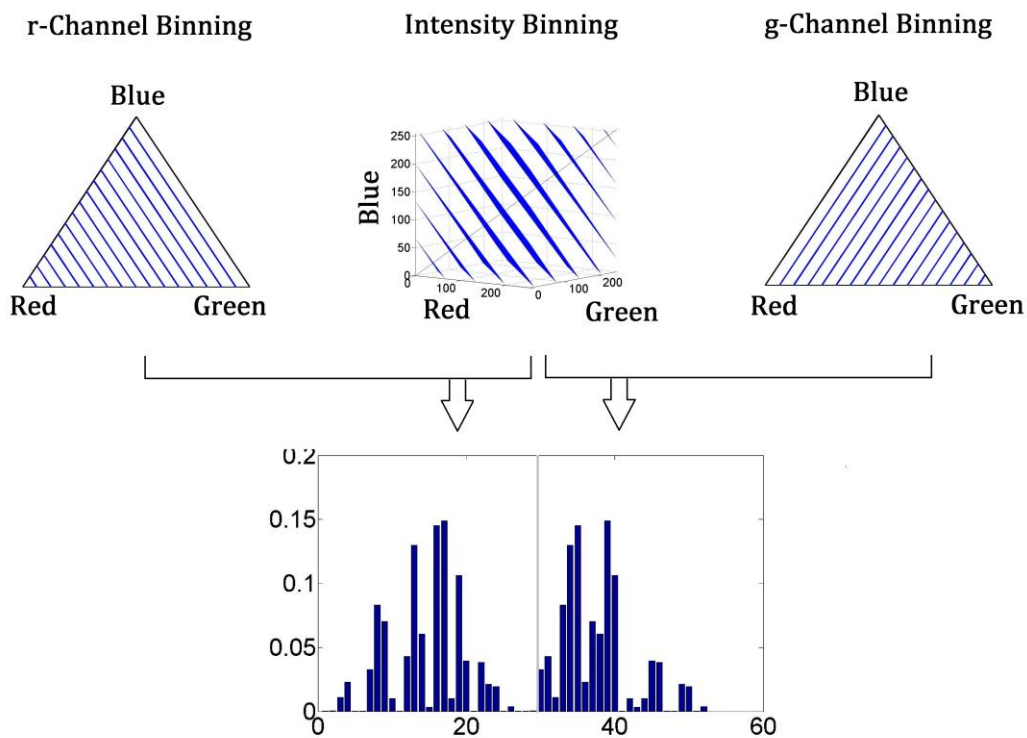


Figure 31: Applied general feature configuration: Concatenated histogram of the *rI*-histogram (top left) and of the *gI*-histogram (top right).

To summarize, the general feature vector configuration is based on two chromatic indices that can be described with two Hues with a difference of 120° , and the Intensity. Two histograms are calculated. One based on the 2-dimensional distribution of the first chromatic index and Intensity (Figure 31 on the top left), and another based on the 2-dimensional distribution of the second chromatic index and Intensity (Figure 31 on the top right). Both histograms are concatenated (Figure 31 on the bottom).

As the goal is to analyze the influence of histogram orientation, this procedure is applied for a Hue of the first chromatic index varying from 0° to 179° with a 1° increment. The second index is defined by the Hue of the first index plus 120° . Examples of the two obtained chromatic indices for different Hues of the first index are shown in Figure 32. It can be seen that with this configuration, histograms based on *rg*-channels, *gb*-channels and *br*-channels are included. This allows analyzing the difference between the standard use of *r*- and *g*-channel and the remaining two permutations. Additionally, combinations of other popular chromatic indices of the literature are included as well (*r-g*, *g-b*, *b-r*). The terminology for a certain feature vector constellation used in the next sections is shown in the last column of Figure 32. As the feature vector constellation is defined by the Hue of the first index, the expression f_α means the two chromatic indices used to calculate feature vector f_α are based on histogram orientation α for the first index and $\alpha+120^\circ$ for the second.

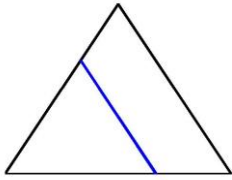
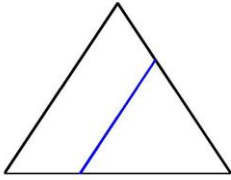
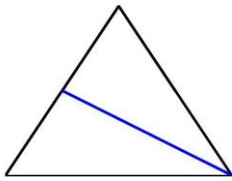
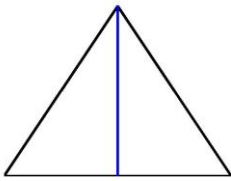
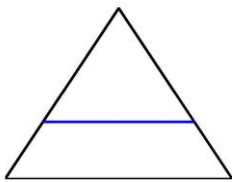
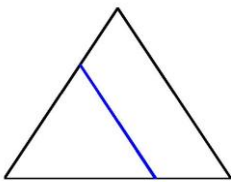
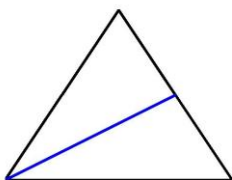
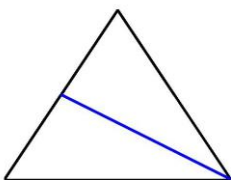
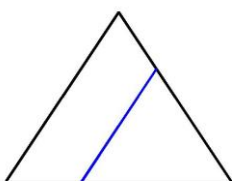
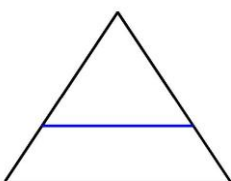
First index		Second index		Terminology
Histogram orientation (α)	Schema of histogram orientation in the rotated Maxwell triangle	Histogram orientation (α)	Schema of histogram orientation in the rotated Maxwell triangle	feature vector f_α based on chromatic indices α , $\alpha+120^\circ$ and intensity
Chromatic index		Chromatic index		
0°		120°		f_0
r		g		
30°		150°		f_{30}
$r-b$		$g-r$		
60°		180°		f_{60}
b		r		
90°		210°		f_{90}
$g-b$		$r-b$		
120°		240°		f_{120}
g		b		

Figure 32: 5 of 180 tested histogram orientations that include all main chromatic indices used in the literature.

5.3 ANN Configuration

For classification, a feed-forward neural network with one hidden layer and error backpropagation, as used in [NAG94] for pearl color classification, was chosen. The training is done in batch mode, meaning the feature vectors of every pearl from the training set are presented to the network at every iteration in parallel. The learning rate is dynamically adapted by using the ‘bold driver’ as proposed in [BAT89], as here an optimal trade between training speed and accuracy can be reached. Sigmoid activation functions are used as they correspond to human biological data processing and weights initialized by ‘normalized initialization’ [GLO10]. For faster convergence a bias neuron was added to the input layer.

The number of neurons in the hidden layer was determined by a brute force search in the range of 5 to 25 neurons. The search is done only once for each one of the eight human classifications (7 agents and the majority vote) prior to a test series to exclude the influence of different ANN topologies on the test series results. For this purpose the feature constellation f_0 and equidistant binning is used. This means, if the network topology is biased towards a certain feature constellation, it will be the standard combination of r - and g -channel and equidistant binning. The optimal number of hidden neurons for each test series is defined by the maximum classification result of the test data (Figure 33).

Human Classification	Neurons in Hidden Layer
Agent 1	11
Agent 2	12
Agent 3	20
Agent 4	24
Agent 5	25
Agent 6	24
Agent 7	16
Agent 8 (Human Majority Vote)	24

Figure 33: Number of neurons in the hidden layer for each test series.

5.4 Training and Evaluation Values

Each ANN is trained with the training data set. Training is done until the mean square error between predicted class labels and human class labels of the whole training data set is below 0.05. At each iteration, the classification rate of the test set, validation set and the whole data is calculated. The artificially assigned class labels for the whole data is stored each time the classification rate of the test set is greater than the maximum of all prior iterations. After the training is stopped, the iteration of the global maximum of the test set classification is assigned as the optimal state of the ANN in means of generalization (first dashed line in Figure 34). The classification rate of all data sets and the artificial class labels at this stage are stored. Additionally, the maximum of training set and validation set classification rate are stored. The obtained values and their ID that will be used in the following sections can be found in Figure 35 in the first 7 rows.

As the classification results of non-uniformly distributed data tend to vary [REI10], each artificial classification was done 25 times. This means for each specific configuration regarding human classification, binning strategy and feature vector, 25 separate ANNs were trained. Afterwards, the obtained evaluation values of all 25 trained ANNs were averaged (rows 8-13 in Figure 35) to reduce the influence of variance. For the later analysis of the artificial majority votes, the class labels of the ANN out of 25 with identical configuration with the maximum test data classification rate are used ($\text{Labels}(\max(\text{Te}_{\max}))$) in Figure 35).

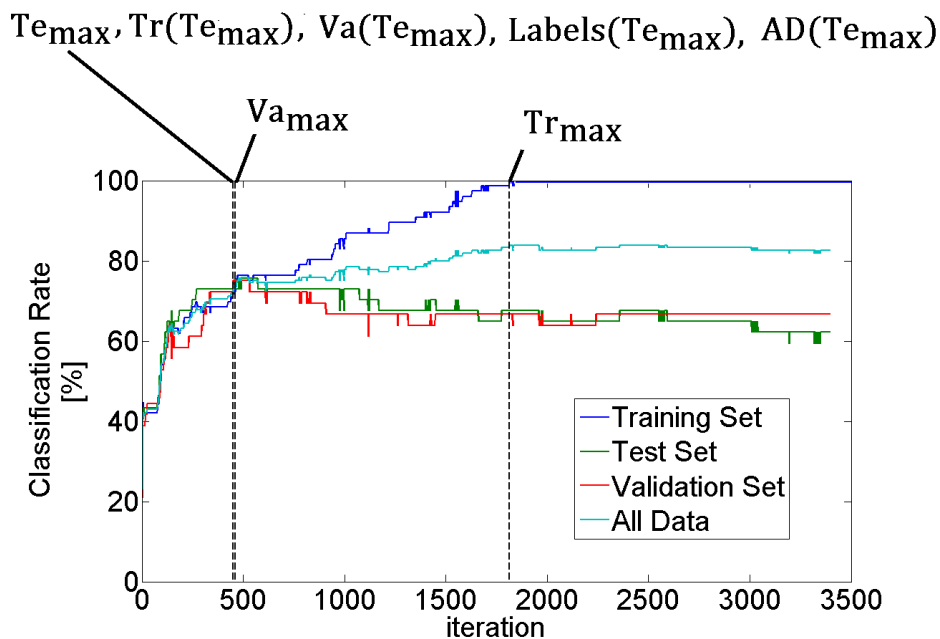


Figure 34: Schema of ANN training visualizing the states at which the corresponding evaluation values are obtained.

Evaluation Value	Description	Obtained after	Used for
Te_{max}	Maximum classification rate of test set	training of one ANN	
Tr_{max}	Maximum classification rate of training set		
Va_{max}	Maximum classification rate of validation set		
$Tr(Te_{max})$	Classification rate of training set at iteration of Te_{max}		
$Va(Te_{max})$	Classification rate of validation set at iteration of Te_{max}		
$AD(Te_{max})$	Classification rate of all data at iteration of Te_{max}		
$Labels(Te_{max})$	Class labels of all data at iteration of Te_{max}		
AV_{AD}	Average of all 25 $AD(Te_{max})$	training of 25 ANN with identical configuration	Qualitative analysis (section 6.1)
$Labels(max(Te_{max}))$	Class labels of all data at maximum of all 25 Te_{max}		
AV_{Tr}	Average of all 25 $Tr(Te_{max})$		Quantitative analysis (section 6.2)
AV_{Te}	Average of all 25 Te_{max}		
AV_{Va}	Average of all 25 $Va(Te_{max})$		
AVX_{Tr}	Average of all 25 Tr_{max}		
AVX_{Va}	Average of all 25 Va_{max}		

Figure 35: ID of evaluation values (1st column), their brief description (2nd column), when they are obtained (3rd column) and their use for evaluation (4th column).

5.4.1 Qualitative Analysis

A qualitative analysis of the influence of histogram orientation and binning strategy will be done with the average of the classification rate of a whole data set. Splitting a data set is done to evaluate the performance of an ANN in regards of two different capacities: the capacity to extract knowledge from labeled data and the capacity to apply the extracted knowledge to unseen data. For analyzing generally if and to which extend histogram orientation and binning strategy influence the classification performance, a separate consideration of these two aspects is not absolutely necessary. The qualitative analysis, done in section 6.1 with the average of the classification rate of a whole data set, is hence focused purely on the theoretical aspects of normalized *rgb* histogram binning.

5.4.2 Quantitative Analysis

In section 6.2, a quantitative analysis of the experimental results is done. For this purpose the average classification rates out of 25 trained ANN for each of the three sets will be used. Classification rates are compared quantitatively, but the results have to be handled with care, as the optimal network configuration per human classification was obtained based on f_0 and equidistant binning. It means the results of all other features and topological binning might not reflect the possible optimum. The analysis serves the goal to get an idea of the general range of classification results, meaning to get an idea if it is generally feasible to classify the color of Tahitian pearls based on its perceived color with the proposed concept.

5.5 Summary

In the previous sections the concept and the parametrization of experiments to analyze the influence of normalized *rgb* histogram binning on the classification of Tahitian pearls based on their perceived color was presented. 8 human classifications (7 agents and their majority vote) will be reproduced artificially with ANN (first loop in Figure 36). The general ANN topology is chosen based on the optimal classification of the test set data with features f_0 and equidistant binning, as this configuration is the standard application of normalized *rgb* histogram binning in the literature (second loop in Figure 36). For each of the 8 human classifications 180 different histogram orientations for each of the two binning strategies (equidistant and topological) are used for a separate artificial classification (loops three and

four in Figure 36). Each of the specific constellations in regards of the mentioned parameters is used to train 25 separate ANNs, to reduce the influence of variance by averaging the obtained 25 classification results (fifth loop in Figure 36). This means, for the conducted analysis 72360 ANNs were trained, tested and validated.

Pseudocode	corresponding section
<code>for agent 1:8</code>	section 4.2
split data in 3 sets according to human classification	section 5.1
for neurons in hidden layer $n=5:25$	section 5.3
for $j=1:25$	section 5.4
train ANN(f_0 , equidistant binning, n)	
get $Te_{j,n,max}$	
end	
end	
get n_{opt} at $\max_j (Te_{j,n,max})$	
for binning strategy $bs=1:2$ (equidistant, topological)	section 3.5
for $\alpha=0^\circ:179^\circ$	section 5.2
for $j=1:25$	section 5.4
train ANN(f_α , bs , n_{opt})	sections 5.3, 5.4
get $Te_{j,max}$, $Tr(Te_{j,max})$, $Va(Te_{j,max})$,	section 5.4
$Tr_{j,max}$, $Va_{j,max}$, $Labels(Te_{j,max})$, $AD(Te_{j,max})$	
end	
get AV_{AD} , AV_{Tr} , AV_{Te} , AV_{Va} , AVX_{Tr} , AVX_{Va}	section 5.4
$Labels(\max_j (Te_{j,max}))$	
end	
end	
end	

Figure 36: Pseudocode of experiments.

6 Results and Discussion

Within this section the experimental results will be analyzed quantitatively (section 6.1) and qualitatively (section 6.2). The first analysis is focused on theoretical aspects of *rgb* histogram binning, while the second is used to estimate if and in which range of accuracy it is possible to classify Tahitian pearls based on their perceived color.

6.1 Qualitative Analysis

Within this section the experimental results will be analyzed qualitatively. For this purpose, the average of the classification results of a whole data set AD_{Av} out of 25 trained ANNs will mainly be used as indicator of global performance variation. This evaluation value cannot be used to quantify the classification performance of Tahitian pearls, as prediction accuracy and generalization accuracy are not evaluated separately. The value serves the single purpose of analyzing if and to which extent histogram orientation and binning strategy have an effect on color object classification with ANN.

6.1.1 Channel Redundancy

In Figure 37 the classification rates for the whole data for feature vectors f_0 , f_{60} and f_{120} with equidistant binning are shown for each human classification (here, and in all following figures with human classification as abscissa, ‘agent 8’ is used as synonym for the human majority vote out of all 7 human votes). The first feature vector corresponds to the standard use of normalized *rg*-channels, while the other two are calculated based on the remaining two channel permutations. It can be seen that the results between the three channel permutations vary for each agent. As shown theoretically in section 3.3, the assumption that only the *rg*-channels have to be used due to redundancy does not hold. Additionally, it can be seen that the general performance of each channel permutation depends on the human classification. This means, not only are the histograms based on the three permutations not redundant, but their descriptive power depends on the human classification and therefore on the data distribution.

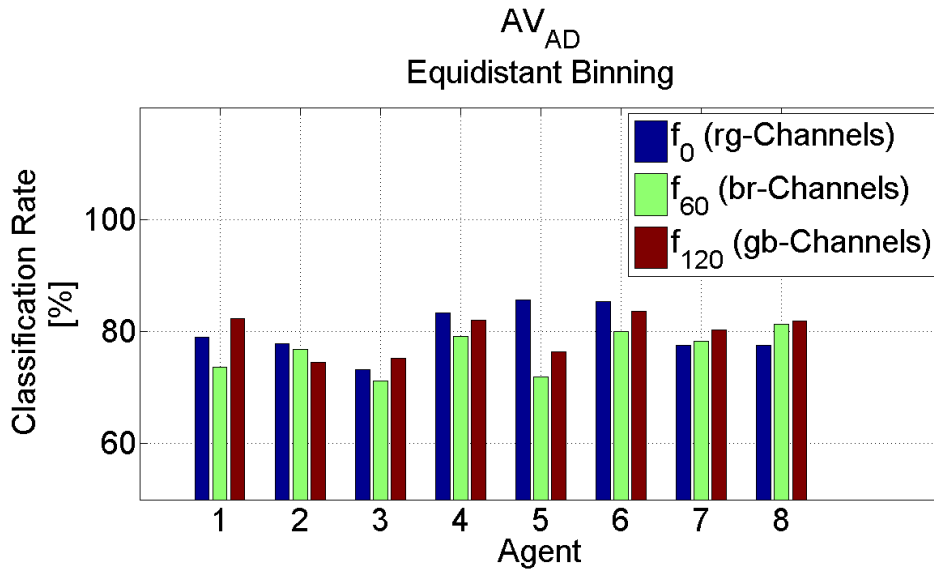


Figure 37: Classification performance for feature vectors based on the three normalized *rgb* channels.

6.1.2 Influence of Histogram Orientation per Agent

In Figure 38, the classification rate for the whole data set for each 179 feature vectors is shown for each human classification. It can be seen that for every human classification the global classification performance varies in a range of at least 15%. It means, the histogram orientation has, from a global point of view, a significant influence on the performance of an ANN with fixed topology.

In Figure 39, the global ANN performance for feature vectors f_0 , f_{60} and f_{120} is shown together with the maximum performance per human classification. The, to the maximum global performance corresponding Hue α for each agent are listed in Figure 40. It can be seen that almost all maxima are at different Hues, which supports the hypothesis that there might be specific features that correspond to the perception of a single agent. Furthermore, it can be seen that not only the standard choice of *rg*-channels, but as well the use of only a handful chromatic indices in the literature is not generally justifiable, as all maxima of the global performance of each human classification are at chromatic indices that have never been used in standard approaches.

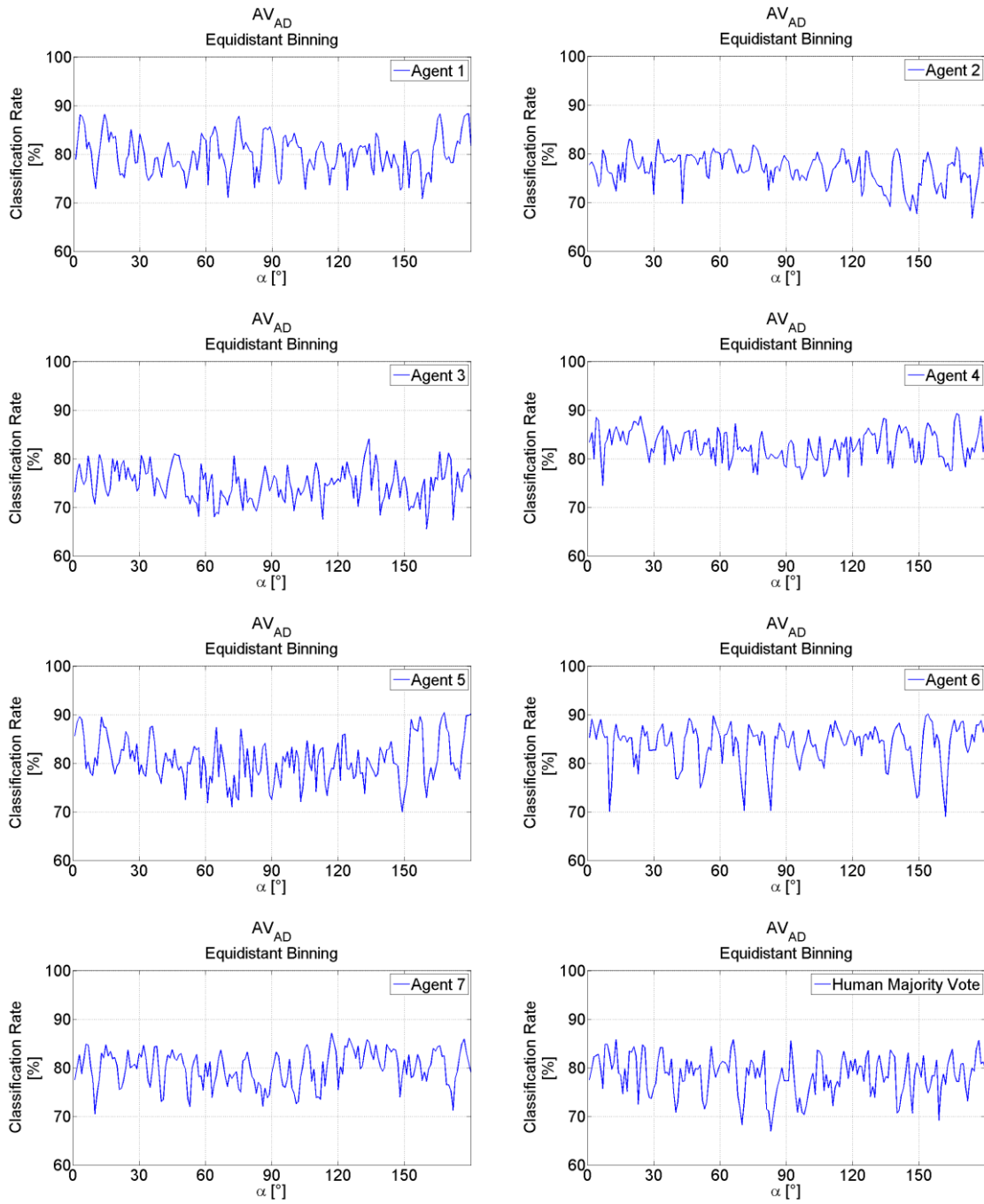


Figure 38: Average classification performance per feature orientation for all 7 agents and the majority vote.

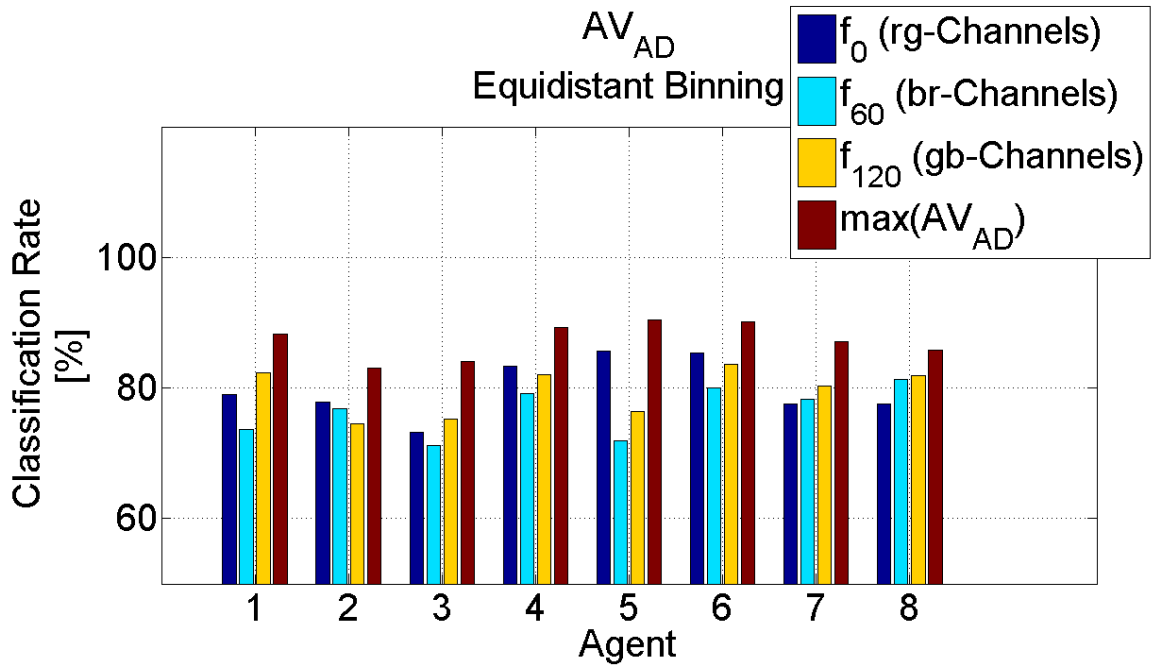


Figure 39: Global classification performance for feature vectors based on the three normalized *rgb* channels and maximum performance.

Human Classification	Agent 1	Agent 2	Agent 3	Agent 4	Agent 5	Agent 6	Agent 7	Agent 8
α of $\max(AV_{AD})$	156°	19°	126°	158°	146°	17°	156°	162°

Figure 40: Histogram orientation at maximum global ANN performance per human classification (correspond to red bars in Figure 39).

6.1.3 Influence of Histogram Orientation per Color Class

To analyze the influence of histogram orientation per color class, the classification rate of each color class of the whole data set at the maximum test set classification rate out of 25 trained ANN was calculated. The following figures show the maximum global performance (blue bars) and the minimum global performance (red bars) for each color class per agent. If there are no blue graphs, the corresponding agent did not use this color class more than two times (and hence these votes were not considered in the artificial classification). If there is no red bar, the minimum classification rate of the corresponding class and agent is 0.

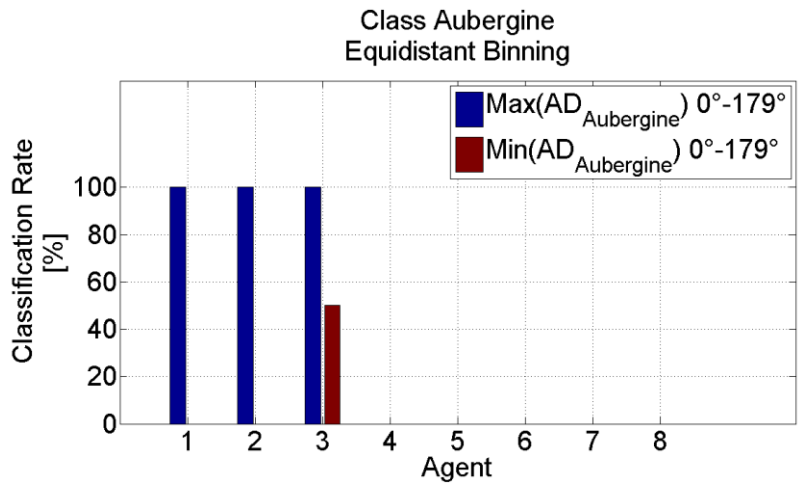


Figure 41: Maximum and minimum global performance for class 'Aubergine' per agent.

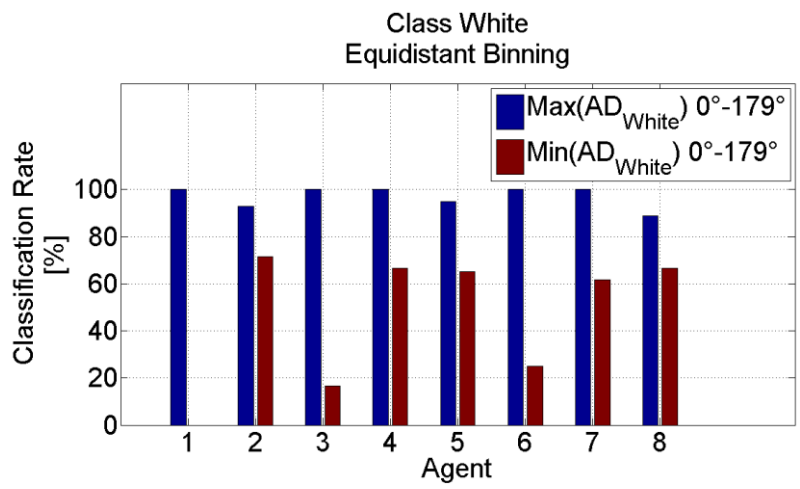


Figure 42: Maximum and minimum global performance for class 'White' per agent.

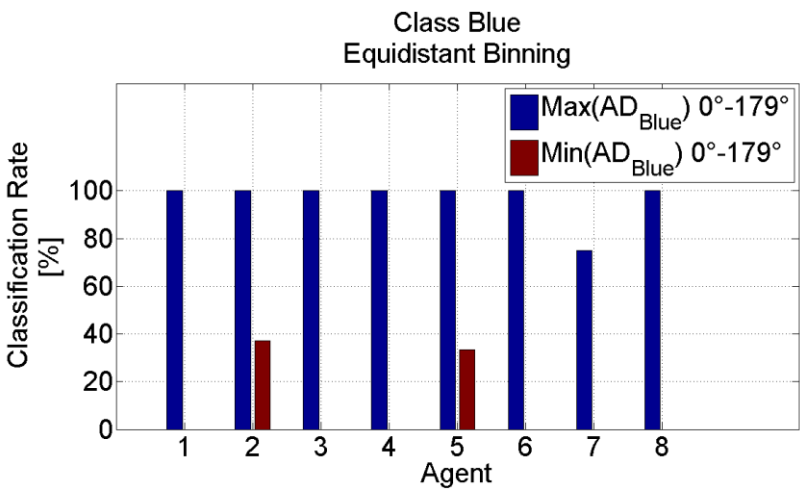


Figure 43: Maximum and minimum global performance for class 'Blue' per agent.

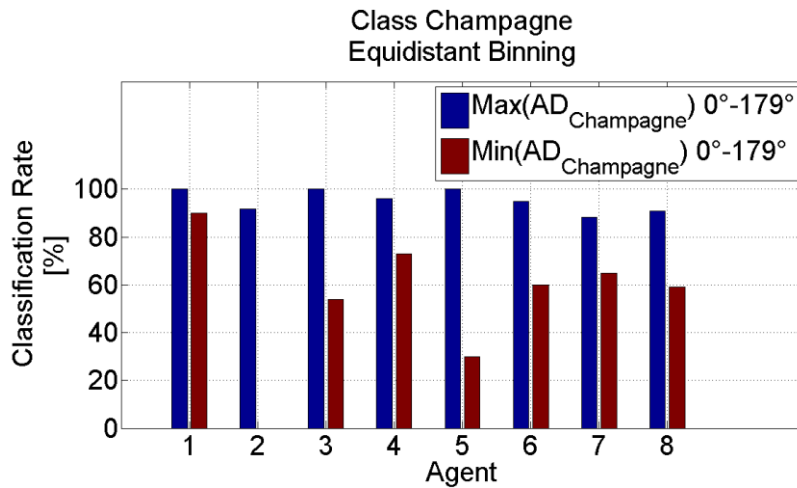


Figure 44: Maximum and minimum global performance for class 'Champagne' per agent.

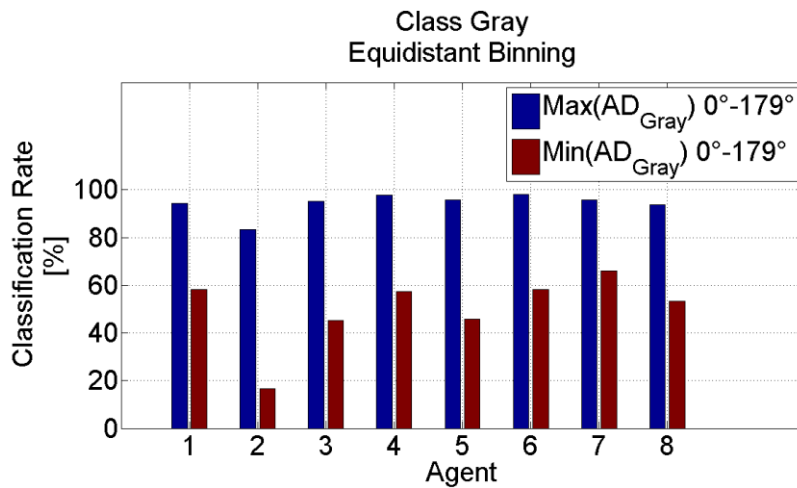


Figure 45: Maximum and minimum global performance for class 'Gray' per agent.

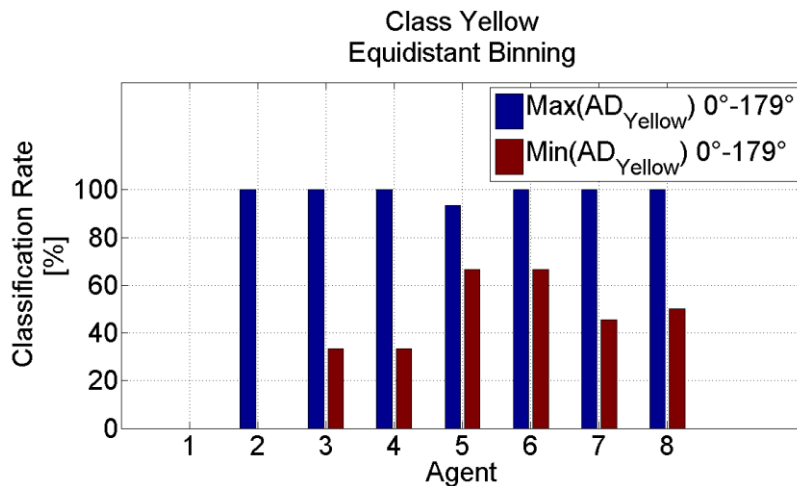


Figure 46: Maximum and minimum global performance for class 'Yellow' per agent.

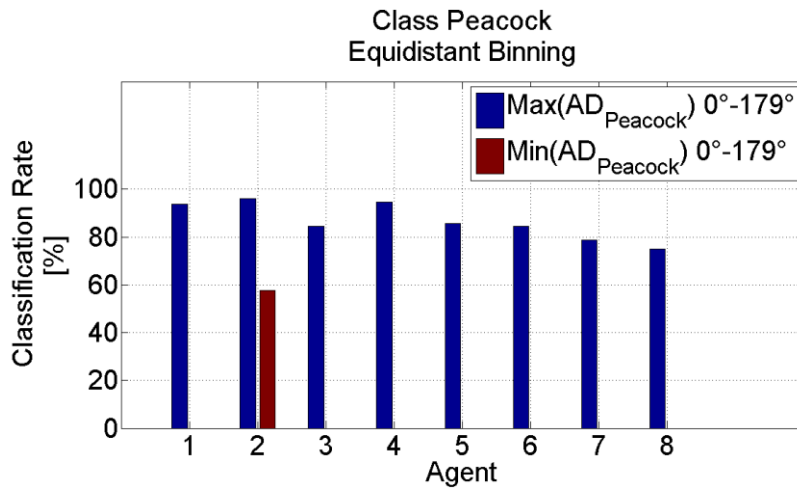


Figure 47: Maximum and minimum global performance for class 'Peacock' per agent.

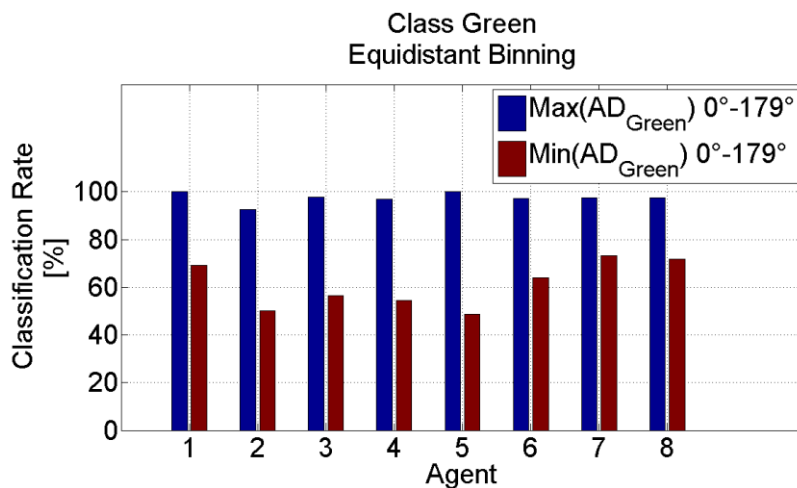


Figure 48: Maximum and minimum global performance for class 'Green' per agent.

As for every graph and for every agent a difference between maximum and minimum exists, histogram orientation has an influence on the classification rate of objects (here pearls) of the same class. The effect on the general classification capacities can be seen in Figure 49. Exemplarily, the global performance of classes 'Aubergine' and 'Blue' are shown for agent 1 over all feature vectors. It can be seen that the classification maximum of class 'Aubergine' at a Hue of 155° does not coincide with the maxima of class 'Blue'. If there are optimal feature vectors for each class, the classification based on one feature vector will unlikely reach 100% as the data distribution of the classes are different, and hence optimal feature vectors for each class will be at different Hues. Again, the data distribution dependent descriptive power of chromatic indices can be observed.

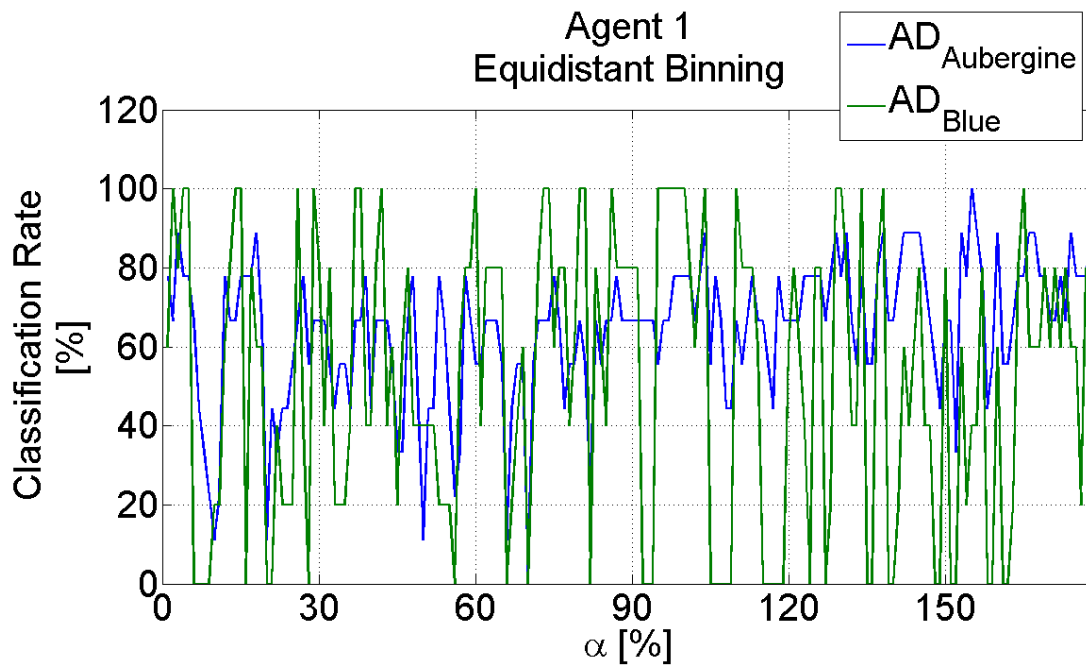


Figure 49: Global performance of classes "Aubergine and 'Blue' for agent one for all feature vectors.

6.1.4 Equidistant Binning vs Topological Binning

In Figure 50 the influence of the binning strategy (equidistant: blue lines, topological: green lines) on the global ANN performance over all feature vectors for all agents is shown. Two characteristic differences can be observed. First, topological binning is subject to lower fluctuation between subsequent feature vectors. Second, in some cases (agents 1, 2, 3 and majority vote) the general performance of topological binning is for almost all feature vectors significantly larger. This is specifically interesting considering that the network topology was optimized based on the feature vector f_0 and equidistant binning, meaning the network configuration is not adapted to topological binning.

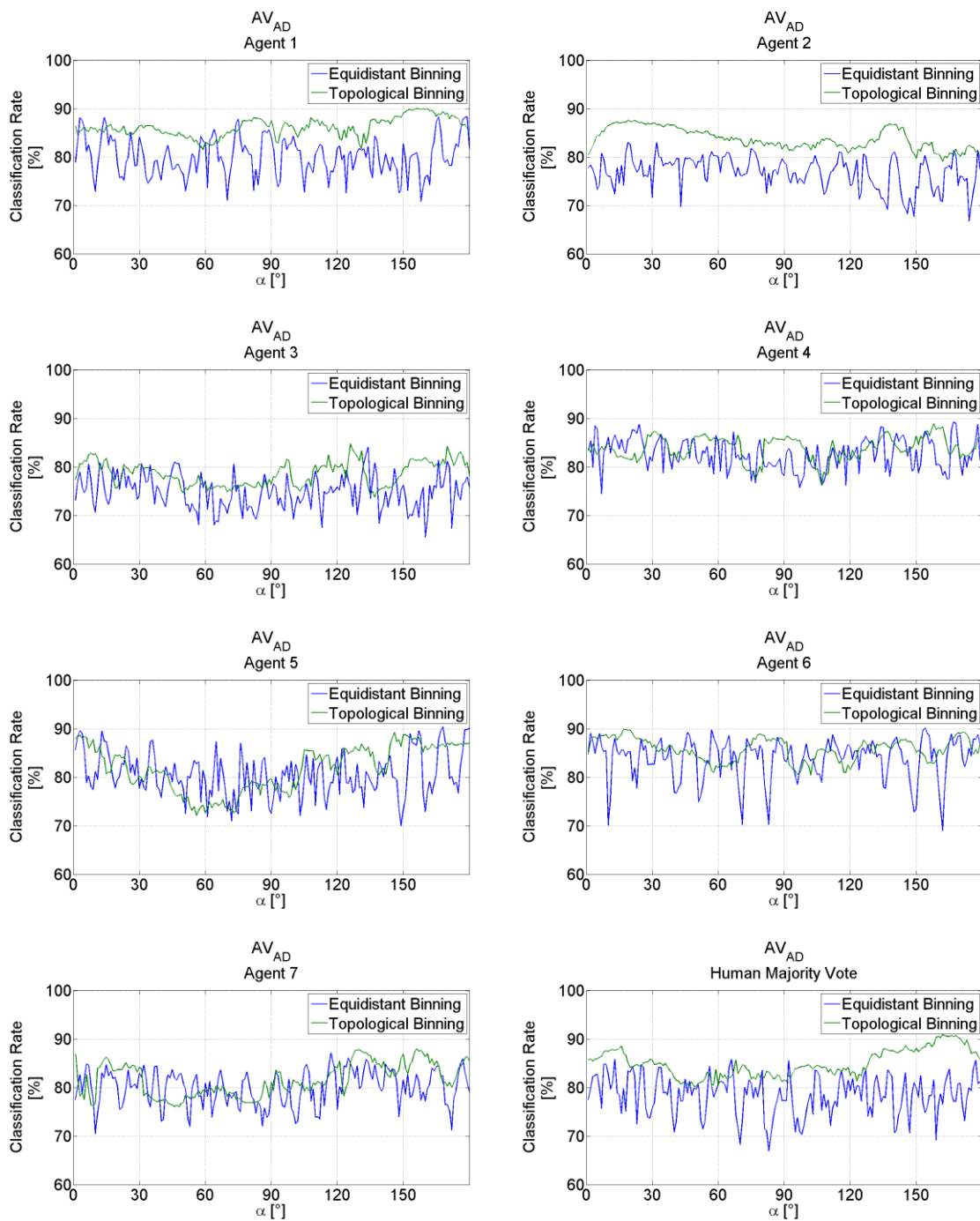


Figure 50: Equidistant binning (blue lines) vs topological binning (green lines) over all feature vectors for all agents.

6.1.5 Summary

The qualitative analysis of the previous sections has shown that histogram orientation as well as the binning strategy has a significant influence on the global performance of the ANN-based color classification of Tahitian pearls. Even though the influence was analyzed with a specific application, some general conclusions can be drawn.

The results indicate that optimal feature vectors depend on the data distribution and hence the whole range of chromatic indices should be considered for a given application. The exclusive use of *rg*-histogram binning, and the general use of only a handful chromatic indices in the literature is a drastic limitation of the possibilities of normalized *rgb* histogram binning for color object classification.

As optimal feature vectors depend on the data distribution, feature selection in the case of multiple classes should not only be done in regards of the general classification result, but in regards of classification accuracy per class as well.

The use of topological binning has by trend a positive influence on the classification result for a given data set and ANN topology. Anyhow, the difference to equidistant binning depends on the histogram orientation and is not for all feature vectors superior. But, seeing the partially drastic impact on the global classification performance (increase of up to 21% for a given data set, ANN topology and feature vector), the use of topological binning should at least be considered.

6.2 Quantitative Analysis

In this section the classification results will be analyzed quantitatively. The analysis serves the goal to estimate if and in which range of classification accuracy it is possible to classify Tahitian pearls based on their perceived color. Therefore, boxplots will be used that show the statistical distribution of the classification rate of a data set over all feature vectors. Whiskers are at the minimum and maximum classification rate. As the network topology of the used ANNs is not adapted to each feature vector and the bin number is fixed to 16 bins, the results allow only a preliminary (and likely pessimistic) estimation. Optimization possibilities will be explored in a future work.

6.2.1 Accuracy Range

In Figure 51 the statistical distribution of the classification rate of training data is shown for each agent. Each median is above 80%, showing that the chosen network topologies are generally able to classify labeled data at their state of maximum generalization in regards of the test set. Depending on the histogram orientation, the training data at the state of maximum generalization can be classified with accuracy close to 100% for each agent. The maximum classification rate of the training data (Tr_{max}) was for every trained ANN at 100%, which is typically not the case if the number of neurons in the hidden layer is too small.

The statistical distribution of the classification results of the test data over all feature vectors is shown in Figure 52. The median values of all agents range between 64% and 77%, which corresponds to the pearl color classification results of NAG94, who obtained pearl color classification accuracy with ANN of 71% for the test data. The orientation dependent maxima range from 73% to 86%.

In Figure 53, the statistical distribution of the classification results of the validation data over all feature vectors is shown. The median of all human classifications range from 64% to 81%, with maxima between 71% and 94%.

Generally, the distribution of classification rates of all data sets for all human classifications shows that the chosen method of using ANN and normalized *rgb* histogram binning is suitable for the color classification Tahitian pearls, specifically, seeing that the median of the non-optimized approaches for test and validation data is scattered around 70% (non-optimized as the network topologies were determined exclusively based on the feature vector f_0). Additionally, maximum classification rate (upper whiskers) of test and validation data for each agent indicate that with a suitable feature selection classification rates of up to 90% are possible.

Noticeable is the variance of classification rates between different agents. One reason might be that some agents are more experienced in pearl classification and their votes are hence more consistent. Another reason might be that the general feature configuration based on two chromatic values and their geometrical relation (120° difference between both Hues) does not ideally map the perception of certain agents.

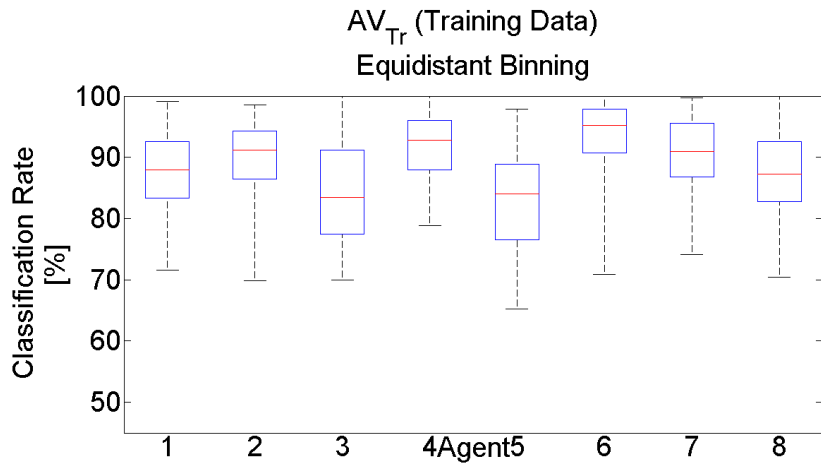


Figure 51: Boxplot of the classification rate for training data per agent.

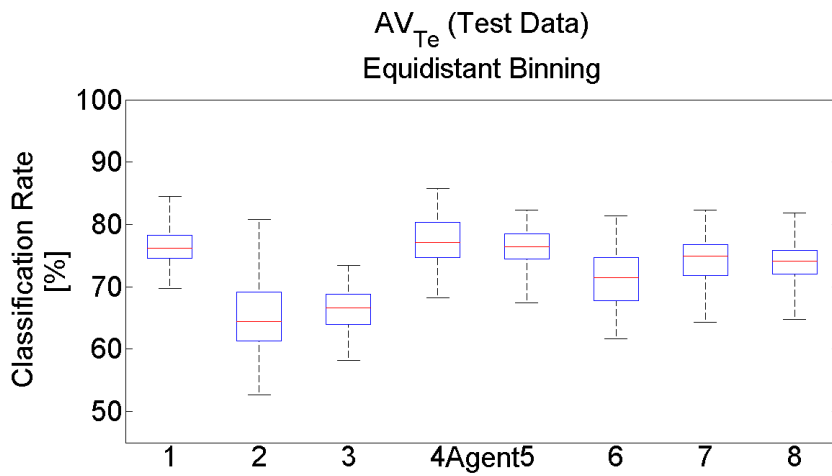


Figure 52: Boxplot of the classification rate for test data per agent.

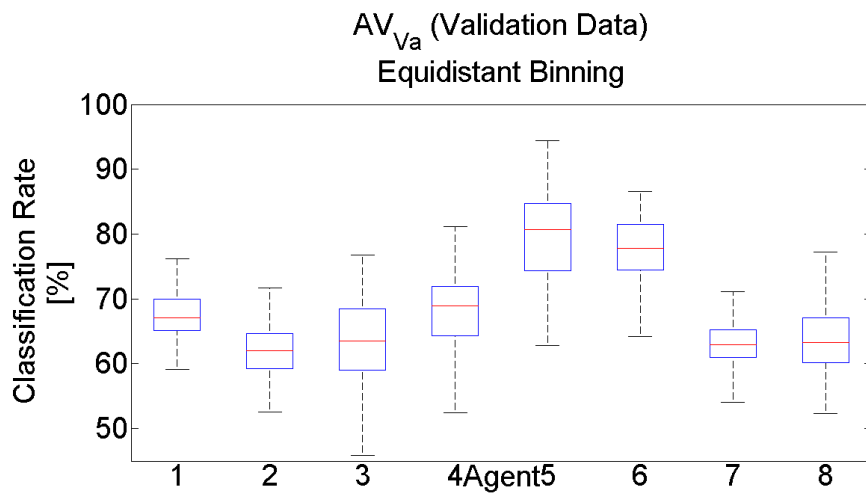


Figure 53: Boxplot of the classification rate for validation data per agent.

6.2.2 Generalization Capabilities

As the validation set is used neither for training nor for model selection, it is seen as a realistic estimation of the generalization capabilities of a trained network. Anyhow, this assumes that the states of all classes are represented in each of the three data sets. In case of the used 150 Tahitian pearls this cannot be guaranteed, due to the large variety of occurring colors and color combinations.

In Figure 54, the statistical distribution of the difference between the classification rate of validation data at the state of maximum generalization in regards of the test set (AV_{Va}) and the maximum classification rate of the validation set (AVX_{Va}) is shown. It can be seen, that the classification rate of the validation data at the state of maximum classification rate of the test data is in the average significantly lower than the maximum possible classification rate of the validation data. A difference of up to 23% is possible. This means that the network is at a certain state capable of predicting the labels of the unseen validation data in an adequate range, but this state does not correspond to the optimum in regards of the test data. The only logical reason is that the pearls represented by the test data do not correspond to the pearls represented by the validation data. This means for future experiments that either more pearls have to be evaluated to increase the possibility that similar pearls are represented in each of the three data sets or exhaustive cross-validation should be used instead of splitting the data in three sets; preferably even both.

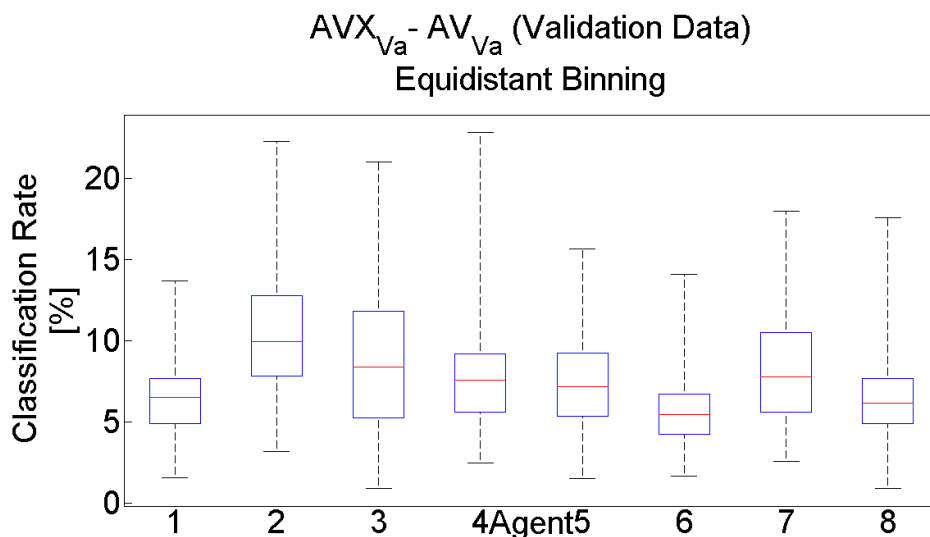


Figure 54: Statistical distribution of the difference between the classification rate of the validation set at the maximum of test set classification (AV_{Va}) and maximum of the classification rate of the validation set (AVX_{Va}).

6.2.3 Preliminary Maximum Classification Results

Out of all experimental results of each trained ANN the maximum classification rate of the test data was identified for each of the 8 human classifications. The according rates are shown in Figure 55. The corresponding histogram orientations and binning strategies are listed in Figure 56. According to the shown results, and seeing that several optimization possibilities exist (adapted ANN topology for each feature, number of bins, additional chromatic indices, etc.) it can be stated that it is generally possible to classify Tahitian pearls based on their perceived color with normalized *rgb* histogram binning and Artificial Neural Networks.

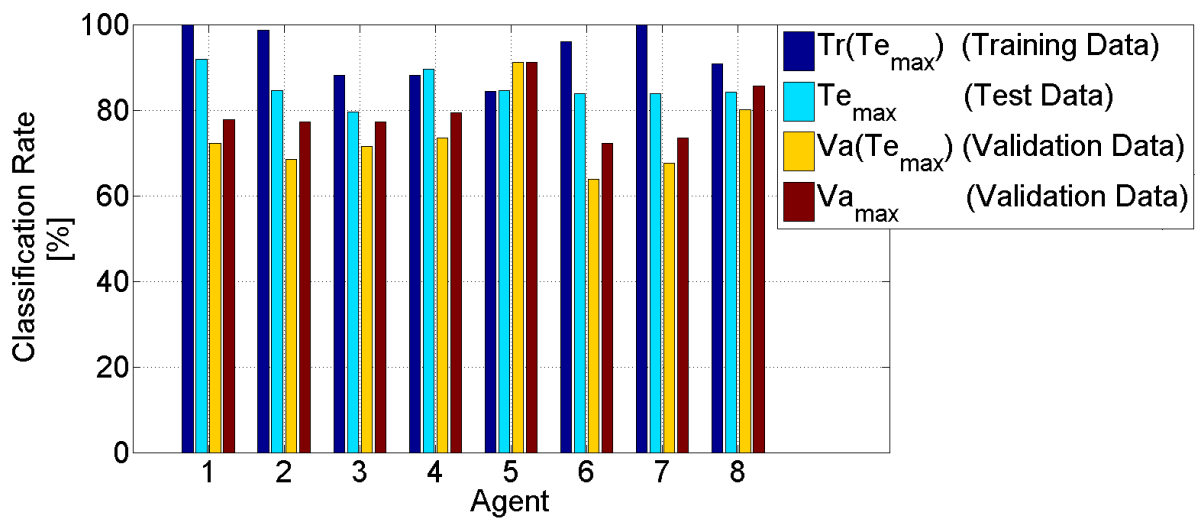


Figure 55: Preliminary maximum classification results out of all experimental results for the 8 human classifications.

Agent	optimal f_α	Optimal binning
1	f_{13}	equidistant
2	f_9	topological
3	f_{154}	topological
4	f_{11}	equidistant
5	f_{15}	equidistant
6	f_{85}	equidistant
7	f_0	topological
8	f_2	topological

Figure 56: Parameters of preliminary optimal classification results per human classification.

7 Conclusion

In this part of the thesis, the results of our research on color classification of Tahitian pearls were presented. Besides investigating the general feasibility of color classification of Tahitian pearls based on human perception, one of the main foci of the presented research lies on theoretical aspects of normalized *rgb* histogram binning.

A quintessence of the presented work is the formalization of chromatic index calculation in the context of normalized *rgb* histogram binning. It had been shown that every chromatic index based on a linear combination of normalized *rgb* channels can be expressed by a single variable; an angle that corresponds to the human perceptual parameter Hue.

The hypothesis that the descriptive power of a chromatic index depends on the data distribution was investigated with experiments using normalized *rgb*-histogram binning with 180 different chromatic index combinations for color classification of Tahitian pearls with Artificial Neural Networks. Separate human classifications of 7 agents that classified a set of 150 Tahitian pearls were used along with the majority vote of all 7 human classifications. This means in total 8 human classifications were used to investigate the influence of different chromatic indices on the classification.

The results show that the choice of chromatic indices affects significantly the classification performance of an ANN with a given topology. The global performance varies within a range of up to 20% over the tested feature vectors. Furthermore does the classification accuracy of each class depend on the chosen index, with variations up to 100% between different feature vectors.

These findings are of great importance for computer vision applied to color object classification. Currently, only a handful of chromatic indices are used in the literature, which is a drastic limitation of possible classification results, seeing the large variance of classification rates over the whole range of possible indices. Especially the use of the same chromatic indices, such as the most popular *r*- and *g*-channels, for applications with different data distributions such as color texture description, image segmentation, vehicle color classification or skin detection stands in sharp contrast to the results of our experiments.

In consequence of the experimental results it is of importance to investigate methods to mathematically identify optimal chromatic indices for a given application. For this purpose the formalized chromatic index calculation could be an essential help. It has to be mentioned

that our analysis was done in regards of normalized *rgb* binning, but the shown results imply the data dependencies of chromatic indices in general, which means the results are of importance for any approach in which normalized *rgb* space indices are used (as for example *rg-SIFT*).

In the literature, the specific topological features of the normalized *rgb* space are partially known. But so far, the effect when considering these features for histogram based color object classification had not been analyzed. In this thesis, topological binning is proposed which takes into account the non-uniform distribution of normalized *rgb* vectors. Its effect on the color classification of Tahitian pearls was investigated. In certain cases, topological binning had a positive impact on the classification rate independently of histogram orientation, with an increase of classification accuracy of up to 18%. As this was not the case for all used human classifications, a general application of topological rather than equidistant binning can so far not be suggested. But seeing the significant impact on certain classifications, topological binning should at least be considered in any application of normalized *rgb* histogram binning.

Even though the conducted experiments were designed primarily to investigate theoretical aspects of normalized *rgb* histogram binning, and hence the ANN topology was not optimized for all used feature vectors, the results allow a preliminary estimation of the expected range of classification accuracy. The average classification rate over all tested feature vectors is distributed for all 8 human classifications around 90% for training data and around 70% for test and validation data, showing that the applied method of *rgb* histogram binning in combination with ANN is generally suitable for the classification of Tahitian pearls based on their perceived color.

8 Future Work

As the possibilities of feature vector generation based on normalized *rgb* histogram binning are theoretically infinite, the brute force approach used in our experiments is not suitable for a standard implementation in computer vision. One of the main questions is how to obtain ideal feature vectors based on normalized *rgb* histogram binning for a given application. As the experiments have shown that the descriptive power of chromatic indices are data dependent, statistical methods such as for example principal component analysis of the data distribution in the rotated Maxwell triangle might be useful to obtain indices that describe ideally the distribution of one object or one class. Another idea is to use linear Support Vector Machine within the rotated Maxwell triangle to obtain chromatic indices that ideally differentiate between different objects or color classes.

In the experiments the bin size of histograms was empirically fixed to 16 bins. As the bin size determines in large parts the precision of data representation of a histogram, the influence of varying the bin size will be analyzed. This will be done specifically to further explore the possibilities of the proposed topological binning, as the positive influence of this approach was partially significant.

Once the feature vector generation is optimized, the ANN topology will be adapted to specific features, to explore if the obtained results with fixed ANN can be further improved.

Two factors that were not considered in our work are image acquisition conditions and surface quality of the pearl. The influence of image acquisition parameters, specifically illumination parameters as well as possible segmentation steps prior to feature vector generation will be explored in the future. But seeing that the experimental results showed generally good classification accuracy, the optimization of the used methods is prioritized.

List of Figures

Figure 1: Tahitian Pearls of different and partially multiple colors.	175
Figure 2: Example images for 7 of the 8 used color classes.	177
Figure 3: Workflow of the experimental classification procedure.	179
Figure 4: Variance of global classification rate depending on the used histogram orientation.	179
Figure 5: Minimum and maximum classification rate for the color class ‘Blue’ over the whole range of tested feature vectors for each human classification.	180
Figure 6: Difference of topological and equidistant binning over all tested feature vectors for 1 human classification.	180
Figure 7: Preliminary optimal results for the artificial classification based on 8 human classifications.	181
Figure 8: Schema of RGB vector normalization.	185
Figure 9: The Maxwell triangle in the RGB space and its 2-dimensional representation after rotation. A division of the Maxwell triangle with planes (left) is equivalent to a division of the 2-dimensional triangle with lines (right).	186
Figure 10: Schema of binning the <i>r</i> -channel of a normalized <i>rgb</i> data distribution in a histogram of 5 equidistant bins.	187
Figure 11: Equivalency between <i>r</i> -channel binning by using scalars in the <i>r</i> -channel (left), planes in the RGB space (middle) and lines in the rotated Maxwell triangle.	188
Figure 12: Concatenated <i>rg</i> -Histogram (right) obtained by concatenating the two independent <i>r</i> - and <i>g</i> -histograms.	189
Figure 13: <i>rg</i> -histogram generation as a division of the rotated Maxwell triangle in rhombs.	190
Figure 14: <i>rg</i> -binning in the RGB space.	191
Figure 15: Two different data distributions (first column and second column) resulting in the same histogram distribution when binned with <i>rg</i> channels (first row) but different histogram distribution when binned with <i>gb</i> channels (second row).	192
Figure 16: Alternative chromatic indices used in the literature and their histograms in the 2D chromatic triangle.	194
Figure 17: The same <i>rgb</i> histogram with 2 bins obtained with two ‘different’ chromatic indices.	196
Figure 18: Normal vector and corresponding plane obtained by rotating n_0 by 240° (left) and corresponding representation in the rotated Maxwell triangle (right).	197
Figure 19: Non-uniform distance between subsequent normalized <i>b</i> -values, calculated for all possible <i>b</i> values of the RGB space.	200

Figure 20: Non-uniform occurrence frequency of unique b values, calculated for all possible b values of the RGB space.	200
Figure 21: Occurrence frequency for equidistant (left) and topological binning (right) of all possible b values of the 8 bit RGB space in 16 bins.	201
Figure 22: Different bin boundaries for equidistant and topological binning of the normalized b channel with 16 bins.	201
Figure 23: The device PackshotCreator (left) used for image acquisition, original images of one pearl captured from three different view angles (top), and the corresponding segmented pearl (bottom).	205
Figure 24: Statistical image values after segmentation.	205
Figure 25: Pearls classified by majority vote of all 7 agents in the 7 classes of the first column.	206
Figure 26: Distribution of majority votes (top) and amount of different class assignments (bottom) for 150 Tahitian pearls classified by 7 agents.	207
Figure 27: Workflow of the conducted experiments.	209
Figure 28: Topology of a feed-forward neural network with one hidden layer.	210
Figure 29: Schema of the learning procedure of ANN by weight adaption.	211
Figure 30: The effect of over-fitting during the ANN learning procedure.	212
Figure 31: Applied general feature configuration: Concatenated histogram of the rI -histogram (top left) and of the gI -histogram (top right).	214
Figure 32: 5 of 180 tested histogram orientations that include all main chromatic indices used in the literature.	216
Figure 33: Number of neurons in the hidden layer for each test series.	217
Figure 34: Schema of ANN training visualizing the states at which the corresponding evaluation values are obtained.	218
Figure 35: ID of evaluation values (1 st column), their brief description (2 nd column), when they are obtained (3 rd column) and their use for evaluation (4 th column).	219
Figure 36: Pseudocode of experiments.	221
Figure 37: Classification performance for feature vectors based on the three normalized rgb channels.	223
Figure 38: Average classification performance per feature orientation for all 7 agents and the majority vote.	224
Figure 39: Global classification performance for feature vectors based on the three normalized rgb channels and maximum performance.	225
Figure 40: Histogram orientation at maximum global ANN performance per human classification (correspond to red bars in Figure 39).	225

Figure 41: Maximum and minimum global performance for class ‘Aubergine’ per agent. ...	226
Figure 42: Maximum and minimum global performance for class ‘White’ per agent.	226
Figure 43: Maximum and minimum global performance for class ‘Blue’ per agent.	226
Figure 44: Maximum and minimum global performance for class ‘Champagne’ per agent.	227
Figure 45: Maximum and minimum global performance for class ‘Gray’ per agent.	227
Figure 46: Maximum and minimum global performance for class ‘Yellow’ per agent.	227
Figure 47: Maximum and minimum global performance for class ‘Peacock’ per agent.	228
Figure 48: Maximum and minimum global performance for class ‘Green’ per agent.	228
Figure 49: Global performance of classes ‘Aubergine and ‘Blue’ for agent one for all feature vectors.	229
Figure 50: Equidistant binning (blue lines) vs topological binning (green lines) over all feature vectors for all agents.	230
Figure 51: Boxplot of the classification rate for training data per agent.	233
Figure 52: Boxplot of the classification rate for test data per agent.	233
Figure 53: Boxplot of the classification rate for validation data per agent.	233
Figure 54: Statistical distribution of the difference between the classification rate of the validation set at the maximum of test set classification (AV_{VA}) and maximum of the classification rate of the validation set (AVX_{VA}).	234
Figure 55: Preliminary maximum classification results out of all experimental results for the 8 human classifications.	235
Figure 56: Parameters of preliminary optimal classification results per human classification.	235

Bibliography

- AGA12 Agatonovic-Kustrin, S., & Morton, D. W. (2012). *The use of UV-visible reflectance spectroscopy as an objective tool to evaluate pearl quality*. *Marine drugs*, 10(7), 1459-1475
- AGA15 Agatonovic-Kustrin, S., & Morton, D. W. (2015). *The use of probabilistic neural network and UV reflectance spectroscopy as an objective cultured pearl quality grading method*. *Modern Chemistry and Applications*, 3(152), 2.
- AVI15 Avila, F., Mora, M., Oyarce, M., Zuñiga, A., & Fredes, C. (2015). *A method to construct fruit maturity color scales based on support machines for regression: Application to olives and grape seeds*. *Journal of Food Engineering*, 162, 9-17.
- BAT00 Batlle, J., Casals, A., Freixenet, J., & Marti, J. (2000). *A review on strategies for recognizing natural objects in colour images of outdoor scenes*. *Image and Vision Computing*, 18(6), 515-530
- BAT89 Battiti, R. (1989). *Accelerated backpropagation learning: Two optimization methods*. *Complex systems*, 3(4), 331-342.
- BRO11 Brown, M., & Süsstrunk, S. (2011, June). *Multi-spectral SIFT for scene category recognition*. In *Computer Vision and Pattern Recognition (CVPR), 2011 IEEE Conference on* (pp. 177-184). IEEE.
- BRU02 Brun, Luc & Tremeau, Alain. , *Digital Color Imaging Handbook*. Chapter 9: Color quantization , pages 589-637 , Electrical and Applied Signal Processing , CRC Press 2002 .
- BUS08 Busin, L., Vandenbroucke, N., & Macaire, L. (2008). *Color spaces and image segmentation*. *Advances in imaging and electron physics*, 151(1), 1.
- CAO10 Cao, Y. L., Zheng, H. W., Yang, J. X., & He, Y. F. (2010, September). *Automatic Shape Grading of Pearl Using Machine Vision Based Measurement*. In *Key Engineering Materials* (Vol. 437, pp. 389-392).
- CER17 Cernadas, E., Fernández-Delgado, M., González-Rufino, E., & Carrión, P. (2017). *Influence of normalization and color space to color texture classification*. *Pattern Recognition*, 61, 120-138.
- CHE01 Cheng, H. D., Jiang, X. H., Sun, Y., & Wang, J. (2001). *Color image segmentation: advances and prospects*. *Pattern recognition*, 34(12), 2259-2281.
- CHE14 Chen, P., Bai, X., & Liu, W. (2014). *Vehicle color recognition on urban road by feature context*. *IEEE Transactions on Intelligent Transportation Systems*, 15(5), 2340-2346.
- CLA09 Clarke, B., Fokoue, E., & Zhang, H. H. (2009). *Principles and theory for data mining and machine learning*. Springer Science & Business Media
- CUI15 Cuif, J. P., & Dauphin, Y. (1996). *Occurrence of mineralization disturbances in nacreous layers of cultivated pearls produced by *Pinctada margaritifera* var. *cumingi* from French Polynesia. Comparison with reported shell alterations*. *Aquatic Living Resources*, 9(2), 187-193.

- DU05 Du, C. J., & Sun, D. W. (2005). *Comparison of three methods for classification of pizza topping using different colour space transformations*. *Journal of Food Engineering*, 68(3), 277-287.
- EGM02 Egmont-Petersen, M., de Ridder, D., & Handels, H. (2002). *Image processing with neural networks—a review*. *Pattern recognition*, 35(10), 2279-2301.
- FON14 Font, D., Tresanchez, M., Pallejà, T., Teixidó, M., Martínez, D., Moreno, J., & Palacín, J. (2014). *An image processing method for in-line nectarine variety verification based on the comparison of skin feature histogram vectors*. *Computers and Electronics in Agriculture*, 102, 112-119.
- GLO10 Glorot, X., & Bengio, Y. (2010, May). *Understanding the difficulty of training deep feedforward neural networks*. In *Aistats* (Vol. 9, pp. 249-256).
- GOL12 Golzarian, M. R., Lee, M. K., & Desbiolles, J. M. A. (2012). *Evaluation of color indices for improved segmentation of plant images*. *Transactions of the ASABE*, 55(1), 261-273.
- GRO06 Groeneweg, N. J., de Groot, B., Halma, A. H., Quiroga, B. R., Tromp, M., & Groen, F. C. (2006). *A fast offline building recognition application on a mobile telephone*. In *International Conference on Advanced Concepts for Intelligent Vision Systems* (pp. 1122-1132). Springer Berlin Heidelberg.
- HAS15 Hassanat, A. B., Alkasassbeh, M., Al-awadi, M., & Esra'a, A. (2015, April). *Colour-based lips segmentation method using artificial neural networks*. In *Information and Communication Systems (ICICS), 2015 6th International Conference on* (pp. 188-193). IEEE.
- HAS16 Hassanat, A. B., Alkasassbeh, M., Al-awadi, M., & Esra'a, A. A. (2016). *Color-based object segmentation method using artificial neural network*. *Simulation Modelling Practice and Theory*, 64, 3-17.
- HAY05 Haykin, S. (2004). *Neural Networks: A comprehensive foundation*. *Neural Networks*, 2(2004).
- HER16 Hernández-Hernández, J. L., García-Mateos, G., González-Esquivá, J. M., Escarabajal-Henarejos, D., Ruiz-Canales, A., & Molina-Martínez, J. M. (2016). *Optimal color space selection method for plant/soil segmentation in agriculture*. *Computers and Electronics in Agriculture*, 122, 124-132.
- IZE08 Izenman, A. J. (2008). *Modern multivariate statistical techniques* (Vol. 1). New York: Springer.
- JOB79 Joblove, G. H., & Greenberg, D. (1978, August). *Color spaces for computer graphics*. In *ACM siggraph computer graphics* (Vol. 12, No. 3, pp. 20-25). ACM.
- KAK07 Kakumanu, P., Makrogiannis, S., & Bourbakis, N. (2007). *A survey of skin-color modeling and detection methods*. *Pattern recognition*, 40(3), 1106-1122.
- KEN69 Kennard, R. W., & Stone, L. A. (1969). *Computer aided design of experiments*. *Technometrics*, 11(1), 137-148.
- KEN76 Kender, J. R. (1976). *Saturation, Hue, And Normalized Color: Calculation, Digitization Effects, and Use*. Carnegie-Mellon Univ Pittsburgh Pa Dept Of Computer Science.

- LEE02 Lee, J. Y., & Yoo, S. I. (2002, June). *An elliptical boundary model for skin color detection*. In Proc. of the 2002 International Conference on Imaging Science, Systems, and Technology.
- LI13 Li, X., Hu, W., Shen, C., Zhang, Z., Dick, A., & Hengel, A. V. D. (2013). *A survey of appearance models in visual object tracking*. ACM transactions on Intelligent Systems and Technology (TIST), 4(4), 58.
- MAE04 Mäenpää, T., & Pietikäinen, M. (2004). *Classification with color and texture: jointly or separately?*. Pattern recognition, 37(8), 1629-1640.
- MAM10 Mamangkey, N. G. F., Agatonovic, S., & Southgate, P. C. (2010). *Assessing pearl quality using reflectance UV-Vis spectroscopy: does the same donor produce consistent pearl quality?*. Marine drugs, 8(9), 2517-2525.
- MEY11 Meyer, G. E. (2011). *Machine vision identification of plants*. Recent Trends for Enhancing the Diversity and Quality of Soybean Products. Krezhova D (ed.) Croatia: InTech.
- NAG94 Nagata, N., Kamei, M., & Usami, T. (1994). *Transferring Human Sensibilities to Machines-Sensitivity Analysis of Layered Neural Networks and Its Application to Pearl Color Evaluation*. In MVA (pp. 528-531).
- NAG97 Nagata, N., Dobashi, T., Manabe, Y., Usami, T., & Inokuchi, S. (1997). *Modeling and visualization for a pearl-quality evaluation simulator*. Visualization and Computer Graphics, IEEE Transactions on, 3(4), 307-315.
- PED06 Pedreschi, F., Leon, J., Mery, D., & Moyano, P. (2006). *Development of a computer vision system to measure the color of potato chips*. Food Research International, 39(10), 1092-1098.
- REI10 Reitermanova, Z. (2010). Data splitting. *WDS's 10 proceedings of contributed papers, Part, 1*, 31-36.
- ROM12 Romani, S., Sobrevilla, P., & Montseny, E. (2012). *Variability estimation of hue and saturation components in the HSV space*. Color Research & Application, 37(4), 261-271.
- ROS04 Rosenberger, C., Emile, B., & Laurent, H. (2004). *Calibration and quality control of cherries by artificial vision*. Journal of Electronic Imaging, 13(3), 539-546.
- SAN10 Van De Sande, K., Gevers, T., & Snoek, C. (2010). *Evaluating color descriptors for object and scene recognition*. IEEE transactions on pattern analysis and machine intelligence, 32(9), 1582-1596.
- SOR03 Soriano, M., Martinkauppi, B., Huovinen, S., & Laaksonen, M. (2003). *Adaptive skin color modeling using the skin locus for selecting training pixels*. Pattern Recognition, 36(3), 681-690.
- SUN03 Sun, Y., & Fisher, R. (2003). *Object-based visual attention for computer vision*. Artificial Intelligence, 146(1), 77-123.
- TAN14 Tang, Y. P., Shao-jie, X., & Zhi-liang, Z. (2014). *Research on Pearl Detecting and Grading Based on Monocular Multi-view Machine Vision*. British Journal of Applied Science & Technology, 4(15), 2136

- THA02 Thaper, N., Guha, S., Indyk, P., & Koudas, N. (2002, June). *Dynamic multidimensional histograms*. In Proceedings of the 2002 ACM SIGMOD international conference on Management of data (pp. 428-439). ACM
- TIA09 Tian, C. (2009, November). *A computer vision-based classification method for pearl quality assessment*. In Computer Technology and Development, 2009. ICCTD'09. International Conference on (Vol. 2, pp. 73-76). IEEE.
- VER00 Vertan, C., & Boujemaa, N. (2000). *Color texture classification by normalized color space representation*. In Pattern Recognition, 2000. Proceedings. 15th International Conference on (Vol. 3, pp. 580-583). IEEE.
- VEZ03 Vezhnevets, V., Sazonov, V., & Andreeva, A. (2003, September). *A survey on pixel-based skin color detection techniques*. In Proc. Graphicon (Vol. 3, pp. 85-92).
- WAN08 Wang, J., & Yagi, Y. (2008). *Integrating color and shape-texture features for adaptive real-time object tracking*. IEEE Transactions on Image Processing, 17(2), 235-240.
- WIL00 Wilson, J. N., & Ritter, G. X. (2000). *Handbook of computer vision algorithms in image algebra*. CRC press.
- WU12 Wu, W., May, R., Dandy, G. C., & Maier, H. R. (2012). *A method for comparing data splitting approaches for developing hydrological ANN models* (Doctoral dissertation, International Environmental Modelling and Software Society (iEMSs)).
- WYS00 Wyszeci, G., & Stiles, W. S. (2000). *Color science* (2nd edition). New York: Wiley.
- YAN95 Yang, J., & Waibel, A. (1995). *Tracking human faces in real-time* (No. CMU-CS-95-210). Carnegie-Mellon Univ Pittsburgh Pa School Of Computer Science
- ZHU13 Zhu, C., Bichot, C. E., & Chen, L. (2013). *Image region description using orthogonal combination of local binary patterns enhanced with color information*. Pattern Recognition, 46(7), 1949-1963.